UNSTEADY GALLOPING OF BRIDGE DECKS DURING THE LAUNCHING PHASE

Dissertation
submitted to and approved by the

Faculty of Architecture, Civil Engineering and Environmental Sciences
Technische Universität Braunschweig

and the

Department of Civil and Environmental Engineering
University of Florence

in candidacy for the degree of a
Doktor-Ingenieur (Dr.-Ing.) /
Dottore di Ricerca in Civil and Environmental Engineering*)

by
Cong Chen
born 28 December 1989
from Sichuan, China

Submitted on	16 April 2021
Oral examination on	18 June 2021
Professorial advisors	Prof. Dr.-Ing. Klaus Thiele Prof. Dr.-Ing. Gianni Bartoli

2021

*) Either the German or the Italian form of the title may be used.

Von der Fakultät Architektur, Bauingenieurwesen und Umweltwissenschaften der
Technischen Universität Carolo-Wilhelmina zu Braunschweig
zur Erlangung des Grades
eines Doktor-Ingenieurs (Dr.-Ing.)
genehmigte Dissertation

Eingereicht am:	16. April 2021
Disputation am:	18. Juni 2021
Berichterstatter:	Prof. Dr.-Ing. Klaus Thiele
	Prof. Dr.-Ing. Gianni Bartoli

To my dear grandpa, Guangzhi Chen

“carving words into stone”
Death’s End (The Three-Body Problem III), by Cixin Liu

Preface

This doctoral thesis was written during the last period of my stay at the Institute of Steel Structures, TU-Braunschweig. I was financially supported by the China Scholarship Council to carry out a doctoral study in Germany. My research began with the fatigue problem of steel structures, but wind engineering gradually attracts me more and I finally decided to work in this area.

Prof. Klaus Thiele, my supervisor, deserves my first and most gratitude, continuously supporting me and this research from every aspect. Moreover, under his supervision, I was given the most freedom to pursue my research interests. I also want to thank Prof. Mathias Clobes, for introducing this research topic to me and continuously encouraging me to carry on with it.

I am very lucky that I have joined the international Ph.D. program between TU-Braunschweig and the University of Florence. With this bridge, I am able to collaborate with the famous wind engineering group at the University of Florence. I am very grateful to Prof. Gianni Bartoli being my Italian tutor, and special thanks must be given to Prof. Claudio Mannini for the many deep and inspiring discussions between us. Thanks to Bernardo Nicese, Dr. Giacomo Zini, Dr. Andrea Giachetti, Dr. Tommaso Massai, Dr. Antonino Maria Marra, Niccolò Barni, and all the other Italian colleagues, I have enjoyed my exchange stay in Florence with their accompany.

Thanks are given to my colleagues at the Institute of Steel Structures of TU-Braunschweig, Dr. Ding Cai, Jonas Pons, Konrad Ritter, Dr. Julian Unglaub, Dr. Thomas Höbbel, Dr. Florian Minuth-Hadi, Anzhi Wang, Niccolo Wieczorek, Marcel Grabowski, Hendrik Jahns, Florian Begemann and all the other colleagues. With them, a pleasant working atmosphere was developed and many impressive activities were organized at the Institute. Among these, the road-bike cycling will be definitely one of the best memories in my lifetime. I also would like to appreciate the support from the laboratory, as well as the administrative staff of the institute.

I appreciate Prof. Craig Miller from the University of Western Ontario and Prof. Acir Loredo-Souza from the Federal University of Rio Grande do Sul as the external reviewers. Comments from them helped improve this thesis a lot. Last, but always most importantly, to my family and friends, thank you for always being there.

Braunschweig, July 2021 Cong Chen

Abstract

The present work deals with the unsteady galloping instability, which arises at low reduced flow velocities, for steel-concrete composite bridge decks during the incremental launching phase. In this particular situation, the light weight and bluff shape of the steel box, which is normally first launched, imply a high proneness to the risk of unsteady galloping. The main goal of this thesis is to understand the unsteady galloping with respect to these special cross sections, which have not been investigated in depth before, and to develop an analytical approach for the modeling of unsteady galloping as a basis for design of bridges.

Wind tunnel tests on three sectional models, among which are a generic bridge deck model with typical open cross section and two reference cylinder models, confirmed the high proneness to unsteady galloping instability for the particular situation of bridge launching. Especially, the typical unsteady galloping which arises due to the interaction with Kármán-vortex induced vibration was observed at the 4° mean flow incidence of the bridge deck model, fixing the galloping onset at the Kármán-vortex resonance wind speed up to a quite high Scruton number (the mass-damping parameter). Moreover, the sensitivity of unsteady galloping behaviors to mean flow incidence was highlighted. At the null mean flow incidence of the bridge deck model, the unsteady galloping was initiated in less understandable manner, being the onset velocity clearly higher than the Kármán-vortex resonance one even for a very low Scruton number.

Subsequently, mathematically modeling the unsteady galloping was carried out, with a modified form of Taumra's nonlinear wake oscillator model. Satisfying predictions have been achieved not only for a 2:1 rectangular cylinder, but also for the bridge deck model at its 4° mean flow incidence. In particular, the typical unsteady galloping behavior, that lower than a certain value of Scruton number galloping arises at the Kármán-vortex resonance wind speed, is well captured by the wake oscillator model. Attention was also paid to the so-called physical considerations in the wake oscillator model. Further modifications for the wake oscillator model were consequentially proposed, exhibiting better agreements with the physics of the near-wake of sharp-edged bluff body, maintaining at the same time a good capability for the predictions of unsteady galloping behaviors.

Finally, the wake oscillator model was further extended for continuous structural system, based on coupling multiple wake oscillators to the structural system via finite element method.

A case study, concerning a steel-concrete composite bridge during the critical launching phase, was presented. In particular, by taking into account the aerodynamic contributions of a lattice launching nose, the potentiality of efficiently suppressing the galloping instability through aerodynamic optimization for the launching nose was revealed in the case study. This has promoted consequent wind tunnel tests on the further optimized launching nose, which combined with numerical predictions from the wake oscillator model further confirmed the aforementioned potentiality.

Contents

Notations

Symbols for matrix and vector are extra indicated with bold font

Greek Variables

α	wind angle of attack or torsional degree of freedom
α_0	mean wind angle of attack (for oscillation body)
β, λ	coefficients in Tamura's nonlinear wake oscillator model
$\boldsymbol{\phi_i}$	mode shape vector for structure
$\boldsymbol{\Phi}, \boldsymbol{\Phi_e}$	mode shape matrix for structure, and the expanded one
$\boldsymbol{\psi_s}, \boldsymbol{\psi}_{sr}$	displacement vector for a structural system, and its reduced form due to boundary conditions
$\boldsymbol{\psi_t}, \boldsymbol{\psi}_{tr}$	displacement vector for combined system of structure and wake oscillators, and its reduced form due to boundary conditions
$\boldsymbol{\psi}_{tn}$	the normalized forms of $\boldsymbol{\psi}_{tr}$, by expanded mode shape matrix $\boldsymbol{\Phi_e}$
$\boldsymbol{\vartheta}, \boldsymbol{\vartheta_r}$	displacement vector for wake oscillators, and its reduced form due to boundary conditions
$\boldsymbol{\xi}$	vector collected the generalized displacement in mode space
δ_0	logarithmic mechanical damping
δ_s	shear layer thickness
ϵ	fraction of vorticity in shear layer being transferred to downstream mature vortex
γ	mode shape factor in VIV theories
μ	dynamic viscosity of flow
ω	circular frequency
ω_0	circular natural frequency
ϕ	mode shape function
$\Phi(\tilde{\tau})$	*Wagner's function*

ρ	air density
ρ_r	correlation coefficient between two points of a distance of r
$\rho_{u,u}$	normalized auto-correlation function of $u(t)$
σ_L	standard deviation of fluctuation lift due to vortex shedding
σ_u	standard deviation of fluctuation part of longitudinal wind speed
τ	reduced time, defined through body's natural circular frequency $\tau = \omega_0 t$
τ_{lag}	reduced time lag
$\tilde{\mu}$	tiny number
$\tilde{\tau}$	reduced time defined as Ut/b_h
υ	ratio of V to V_r
υ_s	ratio of U_S to U
Γ	circulation of a vortex
φ	phase angle
φ_{lag}	phase lag
φ_{Lm}	phase angle by which motion-induced lift leads body's displacement, defined in a range $-\pi \leq \varphi_{Lm} \leq \pi$
ϑ	near-wake inclination angle in Tamura's nonlinear wake oscillator model
ϑ_{eff}	effective rotation angle of near-wake lamina for generating vortex shedding force on oscillation body
ξ_i	the generalized displacement in mode space (corresponding to its mode shape vector $\boldsymbol{\phi_i}$)
ζ_0	mechanical critical damping ratio

Latin variables and Constants

$\widetilde{U}, \widetilde{V}$	instantaneous longitudinal and lateral wind speed
$\bar{c}_i, \tilde{c}_i, \bar{k}_i$	diagonal elements for$\bar{\boldsymbol{C}}$, $\tilde{\boldsymbol{C}}$ and $\bar{\boldsymbol{K}}$ matrices
$\bar{r}$	$r = \frac{\bar{Y}_s}{V}$
$\bar{Y}$	non-dimensional amplitude of Y
$\bar{Y}_s$	steady-state non-dimensional amplitude
$\bar{\boldsymbol{I}}_{\boldsymbol{r}}, \bar{\boldsymbol{C}}_{\boldsymbol{r}}, \tilde{\boldsymbol{C}}_{\boldsymbol{r}}, \bar{\boldsymbol{K}}_{\boldsymbol{r}}$	the reduced forms of$\bar{\boldsymbol{I}}$, $\bar{\boldsymbol{C}}$, $\tilde{\boldsymbol{C}}$ and $\bar{\boldsymbol{K}}$, after applying boundary conditions
$\bar{\boldsymbol{I}}, \bar{\boldsymbol{C}}, \tilde{\boldsymbol{C}}, \bar{\boldsymbol{K}}$	mass of inertia, linear damping, nonlinear damping and stiffness matrices for multiple wake oscillators

$\hat{\boldsymbol{A}}_{\boldsymbol{r}}$,$\hat{\boldsymbol{B}}_{\boldsymbol{r}}$, $\hat{\boldsymbol{G}}_{\boldsymbol{r}}$, $\hat{\boldsymbol{H}}_{\boldsymbol{r}}$	the reduced forms of $\hat{\boldsymbol{A}}$,$\hat{\boldsymbol{B}}$, $\hat{\boldsymbol{G}}$ and $\hat{\boldsymbol{H}}$, after applying boundary conditions
$\hat{\boldsymbol{A}}$,$\hat{\boldsymbol{B}}$, $\hat{\boldsymbol{G}}$, $\hat{\boldsymbol{H}}$	matrices responsible for the coupling between structure and wake oscillators
$\boldsymbol{M_s}$, $\boldsymbol{C_s}$, $\boldsymbol{K_s}$	mass, damping and stiffness matrices for a structural system
$\boldsymbol{M_t}$, $\boldsymbol{C1_t}$, $\boldsymbol{C3_t}$, $\boldsymbol{K_t}$	global mass, linear-damping, nonlinear-damping and stiffness matrices, for combined degrees of freedom of structure and wake oscillators
$\boldsymbol{M}_{sr}$, $\boldsymbol{C}_{sr}$, $\boldsymbol{K}_{sr}$	the reduced forms of $\boldsymbol{M_s}$, $\boldsymbol{C_s}$ and $\boldsymbol{K_s}$, after applying boundary conditions
$\boldsymbol{M}_{tn}$, $\boldsymbol{C1}_{tn}$, $\boldsymbol{C3}_{tn}$, $\boldsymbol{K}_{tn}$	the normalized forms of $\boldsymbol{M}_{tr}$, $\boldsymbol{C1}_{tr}$, $\boldsymbol{C3}_{tr}$ and $\boldsymbol{K}_{tr}$, by expanded mode shape matrix $\boldsymbol{\Phi_e}$
$\boldsymbol{M}_{tr}$, $\boldsymbol{C1}_{tr}$, $\boldsymbol{C3}_{tr}$, $\boldsymbol{K}_{tr}$	the reduced forms of $\boldsymbol{M_t}$, $\boldsymbol{C1_t}$, $\boldsymbol{C3_t}$ and $\boldsymbol{K_t}$, after applying boundary conditions
$\boldsymbol{q_s}$	external force vector for a structural system
$\boldsymbol{q_t}$, $\boldsymbol{q}_{tr}$	external force vector for combined system of structure and wake oscillators, and its reduced form due to boundary conditions
$\boldsymbol{q}_{QS}$, $\boldsymbol{q}_{QSr}$	quasi-steady transverse force vector, and its reduced form due to boundary conditions
$\boldsymbol{q}_{tn}$	the normalized forms of $\boldsymbol{q}_{tr}$, by expanded mode shape matrix $\boldsymbol{\Phi_e}$
$\hat{a}_i$, $\hat{b}_i$, $\hat{g}_i$, $\hat{h}_i$	elements for $\hat{\boldsymbol{A}}$, $\hat{\boldsymbol{B}}$, $\hat{\boldsymbol{G}}$ and $\hat{\boldsymbol{H}}$ matrices
$\hat{e}_i$	coefficent for elements in $\boldsymbol{q}_{QS}$ vector
$\overline{I}_u$, $\overline{I}_v$, $\overline{I}_w$	averaged I_u, I_v and I_w, of spatially discrete points
$\overline{L}_u$	averaged L_u of spatially discrete points
$\overline{U}$	averaged U of spatially discrete points
$\tilde{a}$, $\tilde{b}$, $\tilde{c}$	parameters in Corless&Parkinson's model
$\tilde{w}$	downwash
a	combined with b_h to indicate of the position of elastic center, for elastically supported body
A_1	galloping factor according to quasi-steady thoery
A_{i}	coefficients of polynomials approximating C_{Fy}-α curve (galloping factor A_1 coresponds to the linear slope)
$A_{1,equ}$	equivalent galloping factor for a continuous system
b	width of wind tunnel model or bridge deck (chord length)
b_h	half chord length
b_{avg}	averaged value of top and bottom widths of a wind tunnel model

$C(k)$, $F(k)$, $G(k)$	*Theodorsen's circulation function*, as well as its real and imaginary part
c_α	damping for torsional degree of freedom
C_D, C_L, C_M	drag, lift and moment coefficient (steady part)
c_g	width of the strip of turbulence grid
C'_L,c'_L	standard deviation of lift coefficient fluctuation for the entire prism body and for a unit length of the prism body
C_v	unsteady lift coefficient due to vortex exciting in Corless&Parkinson's model
c_y	damping for heaving degree of freedom
c_ϑ	cofficient related to the damping force for oscillation near-wake lamina, according to unsteady thin airfoil theory
C_{Fy},C_{Fy}^{QS}	transverse force coefficient according to quasi-steady theory
$C_{L,un}$	unsteady lift due to effective rotation angle of near-wake lamina, in Tamura's nonlinear wake oscillator model
C_{L0},c_{L0}	sinusoidal equivalent amplitude of the fluctuation lift coefficient due to vortex shedding for the entire prism body, and for a unit length of the prism body
$C_{lat,0}$	RMS value of the fluctuation lift coefficient due to vortex shedding
C_{Lm0}	amplitude of motion-induced lift coefficient
C_{LmR}, C_{LmI}	portion of C_{Lm0} in phase with $y(t)$, and in phase with $\dot{y}(t)$
C_{Lm}	motion-induced lift coefficient
C_{m0}	potential flow inertia coefficient in Luo&Bearman's model
C_{pb}	base pressure coefficient of bluff body
C_R	derived coefficient for F_R
d	height of wind tunnel model or bridge deck
D, L, M	aerodyanmic drag, lift and moment (steady part)
d_g	mesh size of turbulence grid
d_{ref}, l_{ref}	reference height and length for launching nose model
E	Young's modulus
e	combined with b_h to indicate of the position of gravity center, for elastically supported body
f	slope of the unsteady vortex-excited lift coefficient to the near-wake inclination ϑ in Tamura's nonlinear wake oscillator model
F_b	force reaction due to boundary support

F_L	restoring force of near-wake lamina
F_R	lift variation on near-wake lamina, due to its circulation change induced by vortex discharging
F_y	transverse aerodynamic force
G	gravity center of near-wake lamina
h	width of near-wake behind bluff-body
h^*	non-dimensional form of h, defined h/d
H_i^*, A_i^*	flutter derivatives
$H_n(k)$	Hänkel's functions
h_{avg}	$(h_{std}+h_{sk})/2$
h_{sk}	wake width determined by the distance between minus peaks of skewness of $\widetilde{U}$, being $\widetilde{U}$ transversely measured in the near-wake of bluff body
h_{std}	wake width determined by peak distance of $\text{std}(\widetilde{U})/U_0$, being $\widetilde{U}$ transversely measured in the near-wake of bluff body
I	mass moment of inertia at elastic center
i	$i=\sqrt{-1}$, or used as number counter
I_ϑ	mass moment of inertia for near-wake lamina
I_u, I_v, I_w	turbulence intensities
$I_{\vartheta,a}$	the added inertia of moment for oscillation near-wake lamina, according to unsteady thin airfoil theory
I_{xx}	second moment of area of a cross section
$J_n(k), Y_n(k)$	modified Bessel's functions of first and second kind
K	reduced frequency defined as $b\omega/U$
k	reduced frequency defined as $b_h\omega/U$
k_α	stiffness for torsional degree of freedom
k_ϑ	equivalent rotational stiffness for near-wake lamina
k_y	stiffness for heaving degree of freedom
l	half length of near-wake behind bluff-body
l^*	non-dimensional form of l, defined l/d
l_e	effective length of sectional wind tunnel model (between two end-plates)
l_F	vortex formation length
L_u	longitudinal turbulence integral length

l_V, h_V	streamwise distance and across-flow distance of vortex pairs
$l_{F,net}$	net near-wake length, starting from rear-face of body to the end of near-wake
$l_{FL,O}$	distance between pivot point O and F_L being applyied on near-wake lamina
l_{FL}	length scale for calulating the restoring force F_L on near-wake lamina
l_I	length scale for calulating I_ϑ of near-wake lamina
$l_{s,i}$	spanwise reference length for aerodynamic force calculation at node i of a continuous system)
L_{y1}, L_{y2}, L_{y3}	components of theoretical lift on thin airfoil
m	mass of body per unit length
m^*	mass ratio between body and air
M_ϑ	moment of an oscillation near-wake lamina, according to unsteady thin airfoil theory
M_e	effective oscillation mass of wind tunnel model
$M_{\alpha 2}$	component of theoretical moment on thin airfoil
m_{ij}, c_{ij}, k_{ij}	elements for $\boldsymbol{M_s}$, $\boldsymbol{C_s}$ and $\boldsymbol{K_s}$ matrices
N	nodes of a structural system
n	freqeuncy in Hz
n_0	natural frequency in still air
n_m	frequency at which a wind tunnel model is forced to vibrate
n_o	oscillation frequency in flowing air
N_r, N_{sr}, N_{wr}	total amount of degrees of freedom for the combined system of structure and wake oscillators, as well as the portion respectively for structure and for wake oscillators
n_{st}	Strouhal frequency
n_{vs}	oscillation frequency of near-wake lamina
O	pivot point of near-wake lamina
p	rotational degree of freedom of beam
R	$R = \bar{Y}^2$
r	spanwise distance between two points on slender body
Re	Reynolds number
S_{LL}	power spectral density of fluctuating lift
S_{uu}	power spectral density of u

S_{yy}	power spectral density of y
Sc	Scruton number defined with d^2
Sc^*	Scruton number defined with bd
St	Strouhal number defined with d
t	physical time
T_u	integral time length
t_{lag}	physical time lag
U	mean wind speed
u, v, w	fluctuation part of longitudinal, lateral, and vertical wind speed
u', v', w'	standard deviation of u, v and w
U_g	critical wind speed for across wind galloping, according to quasi-steady theory
U_i	mean wind speed at a single point
U_r	critical wind speed for Kármán-vortex induced vibration
U_{rel}	resultant wind speed due to motion of body
U_S	mean wind seed at the flow separation point of bluff body
u_V	relative wind speed of vortex being transported downstream to incoming wind speed U
V	reduced wind velocity
V_0, V_1, V_2	characteristic reduced wind speeds for quasi-steady galloping response ($V_0 = V_g$)
V_g	reduced form of U_g
V_r	reduced form of U_r
V_{lb}	lower bound of V at which φ_{Lm} becomes alwasys positive
x,y,z	Cartesian coordinate, or degrees of freedom
x_g	upstream distance of turbulence grid to axis of wind tunnel model
Y	non-dimensional displacement of body's motion, defined as y/d
Y_1, ε_{03}, ε_{05}	coefficients in Gao&Zhu's model as a function of K
y_0	amplitude at which a wind tunnel model is forced to vibrate, or initial displacement for free-decaying motion
y_{rms}	RMS value of fluctuation part of $y(t)$

Other Symbols

$\circ$	Hadamard product
Δ	small increment or difference
$(\dot{\ })$, $(\ )'$	differentiation with respect to physical time t, and reduced time τ(or $\tilde{\tau}$)
∞	infinity
std( )	standard deviation of a signal
$^\top$	transform operation for matrix or vector

Abbreviations

AEVS	Alternate Edge Vortex Shedding
CFD	Computational Fluid Dynamics
HFFB	High Frequency Force Balance
ILEV	Impinging Leading Edge Vortices
LEVS	Leading Edge Vortex Shedding
QS	Quasi Steady
RMS	Root Mean Square
TEVS	Trailing Edge Vortex Shedding
VIV	Vortex Induced Vibration

1 Introduction

1.1 Unsteady Galloping

Wind induced structural vibration is an important topic in civil engineering. In recent decades, the development of modern materials and construction techniques has promoted the emergence of a great number of structures characterizing with light-weight and slender fashion, exhibiting an increased susceptibility to the action of wind. Typical examples include tall buildings, chimneys, telecommunication masts and large-span bridges. For some particular cases, wind loading has become the key point in controlling the design process, like the Xihoumen Bridge in China and the Burj Khalifa in Dubai. The dynamic loading due to wind exciting will not only bring damage accumulation for structures in the long term, but also be able to result in an entire collapse of structure in a very short term. For the latter, an infamous example is the collapse of the Tacoma Narrows Bridge on November 7th 1940 in USA.

In natural environment, the dynamic exciting of wind on structures results from various origins. According to Naudascher & Rockwell (2012), these could be:

- EIE: Extraneously induced excitation (turbulence in natural wind);
- IIE: Instability induced excitation (flow instability inherent to the flow created by the structure under consideration, e.g., von Kármán vortices);
- MIE: Motion induced excitation (aerodynamic forces arising from the motion of the body).

For flexible structures with bluff cross section in natural wind, the three kinds of aerodynamic exciting exist simultaneously and relate to each other inseparably. Nevertheless, depending on the dominant, wind induced structural vibration can be classified as buffeting which is due to the atmospheric turbulence, vortex induced vibration (VIV) trigger by the shed vortices, and aeroelastic instability (i.e, galloping and flutter) driven by the motion-induced aerodynamic force.

For this thesis, the across-wind galloping is in object (if not specially noted, galloping in this thesis denotes the across-wind one). It is an aeroelastic instability typical of slender structures with bluff noncircular cross sections, like square or D shapes. Compared to the vortex induced vibration, which could also occur in the across-wind direction, the apparent difference is the unrestricted oscillation amplitude with the increase of wind speed. The quasi-steady (QS) theory is well accepted as the classical approach to treat the across-wind galloping problem, provided that a high reduced wind speed is ensured. Its validity has been confirmed for various cross section types, both in smooth and turbulent flow, and widely adopted in many design codes, e.g., the Eurocode 1 (EN 1991-1-4 2010). Nevertheless, a high value of mass-damping parameter, known as Scruton number (Sc), is usually needed to ensure that the galloping instability occurs in a high reduced wind speed range. Otherwise, the unsteady effects due to shed vortices and fluid memory at low reduced wind speeds become non-negligible, significantly invalidating the quasi-steady prediction. The galloping instability occurring at low reduced wind speeds is usually named “unsteady galloping”, as opposed to the galloping instability initiating at high reduced wind speeds, which can be called “high-speed galloping” or “quasi-steady galloping” due to the good performance of the QS theory.

In particular, the interaction of galloping with Kármán vortex induced vibration represents a typical type of unsteady galloping (if not specially noted, vortex induced vibration in this thesis denotes the one due to von Kármán type vortex). In case that the vortex induced vibration is well separated from galloping, the two kinds of aeroelastic responses can be attained by their respective theories. For the vortex induced vibration, several mathematical models are available in the literature, ranging from the simplest Harmonic model (Wyatt & Scruton 1981), Single-Degree-of-Freedom models (e.g., the Scanlan’s nonlinear model (Ehsan & Scanlan 1990)), to the more complicated Two-Degree-of-Freedom models (e.g., the Skop-Griffin model (Skop & Griffin 1973)). For galloping, the classical approach is the nonlinear quasi-steady galloping theory contributed, e.g., by Prof. Parkinson (Laneville & Parkinson 1971; Parkinson & Brooks 1961; Parkinson & Smith 1964; Parkinson & Sullivan 1979), providing good predictions not only for the reduced onset wind velocity V_g but also for the post-critical response. Under the condition that a high reduced wind velocity is ensured, variation of the Scruton number mainly leads to a quantitative change in the response curve (see Fig. 1.1 (a)). However, if the vortex induced vibration is not well separated from galloping, the two phenomena are able to interact with each other and promote together more complicated, even peculiar, aeroelastic behaviors (see Fig. 1.1 (b)). In particular, the supposed VIV response at the reduced Kármán-vortex resonance wind speed V_r, may turn into the amplitude-unrestricted galloping behavior for low Scruton number (case $b1$ and $b2$ in Fig. 1.1 (b)). Moreover, the actual galloping may arise at a reduced wind velocity lower than the quasi-steady predictions V_g, e.g., case $b3$ and $b4$ for medium Scruton number. The variation of the Scruton number actually leads to a qualitative change of the aeroelastic response. Apparently, the previous mentioned theories respectively for VIV and galloping are incapable to describe this complicated phenomenon.

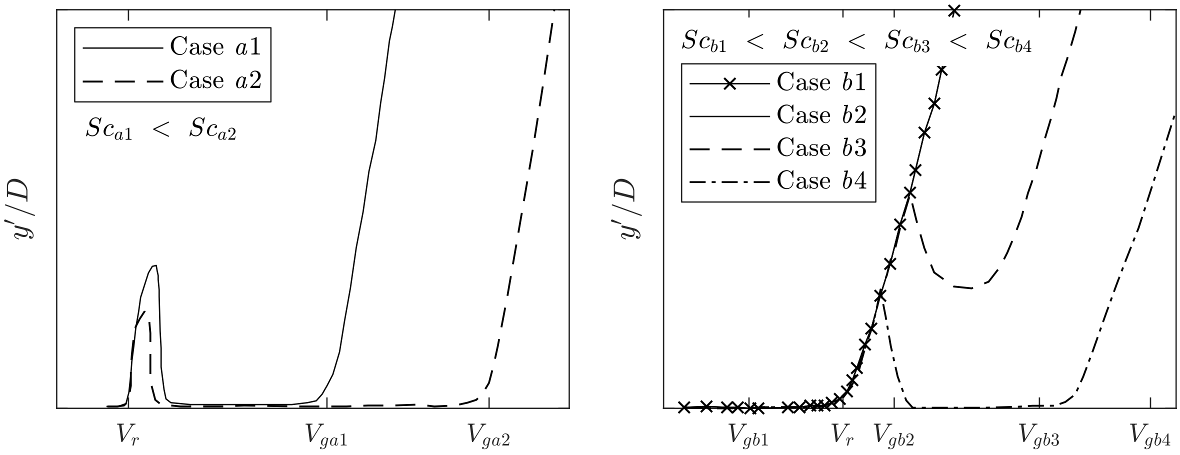

(a) No interaction (b) Interaction

Fig. 1.1: Amplitude-velocity schematic diagrams for interaction and no-interaction between galloping and VIV (by courtesy of Mannini & al. (2014), redrawn and slightly modified).

The unsteady galloping occurring at low reduced wind speeds is not only physically interesting, but also of great importance for modern structures. Indeed, either for the development of construction materials and techniques or just for aesthetic requirements, some structures are nowadays very slender and lightweight. In fact, evidences of unsteady galloping instability have already appeared in the recent engineering practice. Examples are two aesthetic arches in Milan, Italy (Mannini & al. 2016a), a footbridge deck with solid parapets (Cammelli & al. 2017), and a steel beam bridge during the construction phase (Salenko & al. 2017). In particular, the steel-concrete composite bridges during launching phase are supposed to be very relevant to this unsteady galloping, as it will be introduced in the next Section.

1.2 Incremental Launching of Steel-Concrete Composite Bridges

Incremental launching technique is a widely used method for bridge construction, especially for the multi-span continuous beam system. Typically for this method, the bridge superstructure is constructed or assembled at one side of the obstacle to be crossed and then pushed or “launched” to its final position. More usually, the whole launching process is composed by a series of increments: new segment of superstructure is step-by-step jointed to the rear of the launched out superstructure. In modern practice, the length of a new segment is in general a single span, so that the parking status of the superstructure can be properly maintained at the top of the erected piers during the manufacturing period of new segment for the next step launching. This technique is one of the most reasonable way to build a bridge over inaccessible obstacles, such as deep valleys, environmentally sensitive or historically protected areas, and poor terrain conditions for large equipment's operation. Due to its minimal disturbance to the space beneath, this method was also frequently applied for urban viaducts.

In the early 1960s, the modern bridge launching approach was developed and first applied to prestressed concrete bridges. This concept was first implemented on the Rio Caroni Bridge in Venezuela (Podolny & Muller 1994), built in 1962 and 1963 by its originators, Willi Baur and Dr. Fritz Leonhardt of the consulting firm of Leonhardt and Andra (Stuttgart, Germany). Its application to steel bridges was slightly later, not only due to the fact that steel plate was more expensive at that time but also due to the insufficient development of analytical tools. An important issue among these is the stability analysis of steel structures, which is particularly important for the launching process. Nevertheless, the subsequent rapid developments of research in the field of steel structures and in particular the commercial availability of finite-element software, have promoted the competitivity of steel bridges. Moreover, combination of reinforced concrete slabs and steel girder led to the arising of composite bridge cross section, which attained considerable cost reduction. Nowadays, the technique for incremental launching of steel or composite bridges is quite mature and the capability of crossing larger span is also enabled due to its light weight.

During the launching process, the most critical condition occurs when the launched-out girder reaches its maximal length, forming a long cantilever as shown by Fig. 1.2. Here, the static deformation of the structural system reaches its maximum, as well as the shear force and moment at the root of the cantilever. From the structural dynamic point of view, this is also a extreme condition: the fundamental frequency of the whole structural system gets considerably decreased due to the long cantilever. For example, the first bending frequency reached about 0.34 Hz for the Nuttlar Viaduct, Germany, during its critical launching phase, while this natural frequency quickly recovered back to about 0.9 Hz once the girder reached the next pier and entered the parking state (Niemann & Hölscher 2012). For another bridge, Aftetal Bridge, also in Germany, the lowest first bending frequency during the launching phase is about 0.4 Hz (Niemann & Hölscher 2013). It is worth noting here that the low-frequency situation met by these two bridges is actually quite typical during the launching phase, rather than just special cases.

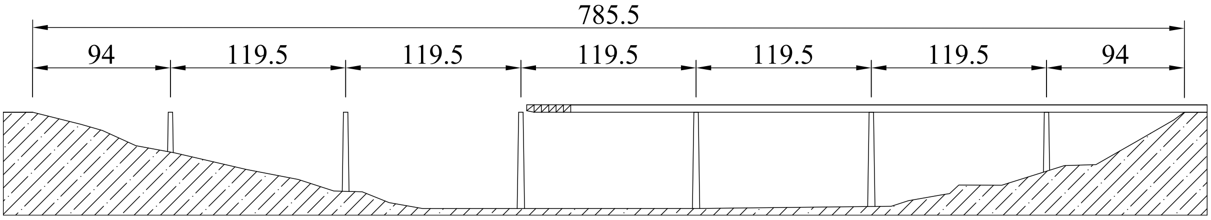

Fig. 1.2: Incremental launching of the Aftetal Bridge, Germany (redrawn according to Hanswille (2014), dimension in m).

The consequence of this significantly decreased natural frequency of the structural system is the increased susceptibility to natural wind, which is maybe the only source of dynamic loading in this situation. On the one hand, the turbulence of the incoming natural wind has more energy distributed in the lower frequency range (see, e.g., the longitudinal turbulence spectra measured by Davenport (1961)), so that structures with lower natural frequencies are generally more sensitive to the same incoming wind. More important is the chance given by this decrease of natural frequency to aeroelastic phenomena. For the Nuttlar Viaduct, the wind tunnel test of the bridge deck (the one in construction phase) reported a Strouhal number $St = 0.07$ in turbulent flow (Niemann & Hölscher 2012). Considering the deck is about 5 m high, the critical wind speed for vortex induced vibration is about $U_r = 64$ m/s for the parking state. This is well above the design wind speed for the Nuttlar Viaduct (about 33 m/s). However, for the situation in critical launching phase, the onset wind speed for vortex induced vibration decreases to about $U_r = 24$ m/s. Clearly, the dynamic exciting due to natural wind is relevant and should be taken into account for bridges in the launching phase.

Extra attention should be paid to the steel-concrete composite bridges: the superstructure is usually launched without the concrete slabs. This results in a considerable reduction of the weight and a increased capability of crossing a larger span. However, the single steel girder without concrete slabs may gain some disadvantages with respect to its aerodynamic properties. Fig. 1.3 (a) and (b) show the difference of Aftetal Bridge in service status and in construction phase. Usually, the single steel box is bluffer than the completed one, presenting higher susceptibility to aeroelastic instability, for example the across-wind galloping. For engineering structures, risk of aeroelastic instabilities must be avoided since its violent behavior may lead to the collapse of the whole structures. In fact, as shown in Fig. 1.3 (c), the aerodynamic outline of the Aftetal Bridge on the first 90 m girder was totally modified during the construction phase with temporary fairings to eliminate the risk of across-wind galloping (Hanswille 2014).

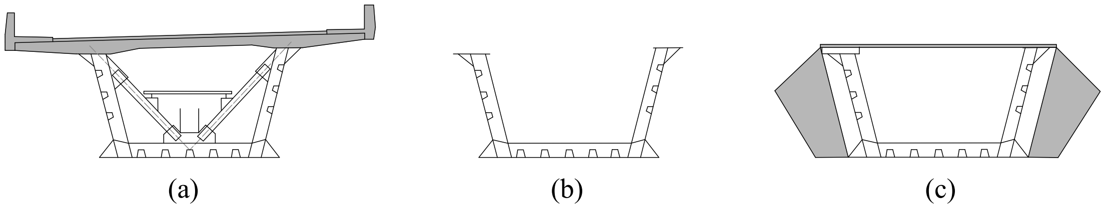
(a) (b) (c)

Fig. 1.3: Cross-section modification of the Aftetal Bridge, Germany, during the launching phase: (a) complete steel-concrete composite deck in service; (b) original steel box, and (c) modified steel box with temporary wind fairings during the launching phase (redrawn from Hanswille (2014)).

At this point, it is clear that the vortex induced vibration and galloping may exist at the same time for steel-concrete composite bridges during the launching phase. Consequently, a relevant and important question arises, that is whether the Scruton number of the structures is high enough so that the two concerned aerodynamic problem can be treated separately. To answer this question, more examples of steel-concrete composite bridges erected by incremental launching method are collected and summarized in Tab. 1.1. The collection is limited to the cases with considerably large main spans and box type cross sections. Without the concrete slab, the main superstructure usually has a form of rectangular or trapezoidal box. For some cases, the top of the steel box is also open, which is typical for the steel girder of composite bridges. The side ratio of the steel box b/d, defined here as the width to the height of the cross section, can be found in a range from 1.6 to 2.9 (except the Vaux Viaduct). This is unfortunately the b/d range in which galloping instability may occur for sharp-edged bluff body (in case of rectangular cross sections, across-wind galloping is possible for side ratio within about $0.75 \leq b/d \leq 3.0$ (Parkinson 1965)). Moreover, the mass ratio m^* of the steel girders during launching phase was found within 500 to 815 ($m^* = m/(0.5\rho d^2)$, where m is the mass of the steel girder per meter and ρ the air density). The damping information is however hard to be collected for these bridges. Therefore, a logarithmic damping $\delta_0 = 0.03$ is assumed here for all the cases. For welded steel structures, this value is supposed to be reasonable (or even overestimated). Finally, the Scruton number $Sc = \delta_0 m^*$ estimated for these bridges is about 15-25. Since the mass ratio is defined by "d^2" rather than "bd", the Scruton number obtained here is actually quite low. This implies that the unsteady galloping due to interaction with VIV is probably very relevant for steel-concrete composite bridges erected by incremental launching method.

Tab. 1.1: Examples of steel-concrete composite bridges erected by incremental launching method. Source of data: Vallsundet Bridge, Kuhlmann & al. (2008); Vaux Viaduct, Navarro & al. (2000) and Dauner & al. (2000); Verrières Viaduct, Berthellemy (2001); Haseltal Bridge, Binder & al. (2005); Lochkov R1 Bridge, Anistoroaiei & al. (2013); Jiubao Bridge, Wang & al. (2015); Nuttlar Viaduct, Niemann & Hölscher (2012) and Wagner (2013); Heidingsfeld Viaduct, Mansperger & al. (2017); Aftetal Bridge, Niemann & Hölscher (2013) and Hanswille (2014).

	Built year	Section type[a]	Main span [m]	d [m]	b/d [-]	m [ton/m]	m^* [-]	δ_0[c] [-]	Sc[d] [-]
Vallsundet Bridge	1998	Trap. (open)	80	2.8	1.8	-	-	0.03	-
Vaux Viaduct	1999	Rect.	130	3.5 -6.5	1.0 -1.8	5.2 [b]	674	"	20.2
Verrières Viaduct	2002	Rect.	144	4.5	1.6	8.6	680	"	20.4
Haseltal Bridge	2006	Trap.	175	4.7	1.7	11.4	815	"	24.5
Lochkov R1 Bridge	2010	Trap. (open)	99	4.8	2.8	11.1	767	"	23.0
Jiubao Bridge	2012	Trap. (open)	85	4.5	2.9	8.4	663	"	20.0
Nuttlar Viaduct	2017	Trap.	115	5.0	2.5	11.0	704	"	21.2
Heidingsfeld Viaduct	2020	Trap.	120	4.6	2.0	7.5	571	"	17.2
Aftetal Bridge	2020	Trap. (open)	119.5	5.0	2.0	7.7	500	"	14.8

[a] Cross section type during the launching phase. "Trap." and "Rect." represent, respectively, the trapezoidal and rectangular cross section, while "(open)" additionally indicates an open form cross section.

[b] Averaged value.

[c] Assumed value.

[d] Scruton number defined as $Sc = \delta_0 m^* = \delta_0 m/(0.5\rho d^2)$.

1.3 Motivation, Objectives and Scope

The research work in this thesis is devoted to the unsteady galloping problem for steel-concrete composite bridges during their launching phase. The motivation arises from two aspects:

- Firstly, it is a fact that a considerable number of steel-concrete composite bridges are nowadays constructed by incremental launching method worldwide. However, according to the author's knowledge, the quasi-steady theory is still used as the main design tool for the galloping problem in this situation. The unawareness of the risk of unsteady galloping may put the concerned structures in a unfavorable or even dangerous situation. An improved approach for providing reliable predictions is in need.
- Secondly, unsteady galloping itself is a complex aeroelastic phenomenon deserving more lights shed on. Since it occurs at relatively low reduced flow velocities, the unsteadiness due to shed vortices and fluid memory plays important role in the flow-structure interaction. In fact, understanding the unsteadiness and non-linearity during flow-structure interaction of oscillation body has always been one of the most important tasks in the communities of wind engineering and bluff body aerodynamics.

Taking the incremental launching of steel-concrete composite bridges as realistic engineering background, this research aims at a further contribution to shedding light on the complex nature the unsteady galloping phenomenon and an exploration of the analytical models for practical prediction purpose. In particular, generic bridge deck is involved to forward the researches on simple geometries, e.g., rectangles, to more complicated but realistic structural cross section.

The research scope is limited in field of fluid-structure interaction on an oscillation body with cross sections of small side-ratio. The dynamic degree of freedom is the across-wind one, so that the main concerned aeroelastic phenomena are galloping and vortex induced vibration. Flutter or vortex induced vibration in the torsional degree of freedom is beyond the scope of this thesis, as well as the aerodynamics for cross sections of large side-ratio. However, they may sometimes be referred, due to either a need of comparison or some related implications.

The research work of this thesis is outlined in a flow chart shown in Fig. 1.4. In Chapter 2, a detailed state of the art concerning the unsteady galloping problem is first presented. The experimental study is organized in Chapter 3 for elaborating the experimental setups, calibrations as well as pre-examinations, and in Chapter 4 for experimental results. Chapter 5 deals with the mathematical modeling of unsteady galloping on the wind tunnel sectional models, with respect to a 2:1 rectangular cylinder and a generic bridge deck model. Efforts to examine the physical foundation in the used Tamura's wake oscillator model is also presented. In Chapter 6, the mathematical model is further extended to flexible continuous structural system, and the critical launching phase of a steel-concrete composite bridge is taken as a case study. Unfortunately, due to a time limitation, the concerned predictions is not validated by wind tunnel aeroelastic tests. This is considered as a future work, which together with a summary conclude this thesis in Chapter 7.

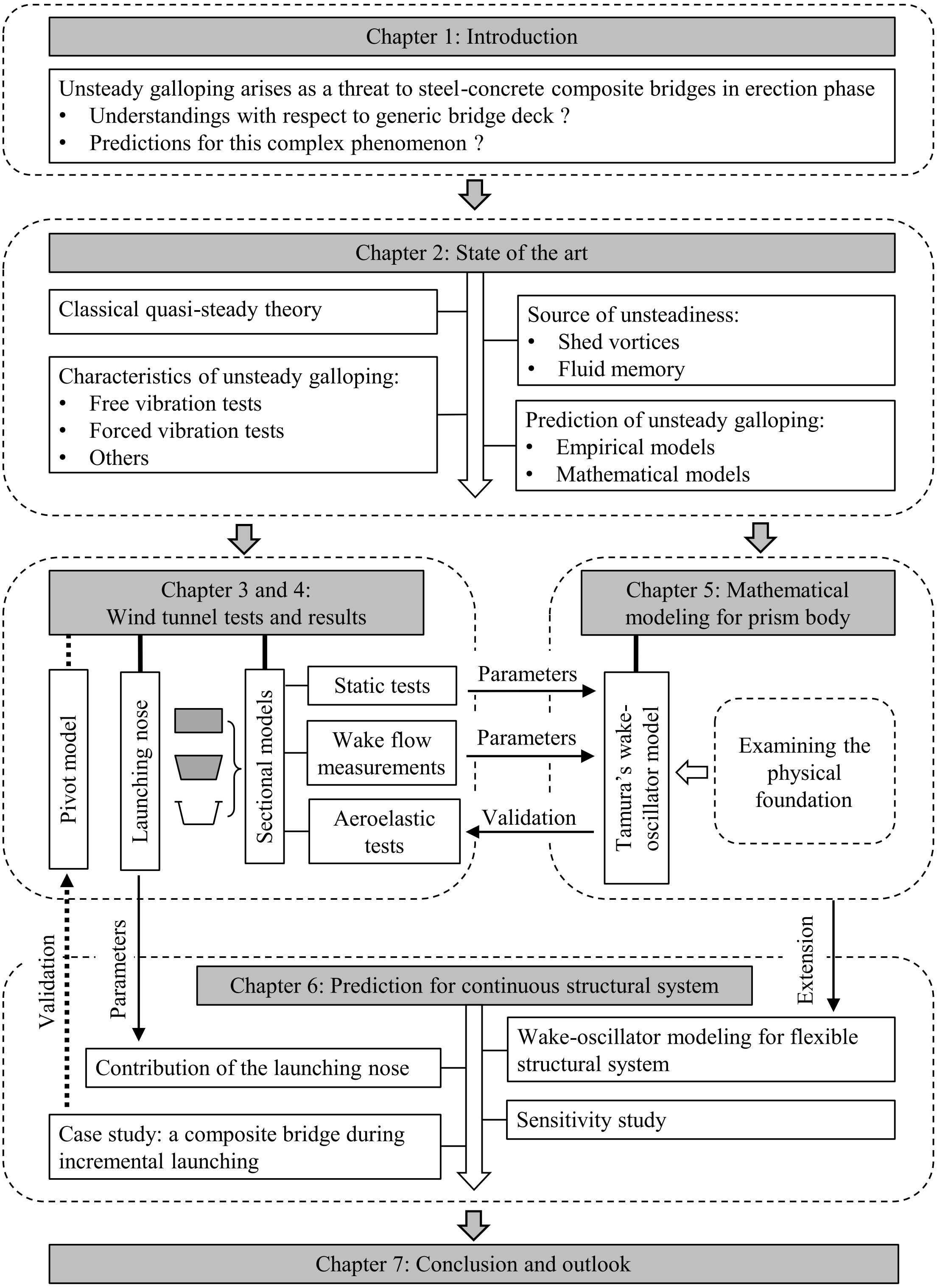

Fig. 1.4: Diagram illustration of the content arrangement for this thesis

2 State of the Art

2.1 Introduction to Bluff Body Aerodynamics and Aeroelastic Phenomena

Bluff body is a concept in contrast to streamlined body. A body can be called streamlined when the flow streamlines follow closely the contour of the body, and the free-stream flow is separated from the surface of body only by a thin boundary layer. In contrast, bluff body characterizes massive flow separation. At a position (which may be not fixed), the boundary layer is unable to attach on the surface of body anymore and becomes free shear layer. This flow layer is still of high shear stress and vorticity, dividing the separated flow region from the outer flow. Moreover, a free shear layer is intrinsically unstable in a sheet form and will roll up towards the wake, forming concentrated vortices downstream which is commonly observed in bluff body flow. Important is that, a body is streamlined or bluff not only depends on the geometry of the body itself but also closely relates to the flow around it. For an airfoil, it is a streamlined body at small wind angle of attack but becomes bluff body at large angles of attack, as shown in Fig. 2.1.

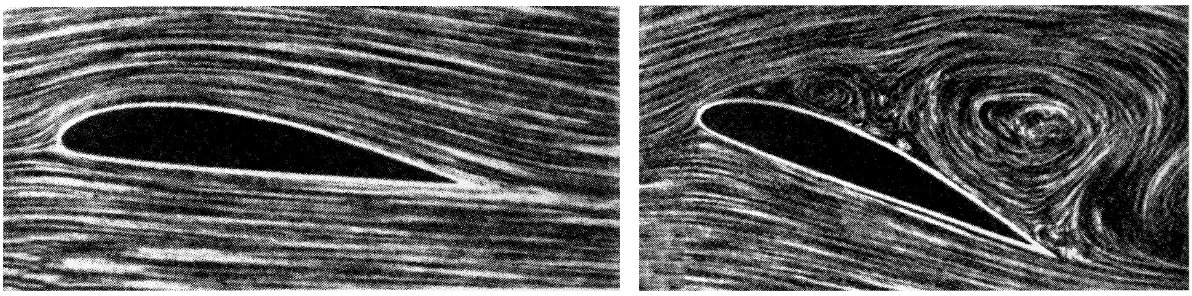

(a) (b)

Fig. 2.1: Example of streamlined body and bluff body (photo copied from Schlichting & Gersten (2016)).

The portion of body downstream the separation position is called after-body. Dependent on the further development of the separated shear layer and its interaction with the after-body, bluff bodies exhibit different aerodynamic properties and subject to various kinds of aeroelastic phenomena when the body is free to oscillate. A good classification with respect to the topic of bluff-body aerodynamics was provided by Matsumoto (1996), as reproduced in Fig. 2.2. Among his classifications, it is needed to point out that the “Low Speed Galloping” particularly refers to a peculiar phenomenon occurring for low side ratio bluff bodies ($0.2 \lesssim b/d < 0.6$) at a velocity lower than the Kármán-vortex resonance wind speed. It is different from the concept of unsteady galloping defined in this thesis. One can refer to Nakamura & Matsukawa (1987) and Nakamura & Hirata (1991) for more detailed information about this peculiar phenomenon.

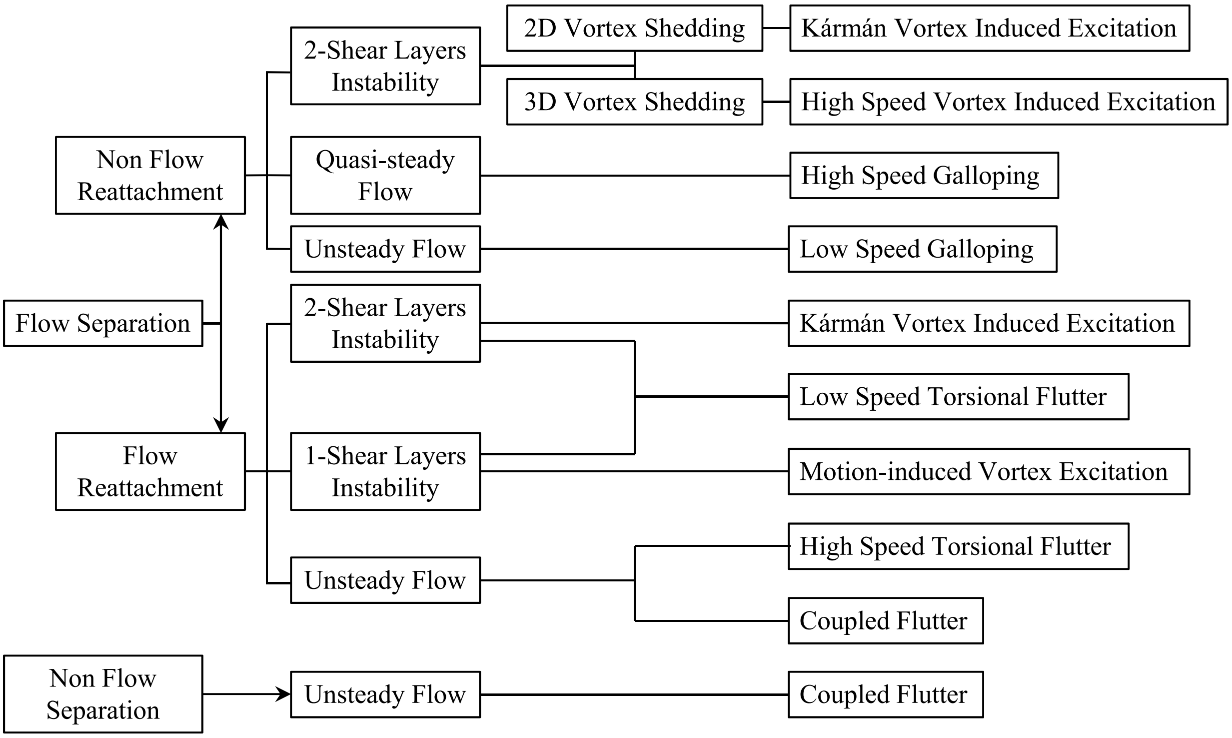

Fig. 2.2: Bluff-body aerodynamics, reproduced from Matsumoto (1996)

For sharp-edged bluff body, like rectangular cross sections, a very important parameter is the side ratio b/d. In a general way, it can be defined as the ratio of the streamwise dimension to across-wind dimension of a bluff body. A good summarization with respect to this topic, namely the dependency of flow pattern and related aeroelastic phenomena on the side ratio of bluff body, is provided by Takeuchi & Matsumoto (1992) and reproduced in Fig. 2.3. From the point of view of the time integrated flow pattern (time averaged flow patter), reattachment of the shear layers on after-body occurs for $b/d > 2.8$. In contrast, if attention is paid to the unsteady flow pattern (transient), intermittent reattachment of the separated shear layers already occurs at about $b/d \approx 2.0$. Such an intermittent behavior is maintained up to about $b/d = 6$, after which the stationary flow reattachment dominates. These flow patterns correspond to stationary body states. In the second half of Fig. 2.3, possible aeroelastic phenomena are indicated for various ratio b/d. The core of these phenomena is aeroelasticity - the mutual interaction between a movable body and its surrounding flow. They are separately introduced in following contexts.

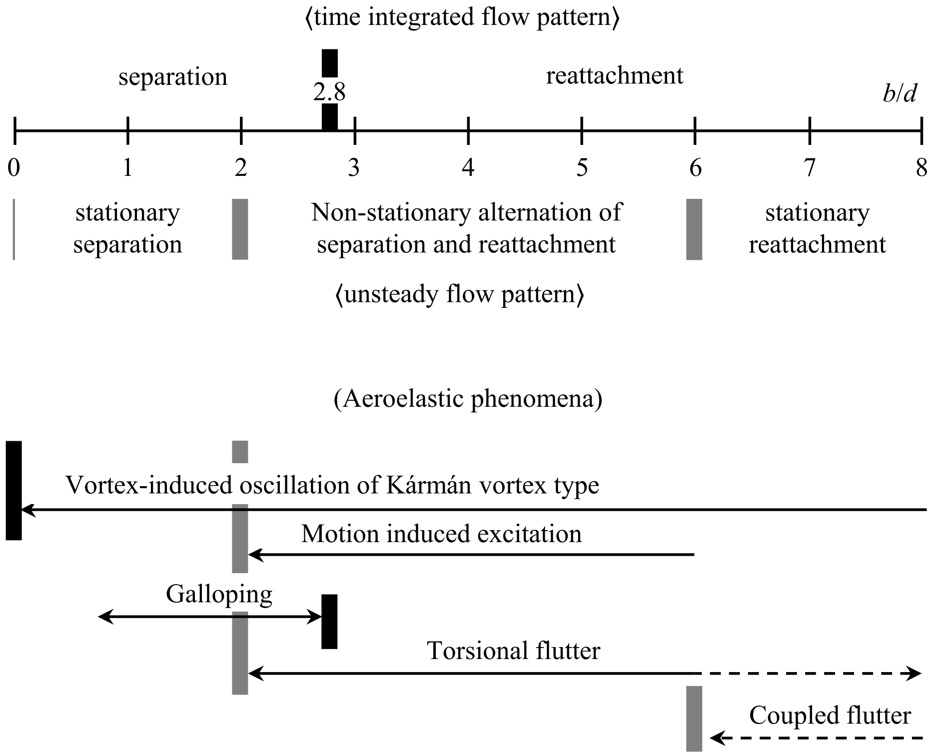

Fig. 2.3: Flow patterns and related aeroelastic phenomena for sharp-edged bluff bodies with various side ratio b/d, according to Takeuchi & Matsumoto (1992).

2.1.1 Vortex Induced Vibration

Shedding of vortices is one of the most important characteristics for bluff-body flow. It may occur for any bluff body, as it results from the instability of the flow profile created by the presence of body. The very famous example is the vortex shedding from a circular cylinder (occurs for *Re* higher than about 80-90, according to Schlichting & Gersten (2016)), leaving in the wake region two rows of clearly visible concentrated vortices being transported downstream. This is the well-known von Kármán vortex street. Here, *Re* is Reynolds number, defined as

$$Re = \frac{\rho U d}{\mu} \tag{2.1}$$

where ρ is the flow density, U the free-stream velocity, d the characteristic length of body (here, the across-flow dimension is used), and μ the dynamic viscosity of flow. Early at the end of the nineteenth century, Strouhal (1878) has noticed that there is a linear relation between the vortex shedding frequency and the free-stream velocity, which allows the definition of a non-dimensional quantity known as Strouhal number

$$St = \frac{n_{st} d}{U} \tag{2.2}$$

where n_{st} refers to the frequency of vortex shed from single side of bluff body. Strouhal number, associated with the vortex shedding process, is highly dependent on the geometry of bluff bodies. For cross sections with round outline (such as the circular cross section), it is also influenced by Re and the surface roughness, since the occurring of flow separation is determined by the boundary layer physical properties. For sharp-edged cross sections like square, flow separation is rather fixed at the upstream sharp edges so that St is less dependent on Re.

Vortex formation and periodically shedding from bluff-body represents a very complex fluid phenomenon. With respect to the shedding pattern, a good classification was provided by Naudascher & Wang (1993) (or in Naudascher & Rockwell (1994)), and schematized here based on rectangular cross sections with varied side ratio and orientation (Fig. 2.4):

- LEVS (Leading Edge Vortex Shedding), flow separation at the leading edge and formation of vortices dominate in the near wake of body;
- ILEV (Impinging Leading Edge Vortices), flow separation at the leading edge and impingement of the leading edge vortices at the side surfaces and/or edges of the body;
- TEVS (Trailing Edge Vortex Shedding), decisive flow separation at the trailing edge and vortex-shedding analogue to the von Kármán street behind circular cylinders;
- AEVS (Alternate Edge Vortex Shedding), vortex shedding occurring in a critical range of incidence where alternatively one vortex separates at the leading edge and the other at the trailing edge.

(a) LEVS

(b) AEVS

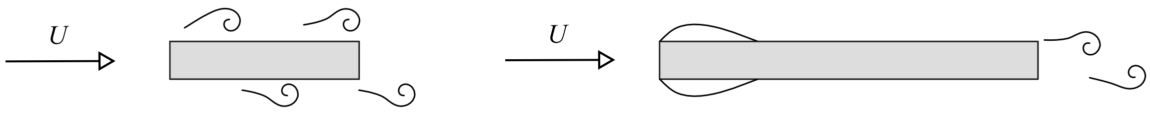

(c) ILEV

(d) TEVS

Fig. 2.4: Schematics of vortex shedding patterns for bluff bodies, due to Naudascher & Wang (1993).

As pointed out in Païdoussis & al. (2010), LEVS, TEVS and AEVS actually all belong to the same class of vortex shedding as the circular cross section. The formation of vortices in this case is a result of wake instability (also known as Bénard - von Kármán instability or 2-shear layer instability as indicated in Fig. 2.2), which involves the mutual interaction of two free shear layers (a more detailed review on this topic is presented in Section 5.2.1). Formation of ILEV is, however, due to another mechanism called Kelvin-Helmholtz instability which occurs for a single free shear layer (corresponds to the 1-shear layer instability in Fig. 2.2). Evidently, the presence of a splitter-plate in the wake cannot suppress the formation of ILEV (see, e.g., Nakamura & Nakashima (1986)). As explained in Naudascher & Wang (1993), formation of ILEV is cultivated by a feedback loop between the leading edge and trailing edge: "*vortices which form in the unstable free shear layers on the two sides of the prism are transported with convection velocity, towards the trailing edges where they generate pressure pulsations that are fed back upstream and trigger the development of new vortices*". Such a mechanism is equivalent to the large-scale vortex structures observed for open cavity flow (see e.g., Rockwell & Naudascher (1978) and Cattafesta III & al. (2008)). It is also worth noting that, in many specific cases, the ILEV do exist but too weak to detect especially if the dominant vortex shedding form is a von Kármán type. An enhancement for ILEV can be achieved by external acoustic exciting (Mills & al. 2002; Stokes & Welsh 1986) or motion of the body itself. The Strouhal number of ILEV can be approximated by (Shiraishi & Matsumoto 1983)

$$St = \frac{n_{st}d}{U} \approx 0.6\frac{Nd}{b} \tag{2.3}$$

where $N = 1, 2, 3, ...$ is the mode of ILEV. In a straightforward manner, N represents how many vortices can simultaneously exist on one side of bluff-body. Eq. 2.3 also means the Strouhal number of ILEV is predictable given that the geometry information of bluff body is known. In fact, the ILEV is found particularly dominant for the H-shape cross section with a proper side ratio (Nakamura & Nakashima 1986; Naudascher & Wang 1993; Schewe 2013), which may be due to the presence of two cavities in the topology of H-Shape. Finally, for modern bridge deck cross section, whose aerodynamics is characterized by separation, reattachment and merging of small eddies structures, several Strouhal numbers corresponding to different shedding patterns may be detectable (e.g. Bruno & Khris (2003)).

As a result of the periodical vortex shedding process, fluctuation of aerodynamic force on bluff body usually contains a component characterized with the vortex shedding frequency n_{st}. If the body itself is movable and features a natural frequency n_0, resonance could occur when the vortex shedding frequency n_{st} matches n_0. This is the well-known vortex resonance condition, corresponding to a critical velocity

$$U_r = \frac{n_0 d}{St} \tag{2.4}$$

For a 2-d bluff body with one degree of freedom y (see Fig. 2.5), the motion is governed by

$$m\ddot{y} + c_y\dot{y} + k_y y = L(t) \tag{2.5}$$

where m, c_y and k_y represent mass, damping, and stiffness, respectively. When the fluctuation lift of stationary body is considered for the above equation, $L(t)$ can be simply written as

$$L(t) = \frac{1}{2}\rho U^2 d C_{L0} \sin(2\pi n_{st} t + \varphi) \tag{2.6}$$

where C_{L0} denotes the amplitude of fluctuation lift due to vortex shedding on stationary body. Eq. 2.5 and Eq. 2.6 represent the harmonic model to approach vortex induced vibration. However, this model conflicts with the realities for at least two aspects: a) the amplitude of vortex induced vibration seldom exceeds $1d$ in experiments (see the review paper by Williamson & Govardhan (2004)), while the harmonic model can predict very high amplitudes; 2) in experiments the maximum amplitude can occur at a flow velocity higher than U_r (see Fig. 2.6).

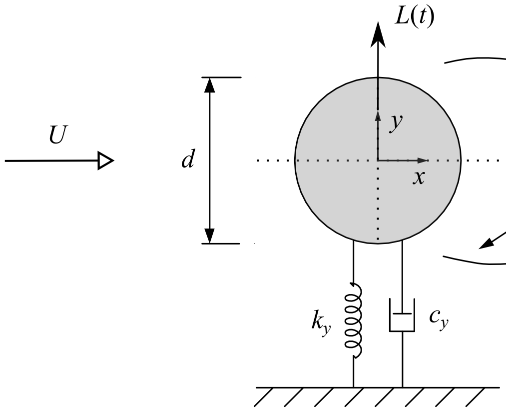

Fig. 2.5: Schematic of vortex induced vibration for a 2-d circular cylinder

In a better way, VIV can be understood as a vortex-shedding triggered, amplitude and velocity restricted aeroelastic phenomenon (“self-limited” nonlinear phenomenon). On the one side, periodical vortex shedding from bluff body is clearly the inducement for VIV, as manifested by the exhibition of forced vibration properties on elastically supported body for $U < U_r$. One the other side, when flow velocity reaches U_r, the vortex shedding process is strongly influenced by the motion of body, occurring the very famous “lock-in” phenomenon (also called “synchronization”): vortex shedding frequency being captured by the motion of body ($n_{st} \approx n_0$), apparently deviating from the Strouhal law $n_{st} = USt/d$, for a certain range of U. When the flow velocity is further increased to a certain point, desynchronization occurs, exhibiting the vanishing of large-amplitude oscillation and the re-obeying of n_{st} to the Strouhal law. A typical example with respect to this process can be found in Feng (1968)’s results (reproduced in Fig. 2.6). Moreover, vibration of bluff body in fluid will inevitably bring added fluid mass. This could lead to different “lock-in” responses, see also Fig.2.6 for Khalak & Williamson (1997)’s results.

Shedding light on the mechanism of VIV, especially for the “lock-in” phenomenon, has always been a task in the community of bluff body aerodynamics. However, Marra (2011), after reviewing a large amount of predictive analytical models, reported that no model is actually able to

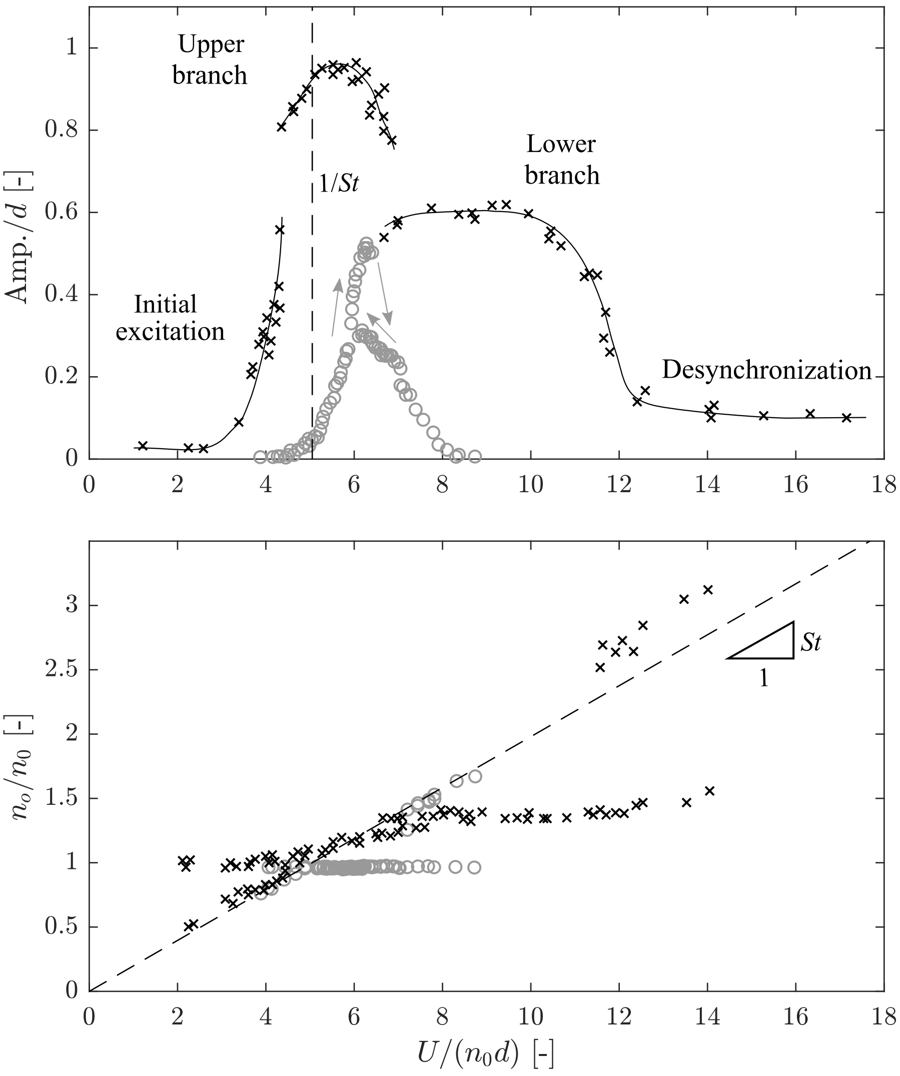

Fig. 2.6: Amplitude and oscillation frequency n_o responses of VIV of a circular cylinder. Grey "○" markers denote experimental test results in air flow with mass ratio $m^* = 248$ and $\zeta_0 = 0.00103$ (Feng 1968); black "×" makers represent experiments in water flow with $m^* = 2.4$ and $\zeta_0 = 0.0045$ (Khalak & Williamson 1997). Mass ratio is defined here $m^* =$ (body mass)/(displaced fluid mass).

properly predict vortex-induced vibrations. Moreover, the frequently observed hysteresis loop in the amplitude-velocity plot of VIV (e.g., in Fig. 2.6), implies a strong non-linearity of the aerodynamic force during VIV. This non-linearity relates not only to the oscillation amplitude, but also (probably) to the different modes of vortex pairs (Williamson & Roshko 1988).

VIV can be induced not only by the von Kármán type vortex shedding patterns (LEVS, TEVS and AEVS), but also by ILEV pattern even it is not detected on a stationary body. Such a case has been observed for rectangular cylinders with various side ratios, for example, the 5:1, 4:1 and 2:1 rectangular cylinders respectively reported by Nguyen & al. (2018), Marra & al. (2015) and Miyata & al. (1983) in free vibration tests. This ILEV induced VIV is classified as "motion induced vortex exciting" in Fig. 2.2 and Fig. 2.3, which emphasizes the importance of enhancement of ILEV due to body's motion. The enhanced ILEV in turn further cultivates the oscillation of body. In Fig. 2.3, "motion induced vortex exciting" is limited for b/d higher than about 2. However, recent wind tunnel free vibration tests also reported this phenomenon for rectangular cylinders with $b/d = 1.5$ (Mannini & al. 2016b) and $b/d = 1.2$ (Matsuda & al. 2013). In forced vibration tests, at a flow velocity about $0.5U_r$ and an amplitude about $0.25d$, ILEV was also observed for a square cylinder (Bearman & Obasaju 1982).

Moreover, it is to mention that vortex shedding is characterized with pronounced three-dimensional features, even on a so-called two-dimensional body (e.g., prism body). As a matter of fact, the unstable shear layers roll up with a limited coherence and then the forming eddies stretch in the spanwise direction. This three-dimensional characteristic can be reflected by the spanwise correlation of vortex shedding force. For a stationary body, one can clearly see from Fig. 2.7 the quick loss of the pressure correlation between two spanwise separated points, although this correlation is strongly enhanced for an oscillation body. In fact, the spanwise correlation of vortex shedding force has always been a very important topic for VIV predictions of slender structures, such as bridges and chimneys (see, e.g., Ehsan & Scanlan (1990) and Ruscheweyh (1994)).

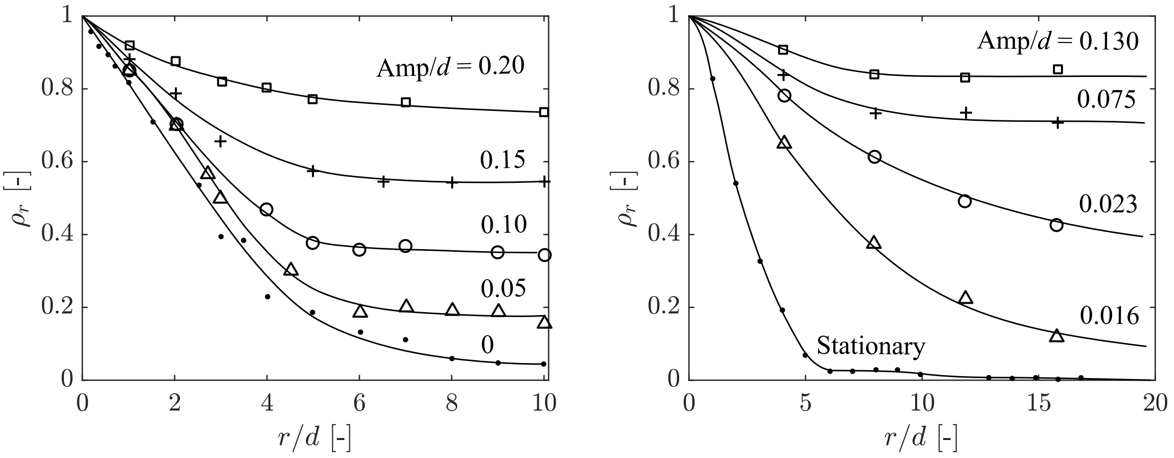

(a) Circular cylinder (b) cylinder

Fig. 2.7: Effect of oscillation amplitude on the correlation coefficient ρ_r of pressures between two points separated by distance r along spanwise axis: (a) results of circular cylinder from Novak & Tanaka (1972); (b) square cylinder from Wilkinson (1981)

Finally, in air flow, it is widely accepted the Scruton number, which is a combination of mass ratio and structural damping, as the controlling parameter for the aeroelastic responses of VIV. This is a result of the big difference between structure density and air density. A good discussion with respect to this topic can be found in Marra & al. (2011). In this thesis, without special notation, the Scruton number is defined as

$$Sc = m^* \cdot \delta_0 = \frac{m}{0.5\rho d^2} \cdot 2\pi\zeta_0 = \frac{4\pi\zeta_0 m}{\rho d^2} \tag{2.7}$$

where ζ_0 is mechanical damping ratio, m the mass of structure per unit length. This definition is kept the same as in Euro-code 1 (EN 1991-1-4 2010). Another widely used definition of Sc is replacing "d^2" in Eq. 2.7 with "db".

2.1.2 Across-wind Galloping

Across-wind galloping, as well as the torsional flutter and the coupled flutter to be introduced later, belong to the category of aeroelastic instability, which is driven by motion-induced-force and features unrestricted oscillations after a critical flow velocity being exceeded. Across-wind galloping denotes the instability occurring in the across-wind direction, typical for slender structures characterized with particular cross sectional geometry, such as rectangular or "D" shape. Under certain conditions that are later defined, these structures can exhibit large amplitude oscillation (one to ten or even more across-wind dimensions of the section) at a frequency close to the natural frequency of structure. This phenomenon was first observed and described in the case of iced transmission lines by Davison and Den Hartog (Davison 1930; Den Hartog 1932). Davison referred to "dancing vibrations" to describe these large amplitude oscillations. The galloping phenomenon had received extensive attentions since the beginning of the 1960s, with the works of Parkinson & Brooks (1961), Novak (1969, 1972) and others. The terminology "galloping" was found rather "appropriate" by Parkinson, due to the visual impression given by vibrating transmission lines, reminiscent of a galloping horse.

Païdoussis & al. (2010) defined galloping as "a velocity-dependent, damping-controlled instability", which highlights the dependence of the negative aerodynamic damping on the incoming flow velocity and the dominance of structural damping in determination of the critical state. The mechanism of generation of negative aerodynamic damping due to body's motion can be explained by the schematics provided by Parkinson (1971) for a square cross section, as shown in Fig. 2.8. At a "certain high" reduced velocity, the downward movement of the square is able to induce higher negative pressure on the bottom side than the upper side. This results in an aerodynamic force downward, in the same direction of the velocity of the body, so that this aerodynamic force works as a negative damping force (remembering that a positive damping force is in the opposite direction of velocity). When the flow velocity is high enough, the generated negative damping is able to overcome the positive damping of structure, making the dynamic system become oscillatorily unstable at its equilibrium position. At "enough high" reduced flow velocity, this mechanism can be not only qualitatively but also quantitatively approached by the quasi-steady theory that will be introduced later. It is to note here, that the previous mentioned "certain high" reduced flow velocity does not equal to the "enough high" one, being the former related to a reduced flow velocity at which body's motion can generate negative damping force.

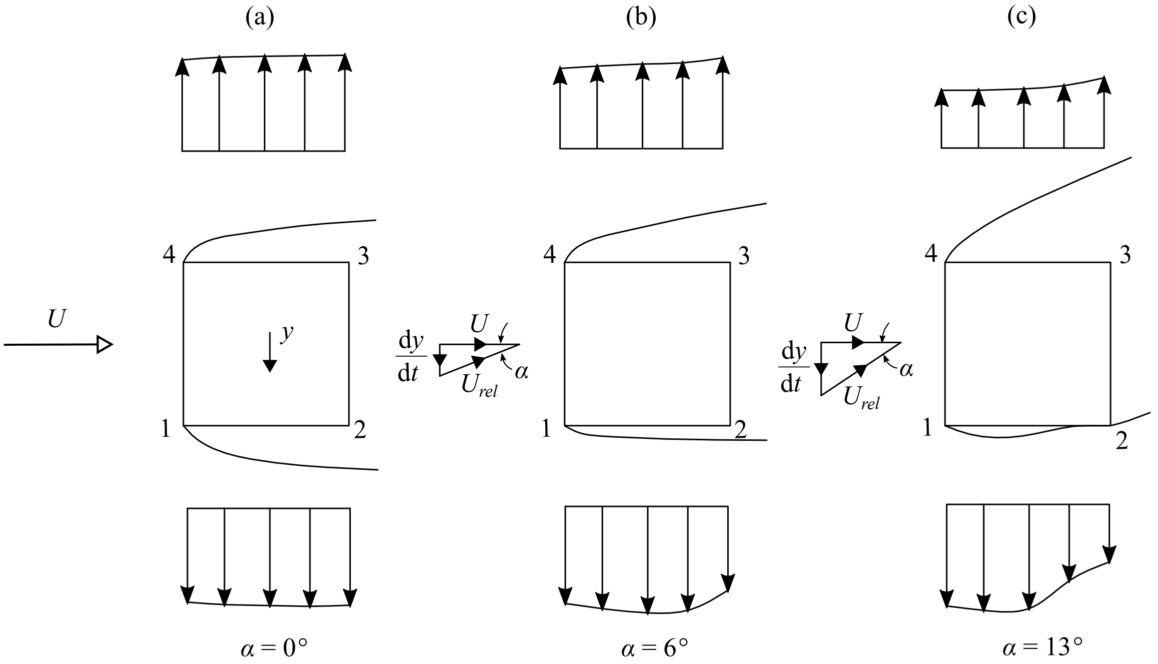

Fig. 2.8: Pressure distributions on lateral sides of a square cylinder during the across-wind galloping oscillation (Parkinson 1971).

As previously mentioned, the across-wind galloping occurs only for certain cross sections. Early in 1930s, Den Hartog (1932) has pointed out a necessary condition for this instability

$$\left.\frac{\mathrm{d}C_L}{\mathrm{d}\alpha}\right|_{\alpha_0} + C_D(\alpha_0) < 0 \tag{2.8}$$

where C_D and C_L, as functions of wind angle of attack α, are the drag and lift coefficients of a cross section. This is the well-known Den Hartog criterion. Clearly, according to this criterion, the circular cross section is not subject to galloping instability. For iced transmission line, the accumulation of ice may change its original cross section (usually close to a circular one) so that occurrence of galloping becomes possible. For rectangular cross sections, this instability could arise for a side ratio $0.75 \lesssim b/d \lesssim 3$ according to Parkinson (1965), being also properly collected in Fig. 2.3. However, it was found later the Den Hartog criterion is only applicable for soft-type galloping which can arise from rest due to a minor perturbation (see e.g., Novak (1971) or Païdoussis & al. (2010)). For hard-type galloping, although this condition is not fulfilled, oscillation can be excited by giving a comparably large perturbation. For rectangular cross sections, hard-type galloping occurs for $0.375 \lesssim b/d \lesssim 0.683$ (Parkinson 1965). For bridge decks, galloping instability is normally not a problem (Cao 2015). Because for large-span bridges (like cable stayed bridges) the deck is usually characterized with more streamlined cross section of large side ratio, while for short-span bridges (like beam bridges) the deck is usually too stiff to give rise to this type of instability. Nevertheless, some examples of bridge deck galloping can be found for a 10-span continuous beam bridge (Hirai & al. 1993) and a 3-

span continuous beam bridge (Ge & al. 2002), both in Japan. Nowadays, the emergence of many lightweight pedestrian bridges also gives rise to the risk of galloping instability, for example, a footbridge with solid parapets in UK (Cammelli & al. 2017). Bridge decks in launching process, which represents a special state as introduced in Section 1.2, may also suffer from this risk.

The quasi-steady theory is a classical approach to the across-wind galloping instability. The terminology "quasi-steady" means that the motion of body is sufficiently slow compared with the velocity of fluid moving. This sufficiency can be characterized by the reduced flow velocity $U/(bn)$, which physically corresponds to a ratio between body's oscillation period $(1/n)$ and the time needed by flow to pass by the body (b/U). Clearly, a high reduced flow velocity corresponds to a relatively slow motion of body. Under this condition, the oscillation body presents like at its stationary state within a every short time interval Δt, in which the unsteady aerodynamic effect due to she vortices, fluid memory, etc., can be all averaged out. Therefore, the aerodynamic force within Δt includes only the steady part (the time-averaged one). Moreover, the added mass effect is also negligible for structures in air flow. Due to these considerations, the aerodynamic forces on an oscillation body, which is characterized with an apparent wind angle of attack and a resultant wind speed, can be deemed equal to the aerodynamic forces on a stationary body attacked by the same wind angle and the same magnitude of wind speed.

For a dynamic system of single degree-of-freedom y, as schematized in Fig. 2.9, the governing equation can be written as

$$m\ddot{y} + c_y\dot{y} + k_y y = F_y \tag{2.9}$$

where F_y is the aerodynamic force acting on the body in the vertical direction. Due to the motion of body, the incident flow has been varied by the relative velocity of the body $-\dot{y}$, forming an apparent wind angle of attack α

$$\alpha = \tan(\frac{\dot{y}}{U}) \tag{2.10}$$

The magnitude of incident wind speed is also varied and can be expressed as

$$U_{rel} = \sqrt{U^2 + \dot{y}^2} = \frac{U}{\cos(\alpha)} \tag{2.11}$$

For the aerodynamic force F_y, it can be expressed as

$$F_y = -[L\cos(\alpha) + D\sin(\alpha)] \tag{2.12}$$

where D and L represent, respectively, the drag and lift under that apparent wind angle of attack α. The minus sign is added here because F_y is assumed downward positive. Now, invoking the

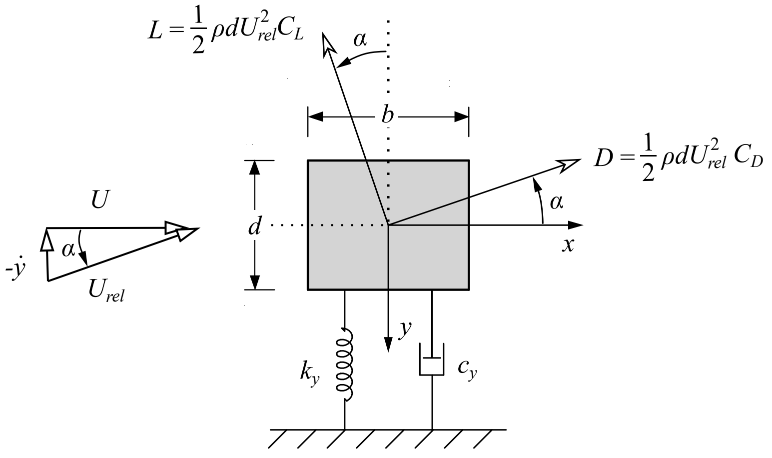

Fig. 2.9: Aerodynamic drag and lift on an oscillation body according to quasi-steady theory.

previously introduced quasi-steady assumption, the drag and lift on the oscillation body equal to the same ones exerting on the stationary body which characterizes a flow incidence of α and a velocity magnitude of U_{rel}. Therefore, F_y can be further written

$$F_y = -\frac{1}{2}\rho d U_{rel}^2 [C_L(\alpha)\cos(\alpha) + C_D(\alpha)\sin(\alpha)] \tag{2.13}$$

where $C_D(\alpha)$ and $C_L(\alpha)$ are the drag and lift coefficients as functions of α for the same body but in stationary state. With Eq.2.11, it allows the definition of a transverse force coefficient

$$C_{Fy}(\alpha) = -\frac{1}{\cos^2(\alpha)}[C_L(\alpha)\cos(\alpha) + C_D(\alpha)\sin(\alpha)] \tag{2.14}$$

so that the expression of F_y becomes

$$F_y = \frac{1}{2}\rho d U^2 C_{Fy}(\alpha) \tag{2.15}$$

Substituting this expression of F_y into Eq. 2.9, there is finally

$$m\ddot{y} + c_y\dot{y} + k_y y = \frac{1}{2}\rho d U^2 C_{Fy}(\alpha) \tag{2.16}$$

It is to note here, on the one hand, $C_{Fy}(\alpha)$ is a function which can be directly determined on a stationary body by varying the wind angle of attack α. On the other hand, in determination of the aerodynamic force for an oscillation body, the expression $\alpha = \tan(\frac{\dot{y}}{U})$ is invoked as the input of the $C_{Fy}(\alpha)$ function in Eq. 2.16. This connection, built between the stationary body and the oscillation body, forms the core of the quasi-steady assumption. Until here, one can already find from Eq. 2.16, that the input force of the dynamic system relates to a self-excited one which depends on the velocity of body $\dot{y}$.

For the instability about equilibrium position, very small oscillation (infinitesimal α) can be assumed so that $C_{Fy}(\alpha)$ can be linearized through Taylor's expansion

$$C_{Fy}(\alpha) \simeq C_{Fy}\big|_{\alpha=0} + \left.\frac{\mathrm{d}C_{Fy}}{\mathrm{d}\alpha}\right|_{\alpha=0} \cdot \alpha \tag{2.17}$$

where the high-order items of α is neglected. It is convenient here to define a factor A_1

$$A_1 = \left.\frac{\mathrm{d}C_{Fy}}{\mathrm{d}\alpha}\right|_{\alpha=0} = -\left.\left(\frac{\mathrm{d}C_L}{\mathrm{d}\alpha} + C_D\right)\right|_{\alpha=0} \tag{2.18}$$

where the expression containing C_D and C_L is a result of substituting Eq. 2.14 in. Moreover, since α is infinitesimal, it is able to write

$$\alpha \simeq \tan(\alpha) = \frac{\dot{y}}{U} \tag{2.19}$$

Substituting Eq. 2.17 - 2.19 into Eq. 2.16, and neglecting the $C_{Fy}\big|_{\alpha=0}$ item which induces only static deformation, one has

$$m\ddot{y} + c_y\dot{y} + k_y y = \frac{1}{2}\rho d U^2 A_1 \frac{\dot{y}}{U} \tag{2.20}$$

By further dividing both sides by m, then moving the right-side item to the left side, there is

$$\ddot{y} + 2\omega_0(\zeta_0 - \frac{\rho d U A_1}{4m\omega_0})\dot{y} + \omega_0^2 y = 0 \tag{2.21}$$

where $\omega_0 = \sqrt{k_y/m}$ is the natural circular frequency. Now, it is able to find that, if $A_1 > 0$, the item $\rho d U A_1/(4m\omega_0)$ is able reduce the total damping of the system. The critical state reaches when the total damping of the system becomes zero

$$\zeta_0 - \frac{\rho d U A_1}{4m\omega_0} = 0 \tag{2.22}$$

And the critical wind speed for this mechanism (galloping instability) is determined as

$$U_g = \frac{4m\omega_0\zeta_0}{\rho d A_1} = 2\frac{n_0 d}{A_1} \cdot Sc \tag{2.23}$$

This critical condition was first presented by Scruton (1960). The A_1 factor is usually called galloping factor as in Euro-code 1 (EN 1991-1-4 2010).

The post-critical behavior of the across-wind galloping involves larger α, which usually introduces nonlinear aerodynamic force into the system. Further development of the quasi-steady theory in this direction was contributed by Prof. Parkinson and his co-workers (Parkinson &

Brooks 1961; Parkinson & Smith 1964), by applying high-order polynomials to approximate the C_{Fy}-α curve. For brevity reason, the analytical approach to solve Eq. 2.16 is given in Appendix A.1. Alternatively, numerical integration can be performed.

2.1.3 Torsional Flutter

Aeroelastic instability can also arise in the torsional degree of freedom, being named torsional flutter throughout this thesis. Differing from the coupled flutter to be introduced later, torsional flutter is a single degree-of-freedom instability exhibiting a nearly pure torsional motion. It is right now well-accepted as the cause for the collapse of Tacoma Narrow Bridge in 1940 (Billah & Scanlan 1991; Larsen 2000), rather than the early explanation which attributed to VIV.

Torsional flutter is also driven by the sustained generation of negative aerodynamic damping after a critical flow velocity being exceeded. However, its physical mechanism is more complicated than the across-wind galloping. As shown in Fig. 2.3, torsional flutter is possible for bluff body with side ratio b/d higher than about 2. For the upper limit of b/d, it is at least up to about 10 (see, e.g., Matsumoto & al. (1997) for rectangular cross section and Scanlan & Tomko (1971) for H-shape cross section). Bluff body within this range of b/d is characterized with complex flow reattachment (either intermittent or stationary, see also Fig. 2.3), the unsteady effect is thus pronounced in this situation. Matsumoto and co-authors carried out extensive experiments with respect to torsional flutter (Matsumoto & al. 1996; Matsumoto 1996; Matsumoto & al. 1997), and they classified torsional flutter by the reduced velocity range as “low speed torsional flutter” and “high speed torsional flutter” (as indicated in Fig. 2.2). For the former, it was found closely related to the convection of impinging leading edge vortices on the lateral surfaces. For the latter, it was deemed to be governed by a similar mechanism as the coupled flutter, namely due to the unsteady local flow separation near the leading edges of bluff body.

Finally, it is to note that the quasi-steady theory (widely used for across-wind galloping), is rather inapplicable for torsional flutter. Although in literature there exist several quasi-steady-theory based methods for torsional flutter predictions, Andrianne (2012) concluded that they were all less reliable, based on his attempts of application to a 4:1 rectangular cylinder and a generic bridge model. Reliable predictions of torsional flutter rely on the experimentally identified flutter derivatives to be introduced in next Section.

2.1.4 Coupled Flutter

When the single degree-of-freedom, either heaving or torsional, is free of instability, divergent motion is still able to arise in a coupled form of the two degrees of freedom, known as coupled flutter (or classical flutter). It is first studied for airfoils, but, after the collapse of Tacoma Narrow Bridge, flutter has become an important topic for the decks of long suspended bridges.

Thin aerofoil theory

The theoretical unsteady approach to coupled flutter is first introduced for a thin plate (or thin airfoil), as schematized in Fig. 2.10 (in line with Pigolotti (2017), the gravity center is differed from the mid-chord). About the elastic center, motions of the system are governed by

$$m\ddot{y} - S\ddot{\alpha} + c_y\dot{y} + k_y y = L \tag{2.24a}$$

$$-S\ddot{h} + I\ddot{\alpha} + c_\alpha\dot{\alpha} + k_\alpha\alpha = M \tag{2.24b}$$

where m, c_y and k_y represent, respectively, the mass, damping and stiffness in heaving degree of freedom, while I, c_α and k_α correspond to the moment of inertia, damping, stiffness in torsional degree of freedom. $S = eb_h \cdot m$ is the static mass unbalance, equal to the product of the mass m and a distance eb_h between the gravity center and the elastic center. L and M are aerodynamic lift and moment, both about the elastic center. a and e indicate the ratios between the separated distances and the half chord length b_h. $a > 0$ denotes the elastic center is downstream the middle of chord, and $e > 0$ means the gravity center is upstream the elastic center (see Fig. 2.10).

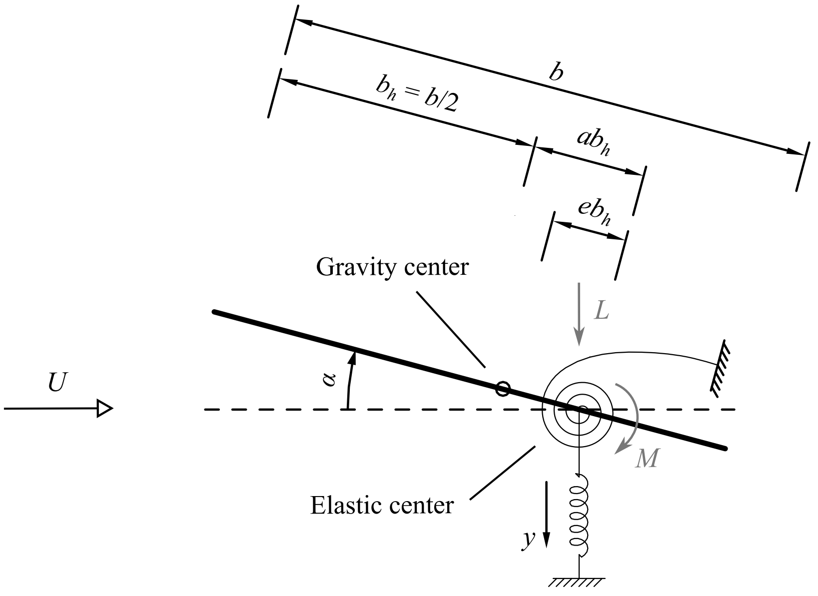

Fig. 2.10: Schematic of a thin plate with 2 degrees of freedom and associated aerodynamic forces.

In order to analytically approach the unsteady lift L and moment M, the thin plate with infinitesimal thickness is supposed to undergo small-amplitude oscillation. Moreover, the flow is assumed inviscid (no boundary layer development and no separation), incompressible and isentropic. Besides, the phenomenological rule that the flow velocity remains finite and tangent to the flat plate at the sharp trailing edge called *Kutta-Joukowski condition* (e.g., see Fung (1993)) is assumed. From basic principles of non-stationary potential flow theory, Theodorsen (1934) showed that the expressions for L and M are linear in y and α as well as their first and second derivatives. For small harmonic oscillation in the heaving and torsional degrees of freedom with the same circular frequency ω (critical condition of flutter), the expression of L and M is obtained in complex form (Simiu & Scanlan 1996; Theodorsen 1934):

$$L = -\rho b_h^2(U\pi\dot{\alpha} + \pi\ddot{y} - \pi a b_h\ddot{\alpha}) - 2\pi\rho U b_h C(k)[U\alpha + \dot{y} + b_h(\frac{1}{2} - a)\dot{\alpha}] \tag{2.25a}$$

$$\begin{aligned} M = &-\rho b_h^2\{\pi(\frac{1}{2} - a)U b_h\dot{\alpha} + \pi b_h^2(\frac{1}{8} + a^2)\ddot{\alpha} - \pi a b_h\ddot{y}\} \\ &+ 2\rho U b_h^2\pi(\frac{1}{2} + a)C(k)[U\alpha + \dot{y} + b_h(\frac{1}{2} - a)\dot{\alpha}] \end{aligned} \tag{2.25b}$$

where $k = b_h\omega/U$ is the reduced frequency defined with half-chord length b_h and oscillation circular frequency ω. $C(k)$ is the *Theodorsen's circulation function*, written in complex form

$$C(k) = F(k) + iG(k) = \frac{H_1^{(2)}(k)}{H_1^{(2)}(k) + H_0^{(2)}(k)} \tag{2.26}$$

which contains Hankel's functions

$$H_n^{(2)}(k) = J_n(k) - iY_n(k) \tag{2.27}$$

with $J_n(k)$ and $Y_n(k)$ the modified Bessel's functions of the first and second kinds. $F(k)$ and $G(k)$ denote, respectively, the real and imaginary part of $C(k)$. Approximated expression of $C(k)$, according to Jones (1945), can be expressed (see, e.g., Fung (1993))

$$C(k) = 1 - \frac{0.165}{1 - \frac{0.041}{k}i} - \frac{0.335}{1 - \frac{0.32}{k}i} \tag{2.28}$$

The real and imaginary parts of $C(k)$ are shown in Fig. 2.11, respectively, as a function of k or $U/(bn)$, being the latter a form of reduced flow velocity commonly used for flutter analysis. One can find, when the reduced flow velocity tends to infinity ($k \to 0$), $C(k) = 1$ is obtained, corresponding to a state in which no fluid memory exists. With $C(k) = 1$, Eq. 2.25 actually becomes the quasi-steady expression of aerodynamic forces exerting on an oscillation airfoil.

An analysis of the force or moment combinations in Eq. 2.25 is supposed to be meaningful. In the thin aerofoil theory (e.g., see Fung (1993)), the lift in Eq. 2.25a consists of two portions:

- the circulatory one

$$L_{y1} = -2\pi\rho U b_h C(k)[U\alpha + \dot{y} + b_h(\frac{1}{2} - a)\dot{\alpha}] \tag{2.29}$$

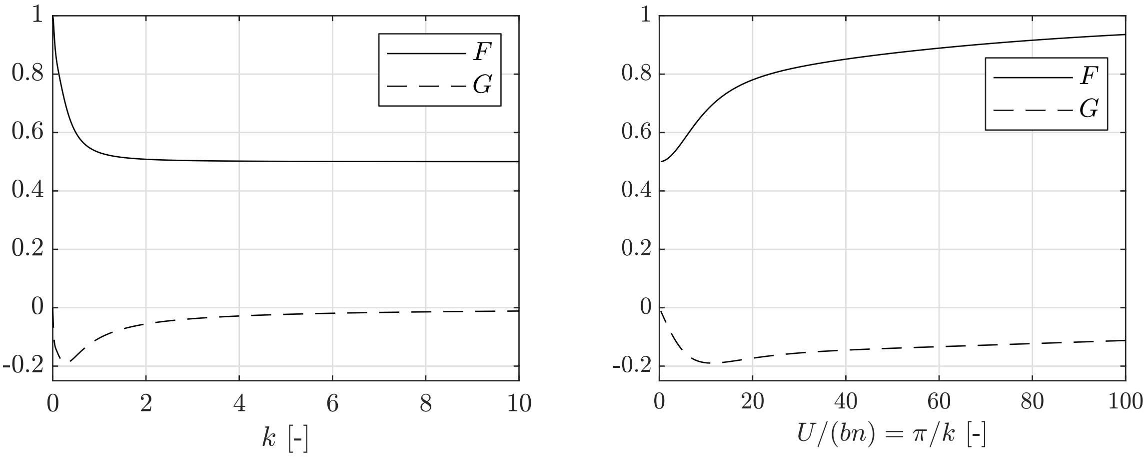

(a) (b)

Fig. 2.11: Real and imaginary parts of *Theodorsen's circulatory function* $C(k) = F(k) + iG(k)$: (a) as a function of k; (b) as a function of reduced flow velocity $U/(bn) = \pi/k$, being $\omega = 2\pi n$.

which is due to the variation of circulation around the aerofoil and exerted at the one forth of chord aft leading edge. This portion of lift is closely related to *Wagner's function* to be introduced later.

- the non-circulatory one $-\rho b_h^2(U\pi\dot{\alpha} + \pi\ddot{y} - \pi a b_h\ddot{\alpha})$. This portion of lift is related to the added mass effect, which means *the wing is forcing a mass of fluid around it to move*. It can be further divided into two parts: a) a lift with center of pressure at the mid-chord

$$L_{y2} = -\rho\pi b_h^2(\ddot{y} - a b_h\ddot{\alpha}) \tag{2.30}$$

of amount equal to the apparent mass $\rho\pi b_h^2$ of an air cylinder times the vertical acceleration at the mid-chord point; b) a lift with center of pressure at the 3/4 chord aft leading edge

$$L_{y3} = -\rho\pi b_h^2 U\dot{\alpha} \tag{2.31}$$

of the nature of a centrifugal force, of amount equal to the apparent mass $\rho\pi b_h^2$ times $U\dot{\alpha}$.

In the pitching degree of freedom, the pure nose-down couple is

$$M_{\alpha 2} = -\frac{1}{8}\rho\pi b_h^4\ddot{\alpha} \tag{2.32}$$

of amount equal to the apparent moment of inertia $\frac{1}{8}\rho\pi b_h^4$ times the angular acceleration $\ddot{\alpha}$. It is interesting to see, in thin aerofoil theory, the apparent mass of a thin plate is equal to the mass of an air cylinder with diameter equal to the chord of the plate, while the apparent moment of inertia is only one fourth of the mass moment of inertia of that air cylinder. Finally, there are $L = L_{y1} + L_{y2} + L_{y3}$ and $M = -L_{y1}(\frac{1}{2} + a)b_h - L_{y2}ab_h + L_{y3}(\frac{1}{2} - a)b_h + M_{\alpha 2}$.

The L_{y1} item (Eq. 2.29), based on *Theodorsen's circulatory function* $C(k)$, is a result of the assumed harmonic motion, mixed the expression of L_{y1} in both frequency and time domains. In the time domain, the equivalent problem had been solved some years before by Wagner (1925) for more general motion. Consider here a thin plate orientated with a small α and immersed in incompressible fluid of flow velocity U. Now, assume an impulsive (or indicial) increment of wind angle of attack $\Delta\alpha$ taking place at the moment $\tilde{\tau} = Ut/b_h = 0$ ($\tilde{\tau}$ is the reduced time). Since the flow must be tangent to the plate, the downwash (the vertical velocity component of the fluid on the thin plate) before and after the motion are, respectively, $\tilde{w} = U\sin\alpha \approx U\alpha$ and $\tilde{w} = U\sin(\alpha + \Delta\alpha) \approx U(\alpha + \Delta\alpha)$. The downwash increment $\Delta\tilde{w} = U\Delta\alpha$ will give an increment of the circulatory lift (exerted at the one fourth aft the leading edge)

$$\Delta L_{y1}(\tilde{\tau}) = -\frac{1}{2}\rho U^2 b \cdot 2\pi \cdot \frac{\Delta\tilde{w}}{U} \cdot \Phi(\tilde{\tau}) \tag{2.33}$$

where 2π in above equation corresponds to the slope of lift coefficient of stationary thin plate, and $\Phi(\tilde{\tau})$ is called *Wagner's function*

$$\Phi(\tilde{\tau}) = 1 - \int_0^\infty [(Y_0(x) + Y_1(x))^2 + \pi^2(J_0(x) + J_1(x))^2]^{-1} e^{-x\tilde{\tau}} x^{-2} dx \quad \text{if } \tilde{\tau} \geq 0 \tag{2.34a}$$

$$\Phi(\tilde{\tau}) = 0 \quad \text{if } \tilde{\tau} < 0 \tag{2.34b}$$

where J_0 and J_1, Y_0 and Y_1 are the previously mentioned Bessel's function of the first and second kind. Alternatively, Jones (1945) approximated $\Phi(\tilde{\tau})$ with exponential functions

$$\Phi(\tilde{\tau}) = 1 - 0.165e^{0.041\tilde{\tau}} - 0.335e^{-0.32\tilde{\tau}} \tag{2.35}$$

with $\Phi(\tilde{\tau}) = 0$ for $\tilde{\tau} < 0$. This approximated $\Phi(\tilde{\tau})$ is shown in Fig. 2.12.

Combined with Eq.2.33 and Fig. 2.12, one can find that there will be only half portion of lift increment generated instantaneously after the impulsive increment $\Delta\tilde{w}$ at $\tilde{\tau} = 0$. The full lift increment is reached with $\tilde{\tau} \to \infty$. Analytically speaking, $\Delta\tilde{w}/U$ represents a kind of variation of wind angle of attack since the motion is assumed under small amplitude. This is apparent for the impulsive motion discussed above, because $\Delta\tilde{w}/U$ can be directly replaced with $\Delta\alpha$.

For a general motion with two degrees of freedom, the downwash over the airfoil is not uniform. But the theory of oscillation airfoil shows that for heaving and torsional oscillation the downwash velocity can be determined at the 3/4-chord point aft leading edge

$$\tilde{w}(t) = U\alpha(t) + \dot{y}(t) + (\frac{1}{2} - a)b\dot{\alpha}(t) \tag{2.36}$$

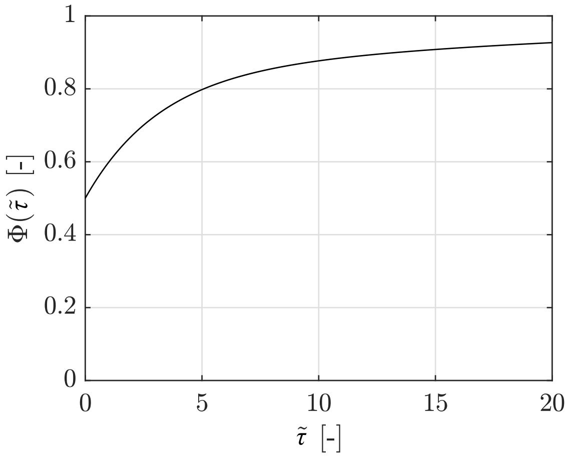

Fig. 2.12: *Wagner's function* after Jones (1945)'s approximation.

or expressed by reduced time

$$\tilde{w}(\tilde{\tau}) = U\alpha(\tilde{\tau}) + \frac{U}{b}y'(\tilde{\tau}) + (\frac{1}{2} - a)U\alpha'(\tilde{\tau}) \tag{2.37}$$

where $(\,)'$ denotes differentiation to the reduced time $\tilde{\tau}$, $(\dot{\,})$ to the physical time. Clearly, there is $(\dot{\,}) = \frac{U}{b}(\,)'$. Further more, the downwash increment can be written in differential form

$$\mathrm{d}\tilde{w}(\tilde{\tau}) = [U\dot{\alpha}(\tilde{\tau}) + \frac{U}{b}y''(\tilde{\tau}) + (\frac{1}{2} - a)U\alpha''(\tilde{\tau})]\mathrm{d}\tilde{\tau} \tag{2.38}$$

For a general motion, the lift at a given reduced time $\tilde{\tau}$ is influence by the past downwash variations in the whole time history. Taking Eq.2.33 and invoking the superposition principle, the expression of lift at the current $\tilde{\tau}$ is obtained as (under the conditions, that the motion starts from rest at the past $\tilde{\tau}_0$ and a downwash increment $\Delta\tilde{w}_0$ is obtained immediately at $\tilde{\tau} = \tilde{\tau}_0$)

$$\begin{aligned} L_{y1}(\tilde{\tau}) &= L_{y1,\tilde{\tau}_0} + \pi\rho U b[\Delta\tilde{w}_0\Phi(\tilde{\tau} + \int_{\tilde{\tau}_0}^{\tilde{\tau}} \mathrm{d}w(\kappa)\cdot\Phi(\tilde{\tau}-\kappa)] \\ &= L_{y1,\tilde{\tau}_0} + \pi\rho U b[\Delta\tilde{w}_0\Phi(\tilde{\tau}) + \int_{\tilde{\tau}_0}^{\tilde{\tau}} \Phi(\tilde{\tau}-\kappa)[U\dot{\alpha}(\kappa) + \frac{U}{b}y''(\kappa) + (\frac{1}{2} - a)U\alpha''(\kappa)]\mathrm{d}\kappa] \end{aligned} \tag{2.39}$$

where $L_{1,\tilde{\tau}_0}$ corresponds to the steady lift before the motion starts (namely $\tilde{\tau} < \tilde{\tau}_0$). For more common initial conditions, namely the thin plate starting from rest with null angle of attack ($L_{1,\tilde{\tau}_0} = 0$) and putting in $\tilde{\tau}_0 = 0$, above equation becomes (see, e.g., Mannini (2006))

$$\begin{aligned} L_{y1}(\tilde{\tau}) &= \pi\rho U b[\Delta\tilde{w}_0\Phi(\tilde{\tau}) + \int_0^{\tilde{\tau}} \mathrm{d}w(\kappa)\cdot\Phi(\tilde{\tau}-\kappa)] \\ &= \pi\rho U b[\Delta\tilde{w}_0\Phi(\tilde{\tau} + \int_0^{\tilde{\tau}} \Phi(\tilde{\tau}\kappa)[U\dot{\alpha}(\kappa) + \frac{U}{b}y''(\kappa) + (\frac{1}{2} - a)U\alpha''(\kappa)]\mathrm{d}\kappa] \end{aligned} \tag{2.40}$$

Finally, it is to note that the *Wagner's function* is linked to *Theodorsen's circulatory function* through inverse Fourier transform (Bisplinghoff & al. 1996)

$$\Phi(\tilde{\tau}) = \frac{1}{2}\int_{-\infty}^{\infty} \frac{C(k)}{ik} e^{ik\tilde{\tau}} \mathrm{d}k \tag{2.41}$$

Bluff body

Flow passing by bluff body characterizes with massive separations, reattachment, bubbles, shear layer instability as well as shedding of vortices. An analytical theory providing a closed solution like the thin aerofoil is actually impossible. Nevertheless, a good practical way to approach the flutter of bluff body has been proposed by Scanlan & Tomko (1971), using the experimentally determined functions which depend on section geometry and reduced frequency of oscillation. Referring to the dynamic system in Fig. 2.10, Scanlan & Tomko (1971) have shown that for small oscillations the self-excited lift and moment on a bluff body may be treated as linear in the structural heaving and torsional displacement and their first two derivatives, so that the expression of L and M can be written in real form (Simiu & Scanlan 1996)

$$L(t,K) = \frac{1}{2}\rho U^2 b[KH_1^*(K)\frac{\dot{y}(t)}{U} + KH_2^*(K)\frac{b\dot{\alpha}(t)}{U} + K^2H_3^*(K)\alpha(t) + K^2H_4^*(K)\frac{y(t)}{b}] \tag{2.42a}$$

$$M(t,K) = \frac{1}{2}\rho U^2 b^2[KA_1^*(K)\frac{\dot{y}(t)}{U} + KA_2^*(K)\frac{b\dot{\alpha}(t)}{U} + K^2A_3^*(K)\alpha(t) + K^2A_4^*(K)\frac{y(t)}{b}] \tag{2.42b}$$

where $K = 2k = b\omega/U$ is the reduced frequency of oscillation defined with the chord length; H_i^* and A_i^* are flutter derivatives as functions of K and dependent on section geometry. In Eq. 2.42, terms in $\ddot{y}$, $\ddot{\alpha}$ have been omitted as being of negligible importance in wind engineering (Simiu & Scanlan (1996)). Above expressions are also mixed in both frequency and time domain. Nevertheless, when harmonic oscillations are assumed for both heaving and torsional degrees of freedom

$$y = \bar{y}e^{i\omega t} \tag{2.43a}$$

$$\alpha = \bar{\alpha}e^{i\omega t} \tag{2.43b}$$

the expressions become completely frequency dependent. Moreover, within this assumption, the flutter derivatives of thin plate can be related to *Theodorsen's circulatory function* (by putting Eq. 2.43 in Eq. 2.25, then comparing the real part of Eq. 2.25 with Eq. 2.42, in which the real part of Eq. 2.43 is substituted in)

$$H_1^*(K) = -\pi\frac{F(k)}{k} \tag{2.44a}$$

$$H_2^*(K) = -\frac{\pi}{4k}[1+\frac{2G(k)}{k+2(\frac{1}{2}-a)}F(k)] \tag{2.44b}$$

$$H_3^*(K) = -\frac{\pi}{4k^2}[2F(k)-2(\frac{1}{2}-a)G(k)k+ak^2] \tag{2.44c}$$

$$H_4^*(K) = \frac{\pi}{2}[1+2(\frac{G(k)}{k}] \tag{2.44d}$$

$$A_1^*(K) = \frac{\pi}{2k}(1+\frac{1}{2})F(k) \tag{2.44e}$$

$$A_2^*(K) = -\frac{\pi}{8k^2}[(\frac{1}{2}-a)k-2(a+\frac{1}{2})G(k)+2k(a^2-\frac{1}{4})F(k)] \tag{2.44f}$$

$$A_3^*(K) = \frac{\pi}{8k^2}[k^2(a^2+\frac{1}{8})+2(a+\frac{1}{2})F(k)+2k(a^2-\frac{1}{4})G(k)] \tag{2.44g}$$

$$A_4^*(K) = -\frac{\pi}{4k}[ak+2(a+\frac{1}{2})G(k)] \tag{2.44h}$$

Flutter derivatives can be either determined by forced vibration tests (e.g., see Matsumoto & al. (1996)) or free-decaying vibration tests (e.g., see Gu & al. (2000)). Fig. 2.13 shows the flutter derivatives for rectangular cross sections of various side ratio b/d. The theoretical ones of thin plate, calculated by Eq. 2.44, are also plotted. It can be found , that for the rectangular cross section with very large side ratio (like $b/d = 20$) the experimentally identified flutter derivatives show good agreement with the theoretical solutions for thin plate. However, for very bluff cross section like the square one, its flutter derivatives are totally different from the ones of thin plate. Nevertheless, flutter derivatives are also very useful for across-wind galloping and torsional flutter predictions. For the former, it characterizes with a change of H_1^* from negative to positive value after a certain reduced wind speed being exceeded, while for the latter it corresponds to a similar change in the A_2^* curve. Through Fig. 2.13, it is also known that the vanishing of torsional flutter for rectangular cross sections may occur at a side ratio $b/d =$ 10-12.5.

Determination of the critical flutter flow velocity can be achieved in frequency domain, substituting the assumed harmonic motions (Eq. 2.43) into the equilibrium equations (combined by Eq. 2.24 and Eq. 2.42). For nontrivial solution ($\bar{\alpha}$ and $\bar{y}$ in Eq. 2.43 are not null), the determinant of the equilibrium equations must vanish, which goes to the eigenvalue problem. However, flutter derivatives are functions of K, dependent on the circular oscillation frequency ω which is unknown. The semi-inverse method is therefore usually used in practice, assuming a range of K to search the solution which makes the determinant vanish at a real value of ω_c (for more details, see, e.g. Simiu & Scanlan (1996)). Once ω_c is found, the critical wind speed can be calculated from the corresponding value of assumed K. The flutter coupling circular frequency ω_c has to be larger than the circular natural frequency of heaving degree of freedom and smaller

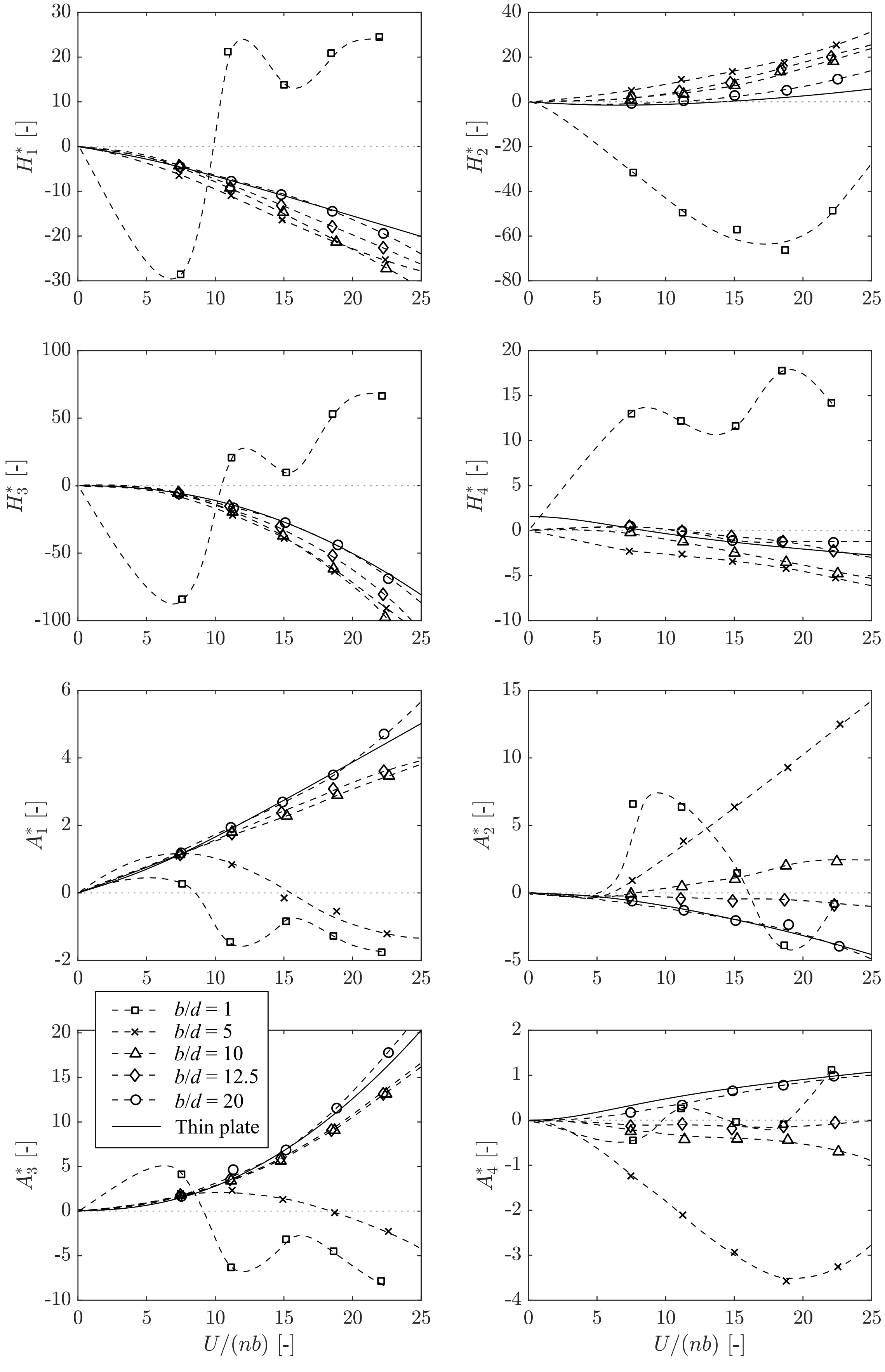

Fig. 2.13: Flutter derivatives of rectangular cross sections with various side ratio b/d (Matsumoto 1996), as well as the theoretical ones of thin plate.

than the one of torsional degree of freedom, which means the torsional natural frequency has to be larger than heaving one for the occurrence of coupled flutter.

The frequency-domain method allows efficient determination of the flutter coupling frequency and the critical wind speed, but not suitable for supercritical and subcritical analyses. Another classical approach to flutter problem involves the use of aerodynamic indicial functions to do calculation in time domain (Scanlan & al. 1974). Unlike *Wagner's function*, which is used for thin plate, the indicial functions of bluff bodies were usually derived from the experimentally determined flutter derivatives (e.g. in Costa & Borri (2006)).

Finally, as stressed by Simiu & Scanlan (1996), the coupled flutter is essentially different from the torsional flutter. For the former, if and when it occurs, it must involve coupled degrees of freedom, being in a condition where it is mainly the coupling terms (not the damping) to govern the response.

2.2 Unsteady Across-wind Galloping

2.2.1 Failure of Quasi-steady Theory and Characteristics of Unsteady Galloping

Despite the success of quasi-steady theory in predictions of the across-wind galloping, the application of this theory is actually conditional. That is the requirement of a so-called high reduced flow velocity, which is aforementioned in Section 2.1.2. Different criteria have been proposed in order to guarantee such a high reduced flow velocity (Païdoussis & al. 2010):

- According to Fung (1955), the criterion is that: any disturbance experienced by the oscillation body at a certain point in its oscillatory motion must be swept downstream sufficiently far, by the time the body comes back to that same point (one period later), for the disturbance to no longer affect the flow around the body. Assuming the disturbances are carried downstream with a velocity equal to free stream velocity U, the distance of disturbances being carried downstream within one period of body's oscillation is U/n_0, where n_0 is the natural frequency of oscillation (here for heaving degree of freedom). Fung (1955) proposed that this distance should be at least 10 times the body's diameter or the characteristic length d (or b), giving that

$$\frac{U}{n_0 d} \geq 10 \quad \text{or} \quad \frac{U}{n_0 b} \geq 10 \tag{2.45}$$

- Blevins (1977) proposed the criterion based on the vortex shedding process, that the vortex shedding frequency n_{st} must be at least two times higher than the oscillation frequency n_o. For wind engineering, n_o can be closely replaced by the natural frequency n_0, so that

  $$\frac{U}{n_0 d} \geq 2\frac{U}{n_{st} d} = 2\frac{1}{St} \tag{2.46}$$

  where St is Strouhal number. This criterion also means that the flow velocity must be two times higher than the resonance wind speed. Later, without further explanation, Blevins (1990) revised this criterion to

  $$\frac{U}{n_0 d} \geq 20 \tag{2.47}$$

  which becomes independent on the vortex shedding process.

- Bearman & al. (1987) proposed a more restrictive criterion for a good performance of the quasi-steady theory, based on the study of a square cylinder

  $$\frac{U}{n_0 d} \gtrsim 4\frac{U}{n_{st} d} = 4\frac{1}{St} \tag{2.48a}$$

  $$\text{or, } \frac{U}{n_0 d} \gtrsim 30 \tag{2.48b}$$

  being the second one as a result of putting $St = 0.13$ (square cylinder) into the first one.

One can find the above criteria are actually inconsistent with each other. It is also to note, for the two criteria proposed by Blevins at different time (Blevins 1977, 1990), the latter is more conservative for a square cross section ($St \approx 0.13$) but less conservative for a 2:1 rectangular cross section ($St \approx 0.08$). Bearman's criterion represents the most restrictive one, and was respected by a 3:2 rectangular as well (Mannini & al. 2016b), where the quasi-steady prediction was found valid for $U/(n_0 d)$ higher than about $3.5/St$. However, as noted by Novak (1972), the square section obeys relatively well to the quasi-steady theory, whereas much higher reduced flow velocity is needed for the 2:1 or 5:2 rectangular cylinder (Santosham 1966; Smith 1962). In particular, Santosham (1966)'s experiments on the 2:1 rectangular cylinder showed that, for the so-called high reduced flow velocity, it could mean 5-6 times $1/St$.

Nevertheless, if a high reduced flow velocity is not ensured, the quasi-steady theory will fail to provide reliable predictions, even in a qualitative manner. Galloping occurring in the low reduced flow velocity range is therefore called unsteady galloping, which is named so to highlight the roles of unsteadiness in the interaction between oscillation body and surrounding flow.

The very typical unsteady galloping is known as an interaction with VIV, which is able to promote unrestricted galloping-type oscillation starting at the critical wind speed for VIV, rather than at the quasi-steady prediction. Early in 1960s, Parkinson & Brooks (1961) have reported this phenomenon for several 2-dimensional cylinders in case of low mechanical damping (see Fig. 2.14). The 5:2 rectangular cross section, although not included in Fig. 2.14, was reported also prone to this combined instability (Smith 1962). In general, it occurs for cross sections prone to both VIV and, to be more precisely, soft-type galloping, because it is noticed that, for the D-shape and the 1:2 rectangular cross section which are prone to hard-type galloping (Novak & Tanaka 1974), this interaction phenomenon does not occur. In Fig. 2.14, for the rectangular ones, it can be found that the post-critical amplitude slope decreases with the increase of side ratio b/d. This is probably related to the smaller incident angle of flow reattachment for larger b/d. Finally, as may be expected, these amplitude curves were found to gradually approach to the quasi-steady solutions when the reduced flow velocity is increased high enough (see Wawzonek (1979) for a square cylinder and Santosham (1966) for a 2:1 rectangular cylinder).

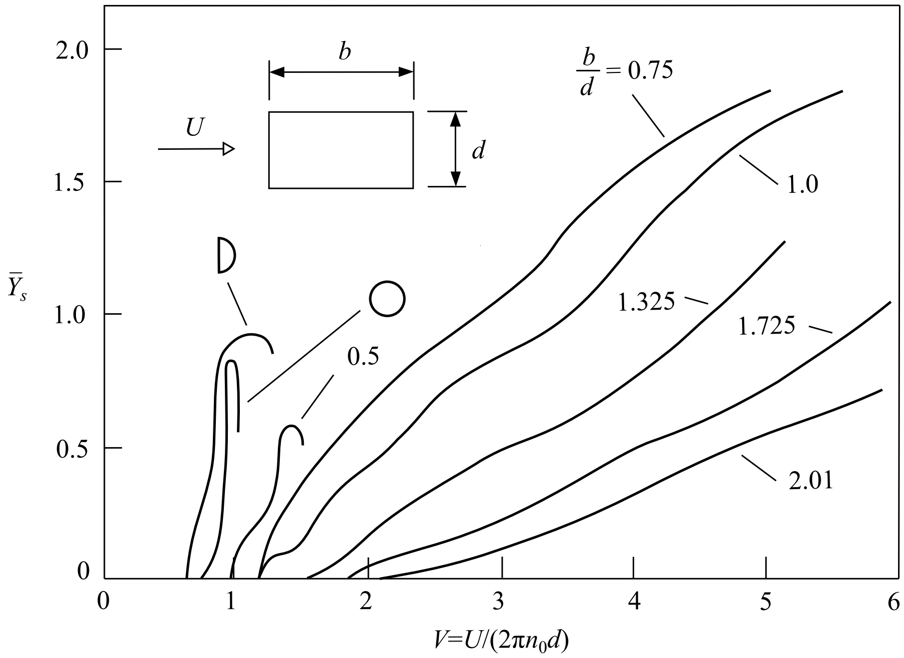

Fig. 2.14: Experimental amplitude-velocity curves for D-shape cylinder, circular cylinder and rectangular cylinders with various b/d, considering a low mechanical damping. Reproduced from Parkinson & Brooks (1961).

With proper increment of the amount of Scruton number, the combined instability is able to exhibit more complicated characteristics. Fig. 2.15 shows the experimental results and the corresponding quasi-steady predictions for a square cylinder (Wawzonek 1979), with Sc varied from a small value to a high one (where the quasi-steady prediction is already valid to some extent). For a very low Scruton number ($Sc = 2.2$), the actual galloping arises at the reduced Kármán-vortex resonance wind speed V_r, rather than at the quasi-steady prediction V_g (here, $V_g \ll V_r$ because of the very low Sc). Increasing Sc to a medium value (15.7-22), galloping still arises at V_r and monotonously increases with V, but a second stable branch with lower amplitude co-exists in a range of V slightly higher than V_r. This low amplitude branch is obtainable by releasing the square cylinder from rest, and either decrement or increment of V stepping outside that flow velocity range will lead the oscillation back to the high amplitude branch. It is to notice that such a low-amplitude branch is not reflected in the quasi-steady predictions. For $Sc = 32$, where VIV and galloping can be separately observed, the quasi-steady theory provides good prediction for the low amplitude branch. However, the high-amplitude branch was found to appear at reduced wind speeds clearly lower than the quasi-steady predictions.

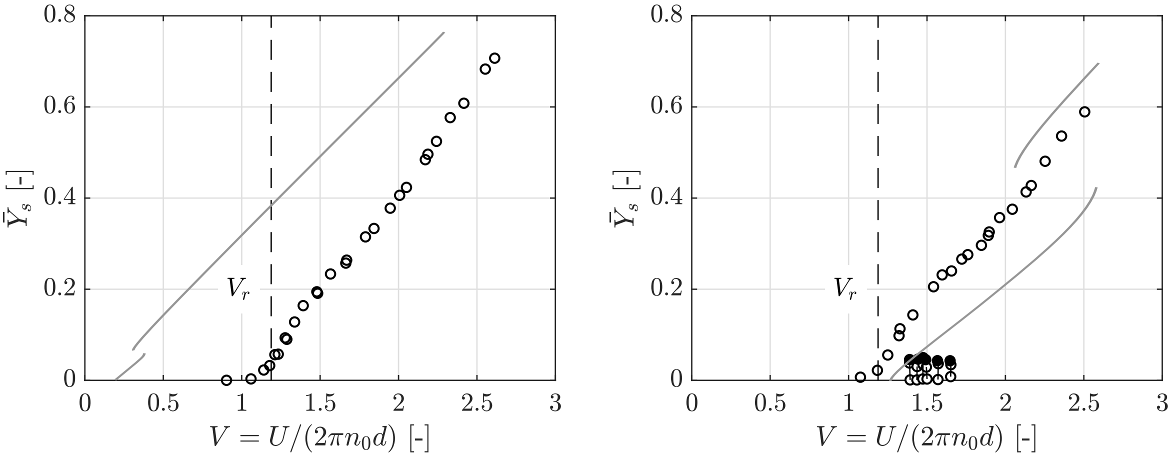

(a) $Sc = 2.2, V_g/V_r = 0.15$ (b) $Sc = 15.7, V_g/V_r = 1.05$

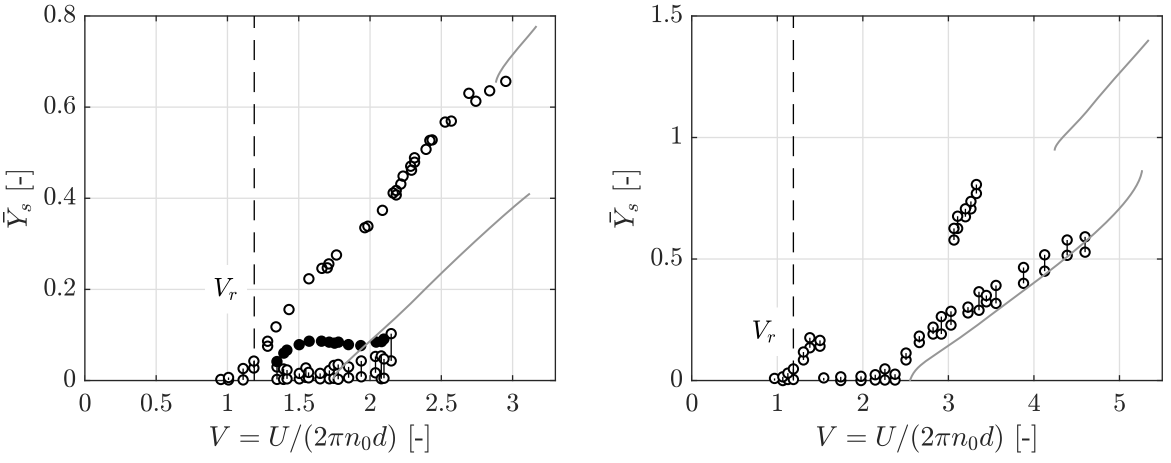

(c) $Sc = 22.0, V_g/V_r = 1.47$ (d) $Sc = 32.0, V_g/V_r = 2.14$

Fig. 2.15: Experimental results of a square cylinder and the quasi-steady predictions (gray solid line) with various Sc (reproduced from Wawzonek (1979)). Solid cycle indicates the unstable amplitude branch, and dashed line the reduced critical flow velocity for VIV.

For the slightly more elongated 3:2 rectangular cylinder, Mannini & al. (2016b, 2018a) reported a different unsteady galloping behavior for the medium magnitude of Sc (Fig. 2.16). For $Sc \leq 42$ ($V_g/V_r \leq 1.63$), the galloping response is similar to the square cylinder of low Sc conditions, arising galloping at V_r. Increasing the Scruton number into a range of $55.5 \leq Sc \leq 61.5$, a VIV peak appears in the amplitude-velocity plot, but the subsequent oscillation does not decrease fully to form the typical VIV response. Instead, the amplitude after the VIV peak first decreases a little then grows again (see Fig. 2.16 (b)). For this *Sc*, the experiments also show an anti-clockwise hysteresis loop, occurring in a reduced velocity range lower than the quasi-steady prediction. Further increasing *Sc*, the oscillation after the VIV peak gradually drops back to the equilibrium position, forming a classical VIV response around V_r. However, for *Sc* not higher than 78, the actual galloping onset was found apparently lower than the quasi-steady prediction. Only when the Scruton number is higher than about 90, the quasi-steady theory is able to provide satisfying predictions. Based on the amplitude-velocity curves of various *Sc*, Mannini & al. (2016b) classified the inference effects between VIV and galloping into four categories: a) Full Interference, b) Partial Interference, c) Low Interference and d) No Interference. The four plots of Fig. 2.16, respectively, correspond to the four classifications.

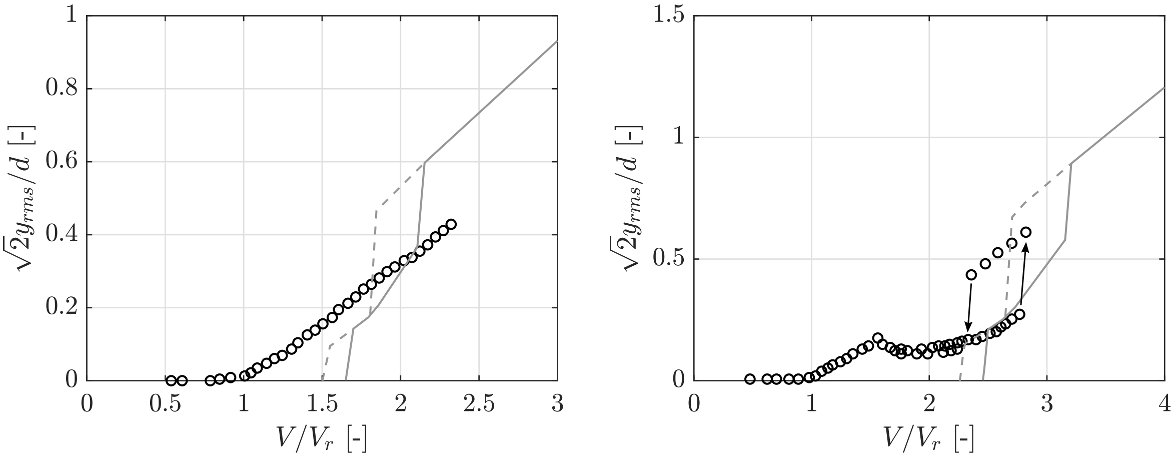

(a) $Sc = 42, V_g/V_r = 1.63$ (b) $Sc = 61.5, V_g/V_r = 2.42$

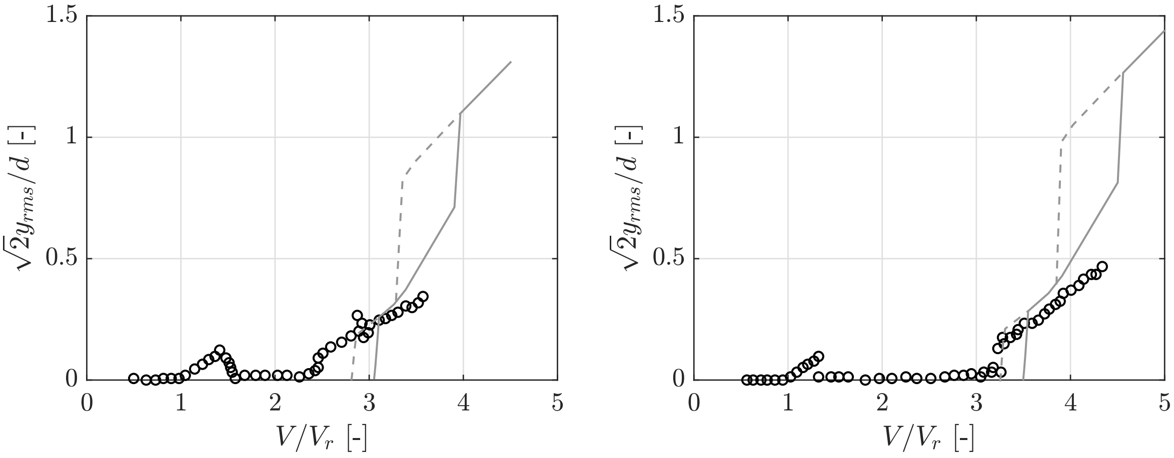

(c) $Sc = 78, V_g/V_r = 3.02$ (d) $Sc = 90, V_g/V_r = 3.46$

Fig. 2.16: Experimental results of a 3:2 rectangular cylinder and the quasi-steady predictions (gray line) with various *Sc* (reproduced from Mannini & al. (2018a))

Through the aerodynamic force measurements on a vibration body, the driving mechanism of unsteady galloping was studied in another but more direct manner. Assuming that a prism body is forced to do harmonic oscillation in the across-wind direction with an amplitude y_0 and a frequency n_m, the motion of the body can be written as

$$y(t) = y_0 \cos(2\pi n_m t) \tag{2.49}$$

The steady-state aerodynamic lift coefficient (characterized also by a frequency n_m), due to this specified motion, can be written as

$$C_{Lm}(t) = C_{Lm0} \cos(2\pi n_m t + \varphi_{Lm}) \tag{2.50}$$

where C_{Lm0} is the magnitude of the lift coefficient at a frequency of n_m, and φ_{Lm} the phase angle relative to the across-wind displacement. This equation can be further written as

$$\begin{aligned} C_{Lm}(t) &= C_{Lm0} \cos(\varphi_{Lm}) \cdot \cos(2\pi n_m t) + C_{Lm0} \sin(\varphi_{Lm}) \cdot [-\sin(2\pi n_m t)] \\ &= C_{LmR} \cdot \cos(2\pi n_m t) + C_{LmI} \cdot [-\sin(2\pi n_m t)] \end{aligned} \tag{2.51}$$

where $C_{LmR} = C_{Lm0} \cos(\varphi_{Lm})$ and $C_{LmI} = C_{Lm0} \sin(\varphi_{Lm})$ are, respectively, the portion of C_{Lm0} in phase with $y(t)$ and in phase with $\dot{y}(t)$. It is easy to understand that, for $0 < \varphi_{Lm} < \pi$, the $C_{LmI} \cdot [-\sin(2\pi n_m t)]$ component will have the same sign as $\dot{y}(t)$. So this component will do positive work (extracting energy from flow) and play a role as negative damping force, implying an instability. Here, it is to mention that, in the linear quasi-steady theory, the phase angle of aerodynamic force is $\varphi_{Lm} = \pi/2$ for $A_1 > 0$, see Eq.2.20.

The forced vibration method is widely used to study the motion-induced aerodynamic force and examine the quasi-steady theory. For a square cylinder in smooth flow, the typical C_{Lm0}, φ_{Lm} and C_{LmI} curves, as functions of reduced flow velocity ($U/(n_m d)$), are shown in Fig. 2.17 (Nakamura & Mizota 1975). One can find that the magnitude of C_{Lm0} shows a significant increase around $1/St$, which is definitely influenced by the resonance effect of vortex shedding. Moreover, it is to note that the phase angle φ_{Lm} quickly changes its sign, from negative to positive, at a reduced flow velocity slightly higher than $1/St$, then gradually approaches to 90° at high reduced velocities. Since "$0 < \varphi_{Lm} < \pi$" implies the instability, it is reasonable to say that the quasi-steady theory begin to qualitatively hold for $U/(n_m d)$ slightly higher than $1/St$. However, for $U/(n_m d) < 1/St$, the quasi-steady theory is definitely invalid. For the more elongated 2:1 rectangular cylinder, results of Nakamura & Mizota (1975) and Washizu & al. (1978) show that the variation of φ_{Lm} with $U/(n_m d)$ is qualitatively the same as the square cylinder, but the transition of φ_{Lm} from negative to positive is less steep and strongly influenced by the oscillation amplitude (especially the position of φ_{Lm} crossing zero).

Fig .2.17 (c) shows a comparison of the experiments with the linear quasi-steady predictions, being the data points with an apparent wind angle of attack lower than 1.8° considered. Close to $1/St$, one can find that the measured destabilizing force is stronger than the quasi-steady predictions. Such a characteristic is also reported for the 2:1 rectangular cylinder, in an even wider range of reduced flow velocity (Nakamura & Mizota 1975; Washizu & al. 1978). Nevertheless, this stronger destabilizing force agrees well with the advancing of galloping onset in the "Low Interference" behaviors, as shown in Fig. 2.16 (c). Finally, Ma & al. (2018) adopted the forced

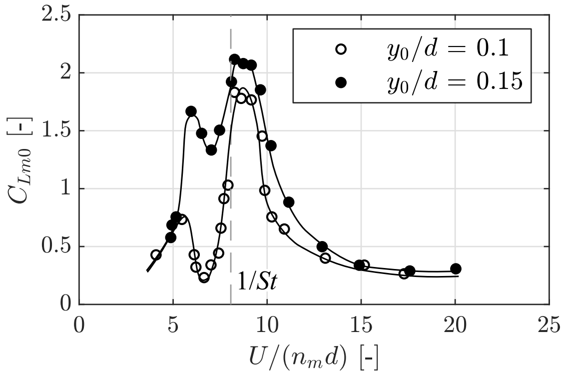

(a) Magnitude of $C_{Lm}(t)$

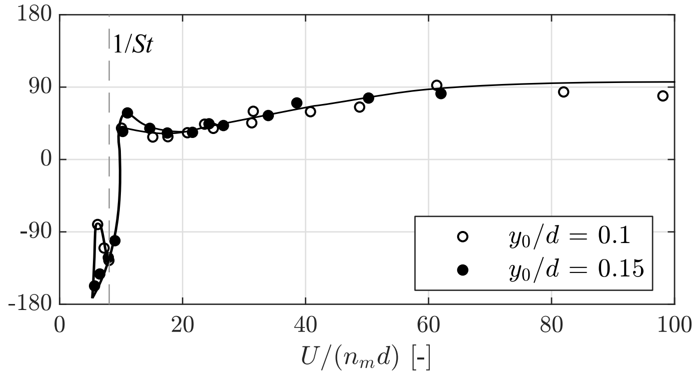

(b) Phase angle by which $C_{Lm}(t)$ leads $y(t)$

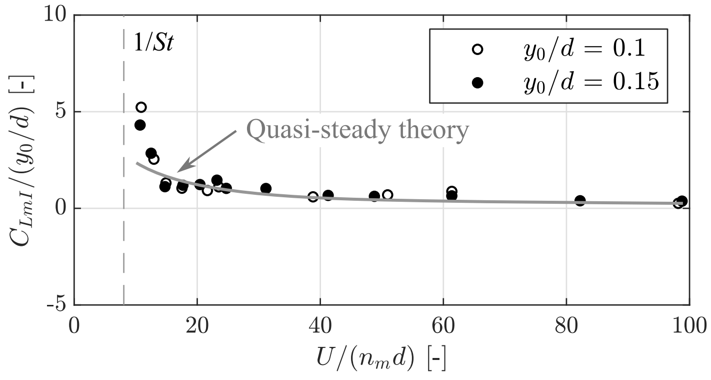

(c) Comparison with linear quasi-steady theory (data points with apparent angle of attack lower than 1.8°)

Fig. 2.17: Characteristics of the motion-induced aerodynamic force measured on a vibration square cylinder (reproduced from Nakamura & Mizota (1975)). $1/St$ denotes the reduced wind speed for Kármán-vortex resonance.

vibration method for a square cylinder, with quite detailed variation of the reduced wind speed and the oscillation amplitude. The measured motion-induced force was used to predict the free vibration test results registered in Wawzonek (1979), showing satisfying agreements.

Motion-induced aerodynamic force can be also measured on a free vibration body, either through pressure measurements (e.g., Bearman & al. (1987)) or direct force measurements (e.g., Gao & Zhu (2016)). Bearman & Luo (1988) compared the phase angles of the motion-induced force, obtained respectively from free vibration tests and forced vibration testes in steady oscillation state. As expected, the agreement is quite good. Nevertheless, for force measurements on a free vibration body, the concerned transient behaviors (e.g., the building-up process of galloping oscillation) can be also studied, see e.g. Gao & Zhu (2016). Recently, the forced vibration test setup also gets some developments. The quite impressive one is reported by Siedziako (2017), consisting of two actuators to force the wind tunnel model to vibrate in any wanted manner (even the random vibration).

The previously introduced unsteady galloping behaviors, either the aeroelastic response or the exciting force, are based on rectangular cylinders with one face perpendicular to the incoming flow. When the front face of these objects is not perpendicular any more, unsteady galloping is still able to arise but may behave in different manner. Fig. 2.18 shows what is encountered for the square cylinder being nosed up 9°. In the left side plot, Carassale & al. (2015)'s forced vibration tests show that the change of sign of the phase angle occurs apparently after V_r. This is quite different from the null wind angle of attack case shown by Fig. 2.17 (b). In the right side plot, Dai (2019)'s free vibration test results confirmed that, in this situation, the galloping arises at about $1.6V_r$ rather than at V_r, even for $Sc = 4$ (this Scruton number is very low so that there is quasi-steady prediction $V_g \ll V_r$). A typical VIV response around V_r is also observed. Similar aeroelastic responses occur also for the 12° mean flow incidence (separately, VIV appears at V_r and galloping arises at $2.2V_r$, with $Sc = 4$). In contrast, for the mean flow incidence not higher than 6°, the typical combined VIV-galloping was observed in case of low Sc (Dai 2019).

For convenience, the phenomenon shown in Fig. 2.18 is named *atypical unsteady galloping*. Qualitatively speaking, this is a phenomenon different from the typical unsteady galloping due to the interaction with VIV. Because, even for a very low Sc, an interaction between galloping and VIV ia actually not observed. From the point of view of the phase angle φ_{Lm}, the difference is exhibited by the lower bound of V, defined here as V_{lb}, higher than which φ_{Lm} becomes positive (in small-amplitude oscillation state). In the case of typical unsteady galloping, V_{lb} seems at about V_r (Fig. 2.17 (b)), while for the *atypical unsteady galloping* it is clearly higher than V_r (Fig. 2.18 (a)). For the quasi-steady theory, V_{lb} is supposed to be of great importance, because it indicates a reduced flow velocity at which the theory becomes at least qualitatively valid (although, quantitatively, the magnitude difference may be still very large).

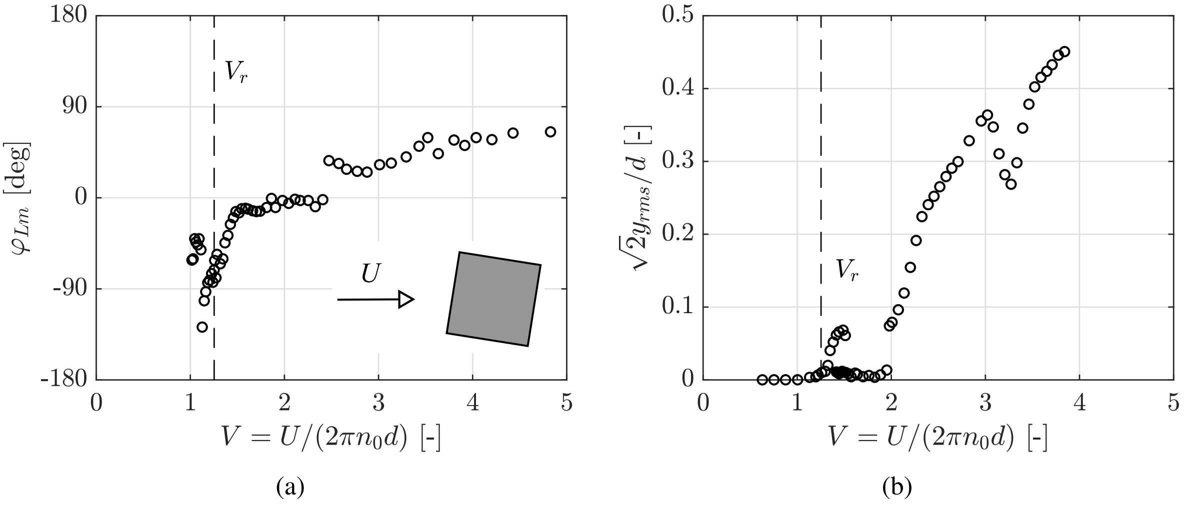

(a) (b)

Fig. 2.18: Instability of the square cylinder with an mean wind angle of attack of 9°: (a) phase angle by which $C_{Lm}(t)$ leads $y(t)$, obtained by forced vibration tests with fixed oscillation amplitude of $y_0/d = 0.1$ (Carassale & al. 2015); (b) amplitude-velocity plot of free vibration tests, with a very low Scruton number $Sc = 4$ (Dai 2019). $St = 0.127$ for $\alpha = 9°$ is used to plot the reduced wind speed for Kármán-vortex resonance V_r (St measured at $Re = 2.6 \cdot 10^3$ (Dai 2019)).

Finally, it may be interesting to think about “why is V_{lb} just right around V_r for the cases of typical unsteady galloping?” and “why is V_{lb} clearly behind V_r for the cases of *atypical unsteady galloping*?”. For the first question, it may be answered by the *asynchronous quenching* effect, that the vortex shedding process is able to stabilize or quench the body’s motion up to the Kármán-vortex resonance wind speed (Mannini & al. 2014). This effect is successfully reflected by Tamura’s nonlinear wake oscillator model to be introduced later. However, for the second question, there exists still no convincing explanations according to the author’s knowledge. Interestingly, a quite similar phenomenon to the *atypical unsteady galloping* has been observed by Santosham (1966), for a 2:1 rectangular cylinder with split-plate presented in the wake (the front face of the cylinder is perpendicular to the incoming flow). There, for a very low Sc, galloping arose at about $V = 3$, while without split-plate it arose at about $V = V_r = 2$.

2.2.2 Sources of Unsteadiness in Across-wind Oscillation

On the one hand, considering a thin plate subjected to sinusoidal oscillation only in heaving degree of freedom, the linear unsteady lift can be expressed as (according to Eq. 2.25)

$$L = -\rho\pi b_h^2 \ddot{y} - 2\pi\rho U b_h C(k)\dot{y} \tag{2.52}$$

While, according to the linear quasi-steady theory for galloping, this lift is simply

$$L = -\frac{1}{2}\rho U^2 \cdot (2b_h)\frac{\mathrm{d}C_L}{\mathrm{d}\alpha} \cdot \frac{\dot{y}}{U} = -2\pi\rho U b_h \dot{y} \tag{2.53}$$

where $\frac{\mathrm{d}C_L}{\mathrm{d}\alpha} = 2\pi$ is the theoretical slope of C_L-α curve for thin plate (here, C_L is defined with chord length $b = 2b_h$). Comparing the above two equations, it is to know that, in the quasi-steady galloping theory, the added mass item related to $\ddot{y}$ is neglected and $C(k) = 1$ is assumed (namely the fluid memory is neglected).

On the other hand, for bluff bodies, the periodical vortex shedding process represents another source of unsteadiness, being neglected in the quasi-steady galloping theory. Its important role has already been reflected in the interaction phenomenon between galloping and VIV.

To sum up, there are three aspects being neglected in the quasi-steady galloping theory, as also noted by Liu & al. (2018):

- the vortex shedding process;
- the fluid memory effect;
- the added fluid mass.

For the last item, it is usually negligible for wind engineering, due to the big difference of the density between structure and air. So, theoretically approaching the unsteady galloping needs to mainly take the first two aspects into account.

2.2.3 Modeling the Unsteady Galloping

(i) Integrating vortex shedding force in addition to quasi-steady motion-induced force

A considerable number of efforts were made to take into account the effect of vortex shedding force in unsteady galloping modeling, clearly due to its important role at low reduced flow velocities. The basic idea in these efforts is to add a fluctuation lift item due to vortex shedding to the classical quasi-steady galloping theory.

Santosham's model (1966) The first attempt in this direction was made by Santosham (1966), who simply added a harmonic force of Strouhal frequency n_{st} to the governing equation of quasi-steady galloping (Eq. 2.16). In water flow, it was found the vortex shedding force is able to quench the self-excited galloping to a certain reduced velocity, which is dependent on the magnitude of vortex shedding force. However, for air flow, the effect is of insignificance.

Corless&Parkinson's model (1988) A more advanced model was proposed by Bouclin (1979), to address the across-flow instability of square cylinders in water flow. The model consists of two coupled oscillators: one is for body's oscillation, considering the quasi-steady galloping force and the vortex shedding induced lift as input; the other is a VIV lift oscillator according to Hartlen & Currie (1970), externally excited by the velocity of body. Later, Corless & Parkinson (1988) further added an inertial coupling-item for the lift oscillator to improve the solutions in the primary resonance range. In non-dimensional form, this modified model is written as

$$Y'' + 2\zeta_0 Y' + Y = \frac{V^2}{m^*} C_v + \frac{V^2}{m^*} C_{Fy}^{QS}(\frac{Y'}{V}) \tag{2.54a}$$

$$C_v'' - \tilde{a}\upsilon \left(1 - \frac{4}{3\upsilon^2 C_{L0}^2} C_v'^2\right) C_v' + \upsilon^2 C_v = \frac{\tilde{b}}{\upsilon^2} Y'' + \frac{\tilde{c}}{\upsilon} Y' \tag{2.54b}$$

where $Y = y/d$, $\upsilon = 2\pi St V = V/V_r$ and $(\ )'$ denotes differentiation with respect to the reduced time $\tau = 2\pi n_0 t$. C_{L0} is the amplitude of fluctuation lift coefficient on stationary body, and $C_{Fy}^{QS} = C_{Fy}$ is the quasi-steady transverse force coefficient (here, the superscript QS is used to highlight its nature of being based on quasi-steady theory). $\tilde{a}$, $\tilde{b}$ and $\tilde{c}$ are three parameters, which have to be determined with forced- or free-vibration tests around the resonance region. For a square cylinder, this model qualitatively captured several important features of the typical unsteady galloping, e.g., the postponement of galloping until V_r for very low Sc and the approaching of solutions to the quasi-steady ones at sufficiently high V. However, the predicted amplitude around V_r was apparently overestimated. Recently, Mannini & al. (2015b) used this model for a 3:2 rectangular cylinder and conducted sensitivity studies for $\tilde{a}$, $\tilde{b}$, $\tilde{c}$ and C_{L0}. The agreement with experiments seems less satisfying, especially when a wide range of Sc is considered.

Tamura&Shimada's model (1987) Nearly in the same time period, a similar mathematical model was proposed by Tamura & Shimada (1987). Instead of directly modeling the fluctuation lift due to vortex shedding, Tamura&Shimada's model adopted the non-liner wake oscillator model, which was originally developed by Tamura & Matsui (1979) for the VIV problem of circular cylinder, to describe the dynamics of the near-wake rotation then relate it to the unsteady lift. In non-dimensional form, Tamura&Shimada's model is written as

$$Y'' + 2\zeta_0 Y' + Y = \frac{V^2}{m^*} f\left(\vartheta - \frac{Y'}{V}\right) + \frac{V^2}{m^*} C_{Fy}^{QS}(\frac{Y'}{V}) \tag{2.55a}$$

$$\vartheta'' - 2\beta\upsilon \left(1 - \frac{4f^2}{C_{L0}^2}\vartheta^2\right) \vartheta' + \upsilon^2\vartheta = \lambda Y'' + \upsilon^2 \frac{Y'}{V} \tag{2.55b}$$

with

$$\beta = \frac{f}{2\sqrt{2}\pi^2 l^*} \quad \text{and} \quad \lambda = \frac{1}{b/d + l^*} \tag{2.56}$$

where f is the slope of the unsteady lift coefficient $C_{L,un}$ with respect to the near-wake inclination ϑ, as indicated in Fig. 2.19 (a) for stationary body. For oscillation body, the effective near-wake inclination $\vartheta_{eff} = \vartheta - Y'/V$ is adopted to calculate $C_{L,un}$. Particularly, the reduced half near-wake length $l^* = l/d$ and the reduced near-wake width $h^* = h/d$ need to fulfill

$$St^2 = \frac{1}{4\pi h^*(l^* + b/d)} \tag{2.57}$$

which may be called a “local-effect” equation. There, the Strouhal number St is deemed to be determined by the wake geometry h^* and l^*. Besides the parameters St, C_{L0} and C_{Fy}^{QS}, which can be easily obtained by static tests, f and h^* (or l^*) are still to be set for the model. Estimation of h^* can be based on flow visualization, and f is related to the *Magnus effect* analogy, in similar way to the circular cylinder (Tamura & Matsui 1979). In Eq. 2.56 and 2.57, the expressions of λ and St are written with b/d to facilitate its more general application (setting $b/d = 1$ for square cylinder, the expressions of λ and St become the original ones in Tamura & Shimada (1987)).

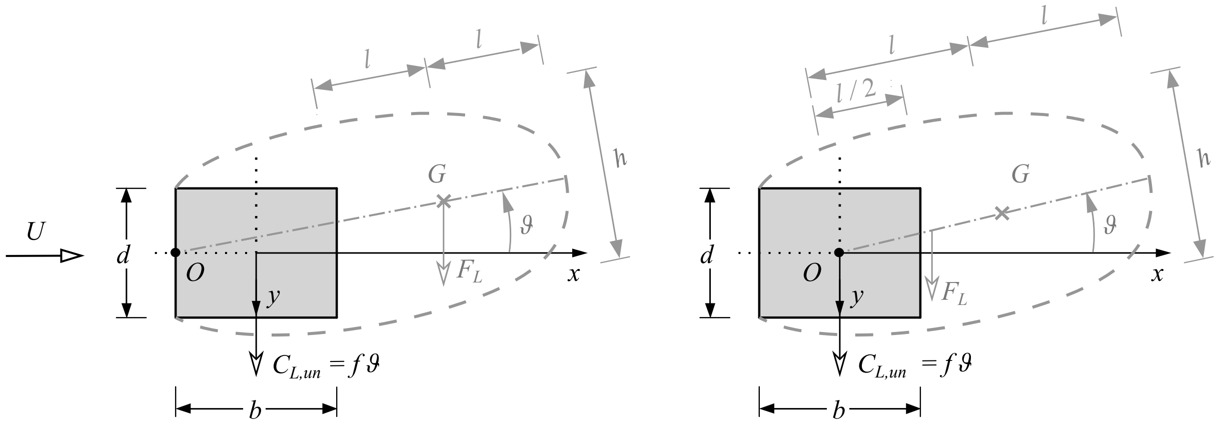

(a) (b)

Fig. 2.19: Schematics of the wake oscillator models (on stationary body): the original “TS-1987” one (Tamura & Shimada 1987); (b) the modified one “TS-2018” by Mannini & al. (2018a).

Recently, Mannini & al. (2018a) modified Tamura&Shimada’s model by pivoting the near-wake lamina about the centroid of the cylinder, and applying the restoring force F_L at one fourth of the chord of the lamina (see Fig. 2.19 (b)). The modification is based on the very first idea of Birkhoff (1953), schematizing the near-wake of bluff body as a lamina oscillating in the rotational degree of freedom. These modifications lead to different expressions of β and λ

$$\beta = \frac{f}{\sqrt{2}\pi^2 l^*} \quad \text{and} \quad \lambda = \frac{1}{l^*} \tag{2.58}$$

as well as the “local-effect” equation between St, l^* and h^*

$$St^2 = \frac{1}{8\pi h^* l^*} \tag{2.59}$$

This modified form of Tamura&Shimada's model was then applied to a 3:2 rectangular cylinder, and for a wide range of *Sc* it provides satisfying predictions on the typical unsteady galloping behaviors. The identification of the f parameter was, however, not through the analogy to *Magnus effect*, which was deemed questionable for sharp-edged bluff body. Instead, they used the pure VIV response of one aeroelastic test case with high *Sc* to calibrate out the parameter f.

Essentially speaking, in Corless&Parkinson'model, the nonlinear lift due to vortex shedding is modeled by an externally excited Rayleigh-type oscillator, while this is achieved by a Van der Pol-type oscillator in Tamura&Shimada's model. Their similarity has been already mentioned in several publications (e.g., Corless & Parkinson (1988) or Parkinson (1989)). Nevertheless, it is necessary to highlight, that Tamura & Matsui (1979)'s nonlinear wake oscillator model (based on Birkhoff (1953)'s linear one, and extended in Tamura & Shimada (1987) for square cylinder) involves some physical considerations about the near-wake of bluff body. Therefore, the parameters, h^*, l^* and f, correspond to clearly physical meanings. A further analysis about these physical considerations is presented in Chapter 5. Finally, to make a difference in this thesis, the original Tamura&Shimada's model is called "TS-1987", and the modified one by Mannini & al. (2018a) is called "TS-2018".

(ii) Attempts to model the unsteady motion-induced force

In either Corless&Parkinson's model (Eq. 2.54) or Tamura&Shimada's model (Eq. 2.55), it is to notice that the quasi-steady transverse force coefficient C_{Fy}^{QS} was adopted for the full range of reduced flow velocities. This is perhaps the most questionable point in these two mathematical models. However, unlike the thin airfoil or flat plate, theoretical approach to the unsteady motion-induced force for bluff bodies actually not exists. Nevertheless, there are some attempts dedicated to an expression of the unsteady motion-induced force for bluff bodies.

Hémon&Santi (2002). Hémon & Santi (2002) suggested a modified version of the quasi-steady theory, by introducing a time lag correction t_{lag} between $\dot{y}(t)$ and $F_y(t)$, which is written as

$$F_y(t) = \frac{1}{2}\rho U^2 d C_{Fy}\left(\frac{\dot{y}(t - t_{lag})}{U}\right) \tag{2.60}$$

For bluff bodies, according to some sounds-reasonable arguments, Hémon & Santi (2002) suggested that the time lag can be chosen as one period of the vortex shedding. Good agreement with experiments has been achieved in Hémon & Santi (2002), while the predictions based on such an idea was found poor by other researchers (Liu & al. (2018) for an square cylinder and (Mannini & al. 2015a) for an 3:2 rectangular cylinder).

Luo&Bearman (1990). Luo & Bearman (1990) took a bold step, assuming that an equation, which was derived in similar to an airfoil oscillating with small amplitude in incompressible flow, can be applied to an oscillation bluff body. This equation can be revised from Eq. 2.52 with several modifications, and is written as

$$L = -C_{mo}\rho\pi(\frac{b}{2})^2\ddot{y} - \frac{\mathrm{d}C_L}{\mathrm{d}\alpha}\rho U\frac{b}{2}C(k)\dot{y} \tag{2.61}$$

where C_{mo} is called the potential flow inertia coefficient, and $\frac{\mathrm{d}C_L}{\mathrm{d}\alpha}$ is the lift-curve slope. If let $C_{mo} = 1$, $\frac{\mathrm{d}C_L}{\mathrm{d}\alpha} = 2\pi$, the above equation becomes Eq. 2.52 (remembering $b_h = b/2$). For a square cylinder ($b = d$), $C_{mo} = 1.53$ was estimated (Luo 1985), and the experimentally measured $-\frac{\mathrm{d}C_{Fy}}{\mathrm{d}\alpha}$ at $\alpha = 0$ was set for $\frac{\mathrm{d}C_L}{\mathrm{d}\alpha}$ (for bluff body, the contribution of drag is considered and the minus sign is due to C_{Fy} defined downward positive). By further assuming a harmonic motion

$$y = \mathrm{Im}[y_0 e^{i\omega_m t}] = y_0\sin(\omega_m t) \tag{2.62}$$

the unsteady lift described by Eq. 2.61 can be expressed in real form (by putting complex form of y into Eq. 2.61, then taking the imaginary part)

$$\begin{aligned} L = &\left[C_{mo}\frac{\rho\pi d^2}{4}\omega_m^2 - \frac{\mathrm{d}C_{Fy}}{\mathrm{d}\alpha}\rho U\frac{d}{2}G(k)\omega_m\right] y_0\ \sin(\omega_m t) \\ &+ \left[\frac{\mathrm{d}C_{Fy}}{\mathrm{d}\alpha}\rho U\frac{d}{2}F(k)\right] y_0\omega_m\cos(\omega_m t) \\ = &\left[C_{mo}\frac{\rho\pi d^2}{4}\omega_m^2 - \frac{\mathrm{d}C_{Fy}}{\mathrm{d}\alpha}\rho U\frac{d}{2}G(k)\omega_m\right] y + \left[\frac{\mathrm{d}C_{Fy}}{\mathrm{d}\alpha}\rho U\frac{d}{2}F(k)\right]\dot{y} \end{aligned} \tag{2.63}$$

where $F(k)$ and $G(k)$ are the real and imaginary part of *Theodorsen's circulatory function* $C(k)$. The above equation contains two force items: one in phase with body's displacement y and the other in phase with $\dot{y}$. For wind engineering, the second item is more important, which is equivalent to damping force. Since $F(k)$ is within 0.5 to 1 (see Fig. 2.11), so that there is

$$\left[\frac{\mathrm{d}C_{Fy}}{\mathrm{d}\alpha}\rho U\frac{d}{2}F(k)\right]\dot{y} \le \left[\frac{\mathrm{d}C_{Fy}}{\mathrm{d}\alpha}\rho U\frac{d}{2}\right]\dot{y} \tag{2.64}$$

where the right side item actually represents the transverse force according to the linear quasi-steady galloping theory. Clearly, the generated aerodynamic damping based on unsteady aerofoil theory is dependent on the reduced frequency (or reduced flow velocity), but it is always lower than the one according to quasi-steady theory. More important is that the sign of the aerodynamic damping generated by these two theories will always be the same. In Luo & Bearman (1990), further analysis was given to a comparison with the experimental data of a square cylinder forced to vibrate. The pronounced good agreement is, however, found by the author of this thesis, somewhat questionable (for example, the expression of Eq.2.61 is only meaningful for small apparent wind angle of attack, however in Luo & Bearman (1990) the good agreement with experiments is achieved for very large apparent attacking angles).

Gao&Zhu (2017) An empirical approach was proposed by Gao & Zhu (2017) to model the motion-induced force for across-wind oscillation:

$$F_y = \frac{1}{2}\rho U^2 (2b) Y_1(K) \left[1 + \varepsilon_{03}(K) \frac{\dot{y}^2}{U^2} + \varepsilon_{03}(K) \frac{\dot{y}^4}{U^4} \right] \frac{\dot{y}}{U} \tag{2.65}$$

where Y_1, ε_{03} and ε_{05} are parameters as a function of the reduced frequency $K = \omega b/U$ (which is the one used in Scanlan's flutter derivatives). The unsteady effect was considered in an "implicit" way, since these parameters are dependent on K. Clearly, this is a combined formulation referring to both the nonlinear quasi-steady theory and the flutter derivatives: if only the linear item is maintained, there is $2Y_1(K) = KH_1^*(K)$ (see Eq. 2.42); or, if the dependence on K is removed, there are $2(b/d)Y_1 = A_1$, $2(b/d)Y_1\varepsilon_{03} = A_3$ and $2(b/d)Y_1\varepsilon_{05} = A_5$ (A_3 and A_5 are high-order coefficients for polynomials approximating the $C_{Fy}(\alpha)$ curve, see Appendix A.1). In Gao & Zhu (2017), these parameters were determined by force measurements on a free-vibration 2:1 rectangular cylinder, which exhibited "Full-Interference" type unsteady galloping. A tendency of these parameters to the quasi-steady ones was observed at high reduced flow velocities.

(iii) Combination of vortex shedding force and unsteady motion-induced force

Liu & al. (2018). Recently, Liu & al. (2018) introduced *Theodorsen's circulatory function* to modify the quasi-steady transverse force item (C_{Fy}^{QS}) in Corless&Parkinson's model, as well as in Tamura&Shimada's model ("TS-1987"). This means that the aerodynamic force on the oscillation body right now consists of two fully unsteady parts: one due to the vortex shedding; and the other due to the body's motion. Although the agreement with experiments, for a square cylinder undergoing typical unsteady galloping, is not significantly improved (compared with the original ones with C_{Fy}^{QS} item), this attempt is definitely very interesting and meaningful.

(iv) Short summary

Previous Sections reviewed the many efforts to model the unsteadiness of aerodynamic force, for bluff bodies undergoing across-wind oscillation at low reduced velocities. The separation of the unsteady aerodynamic force into a portion due to vortex shedding and another portion due to body's motion, provides a clear picture for the mechanism of unsteady galloping. For modeling the unsteady force due to vortex shedding, with the help of lift or wake oscillator model which is originally developed for VIV problem, some achievements have been obtained, for example, Corless&Parkinson'model, and Tamura&Shimada's model as well as its modified form in dealing with the typical unsteady galloping due to interference with VIV. However, for modeling the motion-induced unsteady force, it seems to be still a very tough task. On the one hand, Luo & Bearman (1990)'s bold attempt, by considering *Theodorsen's circulatory function* for bluff body, may be quite inspirational to some extent. On the other hand, one must recognize that the using of *Theodorsen's circulatory function* is definitely inaccurate for bluff body. Remembering that the circulatory function is related to the indicial function by Fourier transform (see Eq. 2.41), it can be found in Scanlan & al. (1974) how big differences between the indicial functions respectively for bluff bodies and for thin airfoil.

2.3 Effect of Incoming Turbulence and 3-dimensional Problem

2.3.1 Turbulence's Effect

Turbulence is the fluctuation part in incoming flow, composed of eddies of different sizes being convected by the flow. In wind engineering, incoming turbulence is normally described in a statistical manner, by the variance of wind speed fluctuation, power spectral density, correlation function, etc. Turbulence in incoming flow is known able to significantly influence the aerodynamics of bluff body, and the concerned mechanisms have been extensively studied and discussed (see, e.g., Bearman & Morel (1983)). Usually, eddies in turbulent flow can distinguish between three types for a given bluff body (as summarized in Mannini (2020)): a) small-scale eddies, with a length scale comparable with boundary layers and separated shear layers' thickness; b) medium-scale eddies, with a size comparable with the vortex formation region; c) large-scale eddies, with a scale much larger than body's dimension. The first topology is able to enhances the mixing and the entertainment of fluid from the near wake and accelerate the growth of the shear layers promoting their earlier reattachment (Gartshore 1973; Nakamura & Ohya 1984; Nakamura & Ozono 1987). The aerodynamics of bluff body is modified due to this mechanism, making the bluff body behave in turbulent flow as if it were more elongated (see, e.g., Laneville & Parkinson (1971) and Mannini & al. (2017)). The large-scale eddies represent a parametric and an external excitation for a dynamic system, which can be modeled by consideration of the variation of instantaneous wind angle of attack (Abdel-Rohman 2001; Lindner 1992; Luongo & Zulli 2011). The role of medium-size eddies is more complicated, since it implies both effects. A realistic turbulent wind flow includes all of these three typologies of flow fluctuations. Their relative portion and importance is able to be reflected by the integral length scale.

With respect to galloping instability, the existence of turbulence was found able to turn a hard-type galloping in smooth flow, which occurs usually for small side-ratio bluff body, into a soft-type galloping, for which sustained vibration arises spontaneously from rest (Laneville & Parkinson 1971; Novak 1972; Novak & Davenport 1970; Novak & Tanaka 1974). In contrast, for larger side-ratio bluff bodies, Novak & Davenport (1970) and Novak (1972) suggest that turbulence attenuates the galloping oscillation until the structure becomes stable in a high turbulence flow (for example the 2:1 rectangular cylinder). This in line with the effect of the small-scale eddies of turbulence being introduced previously. It is worth noting that Laneville & Parkinson (1971) did not find any significant effect of turbulence integral length on the galloping instability of a square cylinder, although they also pointed out that the investigated range of length scales was always comparable with body's dimension. In contrast, recent contribution regarding to a 3:2 rectangular cylinder indicated that the integral length scale plays also a very important role (Mannini & al. 2018b), probably even in a non-monotonic manner. From the point of view of the liner quasi-steady theory (e.g, the galloping factor A_1), their results also showed that the incident turbulence, dependent on intensity, could either suppress or enhance galloping instability. Nevertheless, the classical quasi-steady theory was concluded still applicable by Novak & Davenport (1970) and Laneville & Parkinson (1971), provided that the the transverse force coefficient is measured in the same turbulent flow condition and a higher reduced flow velocity is ensured. Finally, turbulence was found able to impair the regularity of galloping oscillation (Mannini 2020; Mannini & al. 2018b).

For vortex induced vibrations, the most evident effects of incident turbulence include the variation of Strouhal number and the associated shift of lock-in response (see, e.g., Kobayashi & al. (1990) and Mannini & al. (2017)). On the other hand, Vickery (1966) noticed that, for a stationary square cylinder, the Strouhal number is the same as in smooth flow, but the root-mean-square value and correlation length of the fluctuation lift gets significant reduction. The loss of spanwise correlation in turbulent flow was also indicated by Novak & Tanaka (1977) for a forced vibration circular cylinder. Matsumoto & al. (1993)'s results further indicated that a low free-stream turbulence can either increase or reduce the VIV response, depending on the cross-section geometry and the specific exciting mechanism. In general, the VIV response of bluff bodies in turbulent flow still needs extensive investigation.

Finally, according to the author's knowledge, the investigation dedicated to unsteady galloping in turbulent flow is still very limited. Nevertheless, earlier contributions to this topic can be found in Bearman & al. (1987) and Miyata & al. (1983), in which the square cylinder was discussed. In particular for the latter, it implied that turbulence tends to enhance the interference between VIV and galloping for a certain range of Scruton number. Recently, Mannini & al. (2018b) particularly paid their attention to the unsteady galloping problem of a 3:2 rectangular cylinder in turbulent flow. There, the measured C_{Fy} and St through static tests also implied an enhancement of the VIV-galloping interference. Even more impressive are the aeroelastic test results, in which a classical Kármán-vortex-resonance region has never been observed in turbulent flow and the aeroelastic behaviors differ apparently between small-scale turbulence (L_u/d = 0.3-0.9) and large-scale turbulence (L_u/d = 2.6-2.9). Very recently, Mannini (2020) successfully captured the unsteady galloping behavior in large-scale turbulent flow, by means of Tamura's wake oscillator with parameters measured in turbulent flow. In contrast, for small-scale turbulent flow with medium to high intensity, the galloping was found to arise at a reduced flow velocity slightly higher than V_r even for very low Sc. The mechanism for this peculiar phenomenon remains unclarified.

2.3.2 3-dimensional Object

For 3-dimensional structures such as towers and high-rise buildings, the aerodynamic coefficients like C_{Fy}, St and C_{L0} may become position dependent. Particularly in boundary layer turbulent flow, the variation of C_{Fy} with respect to vertical position z is very apparent as reported by Parkinson & Sullivan (1979) and Hu & al. (2015). The calculation of structural dynamic response must consider this variation carefully. In case of high reduced flow velocity ensured, the quasi-steady theory was found still applicable for 3-dimensional structures even in turbulent flow, given that the $C_{Fy}(\alpha, z)$ coefficient was measured in the same flow condition and the mode shape effect was correctly considered (Parkinson & Sullivan 1979; Sullivan 1977). On the other hand, unsteady galloping seemingly occurred during Hu & al. (2015)'s experiments for a vertical square tower, being the galloping-type vibration initiated at about the critical wind speed for VIV rather than at the quasi-steady prediction (predicted U_g/U_r is about 2.1). Clearly, 3-dimensional structures in turbulent flow represent the very complicated cases, but also are the realistic situations for engineering practices. A simplified but realistically useful approach to the instability problem in this situation could be the empirical aerodynamic-damping model (Cheng & al. 2002; Gu & Quan 2004; Kareem & al. 1996), which is usually built on the regression of wind tunnel measurement data.

2.4 Chapter Summary

In this Chapter, an introduction to bluff body aerodynamics and aeroelastic phenomena was first given. In particular, the mechanism of across-wind galloping was elaborated based on the well-known quasi-steady theory. Focuses were then put to the up-to-date knowledge about unsteady galloping, ranging from the overview of its characteristics, via an analysis of the source of the unsteadiness during the oscillation, to the topic about mathematically modeling unsteady galloping, and finally ending with the brief discussion on the effects of incoming turbulence and 3-dimension. One may notice that considerable attentions were also paid to VIV and flutter. This is deemed necessary for a better revealing of the unsteadiness in across-wind galloping. It may be also noticed that the current understandings on unsteady galloping, as well as its mathematical modeling, are limited to the rectangular and square cross sections.

3 Experimental Setup and Configurations

3.1 Facility and Wind Tunnel Models

All the experimental campaigns were carried out in the boundary layer wind tunnel at the Institute of Steel Structures of Technische Universität Braunschweig, Germany. Fig. 3.1 (a) shows the schematic view of the wind tunnel layout, and Fig. 3.1 (b) and (c) show two photos of the wind tunnel. The wind tunnel is a suction Eiffel-type facility with a rectangular cross section of 1.4 m width and 1.2-1.4 m height (adjustable ceiling). The total length of the wind tunnel is 13.05 m, including a 8.75 m long working chamber with two test sections. Test section 1 is used to carry out experiments on sectional models. For a better quality of the smooth flow this section is located at the entrance/inlet of the chamber. Test section 2 is equipped with a High Frequency Force Balance (HFFFB) and a turntable with a diameter of 1.2 m, and used for tests on overall building aerodynamics. The flow speed can be varied continuously up to 25 m/s through a 55 kW motor placed at the outlet. In absence of turbulence generators, the free-stream turbulence intensity is about 1%. Examination of the flow quality will be provided in the following sections.

In this research, all the static and aeroelastic tests for the sectional models were conducted in the Test section 1 of the wind tunnel. The measurements of the overall aerodynamic force on the launching nose were carried out in Test section 2.

Three sectional models were tested in this work. Their cross section geometries are shown in Fig. 3.2. These three cross sections are selected based on the practical engineering cases collected in Tab. 1.1. There, the rectangular and trapezoidal cross sections as well as the open trapezoidal cross section are very common in the incremental launching process of steel-concrete composite bridges. The side ratios of these selected cross sections, defined in this thesis as the overall width b to height d, were purposely set to $b/d = 2$. In view of Tab. 1.1, this side ratio is within the range b/d = 1.6 to 2.9 and therefore should be representative for realistic cases.

There are also some other considerations in the determination of cross sections types for wind tunnel tests. For the 2:1 rectangular cylinder, some experimental results are already available in the literature. Therefore, the presented results of this rectangular cylinder will also serve as

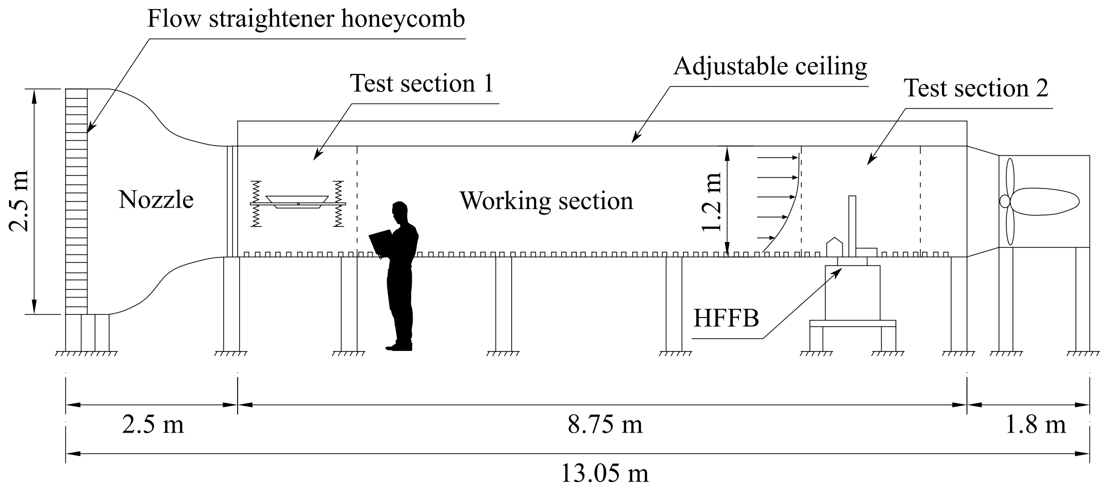

(a) Shematic view of the wind tunnel

(b) Frontal view, from the outlet

(c) Close-up of the motor fan

Fig. 3.1: Boundary layer wind tunnel at the Institute of Steel Structures of TU-Braunschweig: (a) by courtesy of Dr.-Ing. Hodei Aizpurua Aldasoro (Aldasoro 2014); (b) and (c), by courtesy of Dr.-Ing. Luca Pigolotti (Pigolotti 2017).

an important measure to examine the validity of experimental setup, by means of comparison with other literature reports. For the open cross section shown in Fig. 3.2(c), a detailed literature search shows this cross section has never been well studied especially with respect to its aeroelastic behaviors, although it is a very typical cross section for steel-concrete composite bridges during construction phase. This cross section was therefore given a lot of attention in this thesis. It is designed based on the prototype of Aftetal Bridge (previously mentioned in Chapter 1), and its appearance is slightly modified to make it more representative. Nevertheless, this cross section is characterized with its top side open, from which more complex aerodynamic behaviors are expected. For a better understanding of those behaviors, the closed trapezoidal cross-section, with similar geometry, is additionally selected as a reference.

Fig. 3.3 shows how the two cylinder models are composed and manufactured (only the sketch of rectangular cylinder is given, since the way of constructing the trapezoidal one is the same). For the two close-form cylinders, the effective lengths between the two end-plates are $l_e = 1290$

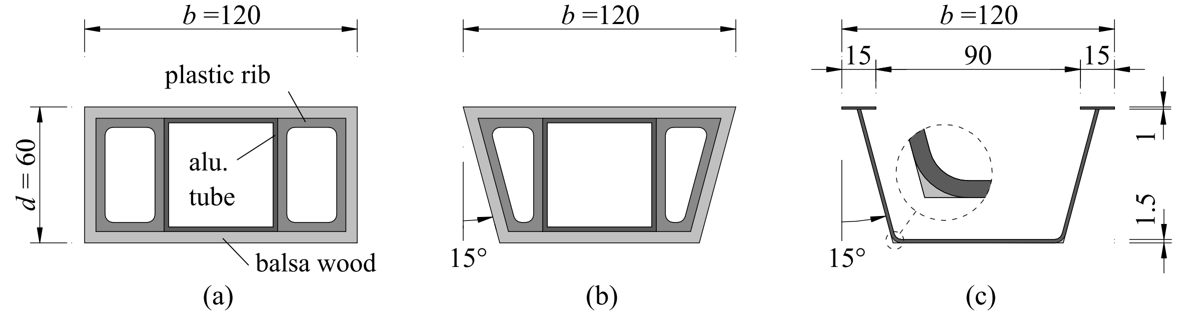

Fig. 3.2: Geometry of the cross sections of the three wind tunnel models: (a) rectangular cross section; (b) trapezoidal cross section; (c) bridge deck with typical open cross section (dimension in mm).

mm. The stiffness of the cylinder is provided by an internal aluminum square tube which has a height of 50 mm and a thickness of 2 mm. Two circular tube connectors made of aluminum were welded to the square tube, to facilitate the installation in the experimental setup. The aerodynamic shape of the rectangular and trapezoidal cylinder is obtained by 5 mm thick balsa wood plates. The remaining space between the square tube and the wooden plates is supported by discretely arranged ABS plastic ribs (see Fig. 3.3, as well as Fig. 3.2 (a) and (b)). These ribs were produced by FDM 3D printer. The smooth surface and especially the sharp corners of the cylinder models are obtained by polishing with sand paper and carefully protected with acrylic varnish. Finally, two 480 mm × 240 mm × 5 mm end-plates were connected to each end of the cylinder by screws, to enforce the bidimensional flow condition. The design of the end-plates followed the instruction given by Obasaju (1979), as well as referred to the size of the end-plates for a 3:2 rectangular cylinder (Mannini & al. 2014).

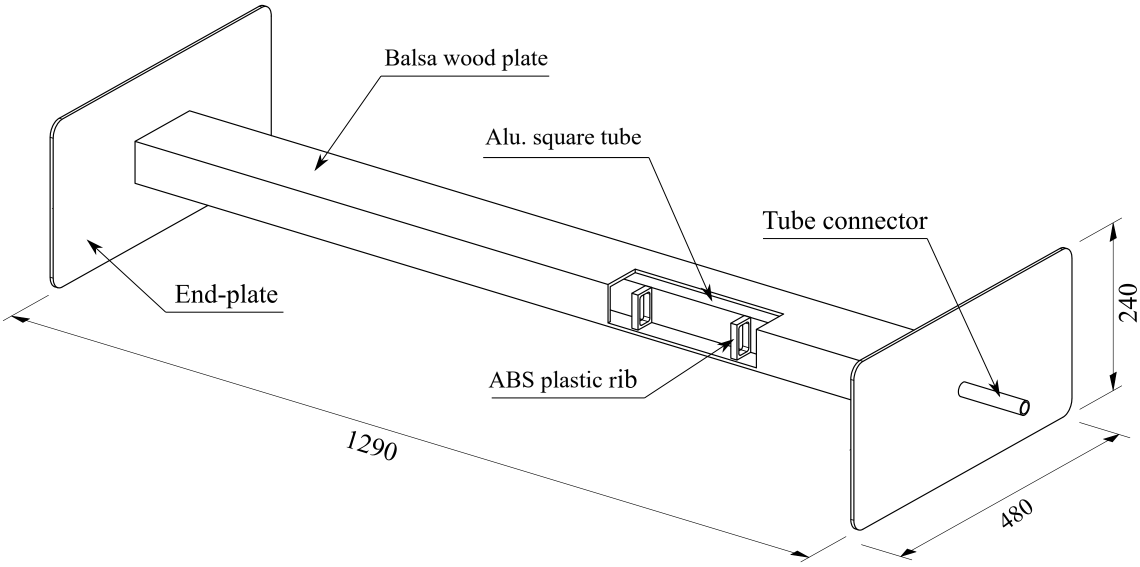

Fig. 3.3: Sketch of the rectangular cylinder model (the open portion for internal view, dimension in mm).

The manufacturing of the bridge deck model with open cross section was relatively more complex. Fig. 3.4 shows an overall view of the model. The effective length of this model is l_e = 1300 mm, slightly larger than those of the two close-form cylinder models. To manufacture the open cross section shown in Fig. 3.2 (c), a 1.5 mm aluminum plate was first folded. Then, nine aluminum hollow ribs and two solid ribs were manufactured by CNC machine. They are connected to the open cross section profile by screws, to enhance the global stiffness. In particular, the two solid ribs were set at the ends, for connections to the tube connectors. Finally, two 15 mm wide and 1 mm thick flanges were installed at the top, by connecting them to the ribs with screws and filling the remaining slit with structural adhesive for aluminum.

However, two round corners were left at the bottom of the cross section due to the folding process of the aluminum plate. Since the aerodynamics of a bluff body is quite sensitive to the corner details (especially the ones close to the locations of flow separation), such round corners may bring significant influence to the flow field around the open cross section (see, e.g., Mannini (2015)). Therefore, the bottom corners of the open cross section were further sharpened by usage of two-component epoxy adhesive, see Fig. 3.2 (c). Finally, the bridge deck model was equipped with the same end-plates as the other two cylinder models. It is also worth noting here that there is no internal core throughout the model, so that the bending stiffness of the model is directly provided by the aluminum open cross section itself and the inside space of the profile is maintained clean.

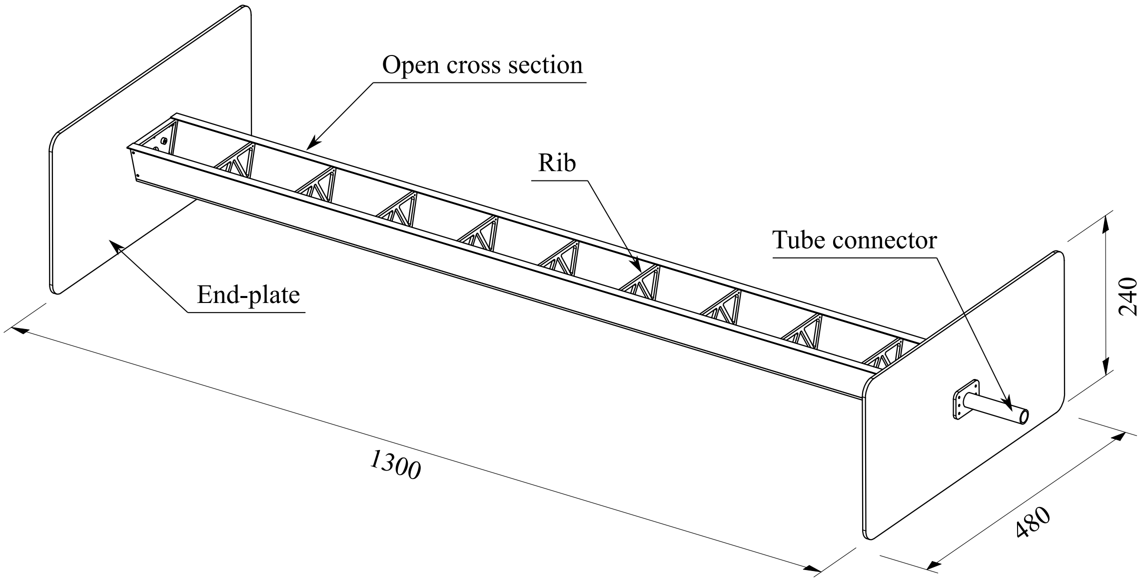

Fig. 3.4: Sketch of the bridge deck sectional model with open cross section (dimension in mm).

Fig. 3.5 shows the photos of the three wind tunnel models, among which the bridge deck model with open cross section is already installed inside the wind tunnel. The finished three wind tunnel models weigh 2.05 kg, 2.02 kg and 1.75 kg, respectively. The wind tunnel blockage ratio is 5%, defined here as the model height to the height of the wind tunnel cross section, and no correction of wind tunnel blockage effect is made to the test results. For convenience, the three sectional models shown in Fig. 3.2 are respectively named “rectangular cylinder”, “trapezoidal cylinder” and “bridge deck model”. Finally, the main information about the three wind tunnel models are summarized in Tab. 3.1.

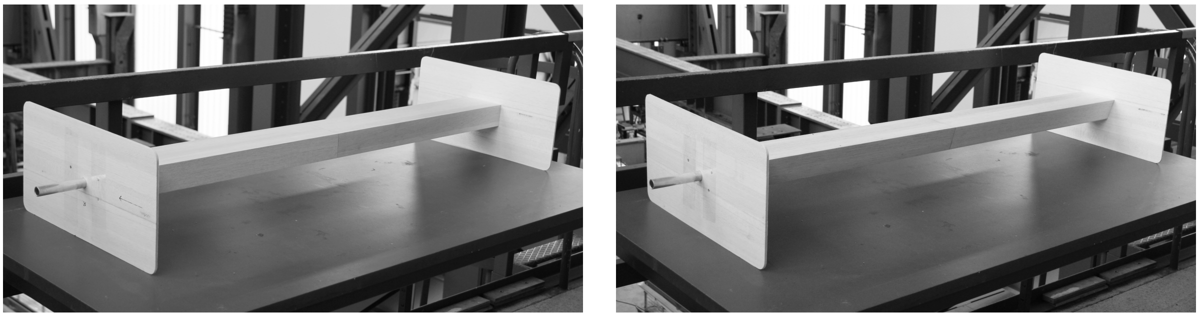

(a) Rectangular cylinder (b) Trapezoidal cylinder

(c) Bridge deck model (in wind tunnel)

Fig. 3.5: Photos of the three wind tunnel sectional models

Tab. 3.1: Summary about the three wind tunnel sectional models

	Rectangular cylinder	Trapezoidal cylinder	Bridge deck model
Section height d [mm]	60	”	”
Section width b [mm]	120	”	”
Effective length l_e [mm]	1290	1290	1300
Aspect ratio l_e/d [-]	21.5	21.5	21.67
Weight [kg]	2.05	2.02	1.75
Blockage ratio [-]	5%	”	”

Due to need, a launching nose model is also tested in this study. Fig. 3.6 shows the sketch of this model and Fig. 3.8 (b) gives a photo. Its design referred to the lattice launching nose used in the construction phase of Nuttlar Viaduct (Niemann & Hölscher 2012). For facilitation of manufacturing, some details has been modified. But the most important characteristics, namely the overall shape and the solid ratio of each side, were maintained representative. The size of the aforementioned sectional models was also taken into account during the design of this launching nose model. For example, the maximum height of the launching nose is aligned to the height of the sectional model, and its width (72 mm) is compatible with the bridge deck model. Therefore, this launching nose will be also applicable for the wind tunnel tests on a whole cantilever model, which is planned as a future work of this thesis.

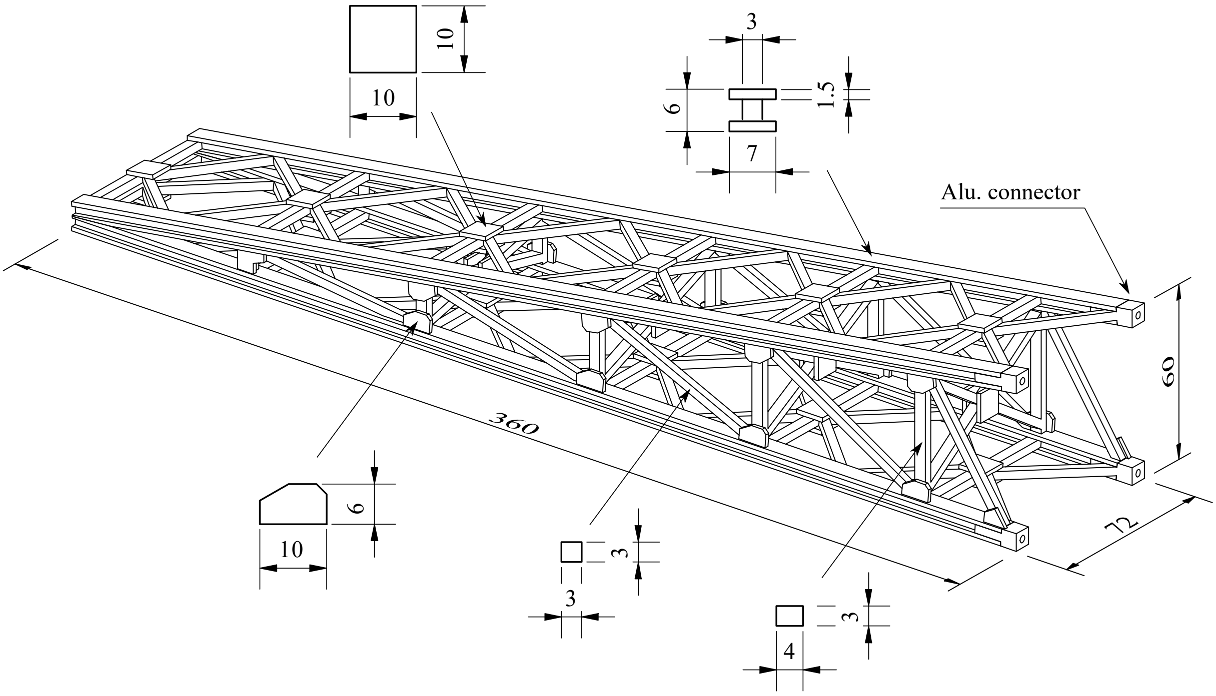

Fig. 3.6: Sketch of the lattice launching nose model, mostly made of wood strip and dimension in mm.

The launching nose model was made of pine-wood strips and aluminum connectors at the four "feet" (particularly indicated in Fig. 3.6). The wooden strips were glued to each other, while two-component-epoxy adhesive was used for the connection between the wooden strips and the aluminum connectors. The connection of this wind tunnel model to the test setup is through the threaded holes on the aluminum connectors. Finally, it should be mentioned that the aim of this model is to understand the basic aerodynamics of the launching nose, and to explore the possibilities of suppressing the galloping problem during launching the phase through aerodynamic optimization for the launching nose. This model is not a scaled one from any prototype.

3.2 Experimental Setup

3.2.1 Static Tests

The aerodynamic force measurements on the stationary sectional models were carried out with the static setup shown in Fig. 3.7. On each side of the wind tunnel, the setup consists of three strain-gauge load cells (one 100 N load cell for the horizontal direction and two 50 N load cells for the vertical direction, type HBM S2M with 0.02% relative error of full scale output), steel connecting rods and an aluminum block. Each load cell is axially loaded due to the presence of two plate-shaped appendices in the connecting rod working as hinged connections. The wind tunnel model was rigidly connected to the aluminum blocks through three screws on each side. The whole setup is fixed on an aluminum frame outside the wind tunnel, which is directly installed to the ground through a layer of rubber gasket. Any direct contact to the wind tunnel structure is avoided. The Data acquisition was performed with a strain/bridge input module (type NI PXIe-4330) at a sampling frequency of 1000 Hz. The flow incidence of the model was manually adjusted with an electronic inclinometer (type SPI-TRONIC Pro3600) with an accuracy of 0.05° within the range -10° to 10°, and 0.1° outside that range.

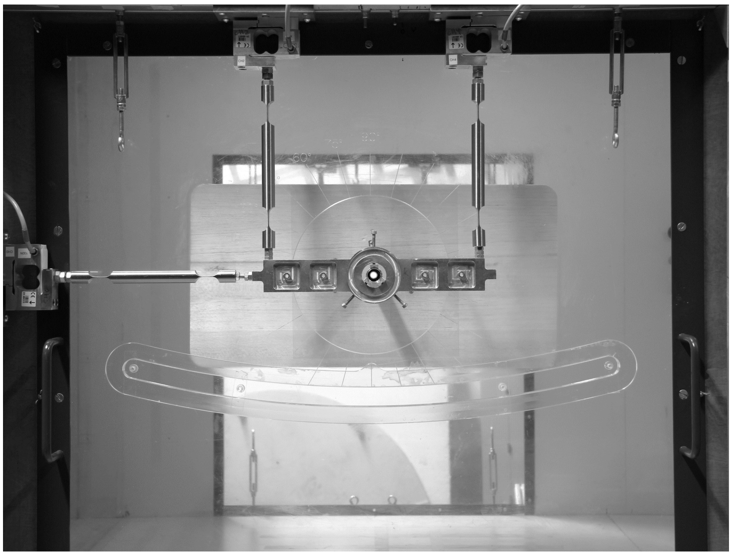

Fig. 3.7: Static setup for sectional models (outside wind tunnel).

The static tests of the launching nose model were conducted with the High Frequency Force Balance (HFFB) installed at the Test section 2 of the wind tunnel (see Fig. 3.8). Instead of directly connecting the launching nose model to HFFB, a solid steel connector was used to support the model at a higher position above wind tunnel ground. This is to obtain a better uniform flow attacking on the model. The incident wind profile shown in Fig. 3.8 (a) is a measured one in absence of any turbulence generator (see Section 3.3.4). Clearly, the thick boundary layer developed on the wind tunnel floor is less preferable for the investigations on the launching nose model, thus eliminated by usage of the steel connector. The model was connected to a steel end-plate with a diameter of 400 mm and a thickness of 2 mm. After a further strengthening by a 80 mm × 70 mm × 3 mm aluminum plate, the model with the end-plate was connected to the steel-connector by screw. Finally, an ABS plastic isolator (produced by 3D printer) was used, to avoid the exposure of the steel connector to incoming flow (see Fig. 3.8 (a)).

The HFFB platform is composed of 4 piezoelectric 3-component force sensors (Kistler Type 9317B6). These sensors are connected to a 90 mm × 90 mm ×25 mm steel plate on top, which

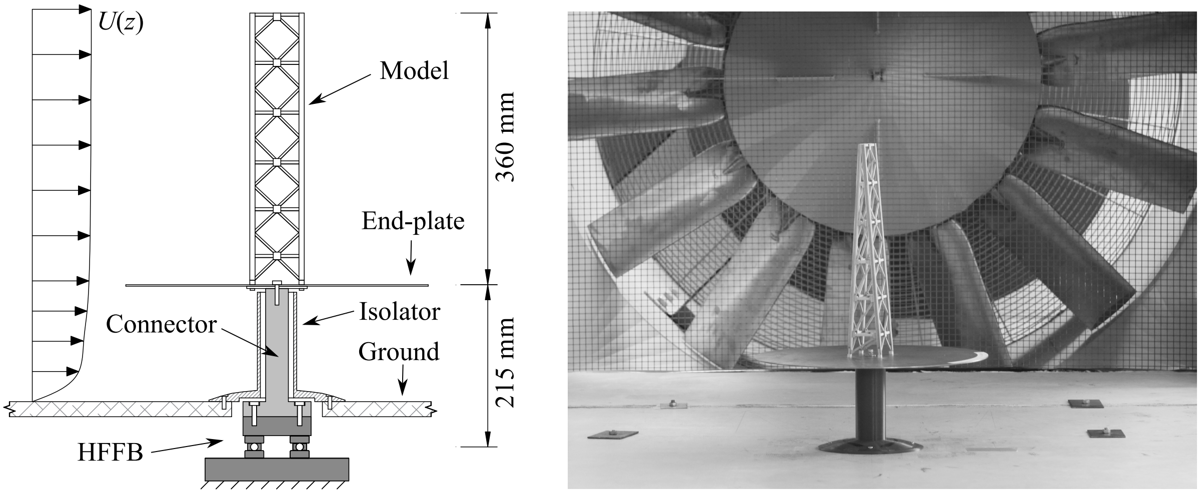

(a) Schematic (b) Photo

Fig. 3.8: Static setup with high frequency force balance (HFFB) for the launching nose model.

provides further connection options for test objects. The supporting substructure is made of steel, in a very massive and stiff way. The piezoelectric force sensors have an ultra-sensitive accuracy (about 0.01 N resolution), as well as a high force range up to ±1 kN in two horizontal directions (X and Y) and ±2 kN in vertical direction (Z). The whole HFFB system, including the substructure, has nearly no amplification for dynamic exciting up to 400 Hz. More details about this HFFB system can be found in Aldasoro (2014).

3.2.2 Aeroelastic Tests

Fig. 3.9 shows the aeroelastic setup, composed by eight coil springs suspending the sectional model from the outside of wind tunnel. The horizontal motion of the wind tunnel model was restricted by two sets of anti-drag cables, connected to the tube connectors of the models through ball bearings. Two specially designed aluminum bars were used to link the wind tunnel model to the springs, providing also place to install the aluminum plate conductors of the eddy current damper. Any connection between spring and hooks was improved by means of nylon cables to avoid possible friction. The dynamic response of the model was measured by two laser displacement sensors (type WayCon LAS-T5-250-10 V) at each side of the wind tunnel. Data were recorded at a sampling frequency of 1000 Hz with a NI PXI-6284 module, a high-accuracy multi-function M-Series module optimized for 18-bit analog input accuracy. Finally, it is to note that coil springs of different stiffness were used for different wind tunnel models, so that the critical wind speeds for vortex induced vibration were purposely set at about 5-6 m/s for the aeroelastic tests (the flow quality at lower wind speed is less satisfying, see Section 3.3.3).

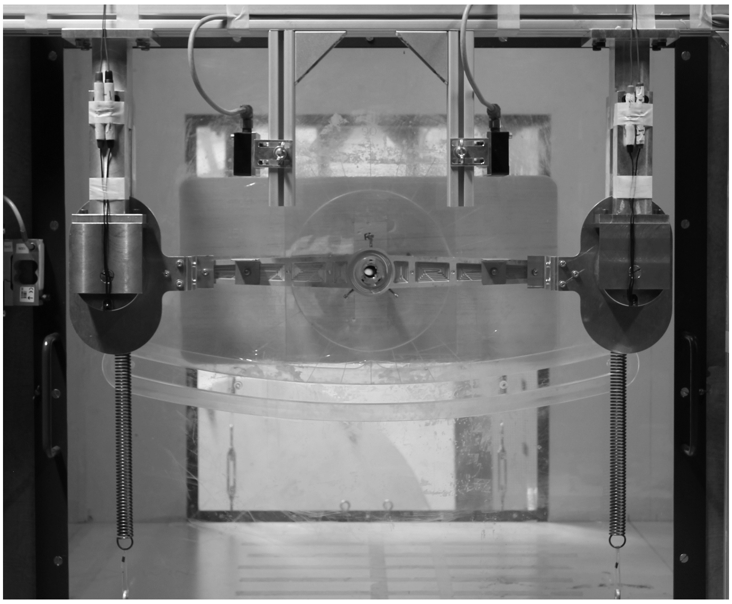

Fig. 3.9: Aeroelastic setup for sectional models (outside wind tunnel).

Additional damping was introduced into the dynamic system by means of eddy current dampers, with the strength controlled by the input electric power. The damper device was first conceived and tested by Pons (2014) during his work at the same wind tunnel facility, and further improved in this study for a better capability of installation. Each damper consists of two position-fixed electromagnets (type Tremba GTo80-0.5000, maximal nominal power 15 W) and a movable conductor plate. The latter was made of 2 mm aluminum plate and fixed on the aforementioned horizontal bar, simultaneously moving with the wind tunnel model. The dynamic tests were carried out with two dampers at the early stage of the experimental campaign (one at each side of the wind tunnel), introducing damping only in the heaving degree of freedom. To reach a higher damping level and, more importantly, to suppress any motion in the pitching degree, the system was later modified including four dampers. The amplitude of the pitching motion was therefore successfully kept below 0.05° throughout the whole dynamic campaign. The gap between the two electromagnets of each damper was set to 5 mm for the two-damper system and 5.4 mm for the four-damper system. Although this gap is quite narrow, especially considering also that the 2 mm thick conductor plate will move between it, any contacts or collision between the conductor plate and the electromagnets was successfully avoided throughout the whole experimental campaign.

3.2.3 Flow Measurements

Flow measurements were performed with a single TFI Cobra 315 Probe (Turbulent Flow Instrumentation, Pty Ltd), as shown in Fig. 3.10. It is a multi-hole pressure probe able to resolve

3-components of velocity and local static pressure in real time with a high time resolution more than 2000 Hz. This device is especially suitable to measure the turbulent flow fields, with the measuring flow angles within a ±45° cone. The Probe is about 160 mm long, with a body diameter of 14 mm and a faceted head with a width of 2.6 mm. The measured raw data is provided by 4 analogue voltage signals, which are first amplified and then sampled by an A/D-converter (type NI PXI-6259). The recorded time history of velocities of 3-components can be easily use to further calculate the mean flow velocity, turbulence intensity, flow pitch and yaw angles, etc. The Cobra probe was particularly optimized for a flow velocity range 2-30 m/s by the manufacturer, considering the maximal wind speed 25 m/s in this wind tunnel. The sampling frequency of Cobra probe was set to 2000 Hz throughout the whole wind tunnel activities. Finally, the supporting system for the Cobra Probe is shown in Fig. 3.10 (c).

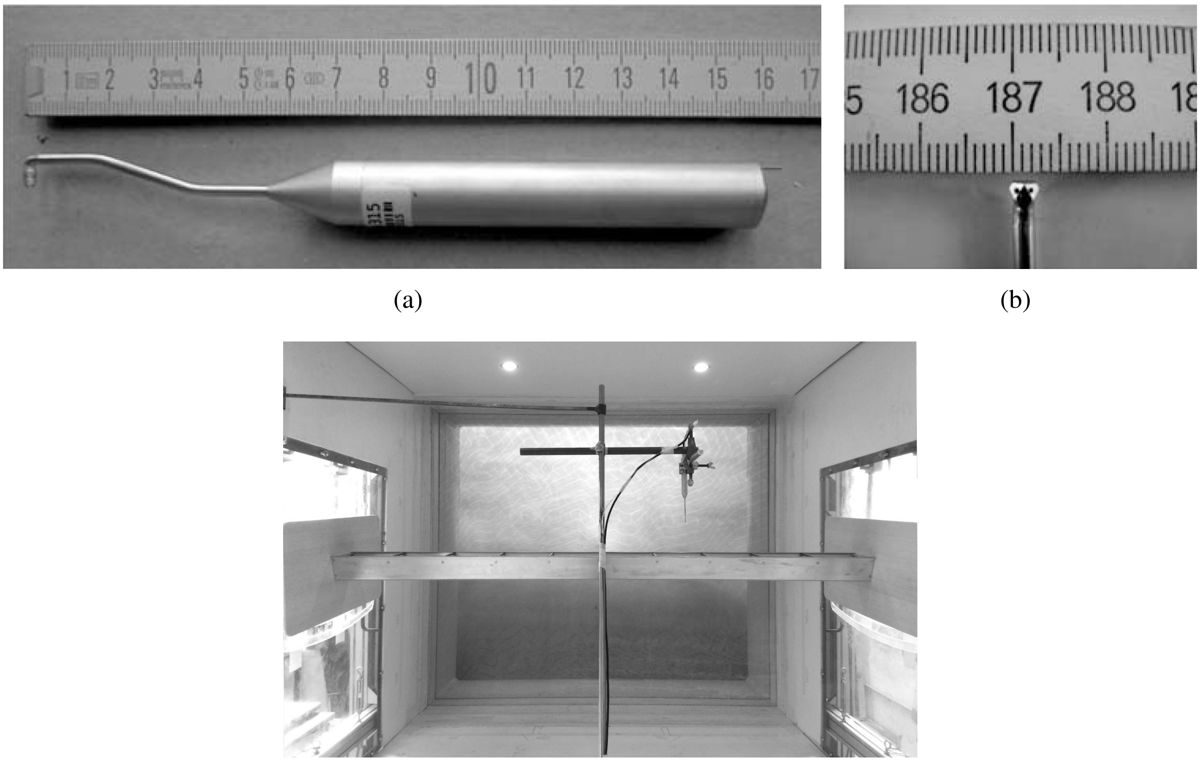
(a) (b)

(c)

Fig. 3.10: TFI Cobra Probe (a)-(b), by courtesy of Dr.-Ing. Hodei Aizpurua Aldasoro (Aldasoro 2014), and its supporting system (c).

For different purposes, the work concerning flow measurements mainly includes two parts:

- Free stream measurements. This is to understand the properties of the incoming flow, e.g., turbulence intensity and flow uniformity. These measurements were conducted where the sectional model was later placed. The measured mean wind speed was also used to build a mapping relationship to the wind speed monitored by a Prandtl tube, which is installed far from the Test section 1 for the overall wind speed in wind tunnel. Through the mapping relationship, a more precise mean wind speed can be estimated when the wind tunnel model was installed inside.

- Wake measurements. Flow measurements in the wake of the sectional model is to obtain information about the near-wake. This is related to the mathematical modeling with Tamura's wake oscillator model, which will be further explained in Chapter 5.

3.2.4 Turbulence Grid

Since the Test section 1 is already quite close to the inlet of wind tunnel (see Fig. 3.1 (a)), the capability of generating turbulent flow by means of grid is rather limited here. In fact, the maximal upstream distance to install a turbulence grid is about 1.0 m, and the existing grids at the wind tunnel facility had a minimum mesh size of 140 mm × 140 mm with 30 mm wide strips. A preliminary examination of the turbulent flow generated by this grid (upstream distance 0.93 m) resulted in a unsatisfying uniformity. Due to this reason, a new turbulence grid was designed and manufactured to gain more compliant turbulent flow.

Fig. 3.11 shows the new turbulence grid used in this research. It is made of wooden bars with a cross section of 23 mm × 23 mm, featuring a mesh size of 100 mm × 100 mm in bi-planar arrangement. The design of this grid followed the instructions given by Roach (1987), and also refereed to the size of a similar turbulence gird documented in Mannini & al. (2018b). The characteristics of the turbulent flow generated with this grid will be presented in Section 3.3.3.

Fig. 3.11: Photo of the used turbulence grid (upstream of the wind tunnel model).

3.3 Pre-examinations

3.3.1 Calibration of the Static Setup

As previously mentioned, the static setup consists of three load cells and the connecting rods on each side of the wind tunnel. Although the relative error of the load cell is already clear (given by the manufacturer), the accuracy of the static setup is actually unknown due to the manual combination of load cells and rods. For instance, whether the steel rods with plate-shaped appendices are perfectly installed will influence the force finally measured by the load cell. Therefore, it is necessary to calibrate the whole static setup to understand the real accuracy. The calibration was carried out by giving known force and moment to the static setup, as shown in Fig. 3.12. There, a weight of known mass is used to apply loading to the measurement system. Considering the plate-shaped appendices of the connecting rod working as hings, the applied vertical force as well as them moment will be measured by “Cell 2” and “Cell 3”, while the applied horizontal force is reflected by the “Cell 1”. By suspending the known weight respectively at “Pos. 1”, “Pos. 2” and “Pos. 3”, vertical force, moment and horizontal force can be measured for calibration purpose. The calibration was made side by side, in absence of wind tunnel model.

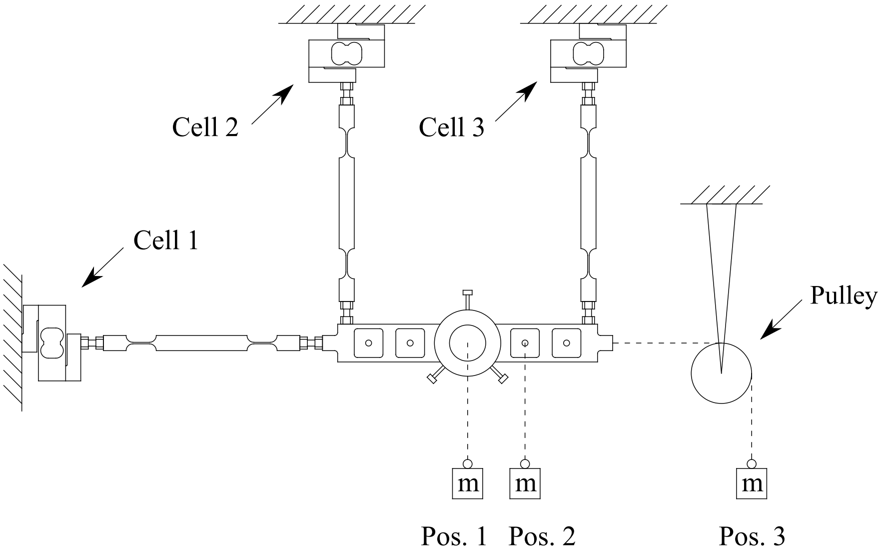

Fig. 3.12: Calibration of the static setup by giving known mass at three different positions.

Fig. 3.13 shows the calibration results, presented corresponding to a sequence of giving known weights at “Pos. 1”, “Pos. 2” and “Pos. 3”. The given force, through the gravity of mass, covered a range from 0.066 N to 16.367 N. For the vertical force (Fig. 3.13 (a)), the measured one agrees well with the given one except at 0.066 N , reporting a relative error, defined here as the relative difference of the measured one to the given one, lower than 0.15% for both sides. The relative error for moment component is slightly higher, but within 0.5% for both sides (Fig. 3.13 (b)).

However, the relative error for the horizontal one is comparably large, reporting a maximum difference about 1.5%. At the same time, the measured one is found always lower than than the given one except for the lowest magnitude (0.066 N).

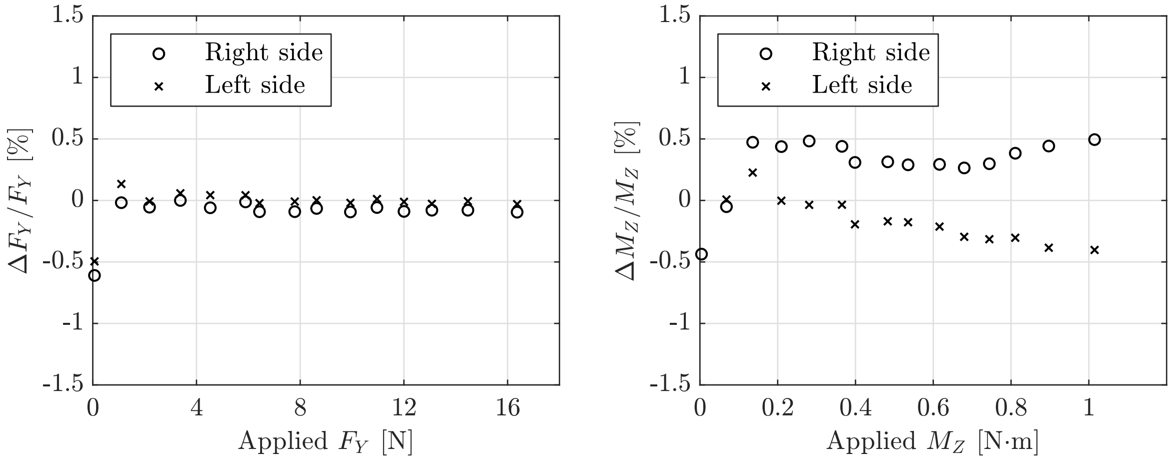

(a) Vertical force F_Y (b) Moment M_Z

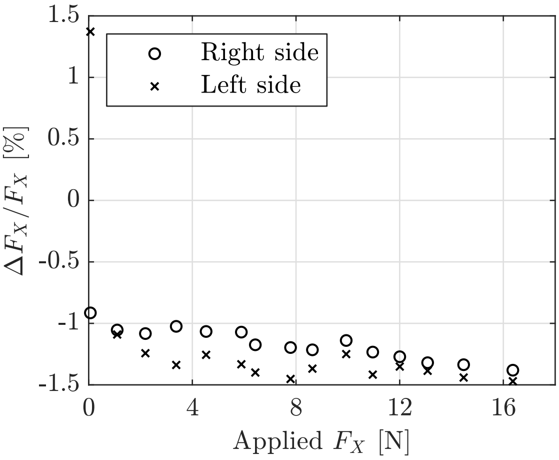

(c) Horizontal force F_X

Fig. 3.13: Results of calibrating the static setup side by side. Δ denotes the relative difference of the measured one to the given one.

To figure out the reason, additional calibration work was devoted to the "Cell 1" sensor, which is responsible for the horizontal force component of the static setup. Fig. 3.14 shows the two steps of additional work. First of all, the "Cell 1" sensor was dismounted from the static setup and vertically installed. Then the vertical force was directly applied to the sensor, by suspending a known weight as shown in Fig. 3.14 (a). The obtained relative error is about 0.02 % for a magnitude of 9.937 N. This indicates that the sensor itself works well. Secondly, the sensor "Cell 1" was installed horizontally but without the rig. The horizontal force was then applied to the sensor by means of nylon cable and pulley, as shown in Fig. 3.14 (b). With still 9.937 N as the given force, the measure value is about 0.91% and 0.80% less, respectively for the right side and left side setup of the wind tunnel. This clearly means, that a small portion of the horizontal force is “eaten” by the pulley, probably due to the friction of the pulley. Considering this, it is decided to introduce no correction to the measured force and moment by the static setup.

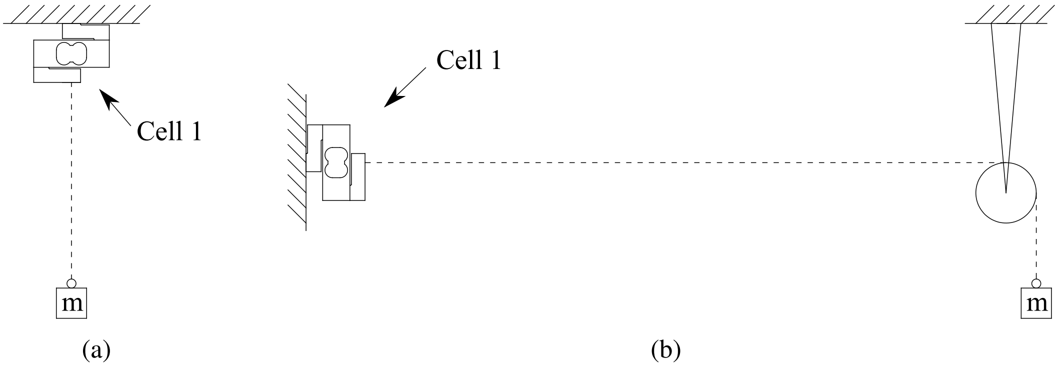

Fig. 3.14: Extra calibration for the horizontal force: (a) vertical loading on “Cell 1”; (b) horizontally loading on “Cell 1” without setup rig.

3.3.2 Linearity of the Damper System

Fluid-structure interaction usually exists strong non-linearity. So the aeroelastic test setup should behave itself as linear as possible, to reduce the mixing of mechanical non-linearity into the aeroelastic responses. An important topic here is the linearity of the mechanical damping, which can be roughly divided into two sources: a) wind tunnel model and its connected affiliations; b) additional damping introduced by damper. For the former, it is important to reach a rigid connection between the assembled components and avoid any possible friction movement. This requires much attention and accuracy during the manufacturing process of the wind tunnel model as well as concerned setup, and it is usually hard to make change again once the manufacturing is completed. Here, more attention is put to the used damper system.

The linearity of the damper system was examined by applying different initial out-of-equilibrium positions to the wind tunnel model, and then comparing the evaluated damping from the free-decaying vibration. Strictly speaking, such an examination should be conducted in void to totally remove the effect of still air, or using a specially designed streamline wind tunnel model which can minimize the influence of surrounding air(e.g, in Santosham (1966)). Unfortunately, these options are not available at the current wind tunnel facility. Therefore, the carried-out examination was performed under the situation, where a considerable amount of additional damping was introduced. By doing so, the portion of the well-known nonlinear damping due to the surrounding still air can be minimized. Maintaining the same input electric power for the damper, Fig. 3.15 shows the displacement decaying records of the bridge deck model, respectively for a small initial displacement (about 1 mm) and a large one (about 19 mm). For both cases, the amplitude envelopes can be well fitted to a decaying function $y = y_0 e^{-2\pi\zeta_0 n_0 t}$, where

y_0 depends on the initial displacement. The evaluated damping by this fitting method reports $\zeta_0 = 1.59\%$ for the case with small initial displacement, and $\zeta_0 = 1.61\%$ for the large one. These two very close values suggest a satisfying linearity of the damper system.

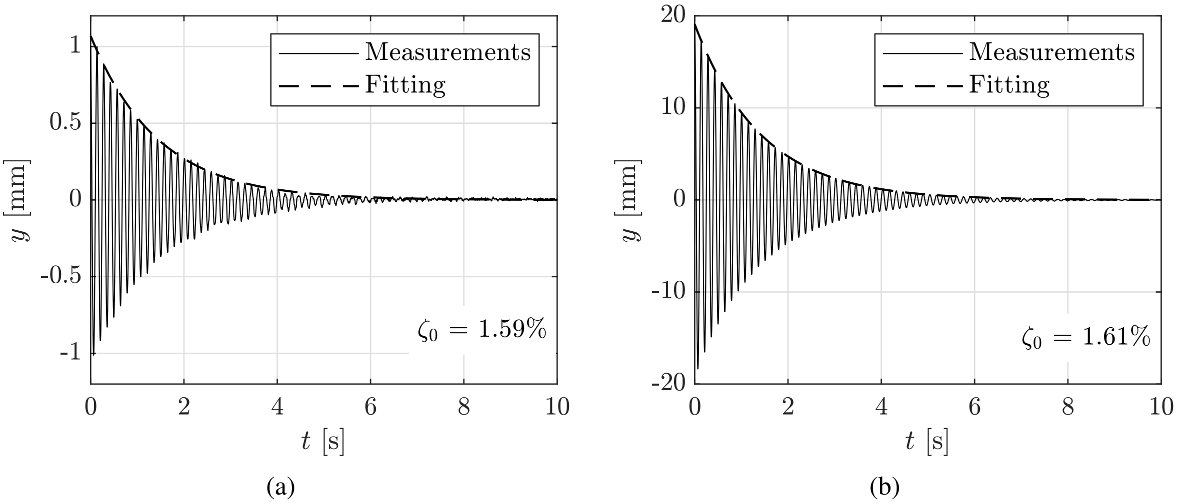

(a)

(b)

Fig. 3.15: Examination of the linearity of the damper system by applying different initial out-of-equilibrium positions (four-damper system with the same input of electric power).

3.3.3 Flow Characteristics at Test Section 1 of Wind Tunnel

Smooth flow

To understand the characteristics of the incoming flow, a total amount of 15 monitoring points were distributed at the position where the wind tunnel model will be installed later. As shown in Fig. 3.16, these monitoring points were arranged in five columns and three rows. They have a horizontal distance of 200 mm and a vertical distance of 90 mm. Flow velocity measurements were conducted with the Cobra probe at a sampling frequency of 2000 Hz. The recording time length in a steady flow is 60 s. The recorded raw data was digitally filtered by a low-pass zero-phase Butterworth filter of 20 orders, at a cut-off frequency of 500 Hz. It was noticed, that the power spectral density of the along-wind fluctuation $S_{uu}(n)$ showed a tendency to be constant in the frequency range higher than 500 Hz. This may be some high frequency noise but cannot be the real energy of the turbulence, therefore they were filtered out.

Fig. 3.17 shows the statistical results of the measurements of the 15 monitoring points. There, $\overline{U}$ represents the spatially averaged value of U of the 15 points. For $\overline{U}$ higher than about 5 m/s, the relative standard deviation $\mathrm{std}(U)/\overline{U}$ of the 15 points is well below 1%, and the maximum deviation to the averaged value is smaller than 2%. This indicates a good uniformity of the incoming flow for this wind speed range. However, the uniformity becomes less satisfying for

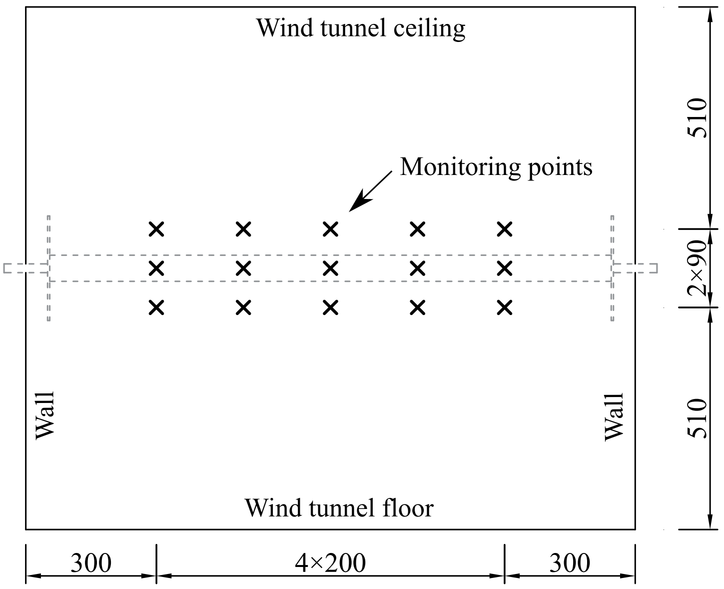

Fig. 3.16: Monitoring points for Cobra probe in smooth flow condition. The dashed line indicates the position where the wind tunnel model will be installed later.

$\overline{U} < 5$ m/s. This problem is also observed for the turbulence intensity, see Fig. 3.18. For $\overline{U} >$ 5 m/s, the averaged turbulence intensity of the 15 points is well below 1% (even the maximum value is just slightly higher than 1%). However, for very low wind speeds (like 3 m/s), the turbulence intensity reaches nearly 3%.

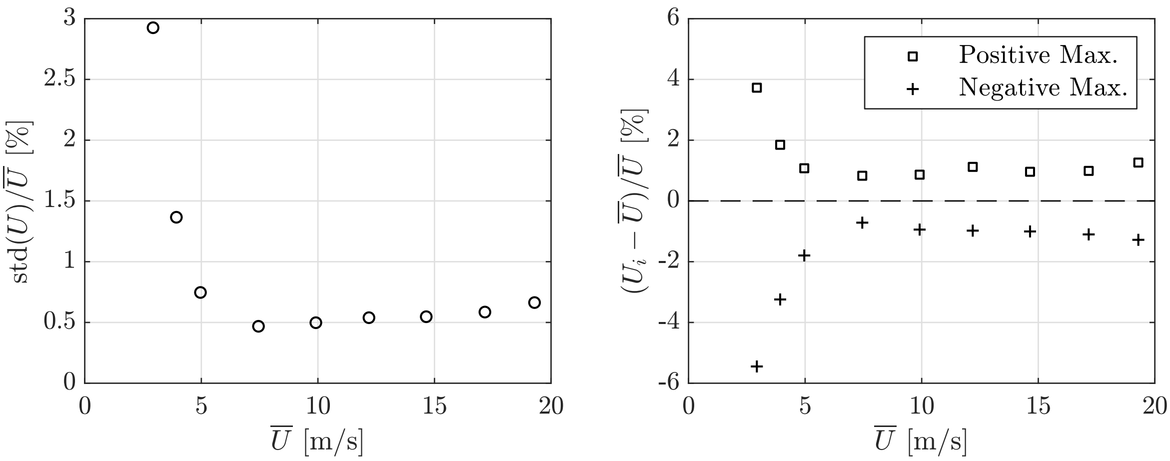

(a) Standard deviation (b) Maximum deviation

Fig. 3.17: Relative deviation of mean wind speed of the 15 monitoring points (smooth flow). $\overline{U}$ denotes the spatially averaged mean wind speed.

This less satisfying flow characteristic for $\overline{U} < 5$ m/s could be due to the wind tunnel facility itself, which is however hard to improve. Another possible reason may arise from the Cobra probe, remembering that its working range of wind speed should be higher than 2 m/s. The measurements with Cobra probe in such a low-velocity flow may involve more uncertainties

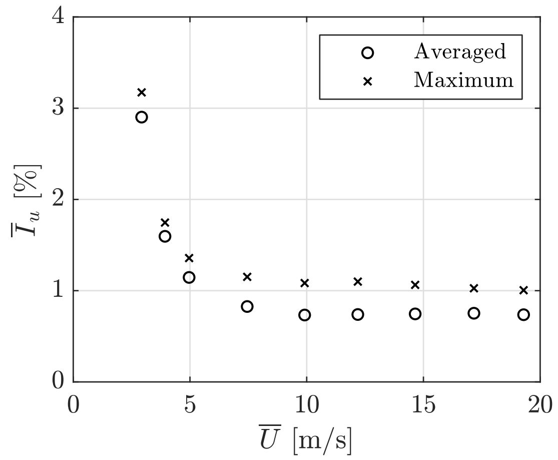

Fig. 3.18: Average and maximum value of the turbulence intensity of the 15 monitoring points (smooth flow).

and errors. To ensure a good uniformity of the incoming flow, all measurements were carried out with a mean wind speed higher than 5 m/s. Finally, the specific values of U and I_u for each monitoring point at given in Appendix A.2.1, for 5 representative wind speed levels.

Turbulent flow

For the measurements of turbulent flow, the positions of the 15 monitoring points were slightly changed (see Fig. 3.19). The horizontal and vertical distance were rearranged to 230 mm and 60 mm, to avoid placing all monitoring points straightforwardly behind the strips of the turbulence grid. The upstream position of the grid to monitoring points was varied in the three distances of x = 94 cm, 74 cm and 54 cm. The following results are therefore labeled as “Gird-X94”,

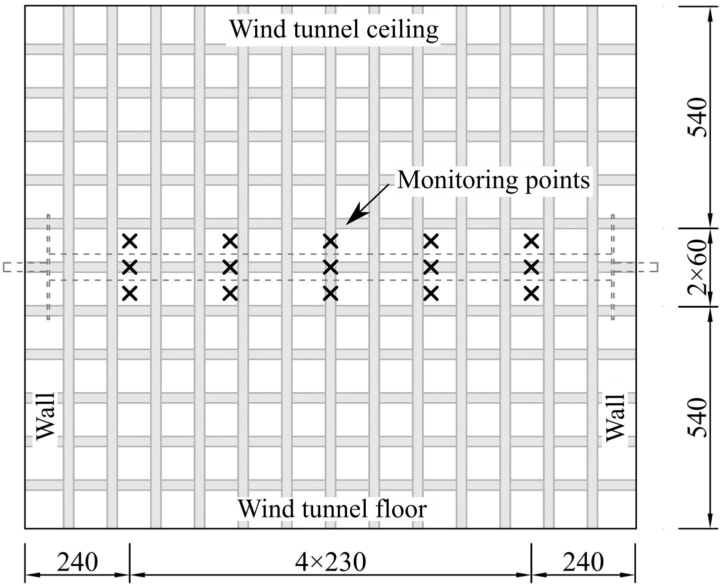

Fig. 3.19: Monitoring points for Cobra probe, with turbulence grid installed upstream. The dashed line indicates the position where the wind tunnel will be installed later.

“Gird-X74”, “Gird-X54”. The sampling frequency of the Cobra probe was set to 2000 Hz. No filter was used for the data processing of turbulent flow measurements.

Fig. 3.20 shows the relative standard deviation of the mean wind speeds of the 15 monitoring points, which stands here as an indicator for the spatial uniformity of the incoming flow. Compared to the results in smooth flow (Fig. 3.17 (a)), the uniformity of the three turbulent flows decrease slightly but still within 2 % for $\overline{U} \geq 5$ m/s.

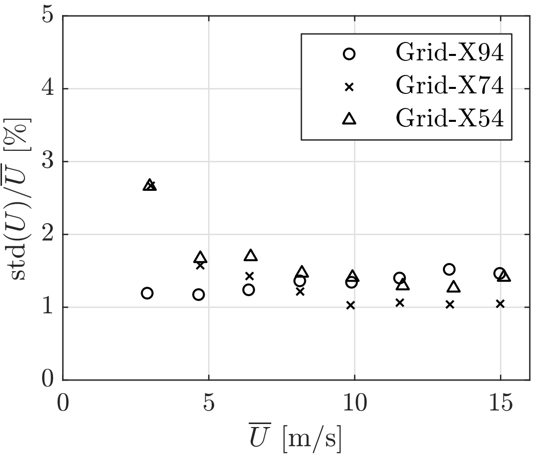

Fig. 3.20: Relative standard deviation of mean wind speed of the 15 monitoring points, with three configurations of the turbulence grid.

Fig. 3.21 (a) shows the spatially averaged along-wind turbulence intensity $\overline{I}_u$, with respect to $\overline{U}$. The averaged value $\overline{I}_u$ was found slightly dependent on $\overline{U}$ at low wind speeds for all of the three configurations, and tend to be constant at high wind speeds. This behavior is very similar to that reported for smooth flow (see Fig. 3.18), which suggests that the higher turbulence intensity at low wind speeds may be not due to the turbulence grid itself. Nevertheless, the spatially

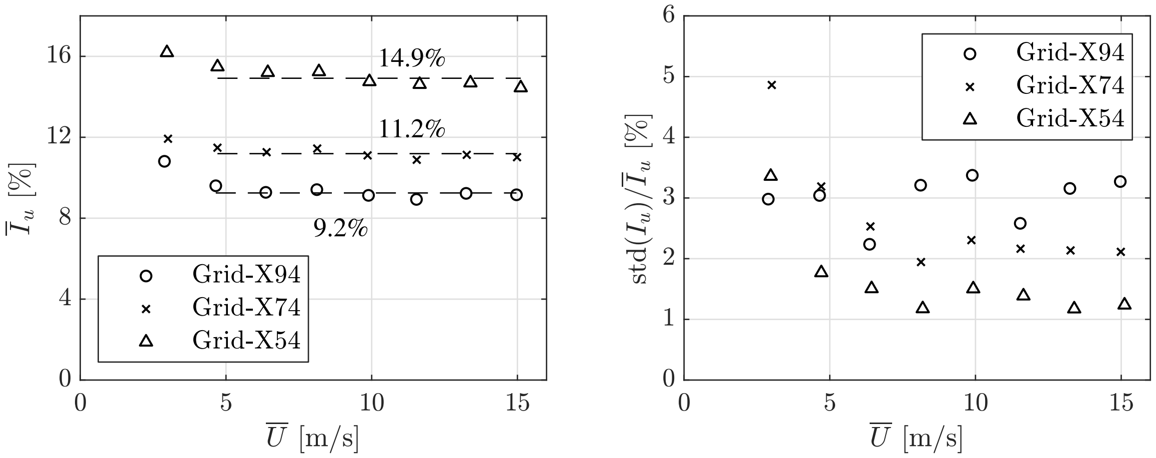

(a) Spatially averaged value

(b) Standard deviation

Fig. 3.21: Turbulence intensity I_u of the 15 monitoring points (turbulent flow).

averaged $\overline{I}_u$ was further averaged for flow velocities higher than about 5.0 m/s, to characterize an overall indicator. They are reported 14.9%, 11.2% and 9.2%, respectively, for the three grid configurations. Fig. 3.21 (b) shows the relative standard deviation of I_u to the averaged value $\overline{I}_u$ for the 15 monitoring points. For $\overline{U} \geq 5$ m/s, they are generally within 4 % and considered well-acceptable for turbulent flow.

Fig. 3.22 shows the ratio of $\overline{I}_v$ and $\overline{I}_w$ to $\overline{I}_u$, where $\overline{I}_v$ and $\overline{I}_w$ denote the spatially averaged turbulence intensities in lateral and vertical direction. The three different grid configurations lead to very similar results, with the ratios $\overline{I}_v/\overline{I}_u$ and $\overline{I}_w/\overline{I}_u$ in a range between 0.8 and 0.9 for $\overline{U} \geq 5$ m/s.

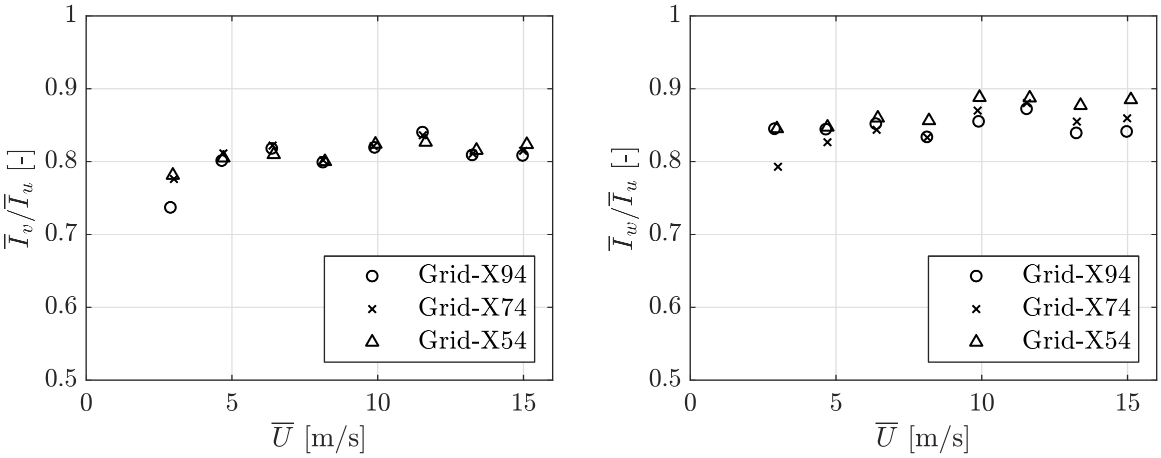

(a) Turbulencen intensity I_v

(b) Turbulencen intensity I_w

Fig. 3.22: Intensity of the other two turbulence components (spatially averaged value).

The along-wind turbulence integral length $L_u = UT_u$ is calculated based on Taylor's frozen eddy hypothesis, where $T_u = \int_0^\infty \rho_{u,u}(t_{lag})\mathrm{d}t_{lag}$ is the integral time length and $\rho_{u,u}(t_{lag})$ is the normalized auto-correlation function of the along-wind fluctuation component $u(t)$ (here, t_{lag} is the time lag). To reduce the uncertainties, the measured $\rho_{u,u}(t_{lag})$ was first approximated by an exponential decaying function and then integrated, adopting the same method as used in Clobes (2008) and Hoebbel & al. (2018).

In Fig. 3.23 (a) the spatially averaged integral length $\overline{L}_u$ is reported, with respect to $\overline{U}$. Compared with the turbulence intensity (see Fig. 3.21), the averaged integral length $\overline{L}_u$ shows a slight trend of increase with $\overline{U}$ for all grid configurations. It is known that the energy distribution of the turbulent flow is characterized by the normalized frequency (nL_u/U) (e.g., see the von Kármán spectrum Eq. 3.1), thus the portion of turbulence energy left outside the sampling frequency (2000 Hz) is actually dependent on U. This portion of energy will be transported into sampled data due to the aliasing effect in the sampling process, but in a form similar to the white noise (this is confirmed by artificially generating a turbulent flow $u(t)$, containing energy only in a frequency band from 500.1 Hz to 3000 Hz, and then sampled at 500 Hz). In frequency domain, the contribution of this “white noise” will slightly “lift” the measured spectrum S_{uu} over the whole frequency band. In particular, the “being-lifted” low-frequency signals is crucial, which will increase the estimation of turbulence integral length. The aliasing effect can be reduced by using a higher sampling frequency so that the turbulence energy left outside the sampling frequency is minimized. In fact, this may be particularly necessary for small scale turbulence transported by high mean flow velocity. Anyway, for $\overline{U} \geq 5.0$ m/s, the spatial averaged values are further averaged over the mean wind speeds to obtain overall indicators for the different turbulent flows.

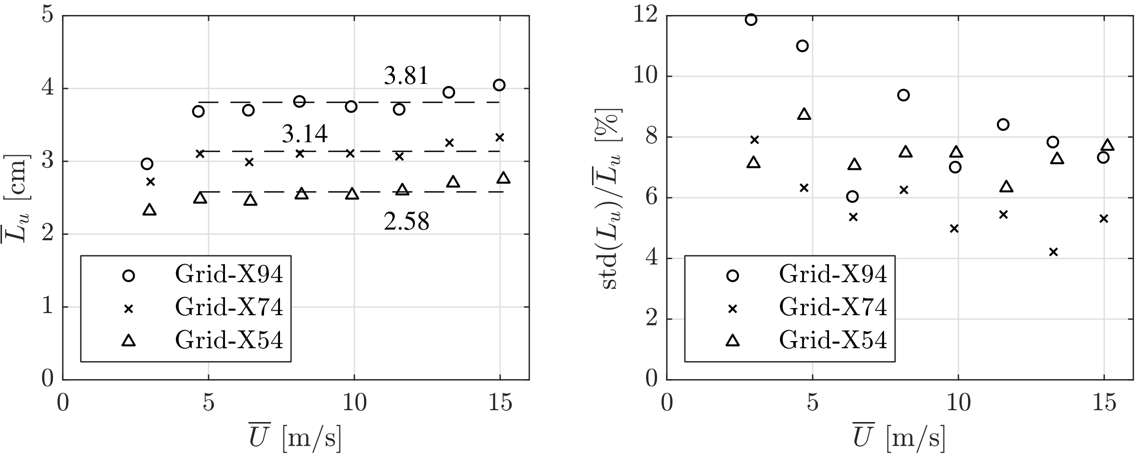

(a) Spatially averaged value (b) Standard deviation

Fig. 3.23: Average and standard deviation of the turbulence integral length L_u of the 15 monitoring points.

Fig. 3.23 (b) shows the relative standard deviation of the estimated turbulence integral length of the 15 monitoring points. Its non-uniformity is apparently larger than that for the mean wind speed and turbulence intensity. In the distribution map provided in Appendix A.2.2, one can find a difference of 1 cm between two monitoring points at the same $\overline{U}$ (see Fig. A.7 (a)). Anyway, the uncertainties in the estimation of the turbulence integral length is a well-known issue in wind engineering (Simiu & Scanlan 1996), especially for full scale measurements (Hoebbel & al. 2018).

Before the presentation of the concerned power spectral density, the commonly used theoretical model for the homogeneous isotropic turbulence proposed by von Kármán (Von Kármán 1948) should be introduced. For the auto spectral density S_{uu} of longitudinal turbulence $u(t)$, it is written in a normalized form:

$$\frac{nS_{uu}(n)}{\sigma_u^2} = \frac{4nL_u/U}{(1+70.8(nL_u/U)^2)^{5/6}} \tag{3.1}$$

where L_u is the turbulence integral length and σ_u the standard deviation of $u(t)$. By putting the measured L_u into the above equation, the von Kármán spectrum S_{uu} provides a way in frequency domain to examine the quality of the grid-generated turbulent flow, which is well-accepted as nominally homogeneous isotropic turbulent flow.

Fig. 3.24 shows the measured power spectral density S_{uu} for the three grid configurations, exemplified by the central measuring point at a mean wind velocity about 10 m/s. Their respective measured integral lengths L_u were used to plot the von Kármán ones. Clearly, the measured spectra show a good agreement with the theoretical ones in the low to medium normalized frequency range, but are overestimated in the high normalized frequency range. This is caused by the previously mentioned aliasing effect. Because the magnitude of S_{uu} at high normalized frequency is relatively small, so that the distortion of the "white noise" due to aliasing effect becomes apparent here, making the measured S_{uu} look like tending to be constant.

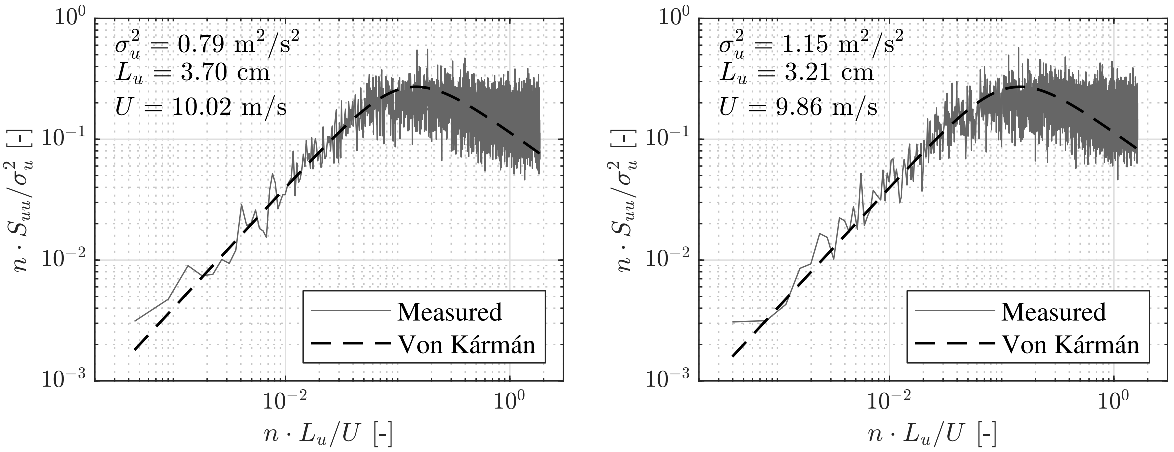

(a) Grid-X94

(b) Grid-X74

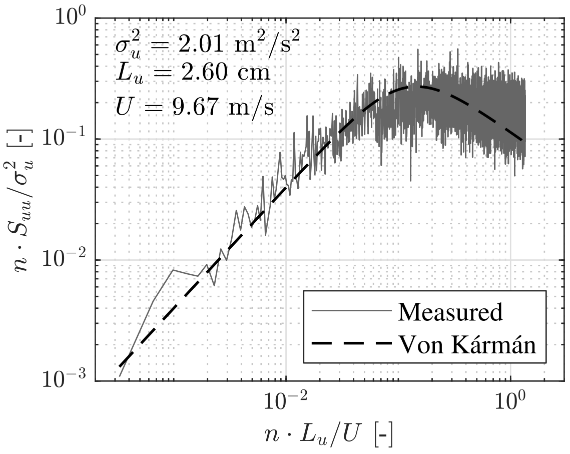

(c) Grid-X54

Fig. 3.24: Examples of the power spectral density S_{uu} at the central monitoring point.

Tab. 3.2 summarized the flow characteristics at the wind tunnel Test section 1. In general, the uniformity of the incoming flow is satisfying, reporting a relative standard deviation of the 15 monitoring points less than 1% for smooth flow and less than 2% for turbulent flow. The intensity of the grid-generated turbulent flow represents typical values of the natural wind filed. However, the length scale of turbulence is quite small, just in the same order of the height of the wind tunnel models. This indicates a big difference from the full scale situation, where the turbulence integral length could be 20 times larger than the bridge deck height. The simulation of turbulent flow in a boundary layer wind tunnel, fulfilling both high intensity and large integral length, has always been a challenge, especially for sectional bridge deck models. With respect to across-wind galloping instability, Laneville & Parkinson (1971) have shown, that mainly the turbulence intensity has an influence on the galloping stability of a bluff body. Recent experimental studies, on the other hand, pointed out, that also the turbulence integral length has an important impact (Mannini & al. 2018b). This suggests that the effect of the turbulence integral length on the galloping instability requires further investigations, which is, however, experimentally very difficult due to the challenge in obtaining large scale turbulent flow. For the ratios $\overline{I}_v/\overline{I}_u$ and $\overline{I}_w/\overline{I}_u$ in Tab. 3.2, it is known that the generated turbulent flow is not fully isotropic but satisfying to some extent.

Tab. 3.2: Summary of the flow characteristics (further averaged value over mean wind speeds higher than about 5 m/s). x_g is the distance between turbulence grid and monitoring points, d_g the grid mesh size 10 cm, d wind tunnel model height 6 cm.

Config.	x_g [cm]	x_g/d_g [-]	std(U)/$\overline{U}$ [-]	$\overline{I}_u$ [-]	$\overline{I}_v/\overline{I}_u$ [-]	$\overline{I}_w/\overline{I}_u$ [-]	$\overline{L}_u$ [cm]	$\overline{L}_u/d$ [-]
No Grid	-	-	$< 1\%$	$\sim 1\%$	-	-	-	-
Grid-X94	94	9.4	$< 2\%$	9.2%	0.81	0.85	3.81	0.64
Grid-X74	74	7.4	$< 2\%$	11.2%	0.82	0.85	3.14	0.52
Grid-X54	54	5.4	$< 2\%$	14.9%	0.81	0.87	2.58	0.43

Fig. 3.25 shows a comparison between the generated turbulent flow and the one generated by a similar grid in Mannini & al. (2018b), as well as the empirical prediction provided by Roach (1987). The presented turbulence intensity I_u *vs.* x_g/d_g agrees well with the results in Mannini & al. (2018b), while Roach's empirical equation reports a slightly lower intensity. For integral lengths, the estimation according to Roach (1987) is also lower than the two experimental ones, which agree fairly well with each other.

Finally, for the convenience of results presentation in following Chapters, the spatially averaged mean wind speed $\overline{U}$ is replace by U to represent the incoming mean wind speed (if without special notation). At the same time, the turbulence intensity and integral length reported in Tab. 3.2 are also simply indicated by I_u and L_u.

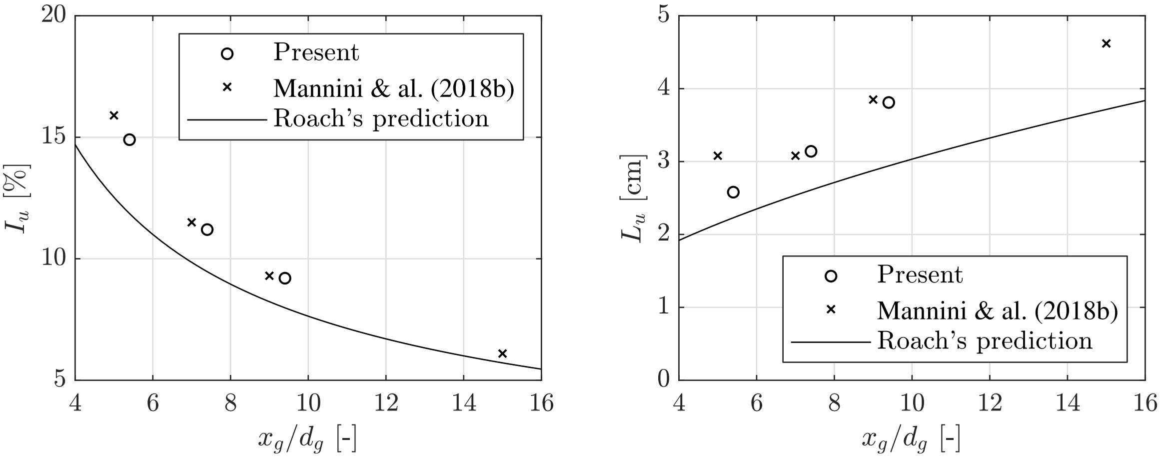

(a) Intensity (b) Integral length

Fig. 3.25: Comparison of the turbulence characteristics with other literature reports. The turbulence grid in Mannini & al. (2018b) features a mesh size 10 cm × 10 cm and strip width c_g = 2.5 cm. Empirical equation provided by Roach (1987) for the prediction of turbulence intensity is $I_u = 1.13(x_g/c_g)^{-5/7}$, and for the integral length it is $L_u/c_g = 0.2(x_g/c_g)^{1/2}$, with c_g = 2.3 cm.

3.3.4 Flow Characteristics at Test Section 2 of Wind Tunnel

The flow characteristics at Test section 2 were examined in absence of any turbulence generators. Measurements were conducted with the Cobra probe prior to the installation of the wind tunnel model. The 10 monitoring points were arranged in one vertical line just above the HFFB (see Fig. 3.26 (a)). In particular, the monitoring points at the heights of 16 cm and 52 cm correspond respectively to the bottom and top of the launching nose model to be installed (see Fig. 3.8). The procedure for data acquisition is the same as in Section 3.3.3.

The profiles of the mean wind speed and the turbulence intensity are shown in Fig. 3.26 (b) and (c), for three different wind speed levels. Apparently, for wind tunnel without any turbulence generators, the flow quality close to the ground is less satisfying. The turbulent boundary layer developed above the ground seems quite thick. For the mean wind speed, good uniformity is available for position higher than about 16 cm. For the turbulence intensity, it is less satisfying either. At $z = 22$ cm, the turbulence intensity is still higher than 2%. Because of this, a steel connector (shown in Fig. 3.8) was used to put the launching nose model at a higher position. Therefore, an approximately uniform smooth flow attacking the wind tunnel model is achieved.

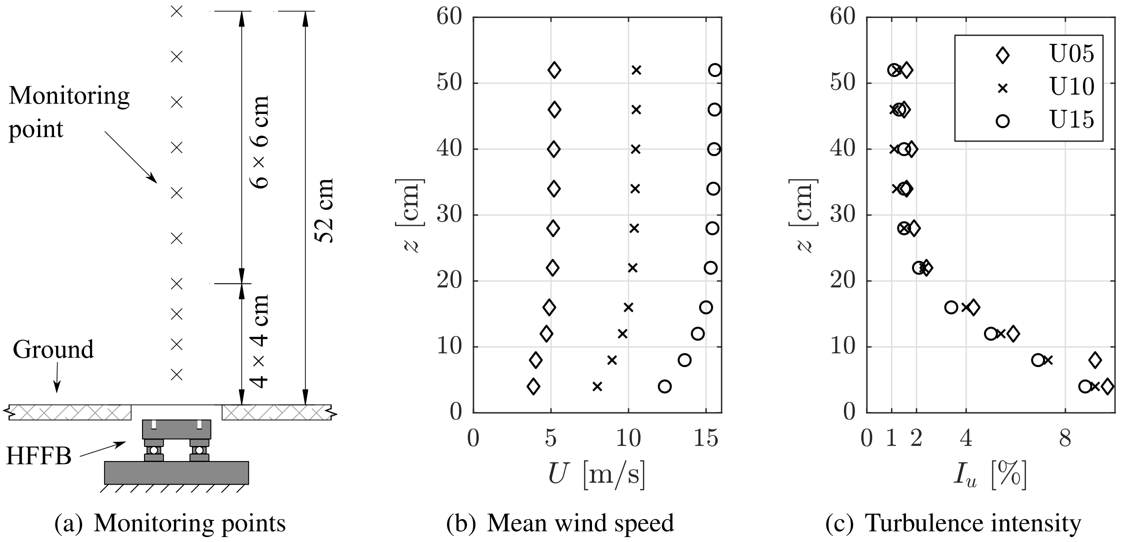

(a) Monitoring points (b) Mean wind speed (c) Turbulence intensity

Fig. 3.26: Flow characteristics for static tests of the launching nose model: (a) monitoring points; (b) approaching mean wind speed U and (c) turbulence intensity I_u. The legend is shared between results of U and I_u.

3.4 Chapter Summary

In this chapter, the experimental facility, the wind tunnel models and the different setups were presented. Some preliminary investigations, performed prior to the formal tests, were given here for an understanding on the accuracy and uncertainties of the setups, as well as the characteristics of incoming flows. The formal wind tunnel tests were performed for different purposes and the corresponding results will be presented in three parts. The first part of tests focused on the aerodynamic forces and aeroelastic behaviors of the three sectional models, whose results will be presented in Chapter 4 as a separated section. The flow velocity measurements in the wake of the sectional models (wake measurements) are arranged in Chapter 5. This part of measurements is closely related to the mathematical modeling with Tamura's wake oscillator model. Finally, the aerodynamic force measurements on the launching nose model will be given in Chapter 6, in combination with the mathematical modeling for continuous structural system.

4 Experimental Results of Sectional Models

4.1 Static Results

For the convenience of result presentations, definitions of aerodynamic force and moment coefficients are first given in Fig. 4.1. For the two close-form cylinder model, the force center is put at the mid-height of cross section. For the bridge deck model, this center is at $5d/12$ to its bottom side, which corresponds also to the gravity center of the cross section.

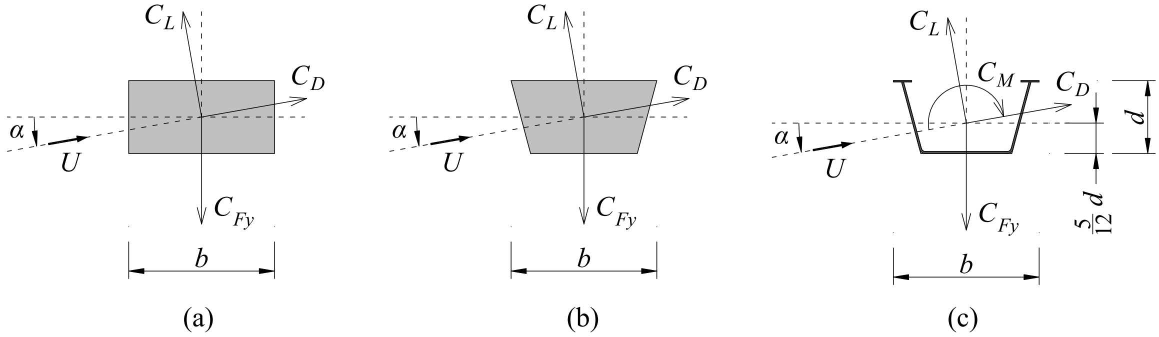

Fig. 4.1: Definition of the aerodynamic force and moment coefficients on the three sectional models.

The aerodynamic drag, lift and moment coefficients are all defined with the height d of sectional models

$$C_D = \frac{D}{0.5\rho U^2 d l_e}, \quad C_L = \frac{L}{0.5\rho U^2 d l_e}, \quad C_M = \frac{M}{0.5\rho U^2 d^2 l_e} \tag{4.1}$$

where D, L and M are the drag, lift and moment. Without special notation, these three coefficients denote the mean value of the steady-state measurements over a time length of 100 s. They are the steady parts of the measured force and moment coefficients. The transverse force coefficient C_{Fy} is defined downward positive, and calculated from C_D and C_L by Eq. 2.14 which is re-given here for convenience

$$C_{Fy}(\alpha) = -\frac{1}{\cos^2(\alpha)}[C_L(\alpha)\cos(\alpha) + C_D(\alpha)\sin(\alpha)]$$

The galloping factor A_1, for strictly across-wind instability, is calculated according to the well-known Den Hartog criterion

$$A_1 = -\left(\frac{\mathrm{d}C_L}{\mathrm{d}\alpha} + C_D\right)\bigg|_{\alpha=\alpha_0}$$

where α_0 denotes a mean flow incidence. If $\alpha_0 = 0$, there is also $A_1 = \frac{\mathrm{d}C_{Fy}}{\mathrm{d}\alpha}\Big|_{\alpha=0}$ according to Eq. 2.18.

From the unsteady part of lift, the Strouhal number and the strength of vortex shedding force can be evaluated. The Strouhal number is defined in this thesis with the model height d

$$St = \frac{n_{st} d}{U} \tag{4.2}$$

where n_{st} is the vortex shedding frequency, identified from the power spectral density of fluctuation lift S_{LL}. The Root Mean Square (RMS) value of vortex shedding force coefficient, named $C_{lat,0}$ in Eurocode 1 (EN 1991-1-4 2010; Ruscheweyh & al. 1996), is obtained by integrating S_{LL} with a frequency band around n_{st}

$$C_{lat,0} = \frac{\sigma_L}{0.5\rho U^2 d l_e} \quad \text{with} \quad \sigma_L = \sqrt{\int_{n_{st}-\Delta n}^{n_{st}+\Delta n} S_{LL}(n)\,\mathrm{d}n} \tag{4.3}$$

where $2\Delta n$ is the frequency band. Respectively, Δn = 3 Hz and Δn = 9 Hz were used for measurements in smooth and turbulent flow. The latter is larger since the vortex shedding force characterizes a wider frequency band in turbulent flow. For both situations, it has been confirmed that a wider frequency band has no significant influence on the results.

$C_{lat,0}$ obtained in this way is inevitably affected by the dynamic amplification effect, unless the first bending natural frequency of the model is very high compared to the vortex-shedding frequency. Unfortunately, the natural frequencies of the three wind tunnel models are not high enough (all around 50 Hz) in the static setup. To correct this bias, the classical dynamic amplification factor for a single-degree-of-freedom system was employed. Firstly, a sensitivity analysis showed that for damping ratios up to 5% the amplification factor exhibits negligible variations, if the ratio of the vortex-shedding frequency to the model natural frequency is lower than 0.84 (this is the maximum frequency ratio encountered during the static tests, occurred for the bridge deck model at α = -5° and U = 14.9 m/s). Consequently, since for sectional models rigidly mounted in the static setup, the damping ratio of the first bending mode is unlikely to be higher than 5%, a null damping ratio was considered to calculate the amplification factor and to correct the $C_{lat,0}$ values. As it will be shown later, this correction is very important.

Finally, for measurements in smooth flow, it is also convenient to use the sinusoidal equivalent amplitude coefficient:

$$C_{L0} = \sqrt{2} C_{lat,0} \tag{4.4}$$

to indicate the strength of vortex shedding force.

4.1.1 In Smooth Flow

Rectangular cylinder

The rectangular cylinder was first tested. Fig. 4.2 shows the mean drag and lift coefficients measured at various wind angle of attack α, at three different Reynolds numbers. The experimental results from Brooks (1960) and Santosham (1966) are also included for comparison. In general, the effects of Re on C_D and C_L are rather limited in the presented results. The drag and lift coefficients reaches their minima at about $\alpha = 7°$, which implies a definite reattachment of free shear layer on the side face of the cylinder according to Parkinson (1971). The agreement with literature reports is fairly good. Nevertheless, one can find that the negative slope of C_L around $\alpha = 0°$ is slightly larger than the reports of Brooks (1960) and Santosham (1966). This implies a larger galloping factor for the presented results.

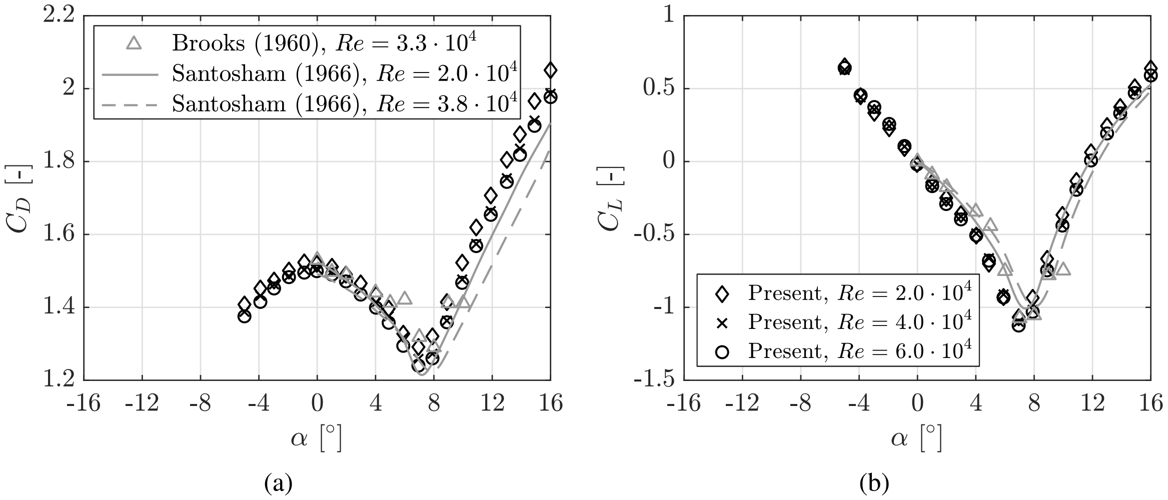

(a) (b)

Fig. 4.2: Mean drag and lift coefficients (C_D and C_L) for the 2:1 rectangular cylinder at various wind angles of attack α. The two subplots share their legends.

Fig. 4.3 shows the galloping factors A_1 at $\alpha = 0°$, for three different Re. They are calculated based on the aforementioned Den Hartog criterion, and the evaluation of the slope of C_L considered only the data points within [-1°, 1°]. Obtained A_1 shows slight dependence on Re, increasing from 5.6 at $Re = 2.0 \cdot 10^4$ to 6.8 at $Re = 6.0 \cdot 10^4$. Nevertheless, limited dependence on *Re* is quite common even for sharp-edged bluff body. From Fig. 4.2 (b), one can also notice the slightly different slopes of C_L in Santosham (1966)'s results between different *Re*.

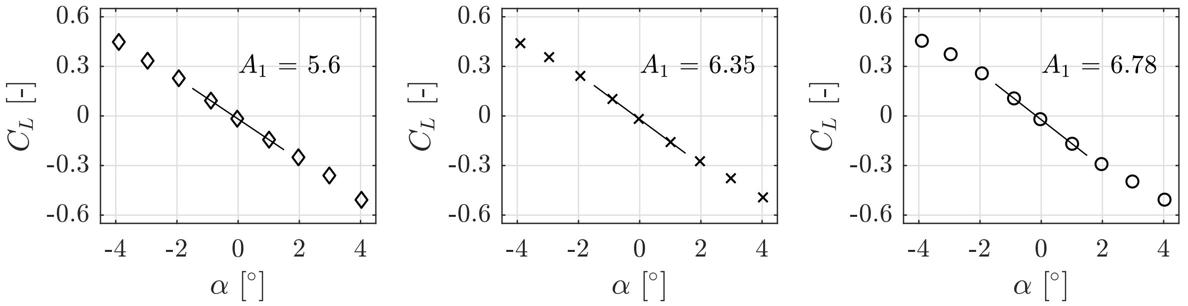

(a) $Re = 2.0 \cdot 10^4$ (b) $Re = 4.0 \cdot 10^4$ (c) $Re = 6.0 \cdot 10^4$

Fig. 4.3: Evaluation of galloping factor A_1 for the 2:1 rectangular cylinder at $\alpha = 0°$.

Fig. 4.4 shows the Strouhal number *St* and the sinusoidal equivalent amplitude of the fluctuation lift coefficient due to vortex shedding C_{L0}. In general, the effect of *Re* is rather limited, except that the C_{L0} coefficient within $-4° < \alpha < 4°$ shows an increase with *Re*. The C_{L0} reported here is already corrected by the previously mentioned dynamic amplification factor. However, the dependence on *Re* is still there and apparently more evident than other aerodynamic coefficients. This issue will be made clear later with more measurements.

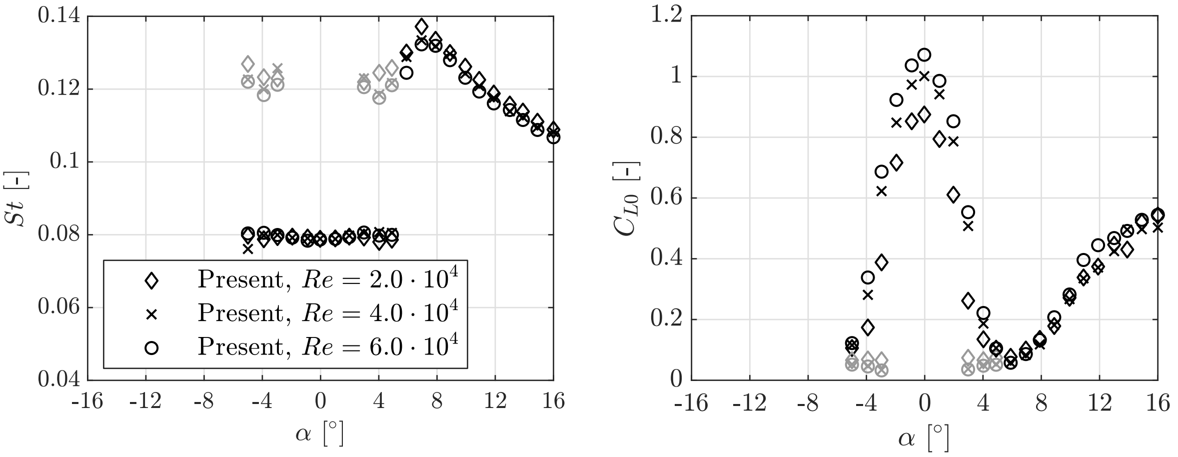

(a) (b)

Fig. 4.4: Strouhal number *St* and strength of vortex shedding force C_{L0} of the 2:1 rectangular cylinder at various α. Gray points in subplot (a) and (b) correspond to a second Strouhal number and its intensity of vortex shedding force.

In Fig. 4.4 (a), a jump of the dominated *St* is visible at about α = 6° (for brevity, only the results of $\alpha \geq 0°$ are discussed here due to symmetry of the cylinder). Before this jump, a second Strouhal number, marked with gray color in Fig. 4.4 (a), can be identified for $3° \leq \alpha \leq 5°$, characterized with a weaker strength of vortex shedding force as shown by Fig. 4.4 (b).

According to Deniz & Staubli (1997), the jump of the dominant *St* and the co-existence of two *St* are related to the transition process of vortex shedding pattern during the increase of α (from LEVS for small α to AEVS for large α, see also see Fig. 2.4 for schematics of LEVS and AEVS). Such a transition process can be also viewed from Fig. 4.5, which shows the power spectra S_{LL} at various α. It is also interesting to note that the strength of vortex shedding force becomes quite low, either for LEVS or AEVS, during this transition process.

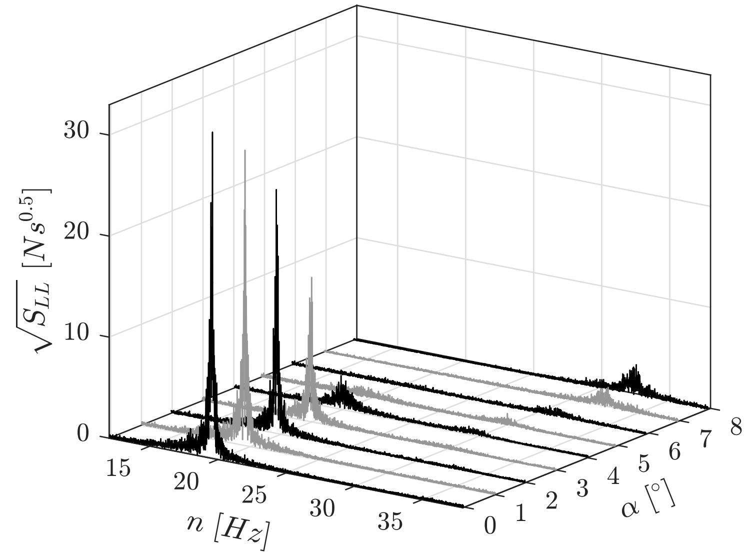

Fig. 4.5: Power spectral density S_{LL} for various α, at $Re = 6.0 \cdot 10^4$. S_{LL} is square-rooted for better view.

To further understand the dependence of C_{L0} on *Re*, the static test setup was re-mounted more than one year later and aerodynamic force measurements were repeated at the null wind angle of attack, with more and higher Reynolds numbers evolved. The new C_{L0}-*Re* relationship is shown in Fig. 4.6, combined also with the uncorrected C_{L0} results. The old results, marked with gray color, are added as well. Some points in the new obtained results must be explained first:

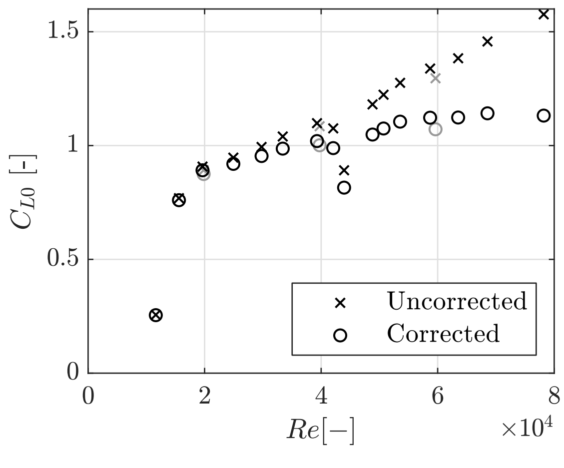

Fig. 4.6: Effects of Reynolds number and dynamic amplification on the C_{L0} coefficient, for the 2:1 rectangular cylinder at $\alpha = 0°$. Gray points denote old results (the ones reported in Fig. 4.4 (b)).

a) the peculiarly low C_{L0} at about $Re = 1.2 \cdot 10^4$ is due to the unsatisfying flow quality of the low wind speed in wind tunnel (U = 3 m/s), see Section 3.3.3; b) the drop of C_{L0} around about $Re = 4.4 \cdot 10^4$ is influenced by the process of $3n_{st}$ passing by n_0 during the increment of wind speed. From the uncorrected data, one can find that the C_{L0} coefficient increases linearly with Re. This trend is actually abnormal, also less reasonable for a sharp-edged body. In contrast, the corrected C_{L0} behaves in a more reasonable way, reaching a constant trend for $Re > 5.3 \cdot 10^4$, although for $2.0 \cdot 10^4 \leq Re \leq 5.3 \cdot 10^4$ a slight increase of C_{L0} with Re is still visible. Finally, one can find the new results and the old ones have a good agreement with each other.

In Tab. 4.1 the presented results are compared with more literature reports particularly at $\alpha = 0°$. The literature data is limited to experimental results obtained in a similar test condition. Clearly, the presented St and C_D coefficients agree well with other literature reports. The obtained A_1 factor also falls correctly into the range 2.9-8.6 suggested by other literature reports, although

Tab. 4.1: Comparison of the global aerodynamic parameters for the 2:1 rectangular cylinder with other literature reports (limited to experimental data, obtained on cylinder model, measured in air flow with low turbulence intensity and $Re > 10^4$). The original collection of literature data is provided by Mannini & al. (2014), except the very recent piece "Gao & al. (2020)". The galloping factor A_1 marked with "*" is inferred by Mannini & al. (2014) from the published graphics.

Reference	blockage [-]	I_u [-]	$Re \times 10^{-3}$ [-]	St [-]	C_D [-]	A_1 [-]
Brooks (1960)	2.8%	< 0.5%	33	0.079	1.53	3.2*
Santosham (1966)	2.6%	< 0.1%	20.4	-	1.53	3.9*
	”	”	38.0	-	1.49	2.9*
Nakaguchi (1968)	-	Smooth	20-60	0.085	1.46-1.54	-
Nakamura & Mizota (1975)	-	Smooth	-	0.083	1.69	6.1*
Washizu & al. (1978)	5.5%	0.3%	-	0.077	1.48	4.71
Miyata & al. (1983)	-	-	-	0.083	-	-
Okajima & al. (1985)	-	< 0.5%	20	0.076-0.079	-	-
Ruscheweyh & al. (1996)	-	2%	-	-	-	4.3*
Deniz & Staubli (1997)	-	Smooth	32	0.087	1.40	7.19
	-	”	48	0.089	1.38	7.82
	-	”	80	0.088	1.26	5.92
Itoh & Tamura (2002)	5%	< 0.5%	16-37	0.078	-	-
Hansen (2013)	-	2%	-	0.066	1.4	8.6
Gao & al. (2020)	5%	< 1%	80-120	0.078	1.27-1.31	4.06
Present	5%	∼1%	20	0.079	1.52	5.6
	”	”	40	0.079	1.51	6.35
	”	”	60	0.079	1.50	6.78

the presented ones ($A_1 = 5.6 - 6.78$) seems quite large. In fact, one can find the variation of the collected A_1 is considerably larger, compared with *St* and C_D. According to Mannini & al. (2014), this big variation of A_1 could be due to the different flow characteristics and test conditions. Finally, it is to note that the Eurocode 1 (EN 1991-1-4 2010) reports $C_D = 1.65$, $St = 0.06$ and $A_1 = 2$ for the 2:1 rectangular cross section. The latter two parameters can be found lower than the collections in Tab. 4.1.

In summary, the static test results of the 2:1 rectangular cylinder show good agreements with the literature reports, so that the static setup as well as the size of used end-plates are validated.

Trapezoidal cylinder

Fig. 4.7 shows C_D and C_L for the trapezoidal cylinder. At $\alpha = 0°$, wind tunnel test reports C_D = 1.53-1.54 and C_L = 0.69-0.76 for the investigated *Re*. From a global point of view, the effect of *Re* is still limited for the cylinder. It is to note that the local maximum of C_D moves to $\alpha = 3°$, mainly due to an inclination of the front face. The two local minimums of C_D occur at $\alpha = -6°$ and $\alpha = 10°$, corresponding to a local maximum and minimum in the $C_L(\alpha)$ plot respectively. Finally, in the $C_L(\alpha)$ plot, there exists a inflection point around $\alpha = -2°$. This may be due to an intermittent re-attachment of the separated shear layer on the upper surface of the cylinder, according to the explanation for the square cylinder by Luo & al. (2003).

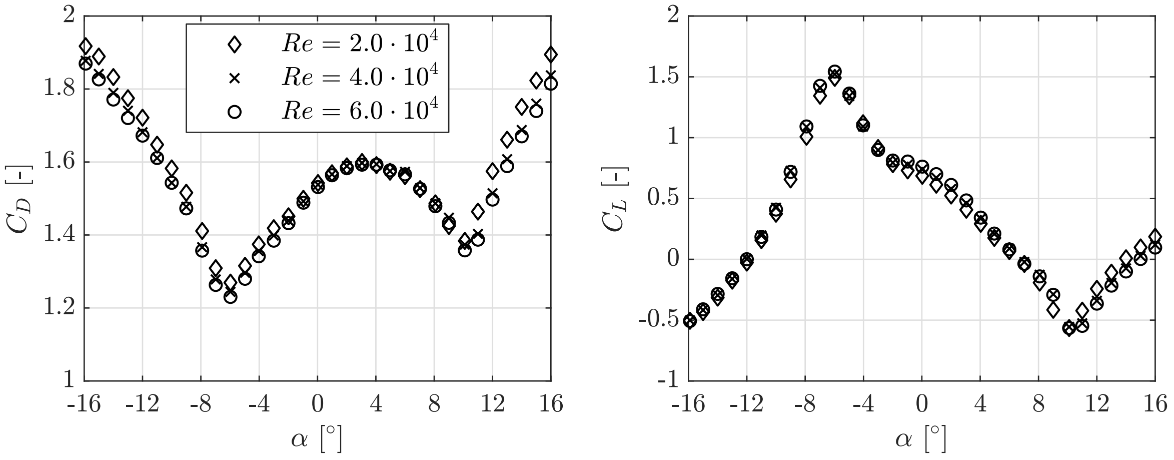

(a) (b)

Fig. 4.7: C_D and C_L of the trapezoidal cylinder at various α.

For brevity, Fig. 4.8 (a) shows only the dominant Strouhal number, although the second one is also observed for some wind angles of attack. For $-3° \leq \alpha \leq 8°$, *St* = 0.088-0.093 was obtained, which is relatively unvaried. Out of this range, jumps of *St* occur and the dominant vortex shedding pattern is supposed to change from LEVS to AEVS. Interesting is that, the local maximum of C_{L0} also moves to $\alpha = 3°$, around which the dependence on *Re* is apparent and qualitatively similar to the rectangular cylinder (see Fig. 4.8 (b)). Quantitatively, the magnitude of C_{L0} at $\alpha = 3°$ is higher than C_{L0} at $\alpha = 0°$ of the rectangular cylinder for the same *Re*.

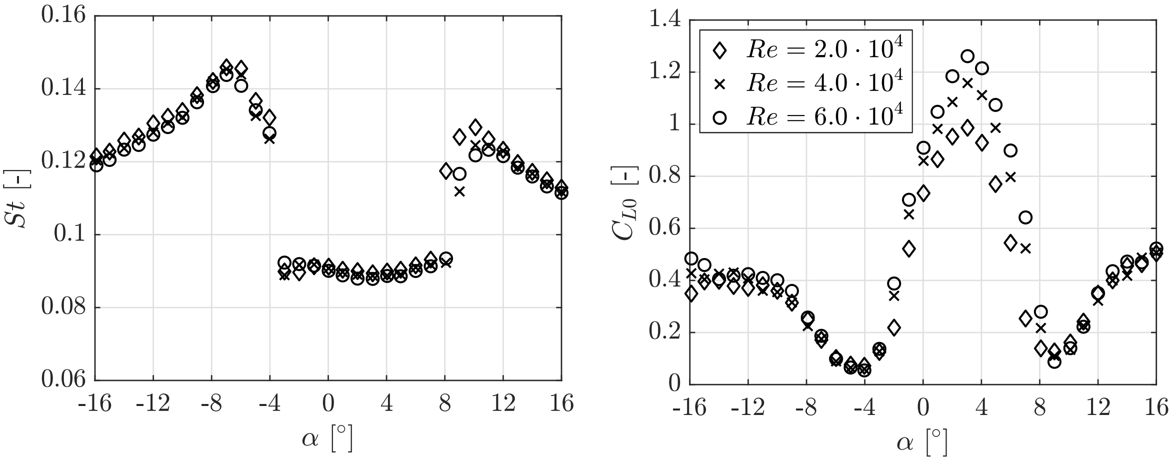

(a) (b)

Fig. 4.8: *St* and C_{L0} of the trapezoidal cylinder at various α.

Bridge deck model

Fig.4.9 shows the C_D, C_L and C_M coefficients for the bridge deck model. The moment coefficient is additionally given here, considering that it may be very useful for engineering practices (due to the high representativeness of the studied object). The effect of *Re* is generally limited as well, but for C_L within $-5° < \alpha < 12°$ one can find relatively apparent dependence on *Re* (a clear reason for this dependence is still unknown). At $Re = 6.0 \cdot 10^4$, the static tests report a drag coefficient $C_D = 1.62$ and a lift coefficient $C_L = 1.41$ for the null wind angle of attack. In fact, one can find the lift coefficient for this bridge deck is positive (upward) for a wide range of angles of attack, from -15° to 9°. For $\alpha = -5°$ at $Re = 6.0 \cdot 10^4$, the lift coefficient reports about $C_L = 2.15$, which is even higher than the drag coefficients within the investigated flow incidences. A local maximum of C_D occurs at about $\alpha = 5°$. Referring to the trapezoidal cylinder, the occurrence of maximal C_D at a non-null wind angle of attack is probably due to the inclination of the front face.

For *St* shown in Fig. 4.10 (a), some limited but clear effects of *Re* can be found for $0° < \alpha < 12°$. Nevertheless, a clear jump of *St* is found around $\alpha = -5°$, which implies a change of vortex shedding pattern. It is very possible that the AEVS pattern dominates for $\alpha < -5°$, but without flow visualization it is hard to imagine how the flow develops on the upper side of the cross section (due to the existence of an open cavity). A change of vortex shedding pattern may also occur around $\alpha = 0°$, since a slight jump of *St* can be found there (in particular clear for $Re = 6.0 \cdot 10^4$). For $0° < \alpha < 10°$ and $\alpha > 12°$, it is supposed that the LEVS and AEVS patterns dominate respectively. In Fig. 4.10 (b), a local maximum of C_{L0} appears about $\alpha = 4°$, showing

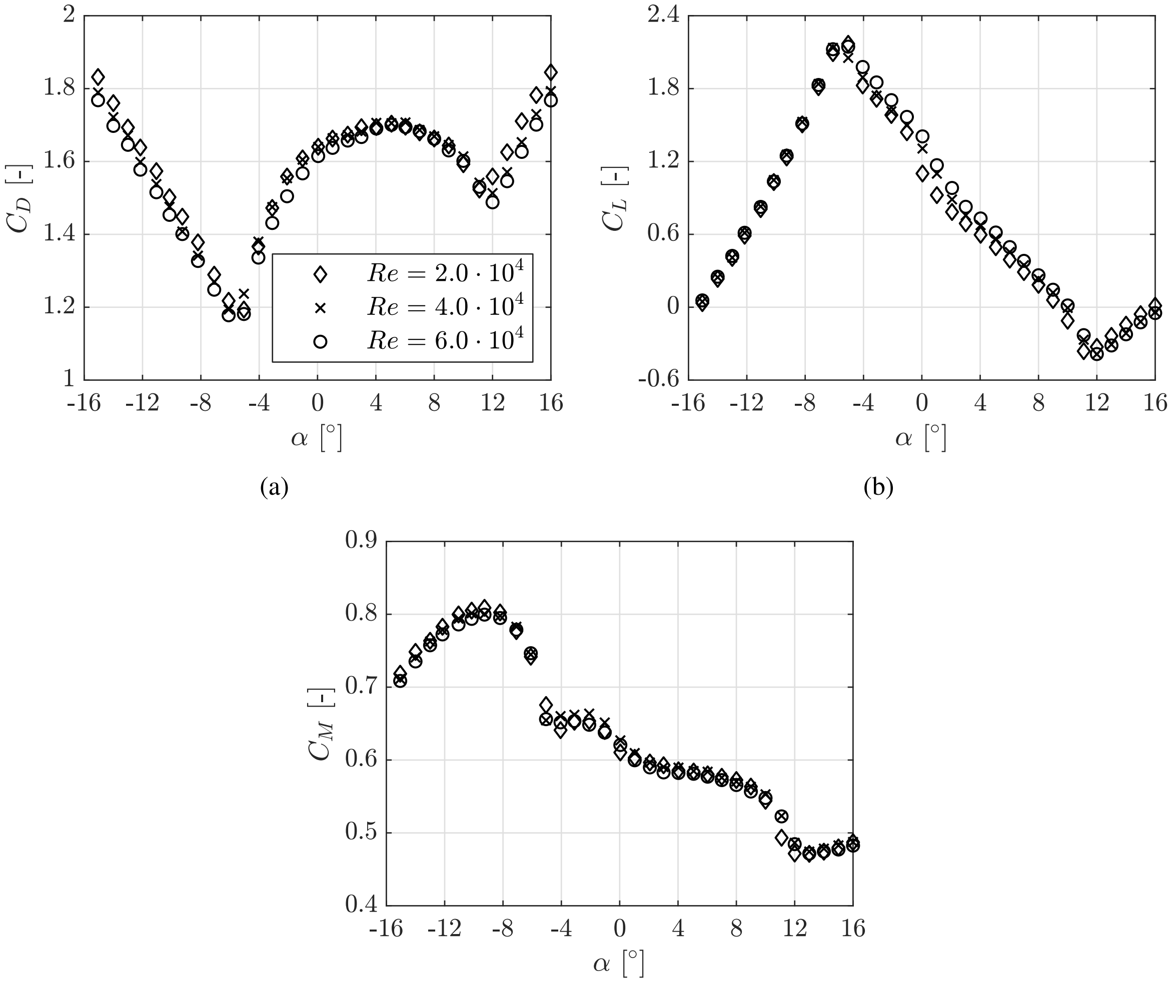

(a)

(b)

(c)

Fig. 4.9: C_D, C_L and C_M of the bridge deck model at various α.

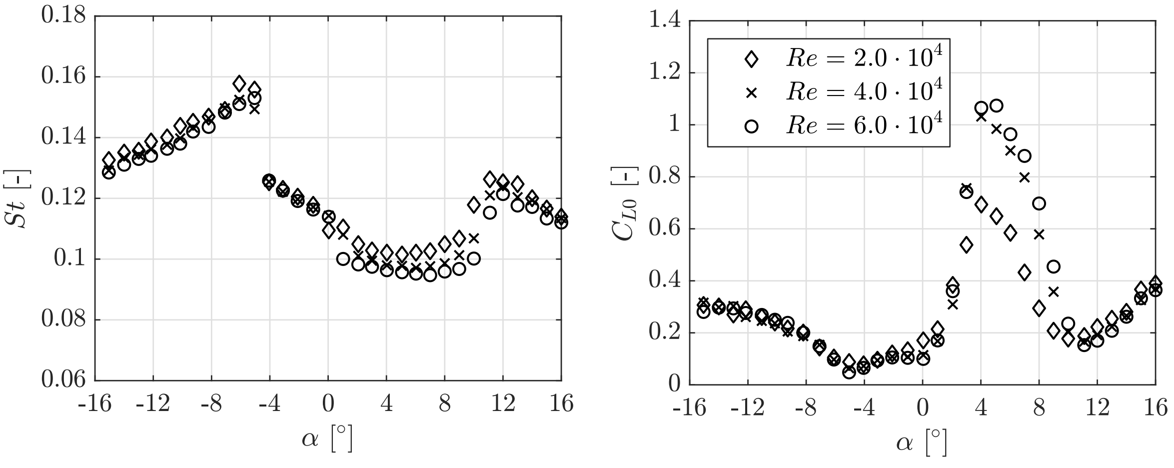

(a)

(b)

Fig. 4.10: St and C_{L0} of the bridge deck model at various α.

also dependence of C_{L0} on Re around this incidence. Such a characteristic is qualitatively similar to the two close-form cylinder models. Nevertheless, attentions should be paid to $-5° \leq \alpha \leq 0°$, where a low magnitude of C_{L0} was maintained in this comparably wide range. This is different from around $\alpha = 10°$, where the recovering of C_{L0} toward higher α is more pronounced. In contrast, the recovering of C_{L0} toward negative α seems to be obstructed within $-5° \leq \alpha \leq 0°$. Finally, for this open cross section, the incoming flow attacking from a negative angle may induce an interaction between the leading-edge-separated shear layer and the “trapped” flow inside the open cavity. Strecha (2014)’s CFD flow visualization on a “U” cross section (b/d = 4.6) has highlighted a complicated flow pattern for such interaction, although it may be not fully applicable here due to the different side ratio.

Fig. 4.11 shows the normalized power spectral density of fluctuation lift for four wind angles of attack, at $Re = 2.0 \cdot 10^4$ ($U = 4.92$m/s). For $\alpha = -7°$ and $\alpha = 4°$, the normalized spectra are

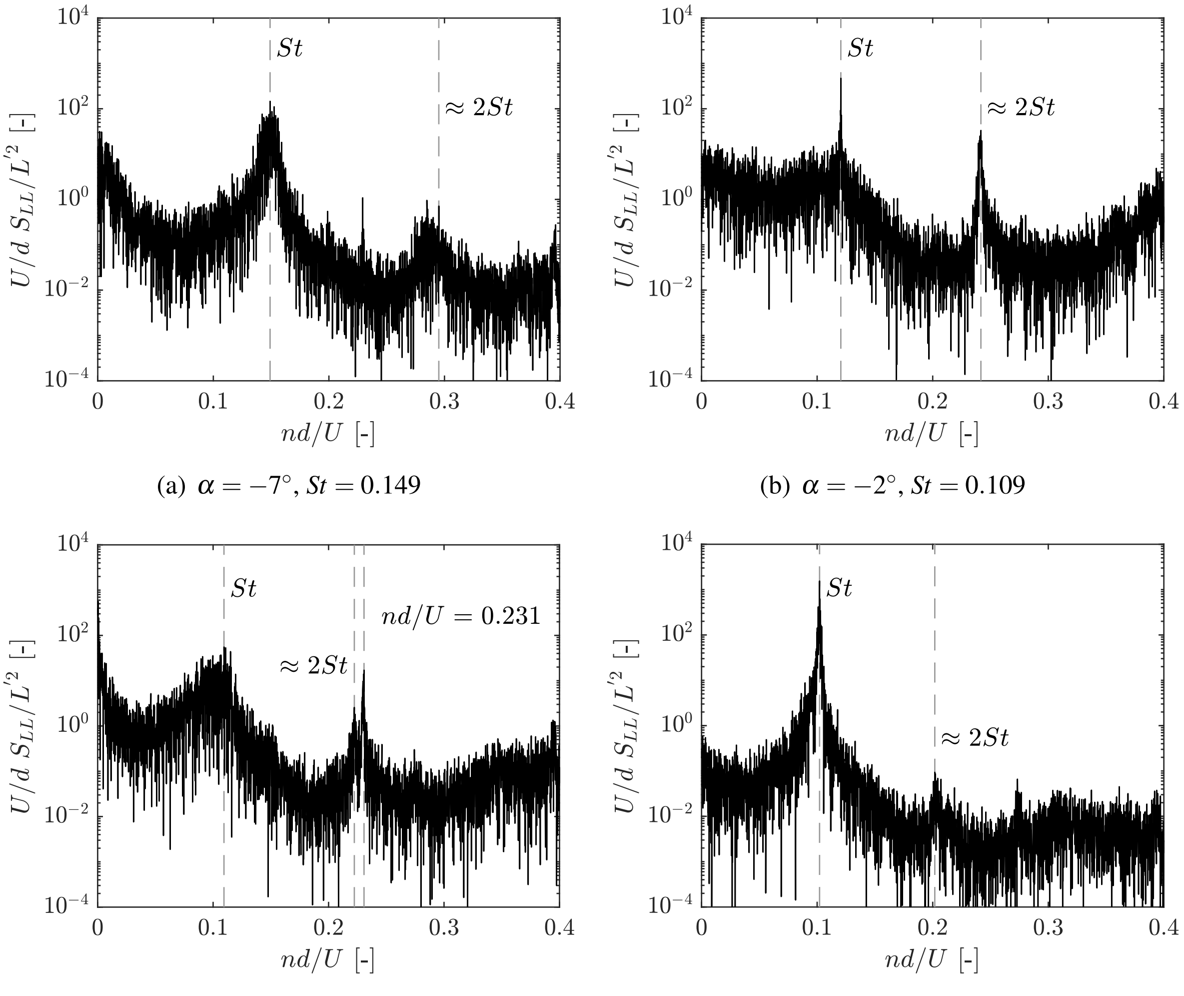

(a) $\alpha = -7°$, $St = 0.149$

(b) $\alpha = -2°$, $St = 0.109$

(c) $\alpha = 0°$, $St = 0.105$

(d) $\alpha = 4°$, $St = 0.102$

Fig. 4.11: Normalized power spectral density of fluctuation lift at various α of the bridge deck model, $Re = 2.0 \cdot 10^4$.

quite similar, except for $\alpha = -7°$ the dominant peak is less sharp. At $\alpha = -2°$, the Strouhal frequency peak is clear but the corresponding frequency band is rather narrow. Therefore, the calculated C_{L0} is quite low (see Fig. 4.10 (b)). At $\alpha = 0°$, the Strouhal frequency peak is less prominent. On the other hand, for nd/U slightly higher than $2St$, one can find a peak at $nd/U = 0.231$. A careful analysis shows this peak roughly corresponds to the super-harmonic of order two of a vortex shedding frequency of $St = 0.114$, which dominates for higher Reynolds number at $\alpha = 0°$ (see Fig. 4.10 (a)).

As for the 2:1 rectangular cylinder, new measurements particularly for the C_{L0}-Re relationship were carried out for this bridge deck model at its $\alpha = 4°$. Fig. 4.12 shows a agreement between the new and old results. Unfortunately, for $6 \cdot 10^4 < Re < 8 \cdot 10^4$, the new measured C_{L0} seems to be influenced by the super-harmonic resonance of order two of the vortex shedding frequency, as exemplified by the normalized spectra in Fig. 4.13. No higher wind speed was reached due to the limitation of the wind tunnel facility. Nevertheless, a constant trend of C_{L0} is found for $4.5 \cdot 10^4 \leq Re \leq 6 \cdot 10^4$. Finally, it is interesting to note that, for this bridge deck model, this super-harmonic resonance occurs with an order of two of n_{st}, while for the rectangular this is with an order of three of n_{st}.

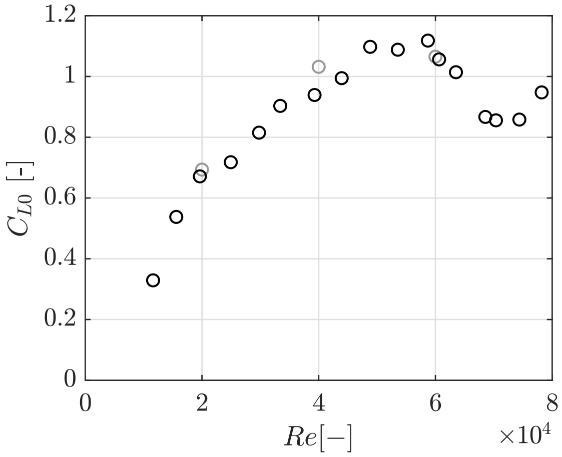

Fig. 4.12: Effect of Re on evaluated C_{L0} at $\alpha = 4°$ of the bridge deck model. Gray points denotes the old results (the ones reported in Fig. 4.10 (b)).

Comparison of the three wind tunnel models

In Fig. 4.14 the static results of the three sectional models are compared. Besides the positive shift of the local maximal C_D, the range of α, featuring a negative slope of C_L, is also positively shifted for the trapezoidal cylinder and the bridge deck model. This range is about $-7°$ to $7°$ for the rectangular cylinder, while they are $-6°$ to $10°$ and $-5°$ to $12°$ for the other two models. Moreover, the differences between the maximal C_L and minimal C_L are 2.25, 2.11 and 2.53, respectively for the three models.

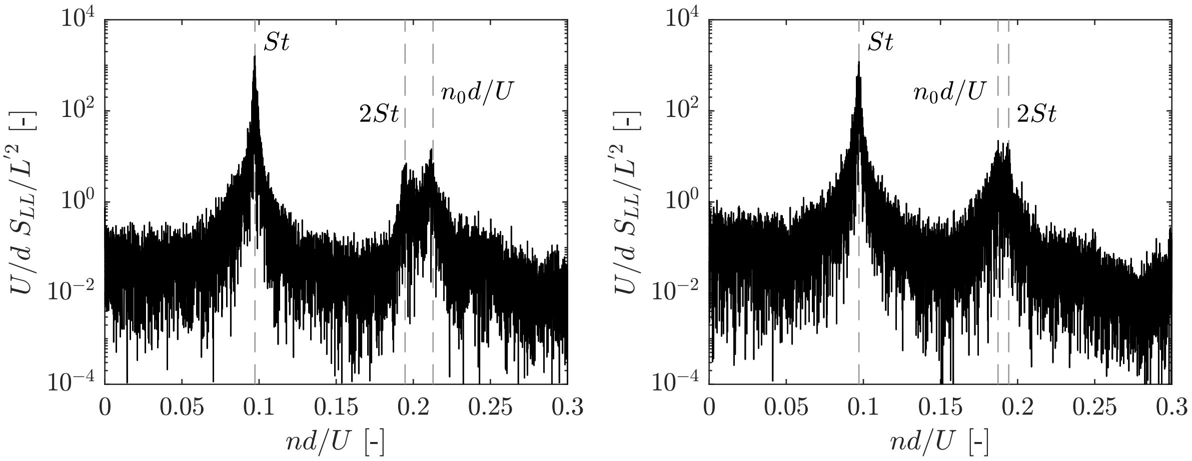

(a) $Re = 6.1 \cdot 10^4$ (b) $Re = 6.9 \cdot 10^4$

Fig. 4.13: Power spectral density of fluctuation lift at $\alpha = 4°$ of the bridge deck model, Reynolds number corresponding to Fig. 4.12.

Around $\alpha = 0°$, the other two models feature a higher *St* than the rectangular cylinder. However, if b_{avg} is considered as the streamwise dimension (b_{avg}, the averaged value of top and bottom width of a cross section), the side ratio b_{avg}/d will be lower for the trapezoidal cylinder and the bridge deck model (b_{avg}/d = 1.73 and 1.62, respectively). Therefore, the increase of *St* for these two models is understandable, referring to the *St* variation with b/d on rectangular cross sections (see, e.g., Shimada & Ishihara (2002)).

For all these three models, a connection is seemingly held between the magnitude of C_{L0} and the $C_L - \alpha$ curve: the local maximum of C_{L0} appears at a flow incidence, which roughly corresponds to the middle of the α range limited by maximal C_L and minimal C_L (check Fig. 4.14 (b) and (d)). Such a characteristic can be also found for the angle cross sections (Slater 1969), as well as for two trapezoidal cross sections and a triangle cross section (Luo & al. 1994). However, according to the author's knowledge, a convincing explanation for this connection is still absent. Finally, all the three models have shown the dependence of C_{L0} on *Re*, around the wind angle of attack where the local maximal C_{L0} appears (see Fig. 4.4 (b), Fig. 4.8 (b) and Fig. 4.10 (b)).

4.1.2 In Turbulent Flow

Static tests in turbulent flow are mainly considered for the 2:1 rectangular cylinder and the bridge deck model. As already stated in Section 3.3.3, the grid-generated turbulent flow features an integral length in the same order of the heights of the sectional models. Small-scale turbulence is called here, as opposed to the large-scale turbulent flow (e.g., $L_u > 20d$) which is a situation for bridge decks in natural wind field. In particular, steady drag and lift coefficients at *Re* = 5.8-6.0·10^4 were presented, while for *St* and $C_{lat,0}$ the results of *Re* = 1.9-2.0·10^4 were

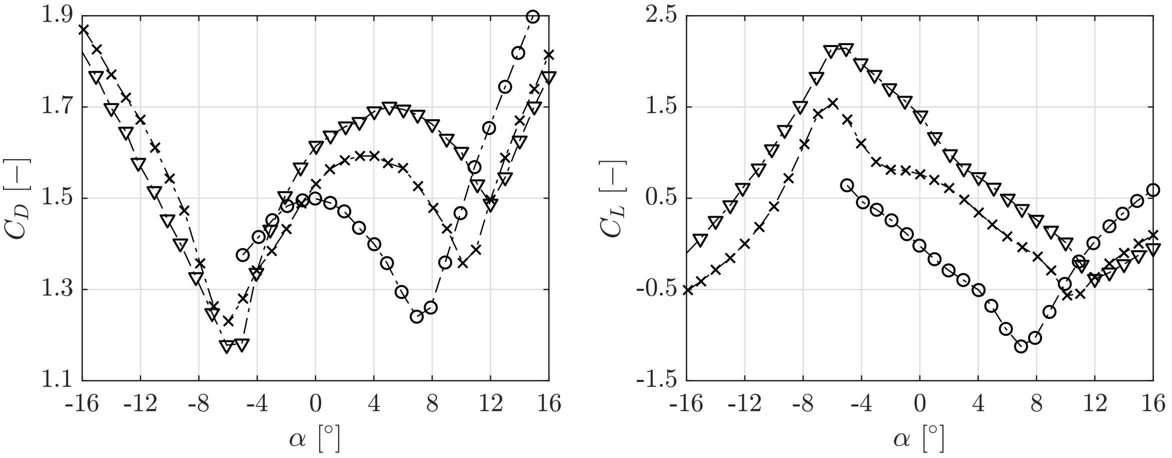

(a) C_D

(b) C_L

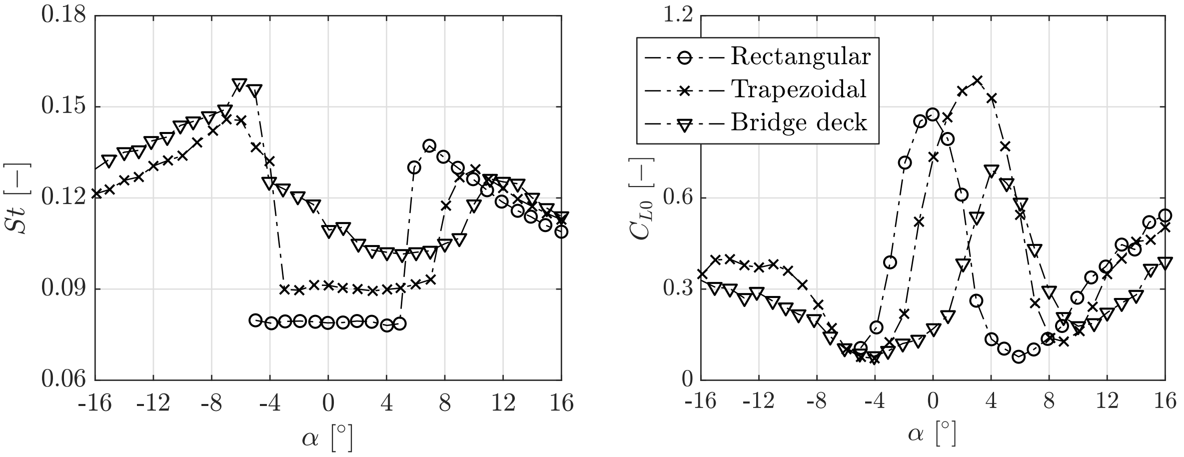

(c) St

(d) C_{L0}

Fig. 4.14: Comparison of the static results of the three sectional models ($Re = 6.0 \cdot 10^4$ for C_D and C_L, $Re = 2.0 \cdot 10^4$ for St and C_{L0}).

given. For the static setup, the dynamic amplification effect is rather limited at Re = 1.9-2.0·10^4, so that no correction was made to the $C_{lat,0}$ coefficient. C_{L0} is not used here anymore, because its “sinusoidal equivalent” concept is less meaningful for the broad-band characteristics of vortex shedding in turbulent flow. Finally, results in smooth flow are included for comparison.

Rectangular cylinder

The 2:1 rectangular cylinder was first tested, being its aerodynamic properties dramatically varied in this small-scale turbulent flow (see Fig. 4.15). For C_D, the hump characteristic around $\alpha = 0°$ is invisible any more in turbulent flow. Instead, C_D exhibits the minimum at $\alpha = 0°$. The effect of varying I_u from 9.2% to 14.9% is not apparent for C_D. In contrast, C_L is very sensitive to this variation, although the difference between smooth and turbulent flow is already apparent. For $I_u = 9.2\%$, a negative slope of C_L is still visible around $\alpha = 0°$, but much flatter than that in smooth flow. Moreover, the α range featuring a negative slope of C_L also gets narrower. Further increase of I_u makes this slope tend to zero and finally becomes positive at I_u = 14.9%.

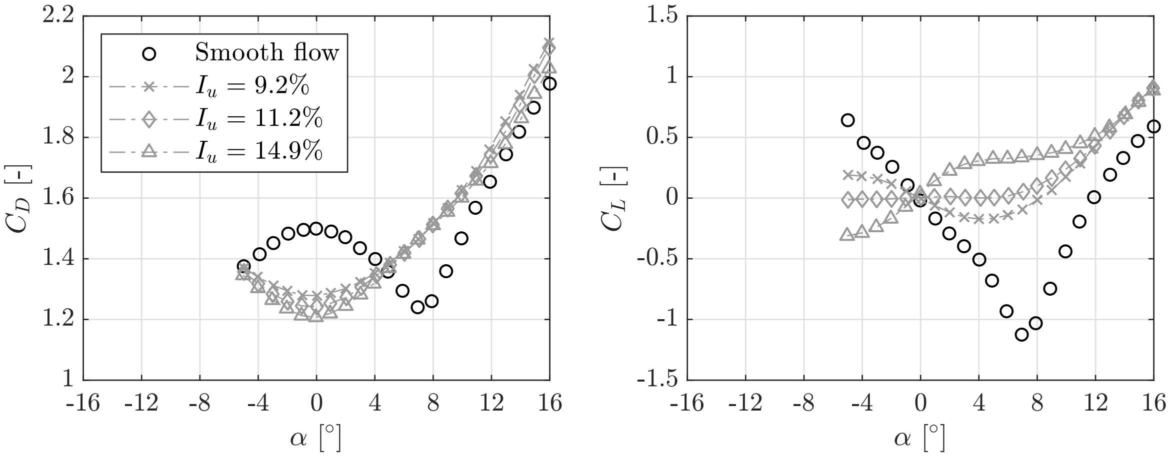

(a) C_D

(b) C_L

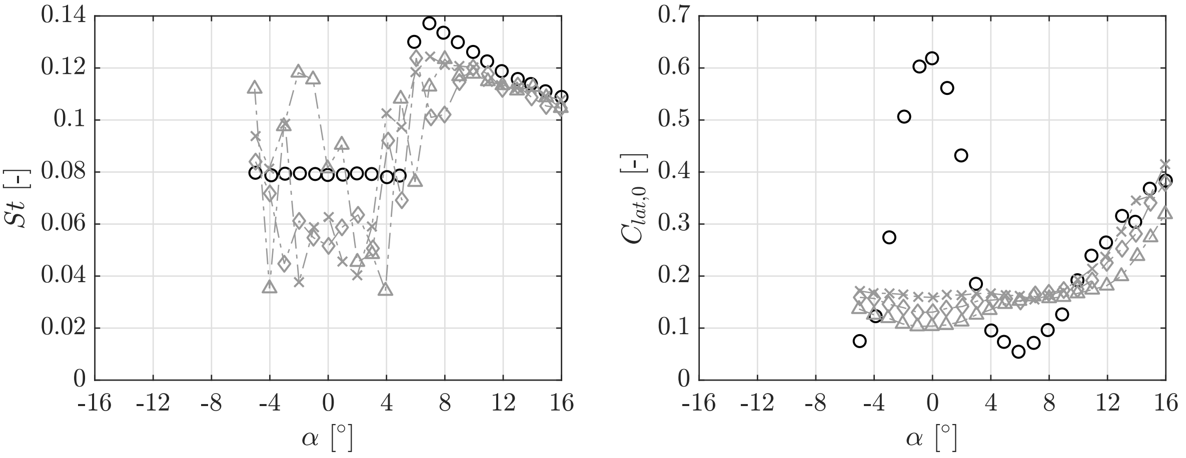

(c) St

(d) $C_{lat,0}$

Fig. 4.15: Turbulence's effect on the aerodynamic coefficients of the 2:1 rectangular cylinder. Subplots share the same legend.

The small-scale turbulence brings also pronounced effects on St and $C_{lat,0}$ (see Fig. 4.15 (c) and (d)). Around $\alpha = 0°$, the identified St is highly disordered, and $C_{lat,0}$ decreases apparently. Moreover, the characteristic of a local maximal $C_{lat,0}$ around $\alpha = 0°$ completely disappears in turbulent flow. These results show a consistency with the fact that the incoming turbulence is able to suppress the unsteady lift due to vortex-shedding and leads to less periodical shedding process. Two examples of power spectral density of fluctuation lift, respectively for $I_u = 9.2\%$ and $I_u = 14.9\%$, are given in Fig. 4.16. One can clearly see the "explosion" of vortex shedding force on the nd/U axis. For $I_u = 9.2\%$, it is still able to observe a concentration of energy around $nd/U = 0.05$. But for $I_u = 14.9\%$, such a feature becomes unapparent. A dominant Strouhal frequency peak is therefore hard to identify and of many uncertainties (corresponding to the highly disordered *St* in Fig. 4.15 (c)). In contrast, for $\alpha > 10°$, the $C_{lat,0}$ coefficient gets recovered and *St* is comparable to the counterpart in smooth flow.

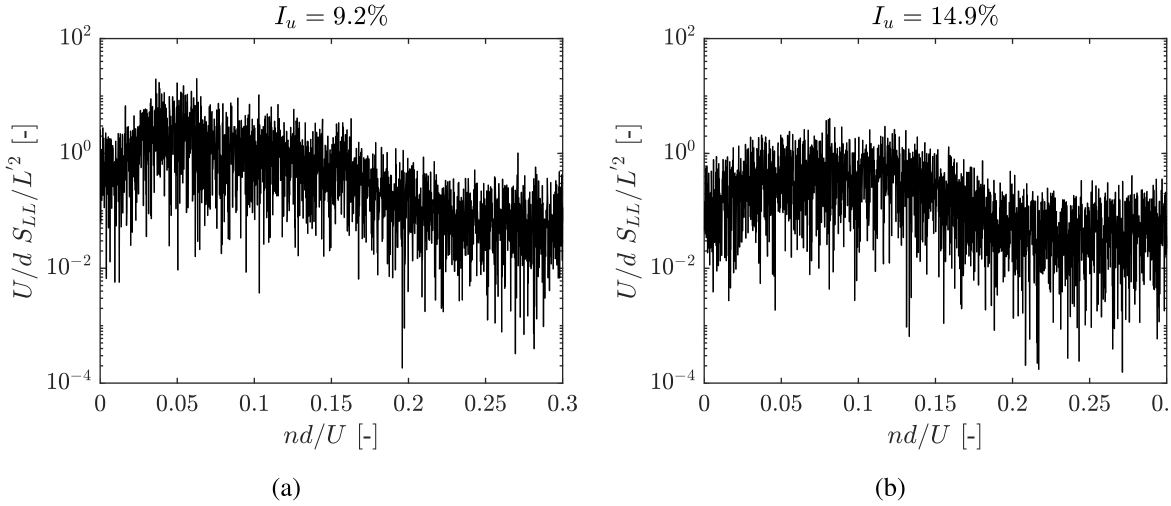

(a) (b)

Fig. 4.16: Normalized power spectral density of fluctuation lift for the 2:1 rectangular cylinder in turbulent flow ($\alpha = 0°$, $Re = 1.9 \cdot 10^4$).

A comparison of C_{Fy} with Laneville (1973)'s results is presented in Fig. 4.17, for two levels of I_u. It needs to first mention that the L_u/d ratios are quite different between the two sets of tests. Nevertheless, an important agreement is achieved: the positive slope of C_{Fy} around $\alpha = 0°$ disappears at a turbulence intensity I_u = 9%-12% for the two sets of results (comparing Fig. 4.17 (a) and (b)). In addition, the agreement in Fig. 4.17 is fairly good, despite that the

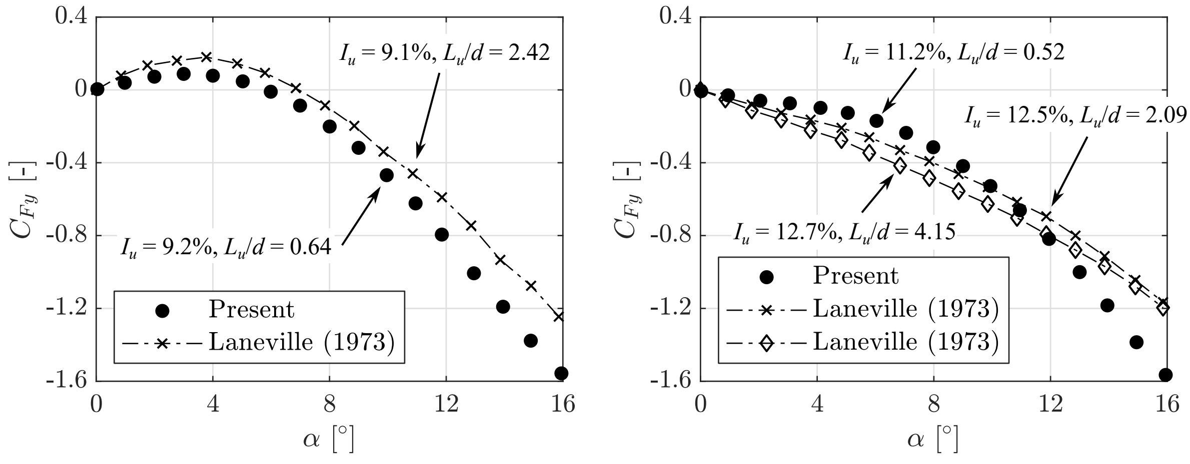

(a) (b)

Fig. 4.17: Comparison of the presented results with data collected from Laneville (1973), with respect to the C_{Fy} coefficient of the 2:1 rectangular cylinder in turbulent flow. The specific values of turbulence intensity and integral length are additionally indicated by arrows. $Re = 6.0 \cdot 10^4$ for the presented results, and $Re = 1.5 - 1.6 \cdot 10^4$ for ones of Laneville (1973) (extra indicated in Mannini & al. (2014)).

L_u/d ratio for Laneville (1973)'s results is about 4 times the presented ones. In fact, in a series of works of Laneville (Laneville & al. 1977; Laneville & Parkinson 1971; Laneville 1973), it has been claimed that the turbulence integral length plays a minor role in the transverse galloping instability for their investigated 1:2, 1:1 and 2:1 rectangular cylinders. The presented results seem to support this conclusion. In contrast, a recent investigation shows that the integral length plays also an important role and its effect may be non-monotonic (Mannini & al. 2018b). There, although the L_u/d ratio has reached at about 8, it is still not enough for bridge decks in reality (for a 5 m high bridge deck, the L_u/d could be more than 20 in natural wind filed). An effort to clarify the integral length effect, covering a wide range of L_u/d, is definitely of great needs. Finally, Bokaian & Geoola (1983) reported that, in a turbulent flow with $I_u = 6.5\%$, the rectangular cylinders with $b/d = 2-2.75$ characterize with disorganized vortex shedding and no Strouhal number was identified. In contrast, for rectangular cylinders with b/d out of this range, the Strouhal number is clearly identifiable. Their results were obtained in water tunnel and no galloping instability was found for this turbulence intensity.

Bridge deck model

In Fig. 4.18, effects of incident turbulence were presented for the bridge deck model. For $I_u = 14.9\%$, the minimal C_D moves to $\alpha = 0°$, while for $I_u = 9.2\%$ the tendency of a maximal C_D around $\alpha = 4°$ can be still found. From the C_L - α plot, up to I_u = 14.9%, one can find the bridge deck model still suffers from the possibility of galloping instability due to the presence of negative slope of C_L. In fact, a galloping factor $A_1 = 5.23$ is evaluated at $\alpha = 4°$ for $I_u = 14.9\%$, which is higher than $A_1 = 4.17$ at the same flow incidence but in smooth flow. Nevertheless, the shrinkage of α range for negative slope of C_L is apparent in turbulent flow.

The identification of St is also difficult for the bridge deck model (examples of S_{LL} were given in Fig. 4.19). Nevertheless, in the range $-4° < \alpha < 6°$, a decrease of St in turbulent flow is apparent (Fig. 4.18 (c)). Interesting is the $C_{lat,0}$ coefficient. For the bridge deck model in turbulent flow with $I_u = 9.2\%$ and $I_u = 11.2\%$, one can still find a maximal $C_{lat,0}$ localizing around $\alpha = 4°$ (Fig. 4.18 (d)). Compared with the results in smooth flow, the strength apparently get decreased, but the corresponding α almost remains.

Compared with the 2:1 rectangular cylinder, it is found the bridge deck model shows a stronger tendency to galloping instability in turbulent flow, being the C_L-α curve characterized with a pronounced negative slope up to $I_u = 14.9\%$. Taking the aforementioned b_{avg}/d ratio, this bridge deck model with $b_{avg}/d = 1.62$ behaves actually closer to a 3:2 rectangular cylinder reported by Mannini & al. (2018b), which is also unstable in a comparable small-scale turbulent flow (up to $I_u = 15.9\%$, and $L_u/d = 0.4$). Moreover, the vortex shedding force coefficient $C_{lat,0}$ was found also stronger for this bridge deck model in turbulent flow, maintaining at the same time the hump characteristic of $C_{lat,0}$ around $\alpha = 4°$ (especially for I_u = 9.2%-11.2%). It is worth

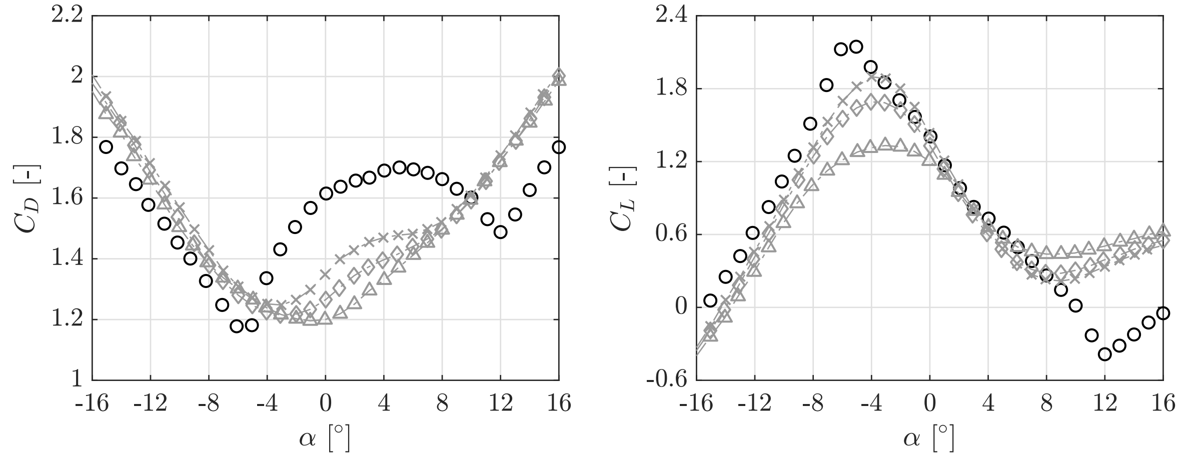

(a) C_D (b) C_L

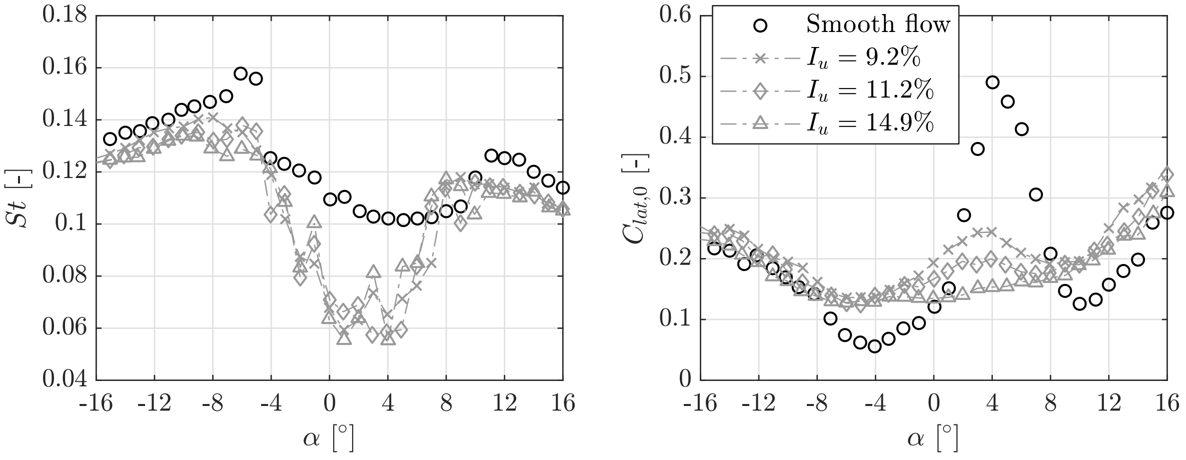

(c) St (d) $C_{lat,0}$

Fig. 4.18: Turbulence's effect on the aerodynamic coefficients of the bridge deck model. Subplots share the same legend.

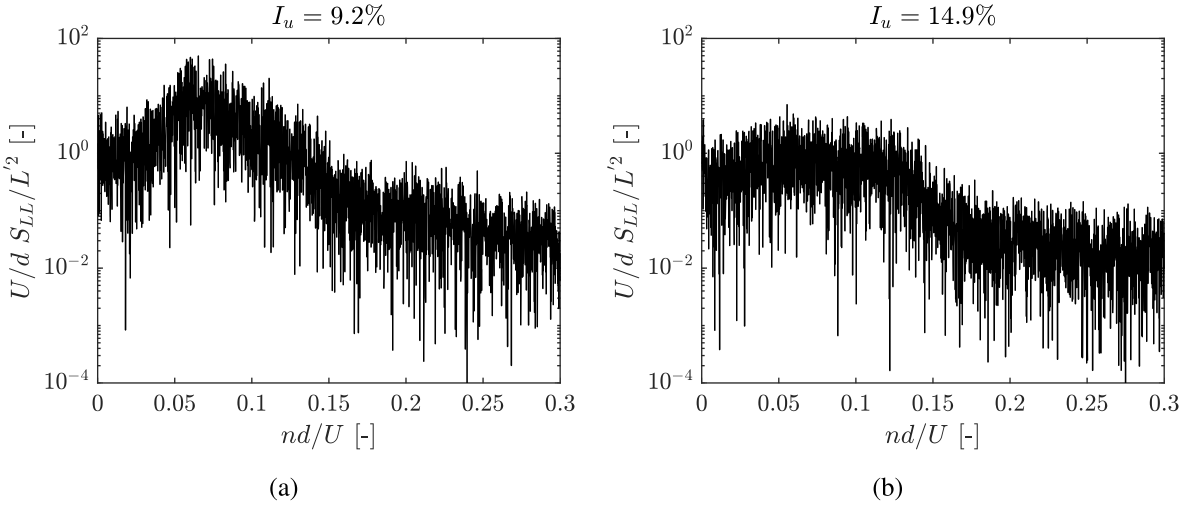

(a) (b)

Fig. 4.19: Normalized power spectral density of fluctuation lift for the bridge deck model in turbulent flow ($\alpha = 4°$, $Re = 1.9 \cdot 10^4$).

reminding that, in smooth flow, the magnitude of the strongest vortex shedding force for the bridge deck model is lower than the 2:1 rectangular cylinder at the same *Re* (see Fig. 4.14 (d)). Comparing Fig. 4.16 and Fig. 4.19, one can also find the energy of vortex shedding force is more concentrated for the bridge deck model, especially for $I_u = 9.2\%$.

4.2 Aeroelastic Results

4.2.1 Effect of Mean Flow Incidences

Aeroelastic tests for the three wind tunnel models started with investigation of the effect of mean wind angle of attack α_0 (here, α_0 is particularly used to indicate the “mean” concept for an oscillation model). The test cases are summarized in Tab. 4.2, where a very low *Sc* was considered to fully detect the possible vibration for each model at different α_0. *St* and galloping factor A_1 from static test results are also supplemented in Tab. 4.2 for prediction purpose. In reduced form, the critical velocity for VIV (Kármán-vortex resonance) is

$$V_r = \frac{1}{2\pi St} \tag{4.5}$$

And the critical velocity of galloping according to QS theory is

$$V_g = \frac{Sc}{\pi A_1} \tag{4.6}$$

with the Scruton number defined as $Sc = 4\pi M_e \zeta_0/(\rho d^2 l_e)$, being M_e the effective oscillation mass of wind tunnel model. Since the considered *Sc* is very small, the calculated V_g is always lower than V_r, as shown by the last column in Tab. 4.2.

Fig. 4.20 shows the aeroelastic results, in terms of amplitude-velocity plot ($\sqrt{2}y_{rms}/d$ *vs.* V). From the results, it can be found that the QS prediction is inaccurate for such low *Sc*, being no galloping type oscillation found for $V < V_r$. The velocity-restricted oscillation occurring for $V < 1$ is due to the “motion-induced vortex exciting” mechanism, which corresponds to a higher vortex shedding mode (see, e.g., Mannini & al. (2016b)). For the rectangular cylinder at α_0 = 0°-3°, the trapezoidal cylinder at α_0 = 0°-3° and the bridge deck model at α_0 = 2°-4°, galloping was found initiated at V_r, as typical for the unsteady galloping due to interaction with VIV.

On the other hand, for the rectangular cylinder at $\alpha_0 = 5°$, the trapezoidal cylinder at $\alpha_0 = -4°$ and the bridge deck model at α_0 = −2°- 0°, galloping clearly started at a reduced velocity higher than V_r. For the bridge deck model at $\alpha_0 = -4°$, galloping was not observed for V up to about 5. Clearly, these cases are essentially different from the typical unsteady galloping cases, although

Tab. 4.2: Characteristics of aeroelastic test cases for the investigation of the effect of the mean wind angle of attack α_0. Galloping factor A_1 was evaluated according to Den Hartog criterion within $[\alpha_0 - 1^\circ, \alpha_0 + 1^\circ]$, with C_D and C_L data of $Re \approx 6 \cdot 10^4$. St of $Re \approx 2 \cdot 10^4$ is given here.

Sectional model	α_0 [deg]	Static results		Aeroelastic test cases							
		St [-]	A_1 [-]	M_e [kg]	n_0 [-]	ρ [-]	ζ_0 [%]	Sc [-]	V_r [-]	V_g [-]	V_g/V_r [-]
Rectangular cylinder	0	0.079	6.78	4.35	7.64	1.19	0.052	5.1	2.02	0.24	0.12
	3	0.079	4.54			1.20	0.045	4.4	2.01	0.31	0.15
	5	0.079	11.6			1.20	0.044	4.3	2.02	0.12	0.06
Trapezoidal cylinder	-4	0.132	12.1	3.88	9.27	1.13	0.074	6.8	1.20	0.18	0.15
	0	0.091	1.50			1.15	0.075	6.8	1.75	1.44	0.83
	3	0.089	5.96			1.17	0.070	6.3	1.78	0.33	0.19
Bridge deck model	-4	0.125	7.28	3.60	9.63	1.20	0.076	6.1	1.27	0.27	0.21
	-2	0.121	6.30			1.19	0.079	6.4	1.32	0.33	0.25
	0	0.109	9.43			1.17	0.083	6.9	1.45	0.23	0.16
	2	0.105	8.25			1.20	0.074	6.0	1.52	0.23	0.15
	4	0.102	4.17			1.19	0.067	5.5	1.56	0.42	0.27

they also feature a V_g much lower than V_r (see Tab. 4.2). In contrast, they should belong to the previously defined *atypical unsteady galloping* (see Fig. 2.18 in Section 2.2.1). From the many investigations devoted to rectangular cylinders with one face perpendicular to the incoming flow (e.g., Parkinson & Brooks (1961), Santosham (1966), Wawzonek (1979),Mannini & al. (2014)), it is easy to be preconceived that the galloping will be initiated at the V_r for $V_g/V_r < 1$, as the typical unsteady galloping behavior. However, the presented results indicate that the α_0 plays also a very important role. This may be particularly vital for bridge decks, since their flow incidences are rather limited around $\alpha_0 = 0^\circ$ in full-scale. Therefore, applying the experiences on rectangular cylinders to bridge decks needs to be cautious about the role played by α_0.

It is interesting right now to have a look at the C_{L0} coefficient re-given in Fig. 4.20 (d). One can find that the test cases characterized with typical unsteady galloping in Fig. 4.20 all features a relatively high C_{L0} coefficient, while the *atypical unsteady galloping* occurs at a flow incidence of considerably low C_{L0} coefficient. Moreover, for the rectangular cylinder at $\alpha_0 = 0^\circ$, trapezoidal cylinder at $\alpha_0 = 3^\circ$ and bridge deck model at $\alpha_0 = 4^\circ$, their C_{L0} coefficients correspond to a local maximum in Fig. 4.20 (d), and their oscillation amplitudes tend to be the largest ones at high V as shown in Fig. 4.20 (a)-(c). Although it may be less suitable to use the static test results to explain the aeroelastic phenomena because the fluid-structure interaction is not fully reflected on the stationary model, it is quite intuitive to relate the strength of vortex shedding force to the unsteady galloping due to interaction with VIV. Especially, such a regularity was

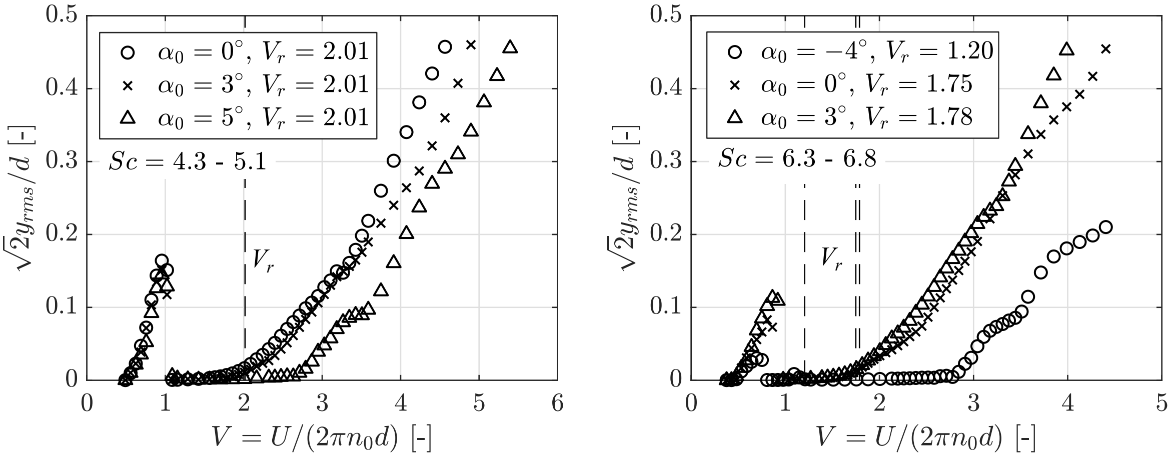

(a) Rectangular cylinder (b) Tra[pezoidal cylinder

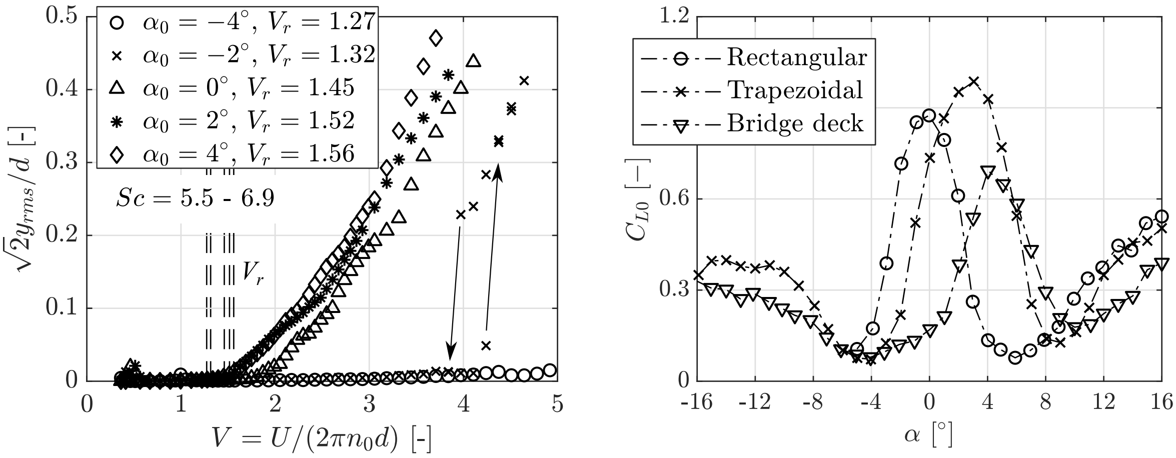

(c) Bridge deck model (d) C_{L0} for three models

Fig. 4.20: Effect of mean flow incidence on the aeroealstic behaviors of the three models, considering only a very low Sc. Dashed line indicate the position of V_r, and V_g is always lower than V_r (see last column of Tab. 4.2). Arrows indicates a sudden change of amplitude. Subplot (d) is extra given here for a convenience of discussion (reproduced from Fig. 4.14 (d)).

observed for all the three wind tunnel models. Therefore, for structures potentially suffering from unsteady galloping problem at low Sc, the wind angle of attack featuring high C_{L0} should be paid particular attentions to.

4.2.2 Effect of Scruton Number

Effect of Sc was then investigated for the three sectional models. Besides the null mean wind angle of attack, attention was also paid to $\alpha_0 = 3°$ for the trapezoidal cylinder and $\alpha_0 = 4°$ for the bridge deck model. For convenience, the classifications for typical unsteady galloping due to interaction with VIV, according to Mannini & al. (2014, 2016b) for a 3:2 rectangular cylinder, are first given here from low Sc to high Sc (although already mentioned in Section 2.2.1):

- Full-Interference. Galloping arises at V_r, presenting a unrestricted and monotonic increase of the post-critical amplitude.
- Partial-Interference. Separation of VIV and galloping can be observed (emergence of VIV peak amplitude), but the galloping-type oscillation is directly connected to the end of VIV region. For the stability about equilibrium position, galloping onset is still deemed at V_r.
- Low-Interference. Clearly separated VIV and galloping behaviors can be observed, but the onset wind speed of galloping is lower than the QS-prediction V_g.

Above three categories are clearly reflected in Fig. 2.16 (a)-(c), as well as Fig. 1.1 (b). Moreover, a new class is defined here due to observations on the square cylinder (see, e.g, Fig.2.15)

- Pre-Separation. Continuously increasing wind speed results in similar post-critical amplitude as the "Full-Interference". However, a second stable amplitude branch can be found in the post-critical region, by giving initial displacement condition from rest.

Rectangular cylinder

Tab. 4.3 lists the test cases for the rectangular cylinder at $\alpha_0 = 0°$, with the Scruton number varied from $Sc = 5.1$, with small-step increment, to $Sc = 200.7$. Correspondingly, the V_g/V_r ratios range from 0.12 to 4.67. Velocity-amplitude results are shown in Fig. 4.21 and Fig. 4.22, where Fig. 4.21 presents an overview of all the test cases and Fig. 4.22 gives them in detail. The varying of Sc in small-step reveals complex dynamic responses for this cylinder, especially for the medium Sc range. In general, the phenomena shown in Fig. 4.21 are consistent with the 3:2 rectangular cylinder reported by Mannini & al. (2016b).

For $Sc \leq 107.1$, the threshold of galloping was found always fixed at V_r (corresponding to V_g/V_r up to 2.5). The amplitude-velocity curve shows a monotonic increase, in a unrestricted manner. In Fig. 4.22 (a), where the results of $Sc = 5.1$ and $Sc = 107.1$ are particularly given, it is interesting to note that the amplitude slopes are almost the same for $V < 3.5$ ($V/V_r < 1.75$ and $\sqrt{2}y_{rms}/d < 0.2$). During the wind tunnel tests, several attempts, namely manually stopping the oscillation model then releasing it from rest, have been carried out for the post-critical range, and no second amplitude branch was found. These characteristics correspond to the classification "Full-Interference". Finally, for the presented results, it is to note that the Strouhal frequency peak n_{st} is invisible in the power spectral density of y for $V > V_r$.

For a slightly higher Scruton number $Sc = 127.9$ (Fig. 4.22 (b)), continuously increasing V without manually stopping the oscillation model will result in a amplitude-velocity curve similar to the "Full-Interference" cases. However, a second medium-amplitude branch was revealed at about $V = 4.4$, by manually stopping the oscillation model and then releasing it from rest (indicated in Fig. 4.22 (b)). The velocity range for this branch is rather limited, and either

Tab. 4.3: Characteristics of aeroelastic test cases for the rectangular cylinder at $\alpha_0 = 0°$, with various values of Sc.

Static results		Aeroelastic test cases								
St [-]	A_1 [-]	Config.	M_e [kg]	n_0 [-]	ρ [-]	ζ_0 [%]	Sc [-]	V_r [-]	V_g [-]	V_g/V_r [-]
0.079	6.78	#R0-0	4.35	7.64	1.19	0.052	5.1	2.02	0.24	0.12
		#R0-1			1.20	0.135	13.3		0.62	0.31
		#R0-2			1.18	0.291	29.0		1.36	0.68
		#R0-3			1.17	0.458	46.2		2.17	1.07
		#R0-4			1.16	0.625	63.2		2.97	1.47
		#R0-5			1.18	0.794	79.3		3.72	1.85
		#R0-6			1.18	0.934	93.4		4.39	2.17
		#R0-7			1.19	1.079	107.1		5.03	2.49
		#R0-8			1.18	1.279	127.9		6.00	2.98
		#R0-9			1.20	1.387	136.6		6.41	3.18
		#R0-10			1.18	1.464	145.9		6.85	3.40
		#R0-11			1.18	1.624	162.0		7.61	3.77
		#R0-12			1.19	1.733	171.5		8.05	3.99
		#R0-13			1.18	1.857	184.8		8.67	4.30
		#R0-14			1.19	2.020	200.7		9.42	4.67

decrease or increase of wind speed stepping out this range will lead the oscillation jump back to the high-amplitude branch. Moreover, the Strouhal frequency peak n_{st} is visible in the power spectra S_{yy} for this medium-amplitude oscillation. The existence of this branch is very probably due to the combined effect of VIV and galloping, since pure VIV response usually features a clockwise hysteresis loop while the hysteresis loop in galloping response is usually anti-clockwise (Ma & al. 2018). Nevertheless, this unsteady galloping behavior belongs to the “Pre-Separation” category, which was also observed for a square cylinder in smooth flow (Wawzonek 1979) and a 3:2 rectangular cylinder in slightly turbulent flow (Mannini & al. 2016b).

The spontaneous separation of galloping and VIV begins when Sc reaches about 136.6 (Fig. 4.22 (c)). There, one can clearly see a amplitude peak at $V \approx 3.5$, after which the further increment of velocity results in an amplitude decrease. However, this separation is just “partial”. The subsequent oscillation amplitude for $V > 3.5$ does not drop to null, but gradually increases again with the further increment of V. At about $V = 5.4$, the oscillation suddenly jumps to a high-amplitude branch. Continuously decreasing V after this jump, the oscillation can be maintained at the high-amplitude branch until about $V = 3.7$, after which the oscillation drops back to the lower amplitude branch. An anti-clockwise hysteresis loop can be observed here. Further examination of the S_{yy} power spectra indicates the appearance of n_{st} frequency peak

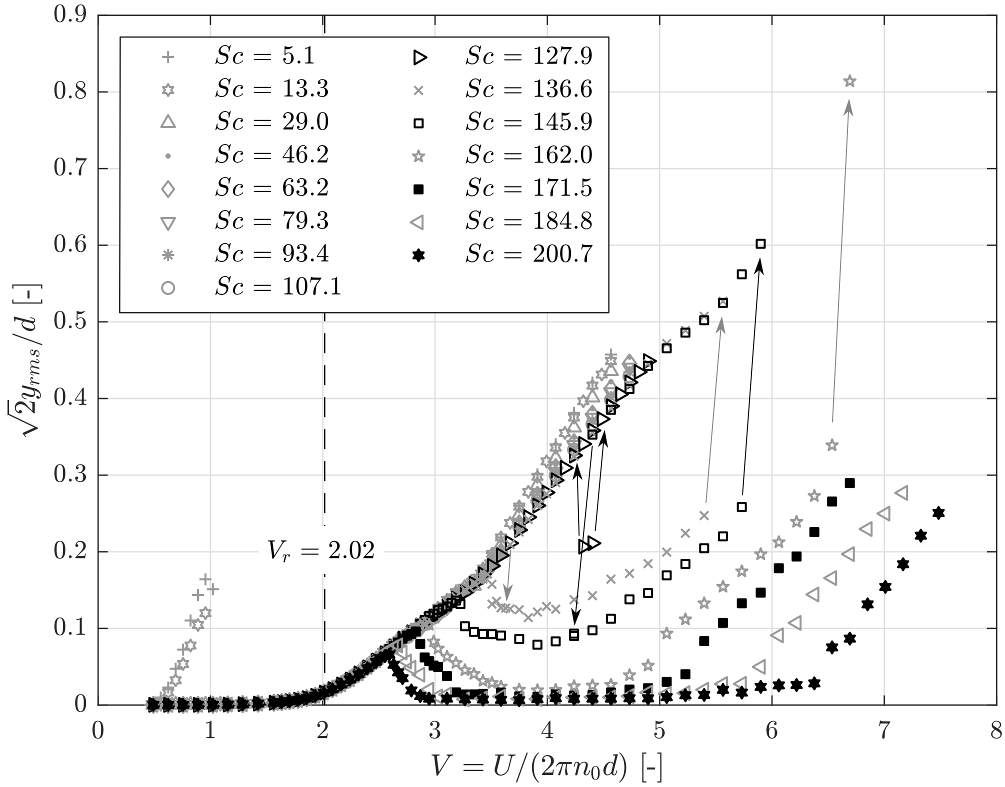

Fig. 4.21: Effect of Scruton number on the across-wind response of the 2:1 rectangular cylinder. Arrows indicates a sudden change of amplitude.

immediately after the separation point at $V \approx 3.5$, but just for the low amplitude branch. From the point of view of frequency response, the vortex shedding process can be deemed decoupled from the motion of body for the low amplitude branch. However, the unsteady effect of vortex shedding on the galloping oscillation is still strong, resulting in the galloping oscillation being directly connected to the end of VIV synchronization region. Moreover, n_{st} is still invisible for the oscillation at the high amplitude branch. For $Sc = 145.9$, also shown in Fig. 4.22 (c), it is essentially the same as $Sc = 136.6$, except a lower VIV peak amplitude and a narrower hysteresis loop. These two cases belong to the "Partial-Interference" category. In this situation, the onset of galloping can be deemed still at V_r, since oscillation starts there and never dies out again.

Increasing Sc up to 162.0 (Fig. 4.22 (d)), a complete and classical VIV response can be observed, and a new galloping-type oscillation arises at $V \approx 5.0$. However, the QS-theory prediction for this case is at $V_g \approx 7.6$ so that the unsteady effect is still non-negligible. Moreover, at $V \approx 6.5$, a violent jump occurs, resulting in a doubled amplitude for that small-step velocity increment. Such a large jump was not expected during the wind tunnel tests, so that the wind tunnel was stopped immediately for safety consideration. The mini-plot inside Fig. 4.22 (d) shows the envelope of time-displacement history for this violent jump. One can find that a considerably long time is needed to cultivate this jump. Although no further measurement was carried out after this jump, it is reasonable to infer that there is hysteresis behavior around this reduced velocity.

The last three test cases, with considerably high Scruton number, all show complete VIV response and newly-arising of galloping oscillation. However, none of the observed galloping

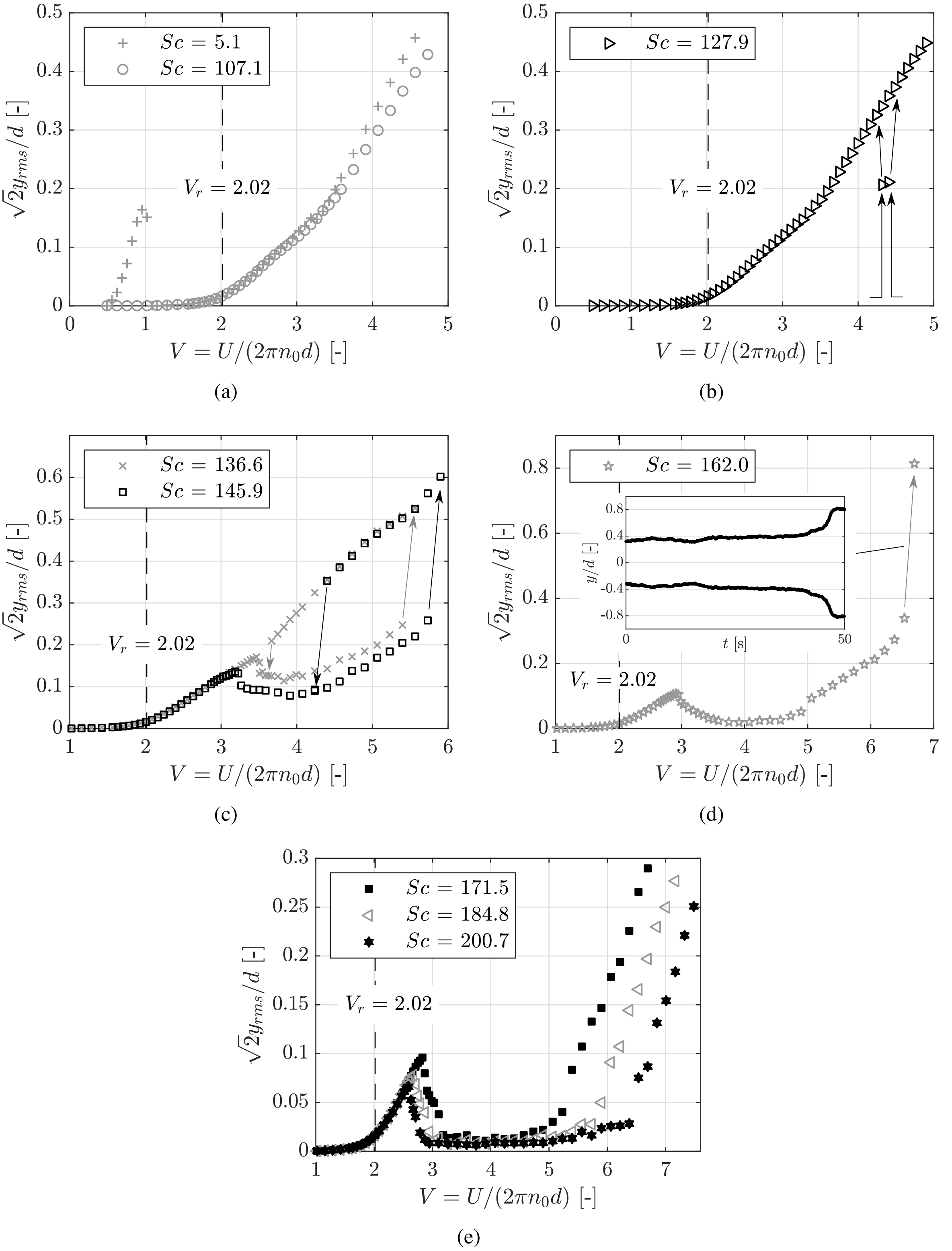

(a) (b)

(c) (d)

(e)

Fig. 4.22: Same results as in Fig. 4.21 but with divided plots for better view.

onset agrees with the QS-theory prediction, although the V_g/V_r ratio for the last case is already about 4.7. In the galloping-universal plot Fig. 4.23, the actual galloping onset is indicated at about $0.7V_g$. Together with the test case of $Sc = 162.0$, the last four test cases can be classified as "Low-Interference" cases, where separated VIV and galloping can be observed but the galloping onset is advanced to some extent by the unsteady effect. Finally, it is understandable for the 2:1 rectangular cylinder, that the QS prediction is still not applicable for Sc up to even about 200 (V_g/V_r up to 4.7). In an early work (Santosham 1966), a high reduced velocity of 5-6 times V_r was found necessary for the application of QS theory to this cylinder.

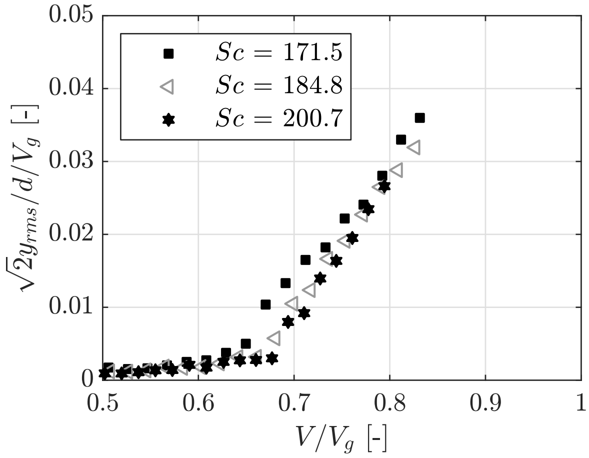

Fig. 4.23: Last three test cases (#R0-12 to #R0-14) of the 2:1 rectangular cylinder in universal plot.

The amplitude modulation phenomenon (or beat phenomenon), has been frequently observed for this 2:1 rectangular cylinder. It is particularly clear and of regularity for the "Full-Interference" cases, in a reduced velocity range about $V_r < V < 3.5$ (where the RMS-amplitude nearly does not change for varied Sc, see Fig. 4.22 (a)). Fig. 4.24 (a) and (b) show two time-history records at $V/V_r = 1.46$ respectively for $Sc = 5.1$ and $Sc = 107.1$. There, the saw-tooth envelope of the amplitude can be found for both cases. For $Sc = 5.1$, the modulation process was found clearly faster than that for $Sc = 107.1$ (compare Fig. 4.24 (a) and (b)). From the normalized power spectra for $Sc = 5.1$ (Fig. 4.24 (c)), a pitchfork shape around the natural frequency n_0 can be found. Finally, as previously mentioned, the Strouhal frequency n_{st} is invisible.

Fig. 4.24 (d) collects the frequency peaks from the power spectra S_{yy} for $Sc = 5.1$ and $Sc = 107.1$, at various reduced wind speeds. The term "1st peak" denotes the dominant peak in the spectrum, while "2nd peak" is the second strongest peak. With increase of V, the vortex shedding frequency n_{st}, which is dominant for $V < V_r$, gradually evolves into the model's main oscillation frequency, with a value slightly lower than n_0. On the other hand, for evolution of the "2nd peak" with V, the natural oscillation frequency n_0 gradually becomes the right-side peak in the spectral pitchfork during amplitude modulation phenomenon, with a value slightly higher than n_0. After the amplitude modulations disappear at higher V, the "2nd peak" becomes

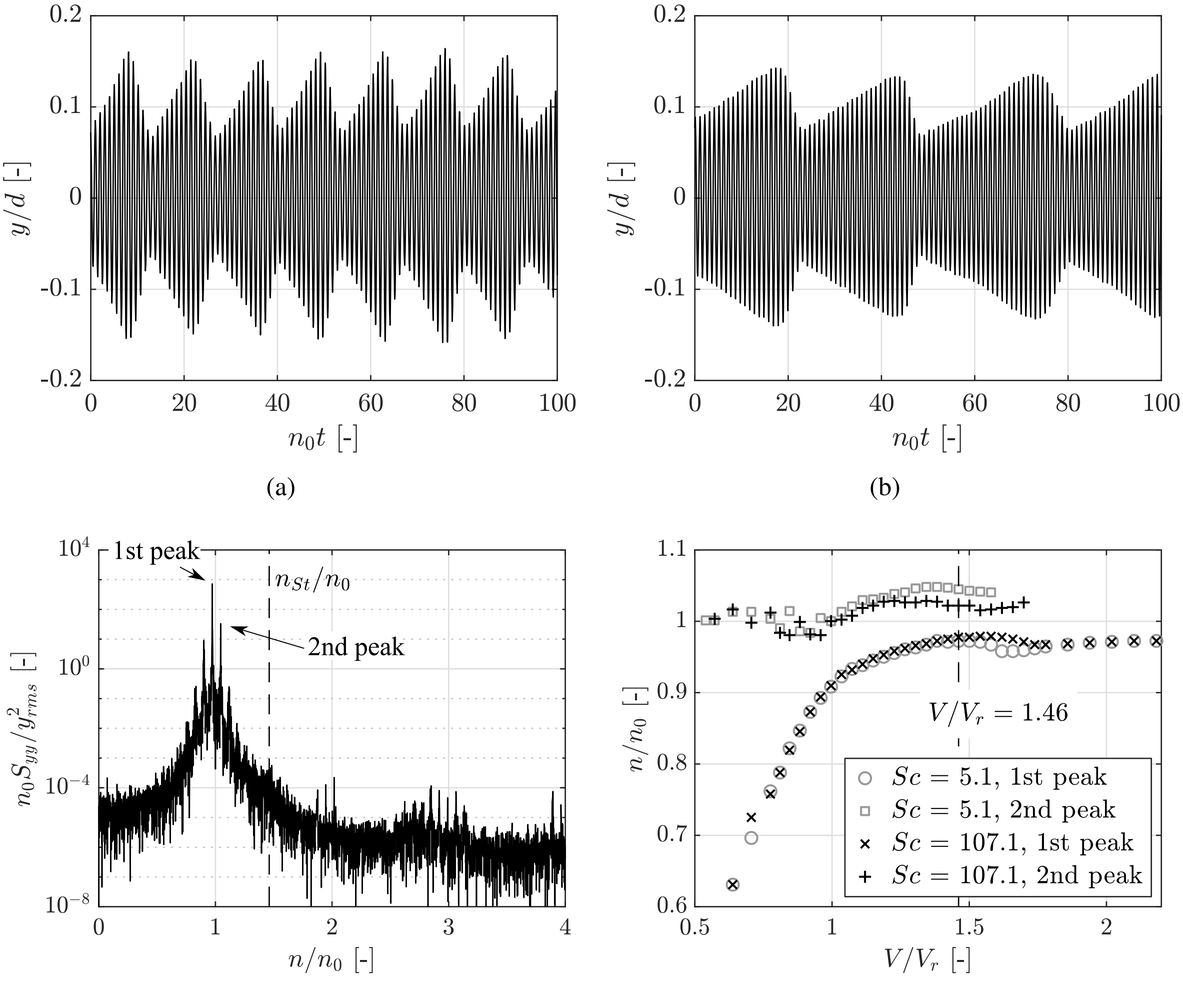

(a) (b)

(c) (d)

Fig. 4.24: Time records for test cases of $Sc = 5.1$ (a) and $Sc = 107.1$ (b) at $V/V_r = 1.46$; (c) normalized power spectral density of displacement response y for test case of $Sc = 5.1$ at $V/V_r = 1.46$; (d) collected frequency peaks at various reduced wind speeds for the two test cases, being '1st peak' the dominant peak in the spectrum and '2nd peak' the second strongest peak.

the superharmonic of order two of the '1st peak', thus not included in the plot. Similar results were also presented by Itoh & Tamura (2002) for the 2:1 rectangular cylinder. In Fig. 4.24 (d), the gap between the "1st peak" and "2nd peak" can be found smaller for $Sc = 107.1$, consistent with the longer period of amplitude modulation shown in Fig. 4.24 (b). In Santosham (1966), this frequency gap was named "modulation frequency". Finally, it is to note that the "1st peak" of the two Sc cases match perfectly again for $V/V_r > 1.75$, corresponding to the velocity range where the RMS amplitudes of the two Sc cases show clear difference (see Fig. 4.22 (a)).

Finally, some literature reports were collected to make a comparison for this 2:1 rectangular cylinder, shown in Fig. 4.25 for four different magnitudes of Scruton number. In general, the agreement between the presented results and other reports is quite good, confirming the carried-out tests. Nevertheless, some points need to be pointed out. Firstly, in Fig. 4.25 (a), one can find the amplitude slope of Santosham (1966)'s results decreases slightly around $V = 5.0$. This trend is not reached for the presented results, since the wind speed was not pushed so high. However, in Fig. 4.21, one can clearly see such a trend although that is for another Scruton number. Secondly, in Fig. 4.25 (c), all the three groups of results show two amplitude branches for V higher about 3. However, the high-amplitude branch in Yamada & Miyata (1984)'s results extended more toward to the VIV lock-in range than the presented results. Itoh & Tamura (2002)'s results are actually more different from the other two groups: for $V > 3$, the oscillation will not go to the low amplitude branch but continue to "climb" with the high amplitude branch. Finally, although not included here, Gao & Zhu (2016)'s experiments show that the "Full-Interference" behavior is maintained at least up to $Sc = 105.2$ for the 2:1 rectangular cylinder.

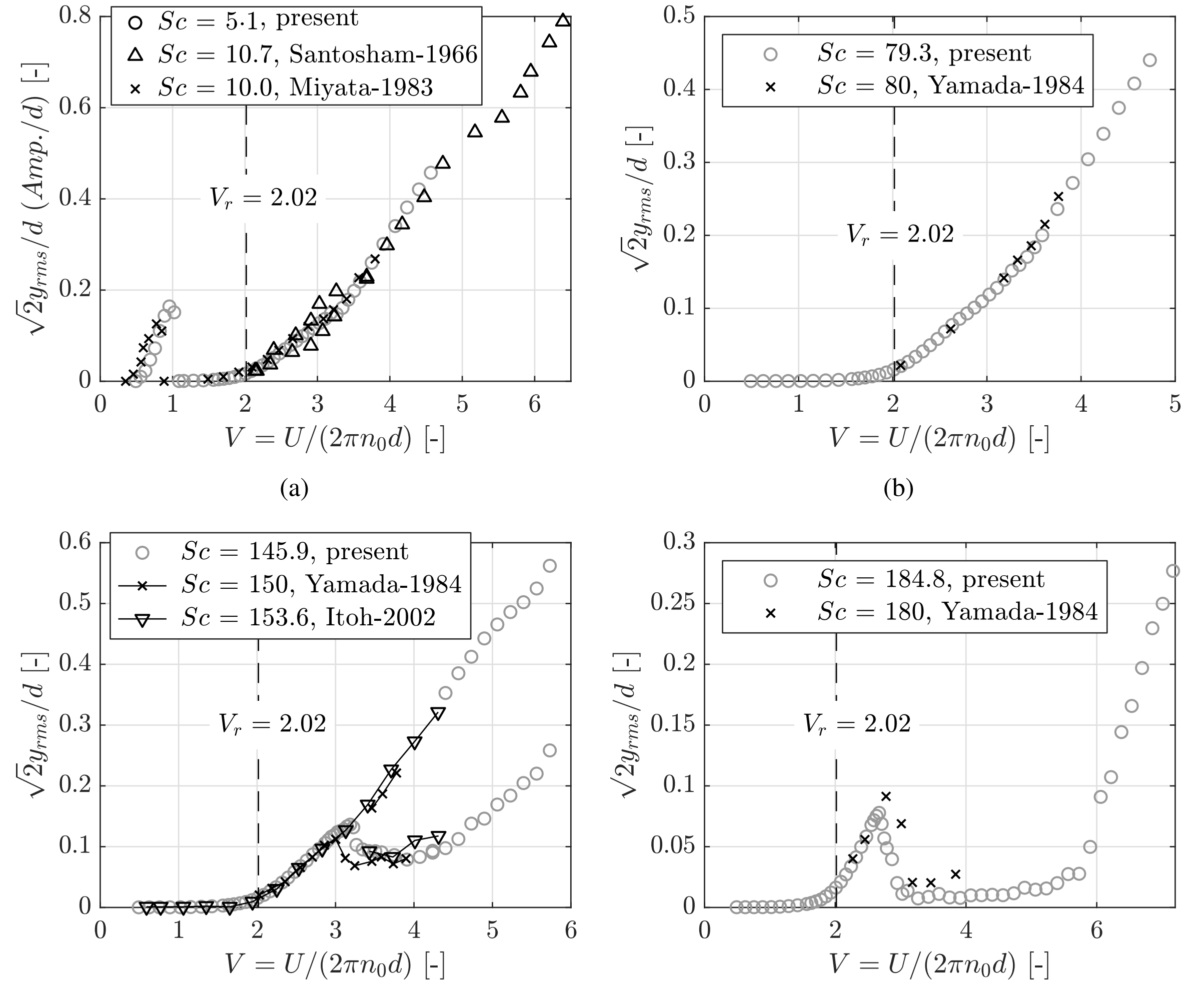

(a)

(b)

(c)

(d)

Fig. 4.25: Comparison of the present results of the 2:1 rectangular cylinder with other literature reports, for several selected Scruton numbers. In the legend, "Santosham-1966", "Miyata-1983", "Yamada-1984" and "Itoh-2002" represent results, respectively, taken from Santosham (1966), Miyata & al. (1983), Yamada & Miyata (1984) and Itoh & Tamura (2002). V_r is calculated with $St = 0.079$.

Trapezoidal cylinder

For the trapezoidal cylinder, tests with varied Sc were carried out for the mean flow incidence of $\alpha_0 = 3^\circ$ and $\alpha_0 = 0^\circ$. However, the response curves are quite similar with the results of the rectangular cylinder. For the purpose of brevity, they were presented in Appendix A.3.1.

Bridge deck model

In Tab. 4.4 the aeroelastic test cases are listed for the bridge deck model at its mean wind angles of attack $\alpha_0 = 0^\circ$ and $\alpha_0 = 4^\circ$. It can be found the effective oscillation mass M_e is slightly different for test case #B0-9, as well as #B4-6 to #B4-8. This is because four dampers were used for these test cases, while two dampers for other cases. The analysis of dynamic results starts for $\alpha_0 = 4^\circ$, where unsteady galloping due to strong interaction with VIV occurs.

Tab. 4.4: Aeroelastic test cases for the bridge deck model at $\alpha_0 = 0^\circ$ and $\alpha_0 = 4^\circ$, with various Sc.

α_0 [deg]	Static results		Aeroelastic test cases								
	St [-]	A_1 [-]	Config.	M_e [kg]	n_0 [-]	ρ [-]	ζ_0 [%]	Sc [-]	V_r [-]	V_g [-]	V_g/V_r [-]
0	0.109	9.43	#B0-0	3.60	9.63	1.17	0.083	6.9	1.45	0.23	0.16
			#B0-1			1.18	0.170	14.0		0.46	0.32
			#B0-2			1.17	0.297	24.6		0.83	0.57
			#B0-3			1.17	0.473	39.0		1.31	0.90
			#B0-4			1.16	0.633	52.8		1.77	1.22
			#B0-5			1.15	0.823	69.0		2.32	1.60
			#B0-6			1.14	1.037	88.0		2.96	2.04
			#B0-7			1.15	1.273	106.7		3.58	2.47
			#B0-8			1.15	1.583	132.8		4.47	3.08
			#B0-9	3.67	9.53	1.18	0.803	67.4	1.45	2.26	1.56
4	0.102	4.17	#B4-0	3.60	9.63	1.19	0.067	5.5	1.56	0.42	0.27
			#B4-1			1.18	0.163	13.3		1.01	0.65
			#B4-2			1.18	0.270	22.1		1.68	1.08
			#B4-3			1.17	0.470	38.7		2.96	1.90
			#B4-4			1.19	0.617	50.3		3.84	2.46
			#B4-5			1.16	0.837	69.6		5.32	3.41
			#B4-6	3.67	9.53	1.17	0.983	83.0	1.56	6.33	4.06
			#B4-7			1.16	1.253	106.4		8.13	5.21
			#B4-8			1.18	1.387	115.8		8.85	5.67

Fig. 4.26 shows the aeroelastic results for the bridge deck model at $\alpha_0 = 4^\circ$. Typical “Full-Interference” behaviors were observed for $Sc \leq 69.6$, corresponding to $V_g/V_r \leq 3.41$. The invariance of oscillation amplitude regardless of Sc is also observed for this bridge deck model, up

to $\sqrt{2}y_{rms}/d = 0.25$ ($V/V_r < 1.9$), beyond which the dependence of amplitude on Sc becomes clear again. Like the 2:1 rectangular cylinder, amplitude modulation phenomenon was observed for $1 < V/V_r < 1.9$ (for brevity, it is not shown here again, one can refer to the published paper Chen & al. (2020) for more details). Unlike the 2:1 rectangular cylinder, further increasing Sc will not lead the oscillation to a typical "Partial-Interference" behavior. For $Sc \geq 83$, the amplitude after the VIV peak drops directly back to null. Nevertheless, a second branch of high amplitude was newly detected for $Sc = 83 - 115.8$ in a velocity range far behind the VIV region (see Fig. 4.26), by releasing the wind tunnel model from a higher displaced position.

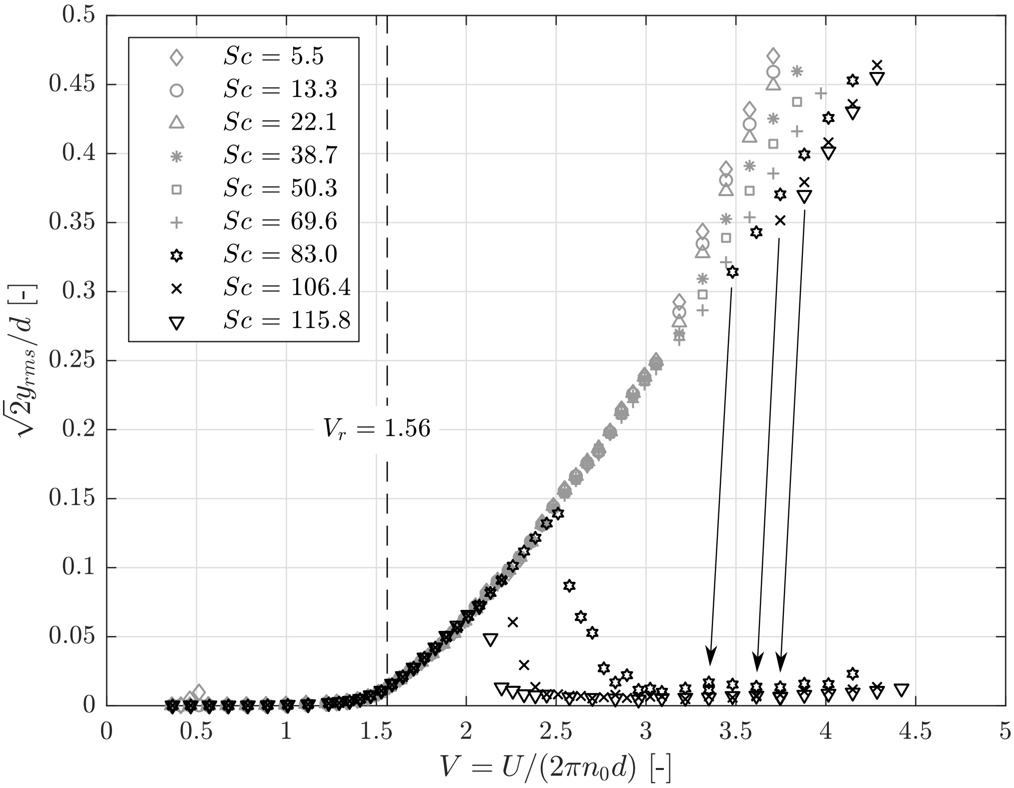

Fig. 4.26: Effect of Scruton number on the across-wind response of the bridge deck model at $\alpha_0 = 4°$.

For the bridge deck model at the its $\alpha_0 = 4°$, the cases corresponding to "Pre-Separation" and "Partial-Interference" were not observed. The last three test cases probably belong to the "Low-Interference" cases, although this is not confirmed by the wind tunnel tests, due to safety reason purposely not reaching the spontaneous galloping onset wind speed. From the galloping universal plot (Fig. 4.27), the upper amplitude branch can be found to extend to a reduced velocity less than $0.5V_g$, suggesting that a large hysteresis loop may exist here.

At $\alpha_0 = 0°$, the observed aeroelastic behaviors are essentially different, as illustrated in Fig. 4.28 and Fig. 4.29. In Section 4.2.1, it has shown that for this α_0 the galloping arises behind V_r even for a very low Sc. Slightly increasing Sc to 24.6, the galloping onset wind speed is maintained unchanged at about $V = 2$ (see Fig. 4.29 (a)). For $Sc = 39$ to $Sc = 69$, the onset wind speed varies

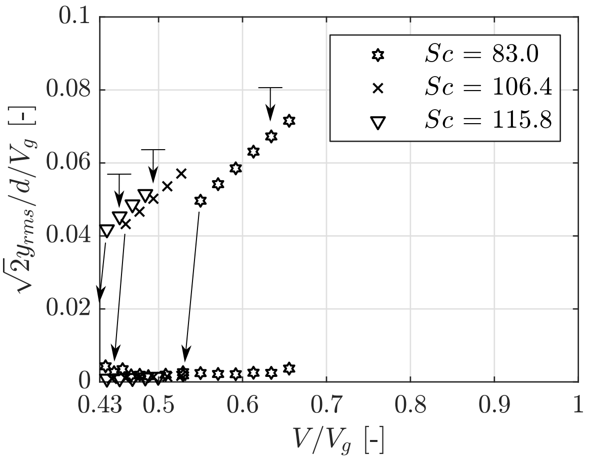

Fig. 4.27: Last three test cases (#B4-6 and #B4-8) of the bridge deck model in universal plot ($\alpha_0 = 4°$).

with the increased *Sc* (Fig. 4.29 (b) and (c)). Moreover, these three test cases all characterize with a jump of amplitude after the onset, leaving a hysteresis loop visible in the amplitude-velocity plot. For $Sc = 88$ to $Sc = 132.8$ (Fig. 4.29 (d)), the difference of onset wind speeds become again small. Meanwhile, one can find the post-critical amplitudes for $Sc = 88 - 132.8$ are quite different from the test cases of $Sc = 6.9 - 69$. For the latter, the amplitude branches are qualitatively maintained in the same "bunch", while for $Sc = 88 - 132.8$ the oscillations go out of this "bunch" (see Fig. 4.28). It is worth noting that, for all the test cases except the last

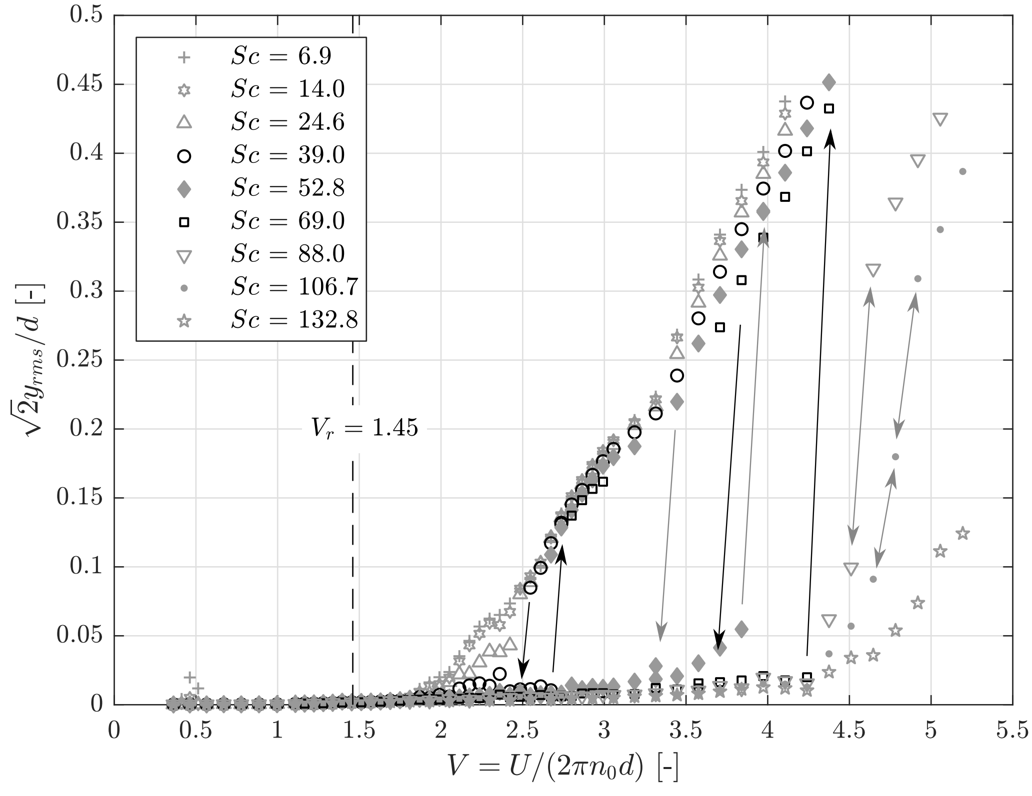

Fig. 4.28: Effect of Scruton number on the across-wind response of the bridge deck model at $\alpha_0 = 0°$.

one in Fig. 4.28, the actual galloping onset was found at a flow velocity higher than the QS prediction. The onset velocity for the last test case ($Sc = 132.8$), shows a good agreement with the QS prediction (see Fig. 4.30).

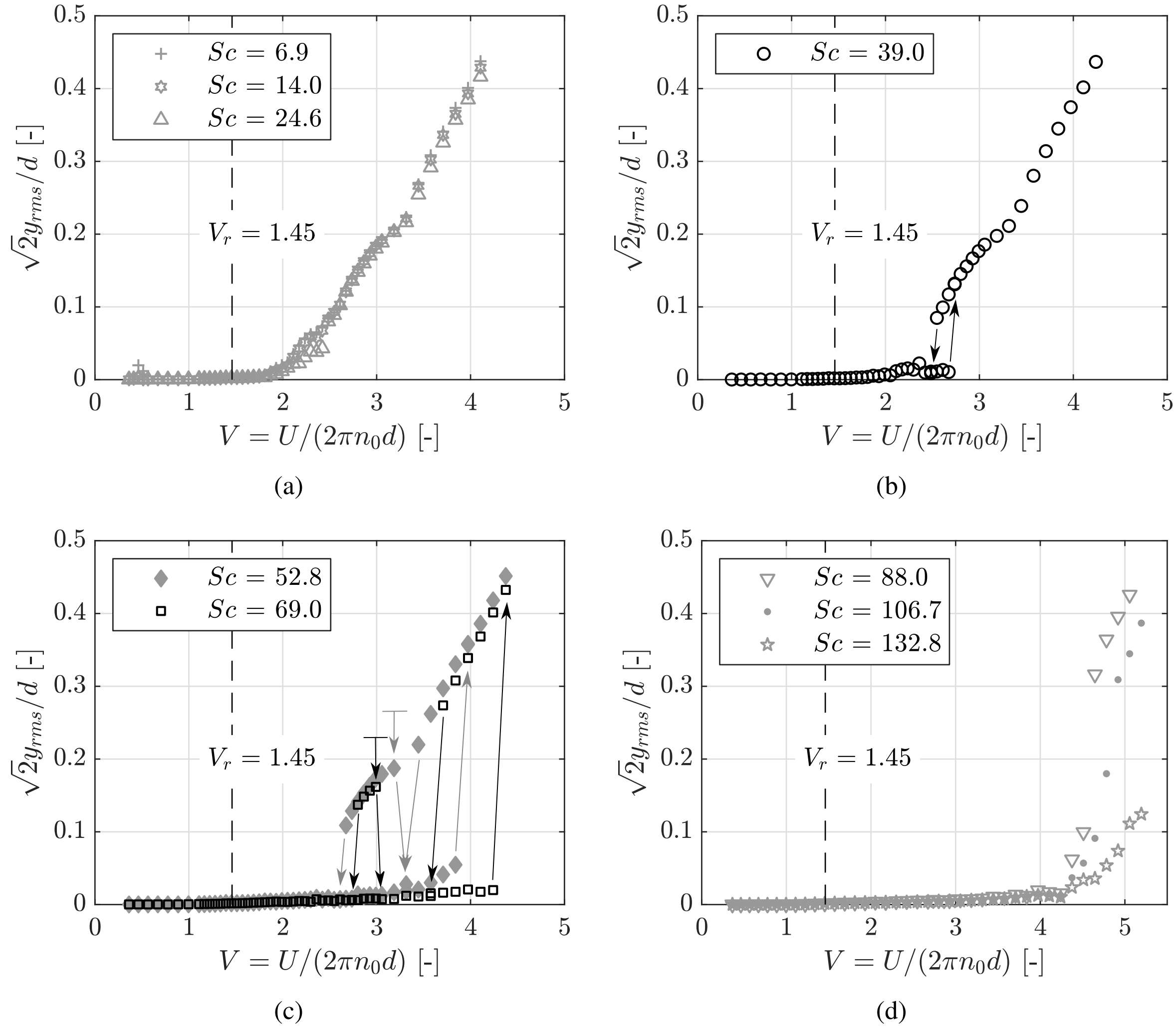

Fig. 4.29: Same results as in Fig. 4.28 but with divided plots for better view.

Moreover, a quite interesting phenomenon was observed for the test case of $Sc = 52.8$ and $Sc = 69.0$. In addition to the anti-clockwise hysteresis loops near the galloping onset, a second amplitude branch was found around $V = 2V_r$, by manually releasing the model from a higher displaced position (see Fig. 4.29 (c)). This branch was found in a quite limited wind speed range. Indeed, an increase or a decrease of the wind speed stepping outside this range will make the oscillation die out, as shown by the arrows in Fig. 4.29 (c). A repetition of the test case of $Sc = 69.0$ with four dampers, named “#B0-9”, was carried out several weeks later, remounting the aeroelastic setup. The double-check shown in Fig. 4.31 further confirms the existence of such a response branch. Since this amplitude branch locates around $2V_r$, it is probably due to a slight interaction of galloping with the vortex-shedding process with shedding frequency about

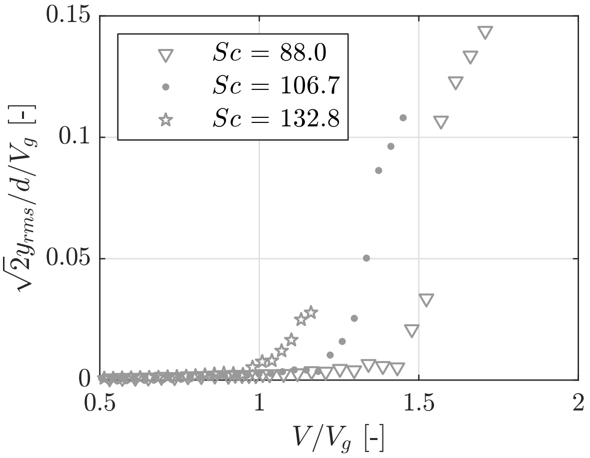

Fig. 4.30: Last three test cases (#B0-6 and #B0-8) of the bridge deck model in universal plot ($\alpha_0 = 0°$).

$2n_0$. For this reason, it may be inferred that the vortex shedding process still plays a role for the *atypical unsteady galloping* occurring at low reduced velocities, although a clear VIV response around V_r was never observed during the experiments.

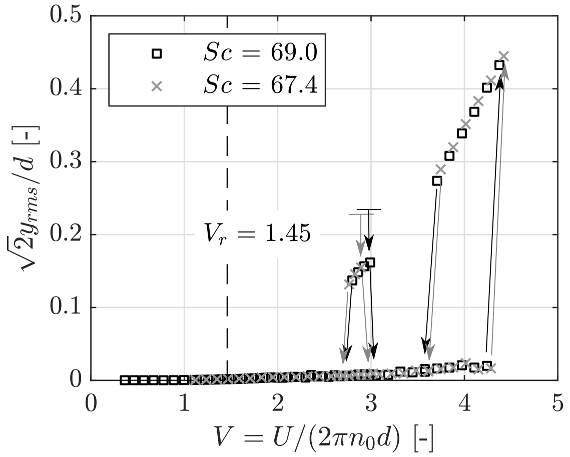

Fig. 4.31: Aeroelastic response of test case “#B0-9” (a repetition of test case “#B0-5” with 4-damper system).

4.2.3 Effect of Incoming Turbulence

Aeroelastic tests in turbulent flow were focused on the bridge deck model, since it shows stronger tendency to across-wind galloping than the other two cylinder models through the static tests. The carried out test cases, with detailed experimental conditions, are summarized in Tab. 4.5.

Firstly, the effect of α_0 on aeroelastic response was shown in Fig. 4.32. For test cases with $I_u = 11.2\%$ and $I_u = 14.9\%$, the damper system was activated to suppress some unwanted vibrations

Tab. 4.5: Characteristics of aeroelastic test cases for the bridge deck model studied in turbulent flow.

I_u [-]	α_0 [deg]	Static results		Aeroelastic test cases								
		St [-]	A_1 [-]	Config.	M_e [kg]	n_0 [-]	ρ [-]	ζ_0 [%]	Sc [-]	V_r [-]	V_g [-]	V_g/V_r [-]
9.2%	4	0.065	7.79	# X94B4-0	3.89	6.94	1.22	0.037	3.2	2.44	0.13	0.05
				# X94B4-1			1.21	0.268	23.2		0.95	0.39
				# X94B4-2			1.21	0.582	50.4		2.06	0.85
				# X94B4-3			1.21	0.824	71.3		2.91	1.19
				# X94B4-4			1.21	1.089	94.1		3.85	1.58
				# X94B4-5			1.20	1.470	128.4		5.25	2.15
				# X94B4-6			1.21	1.722	149.2		6.10	2.50
	2	0.063	10.01	# X94B2-0	3.89	6.94	1.20	0.033	2.9	2.52	0.09	0.04
	0	0.068	11.09	# X94B0-0	3.89	6.94	1.19	0.031	2.7	2.35	0.08	0.03
	-2	0.087	5.46	# X94B-2-0	3.89	6.94	1.20	0.036	3.1	1.82	0.18	0.10
11.2%	4	0.058	6.79	# X74B4-0	3.77	6.22	1.18	0.043	3.7	2.73	0.17	0.06
				# X74B4-1			1.18	0.312	26.8		1.26	0.46
				# X74B4-2			1.19	0.597	51.0		2.39	0.88
				# X74B4-3			1.18	0.830	71.4		3.35	1.23
				# X74B4-4			1.20	1.126	94.7		4.44	1.63
				# X74B4-5			1.20	1.126	118.2		5.54	2.03
				# X74B4-6			1.21	1.682	140.8		6.60	2.42
	2	0.069	9.47	# X74B2-1	3.77	6.22	1.19	0.313	26.6	2.31	0.89	0.39
	0	0.071	9.30	# X74B0-1	3.77	6.22	1.18	0.312	26.7	2.24	0.91	0.41
	-2	0.079	3.67	# X74B-2-1	3.77	6.22	1.19	0.311	26.5	2.00	2.30	1.15
14.9%	4	0.055	5.23	# X54B4-0	3.76	5.14	1.20	0.048	4.0	2.87	0.24	0.09
				# X54B4-1			1.20	0.286	24.1		1.47	0.51
				# X54B4-2			1.20	0.561	47.2		2.87	1.00
				# X54B4-3			1.20	0.807	67.9		4.14	1.44
				# X54B4-4			1.16	1.054	91.9		5.59	1.95
				# X54B4-5			1.17	1.381	119.7		7.29	2.54
	2	0.064	7.19	# X54B2-1	3.76	5.14	1.17	0.283	24.5	2.49	1.08	0.44
	0	0.064	4.16	# X54B0-1	3.76	5.14	1.15	0.284	24.8	2.51	1.90	0.76

in the torsional degree of freedom (as an example, without additional damping from dampers, torsional vibration up to 0.3° was found for $\alpha_0 = 2^\circ$ in case of $I_u = 11.2\%$). In turbulent flow, for a nearly same Sc, the actual galloping was found always first initiated at the $\alpha_0 = 4^\circ$. In contrast, from Tab. 4.5, one can find the galloping factor A_1 at $\alpha_0 = 4^\circ$ is not the highest one. Remembering the similar tests in smooth flow (Section 4.2.1), where galloping was found first initiated around $\alpha_0 = 4^\circ$ for low Sc, such a characteristic is also maintained in turbulent flow.

It may be reasonable to take $\alpha_0 = 4°$ of this bridge deck model as the “most-disadvantageous angle” in low *Sc* conditions, because the galloping arises at a lower reduced velocity than the other angles for the same *Sc*. Finally, if one goes back to have a look at the $C_{lat,0}$ coefficient (Fig. 4.18 (d)), a local maximum of $C_{lat,0}$ around $\alpha = 4°$ can be found (especially for $I_u = 9.2\%$ and $I_u = 11.2\%$). Such a characteristic seems to be very useful in identifying the “most-disadvantageous angle” for low-*Sc* galloping, either in turbulent flow or in smooth flow.

In Fig. 4.32, another important feature should be pointed out: the galloping always arises behind V_r in this small-scale turbulent flow. Nevertheless, the range of α_0, where galloping can be observed, gets narrowed with the increasing of I_u. This trend is consistent with the narrowed α range characterizing a negative slope of C_L (see Fig. 4.18 (b)). Finally, no apparent VIV-type oscillation was found around V_r even for *Sc* low as 3.

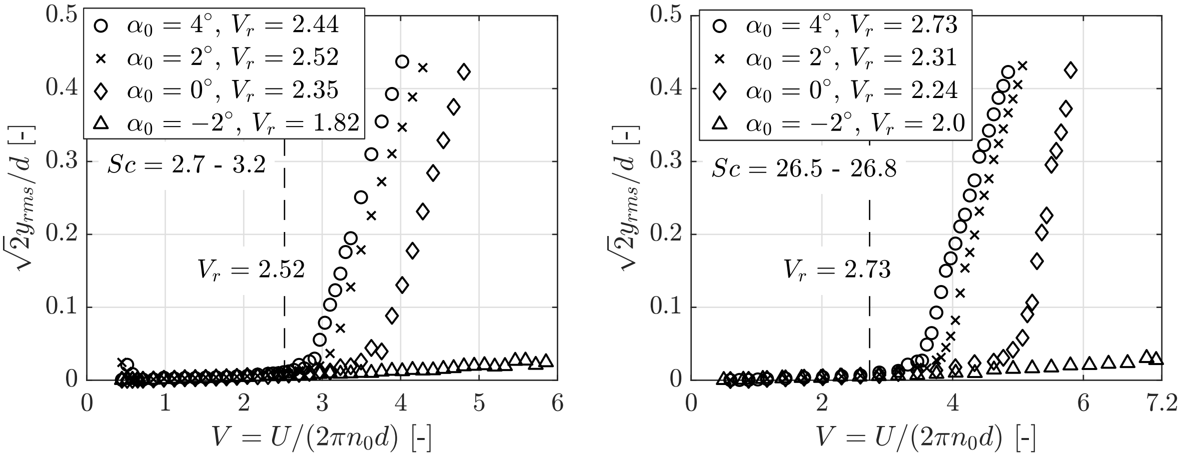

(a) $I_u = 9.2\%$ (b) $I_u = 11.2\%$

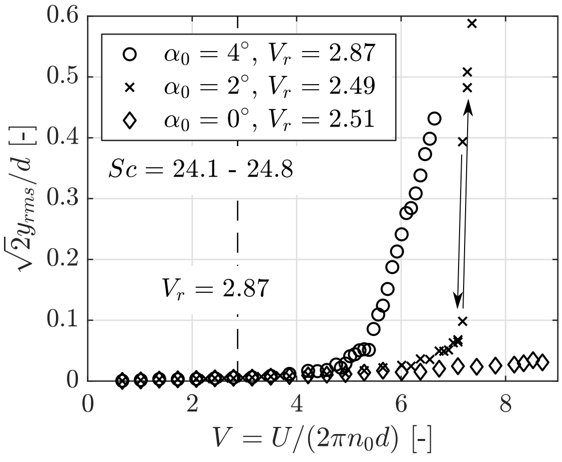

(c) $I_u = 14.9\%$

Fig. 4.32: Effect of α_0 on the aeroelastic behaviors of the bridge deck model in turbulent flow.

Subsequently, Scruton number was particularly varied at $\alpha_0 = 4°$, with results shown in Fig. 4.33. Unlike in smooth flow (galloping onset being fixed at V_r for $Sc \leq 69.6$), the onset velocity of galloping clearly varies with the increase of *Sc*. For the first two turbulence intensities, one can also observe a decrease of the amplitude slope when *Sc* is increased from the lowest value to the medium value (about 94).

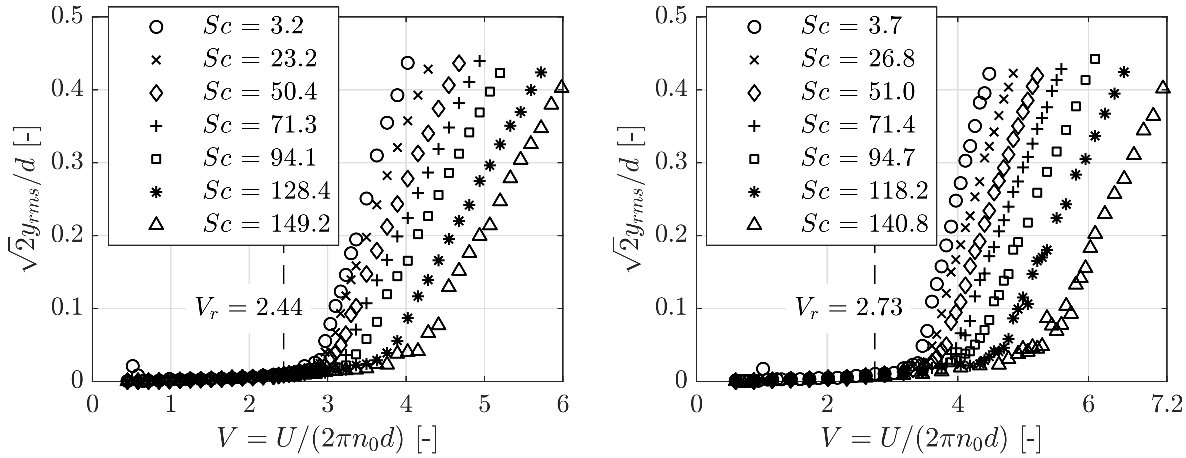

(a) $I_u = 9.2\%$ (b) $I_u = 11.2\%$

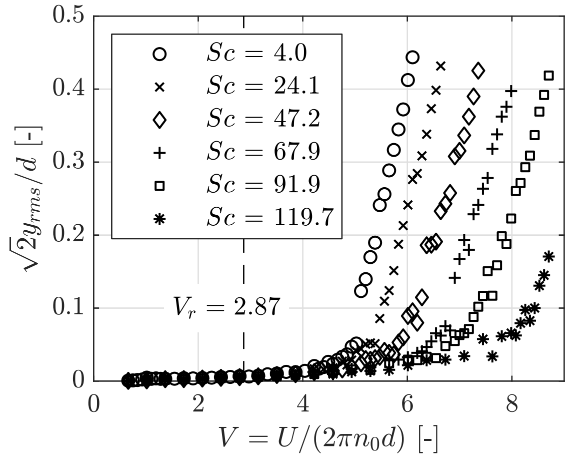

(c) $I_u = 14.9\%$

Fig. 4.33: Effect of *Sc* on the aeroelastic behaviors of the bridge deck model in turbulent flow ($\alpha_0 = 4°$).

In Fig. 4.34, the last three test cases of each I_u were presented in the galloping universal plot. These test cases all feature with comparably high Scruton number, leading to a V_g/V_r ratio between 1.44 to 2.54 (see Tab. 4.5). It is to note that, for the first two turbulence intensities, the increase of *Sc* make the galloping onset gradually approach to a value about $0.7V_g$ and $0.8V_g$, respectively. However, with the increase of *Sc*, this approaching process is found “left-side towards” in the universal plot. This means that the arising of galloping at V_g has been met for a certain *Sc*, for example $Sc = 94.7$ for $I_u = 11.2\%$, but further increasing *Sc* leads to the galloping onset pass by V_g and reach at a value clearly lower than V_g (see Fig. 4.34 (a) and (b)). For $I_u = 14.9\%$, the three test cases with the increase of *Sc* also show this “left-side towards” approaching process, although their galloping onset velocities are all above the QS predictions.

Theoretically speaking, with a high enough Scruton number, the across-wind galloping should follow well the QS theory. However, in the presented results, the investigated *Sc* seems not high enough, so that the full picture of the approaching process is unfortunately unavailable.

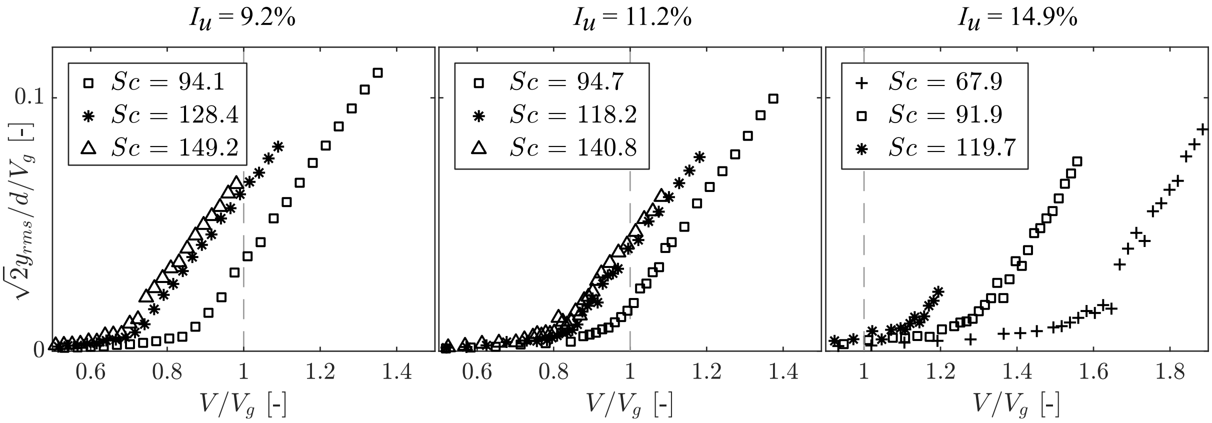

Fig. 4.34: Galloping universal plot for the last three test cases of each turbulent flow ($\alpha_0 = 4°$).

In Fig. 4.35, the effects of turbulence intensity is shown, for four different *Sc*. Results in smooth flow are also included for comparison purpose. For $Sc \leq 69.6$ (Fig. 4.35 (a) and (b)), due to the "Full-Interference" behaviors, the galloping in smooth flow arises at a reduced flow velocity lower than that in turbulent flow. In contrast, when the "Full-Interference" in smooth flow ends for $Sc \geq 83.0$, the galloping instability about the equilibrium position seems to be enhanced in turbulent flow, in particular for the $I_u = 9.2\%$ and $I_u = 11.2\%$ (see Fig. 4.35 (c) and (d), where *Sc* for turbulent flow is even higher). This enhancement agrees with the higher galloping factor A_1 in turbulent flow, see Tab. 4.5, qualitatively confirming the validity of QS theory for high Scruton number. Moreover, for this small-scale turbulent flow, the increase of I_u leads to a furhter postpone of galloping onset for a given *Sc* level.

Finally, the aeroelastic responses of the bridge deck model qualitatively agree well with a 3:2 rectangular cylinder tested in a similar turbulent flow condition (Mannini & al. 2018b). These agreements include: a) galloping was always initialized behind V_r; b) pure VIV oscillation was not observed; c) the phenomenon of "fixing galloping onset at a specific V regardless of *Sc* variation" was not observed any more. However, for very low turbulence intensities (about $I_u < 5.4\%$) or large-scale turbulent flow ($L_u/d \geq 2.6$), Mannini & al. (2018b) showed that the galloping can be still initiated at V_r for low-*Sc* cases.

4.3 Chapter Summary

In this chapter, extensive experimental results have been presented. In particular, the 2:1 rectangular cylinder has been used to confirm the validity of the experiential setups, by comparing

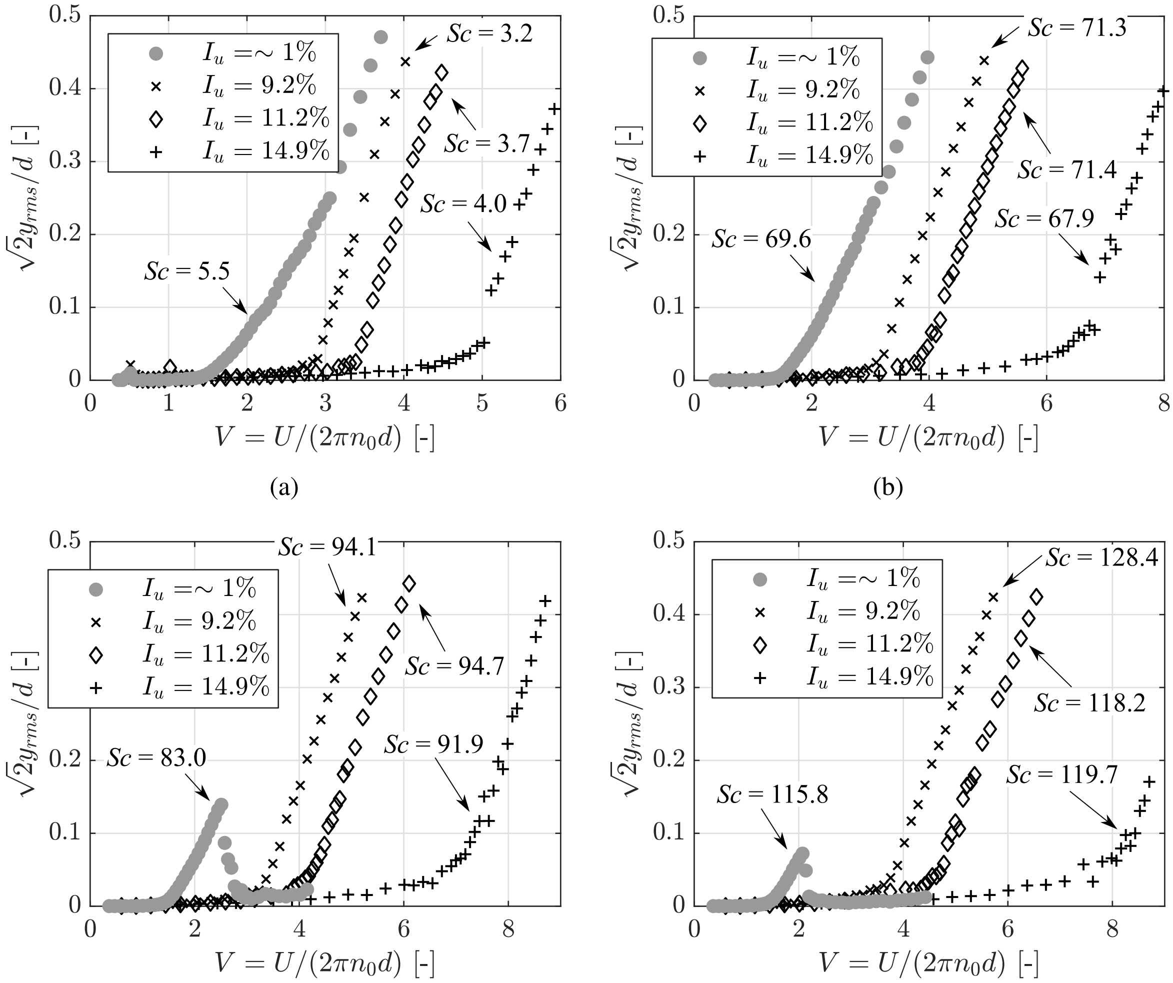

(a) (b)

(c) (d)

Fig. 4.35: Effect of turbulence intensity on the aeroelastic behaviors of the bridge deck model at $\alpha_0 = 4°$, for 4 different levels of Scruton number (results in smooth flow are also included).

with other literature reports. Besides, a comparably full picture of the galloping response of this rectangular cylinder was provided, covering a range of $5 < Sc < 200$ with small-step increment. Such a picture is supposed to contribute a deeper understanding for the galloping instability of this typical cylinder body.

The bridge deck model with open cross section has been paid rather more attention. At the mean flow incidence $\alpha_0 = 4°$, the galloping was found strongly interacting with the vortex induced vibration, being the actual galloping fixed at the Kármán-vortex resonance wind velocity for Scruton number up to at least 70 (corresponding to the V_g/V_r ratio about 3.4). Slightly different from the aeroelastic responses of the 2:1 rectangular cylinder, the "Partial Interference" as well as "Pre-Separation" behaviors were not observed for this bridged deck model. The important role played by the mean flow incidence was also highlighted. At $\alpha_0 = -2°$-$0°$ of the bridge deck model, the typical unsteady galloping due to the interaction with VIV was not observed any more. Instead, galloping arises at a reduced flow velocity clearly higher than V_r, even for a very low Sc number. This unsteady galloping behavior was named *atypical unsteady galloping* in this thesis, as opposed to the typical one. Such an atypical one was also observed for the rectangular cylinder at $\alpha_0 = 5^\circ$ and the trapezoidal cylinder at $\alpha_0 = -3^\circ$. Interesting is that, for all the three models, it was found that the *atypical unsteady galloping* always arises at a flow incidence with comparably weak vortex shedding force.

In grid-generated turbulent flow, a strong tendency to galloping instability is also observed for the bridge deck model. With I_u up to about 14.9%, static tests still indicate a positive galloping factor A_1 around its null flow incidence and aeroelastic tests confirmed this instability. Differing from in smooth flow, apparent interaction between VIV and galloping was not observed in turbulent flow, and the arising of galloping instability was found always behind V_r even for every low Sc.

Finally, the test results shown in this Chapter will serve as the input parameters for the mathematical model in the next Chapter, as well as the references to examine the performance of the mathematical model.

5 Mathematically Modeling the Unsteady Galloping for Prism Body

This chapter deals with the mathematical modeling of unsteady galloping behaviors for prism body (to be more specific, the wind tunnel sectional models). Nonlinear wake oscillator model of Tamura's form is adopted for this task. Attention was first paid to the prediction capability of the used wake oscillator model. Then, combined with wake flow measurements, the so-called physical considerations in wake oscillator model were examined. A new method to identify a key parameter for the wake oscillator model was also conceived during the wake measurements, thus additionally presented in this chapter. Finally, some further modifications were made to the wake oscillator model, for a better reflection of the physical considerations on sharp-edged bluff bodies such as rectangular cylinders.

5.1 Modeling with "TS-2018" Wake Oscillator Model

The modified version of Tamura&Shimada's wake oscillator model, "TS-2018" (Mannini & al. 2018a), is selected to model the unsteady galloping. One important origin for the using of wake oscillator model is due to its so-called physical considerations (Birkhoff 1953; Tamura & Matsui 1979). Mathematical modelings were made for the 2:1 rectangular cylinder and the bridge deck in smooth flow condition. Aiming at these two objects actually represents a further exploration of the prediction capability of the wake oscillator model, due to the following two facts.

a) Either literature reports (e.g., Novak 1972; Santosham 1966) or the previous wind tunnel results indicate that, the 2:1 rectangular cylinder shows more pronounced proneness to the unsteady galloping due to interference with VIV than the square or 3:2 rectangular cylinder. Mathematical modeling for this cylinder is therefore supposed to be more challenging, although similar works have been carried out for the square cylinder (e.g., in Tamura & Shimada (1987)) and for the 3:2 rectangular cylinder (Mannini & al. 2018a).

b) It is probably the first time that the wake oscillator model is applied to a generic bridge deck, whose geometry is much more complex than the rectangular ones.

For convenience, the two coupled equations of "TS-2018" wake-oscillator model (Eq. 2.55 in Section 2.2.3) are re-given here:

$$Y'' + 2\zeta_0 Y' + Y = \frac{V^2}{m^*} f\left(\vartheta - \frac{Y'}{V}\right) + \frac{V^2}{m^*} C_{Fy}^{QS}\left(\frac{Y'}{V}\right) \tag{5.1a}$$

$$\vartheta'' - 2\beta\upsilon\left(1 - \frac{4f^2}{C_{L0}^2}\vartheta^2\right)\vartheta' + \upsilon^2\vartheta = \lambda Y'' + \upsilon^2\frac{Y'}{V} \tag{5.1b}$$

where Y and ϑ denote, respectively, the non-dimensional transverse motion of body and the rotation angle of near-wake lamina. For wind tunnel sectional models, the mass ratio is $m^* = M_e/(0.5\rho d^2 l_e)$. $(\ )'$ represents differentiation to non-dimensional time $\tau = 2\pi n_0 t$, and $\upsilon = n_{st}/n_0 = V/V_r$ is the frequency ratio. With the "local-effect" equation of "TS-2018", $St^2 = 1/(8\pi h^* l^*)$ (Eq. 2.59), parameters β and λ, described by Eq. 2.58, can be re-written with h^*

$$\beta = \frac{4\sqrt{2}}{\pi} St^2 h^* f \quad \text{and} \quad \lambda = 8\pi St^2 h^* \tag{5.2}$$

Therefore, five aerodynamic parameters need to be set for the mathematical model: a) the quasi-steady force coefficient C_{Fy}^{QS}; b) the amplitude of fluctuation lift coefficient due to vortex shedding C_{L0}; c) St; d) the normalized near-wake width $h^* = h/d$; e) the slope f, relating the near-wake rotation to the induced unsteady lift. The first three are available from the static test results (Tamura & Matsui (1979); Tamura & Shimada (1987)). Identification of h^* is also relatively easy if flow visualization is provided for a stationary body. More crucial is the setting of parameter f. For circular cylinder (Tamura & Matsui 1979), identification of f is related to the *Magnus effect* analogy. However, for sharp-edged bodies (especially the studied bridge deck), such an analogy seems very questionable. Alternatively, based on the physical definition of f (the slope between unsteady lift coefficient and near-wake rotation), the identification of f would be possible if reliable flow visualization and synchronous force measurements were carried out on a stationary body. Unfortunately, such complicated measurements are not available in the current wind tunnel facility. At this stage, the method proposed by Mannini & al. (2018a) is adopted, using a set of aeroelastic test results of high Sc to calibrate this parameter in the VIV region.

Eq. 5.1 were numerically solved by the ODE45 solver of Matlab®. The relative and absolute error tolerance of the solver were respectively set to 10^{-6} and 10^{-8}, well balancing the computational cost and accuracy (tests with lower or higher tolerances were also carried out). The performance of the mathematical model was examined by comparison with the experimental results in a wide range of Sc, in terms of the amplitude-velocity curves. The quasi-steady galloping solutions were also reported as a reference, by integrating only Eq. 5.1a after setting $f = 0$.

5.1.1 The 2:1 Rectangular Cylinder at $\alpha_0 = 0^\circ$

Fig.5.1 shows the schematic of wake oscillator model for the 2:1 rectangular cylinder at $\alpha_0 = 0^\circ$. Motion of body is defined downwards positive, while for the rotation of the wake lamina it is anti-clockwise positive. Combined with Eq. 5.1a and assuming a stationary state for the cylinder, it is known that a positive ϑ will generate a downward unsteady lift. This is compatible with many CFD simulation results about this cylinder (e.g. see Shimada & Ishihara (2002)).

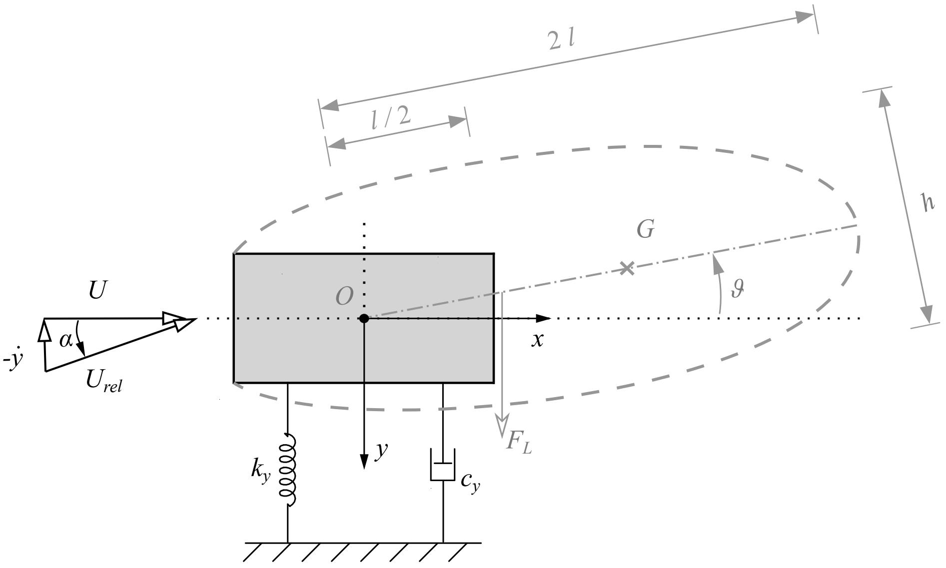

Fig. 5.1: Schematic of the “TS-2018” wake oscillator model for the 2:1 rectangular cylinder. Pivot position O, gravity center of the equivalent near-wake lamina G, and the position of the restoring force F_L being applied are particularly indicated.

Parameter setting

Fig.5.2 (a) and (b) show, respectively, the approximations of C_{Fy}^{QS} and C_{L0} coefficients from static test results. The experimental C_{Fy}^{QS} coefficient was calculated through Eq. 2.14 with the measured drag and lift coefficients at $Re = 6 \cdot 10^4$, then approximated with cubic spline interpolation for mathematical model use. For the C_{L0} coefficient, static test results have shown non-negligible dependence on Re. For this reason, C_{L0} was approximated by a piecewise-function as shown by Fig.5.2 (b). There, problematic data points for $Re < 2 \cdot 10^4$ and around $Re = 4.4 \cdot 10^4$ were already excluded (see Fig. 4.6 for comparison). Finally, a constant $St = 0.079$ was set.

Due to the lack of equipment for flow visualization, estimation of h^* therefore relies on literature reports. Tamura & Shimada (1987) adopted $h^* = 1.8$ for the square cylinder, according to the flow patterns registered by Mizota & Okajima (1981). Mannini & al. (2018a) supposed $h^* = 1.8$ also reasonable for a 3:2 rectangular cylinder, combining with a double-check of the CFD simulations in Shimada & Ishihara (2002). Moreover, they (Mannini & al. 2018a) performed sensitivity study for h^*, highlighting the insensitivity of wake-oscillator model solutions to this

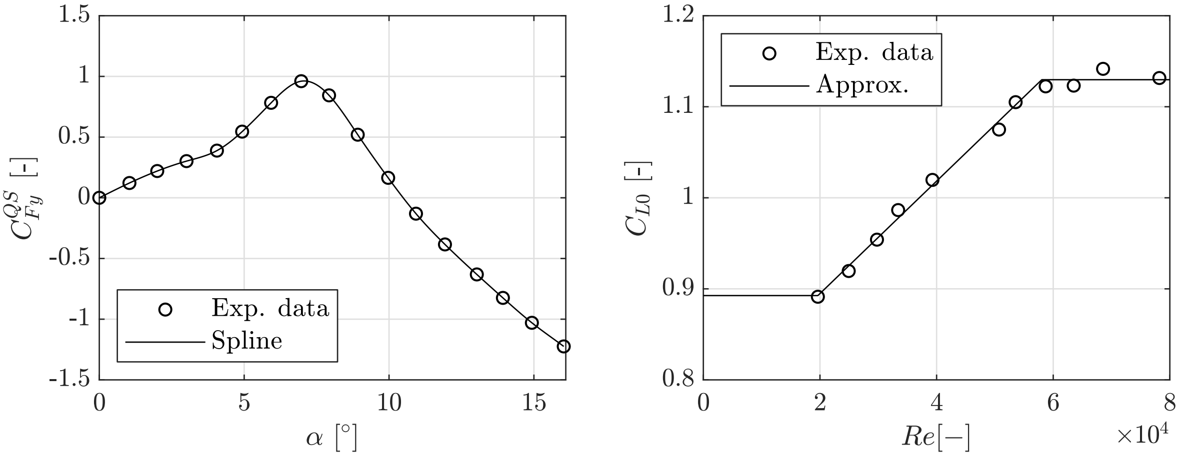

(a) (b)

Fig. 5.2: Approximating the static test results of the 2:1 rectangular cylinder: (a) cubic spline interpolation of $C_{Fy}^{QS}(\alpha)$ data ($Re = 6 \cdot 10^4$); (b) piecewise-linear approximation of the $C_{L0}(Re)$ data.

parameter. For the 2:1 rectangular cylinder in object, however, a value of $h^* = 2.1$ is found more reasonable after a crosscheck of the unsteady flow patterns reported in several publications (Mizota & Okajima 1981; Shimada & Ishihara 2002, 2012; Yu & Kareem 1998).

After setting above 4 parameters, numerical integration was performed with a set of known f values to do the calibration procedure reported in Mannini & al. (2018a): comparing the numerical results with the experimental ones of a high Scruton number ($Sc = 201$) in the VIV region. This procedure is shown in Fig. 5.3. Due to a private communication with Dr. Mannini (University of Florence, Italy), the priority of this calibration is a comparable amplitude slope

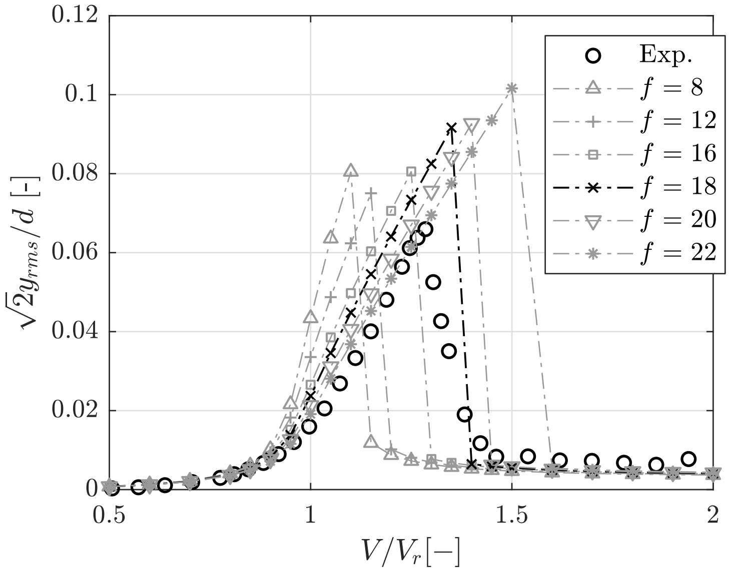

Fig. 5.3: Calibration of the f parameter with aeroelastic test results of $Sc = 201$, $h^* = 2.1$ and initial condition $[Y, Y', \vartheta, \vartheta'] = [0.001, 0, 0, 0]$.

between the numerical and experimental results. Therefore, $f = 18$ or $f = 20$ is supposed to be suitable one. Here, $f = 18$ is chosen, considering its slightly smaller peak amplitude and a better match of V at which the VIV peak appears. However, with $f = 18$, one can find that the VIV peak amplitude is overestimated (39% higher than experiments). This is partially due to C_{Fy}^{QS} of $Re = 6 \cdot 10^4$ being used, while the experimental VIV response arises at $Re \approx 2.3 \cdot 10^4$ (see the different A_1 in Fig. 4.3 for different Re). Attempt of adopting C_{Fy}^{QS} of $Re = 2.0 \cdot 10^4$ was also made, showing that the numerical results of $h^* = 2.1$ and $f = 18$ peaked at $V/V_r = 1.30$ and the amplitude was about 22% higher than the experiments. Nevertheless, C_{Fy}^{QS} at $Re = 6.0 \cdot 10^4$ will be continuously adopted, since it is more accurate for galloping predictions at high reduced velocities. Finally, the obtained f value can be found much higher than $f = 9$ for the 3:2 rectangular cylinder ((Mannini & al. 2018a)), as well as $f = 1.16$ for the square cylinder (Tamura & Shimada 1987).

Numerical results

After all the parameters being set, the mathematical model is solved for different test cases listed in Tab. 4.3. It is to note that $h^* = 2.1$ and $f = 18$ are kept unvaried for different Sc.

Fig. 5.4 compared the numerical solutions with wind tunnel test results, covering a wide range of Sc from 5.1 to 200.7. For a very low Scruton number $Sc = 5.1$ (Fig. 5.4 (a)), the wake oscillator model successfully postpones the galloping onset until V_r, although the predicted amplitude is overestimated. This postponement is successfully maintained up to $Sc = 107.1$ (Fig. 5.4 (b)), agreeing very well with the experimental observations. For $Sc = 127.9$, wind tunnel tests start to show a second amplitude branch, in addition to the main one. This behavior is also captured by the mathematical model, in a slightly lower range of V. For $Sc = 136.6$, wind tunnel tests show the “Partial-Interference” behavior, where spontaneous separation of VIV and galloping occurs (VIV peak emerges) but galloping-type oscillation continues right after this separation. This behavior is reflected in the mathematical model, for the solutions attained form small initial conditions. However, the upper amplitude branch extents down back to the VIV lock-in range, which is not reached in the experiments (but almost, see Fig. 5.4 (d)). Moreover, the range of V, where two amplitude branches co-exist, is narrower in the mathematical predictions (especially for the upper limit). For $Sc = 145.9$ (Fig. 5.4 (e)), around $V = 2V_r$, the mathematical model shows the co-existence of 3 amplitude branches, agreeing the medium one well with the experiments. The high amplitude branch agrees also with the experimental ones, but it extents again down to the VIV lock-in region (as for $Sc = 136.6$). Such a behavior continues for $Sc = 162.0$ (Fig. 5.4 (f)), where the “Low-Interference” behavior is experimentally observed. Moreover, a large amplitude jump has been observed at $V/V_r = 3.30$ in wind tunnel tests, while in the mathematical predictions this occurs at a lower reduced wind speed. For $Sc = 184.8$ and $Sc = 200.7$, numerical solutions with small initial conditions well predict the VIV response but overestimate

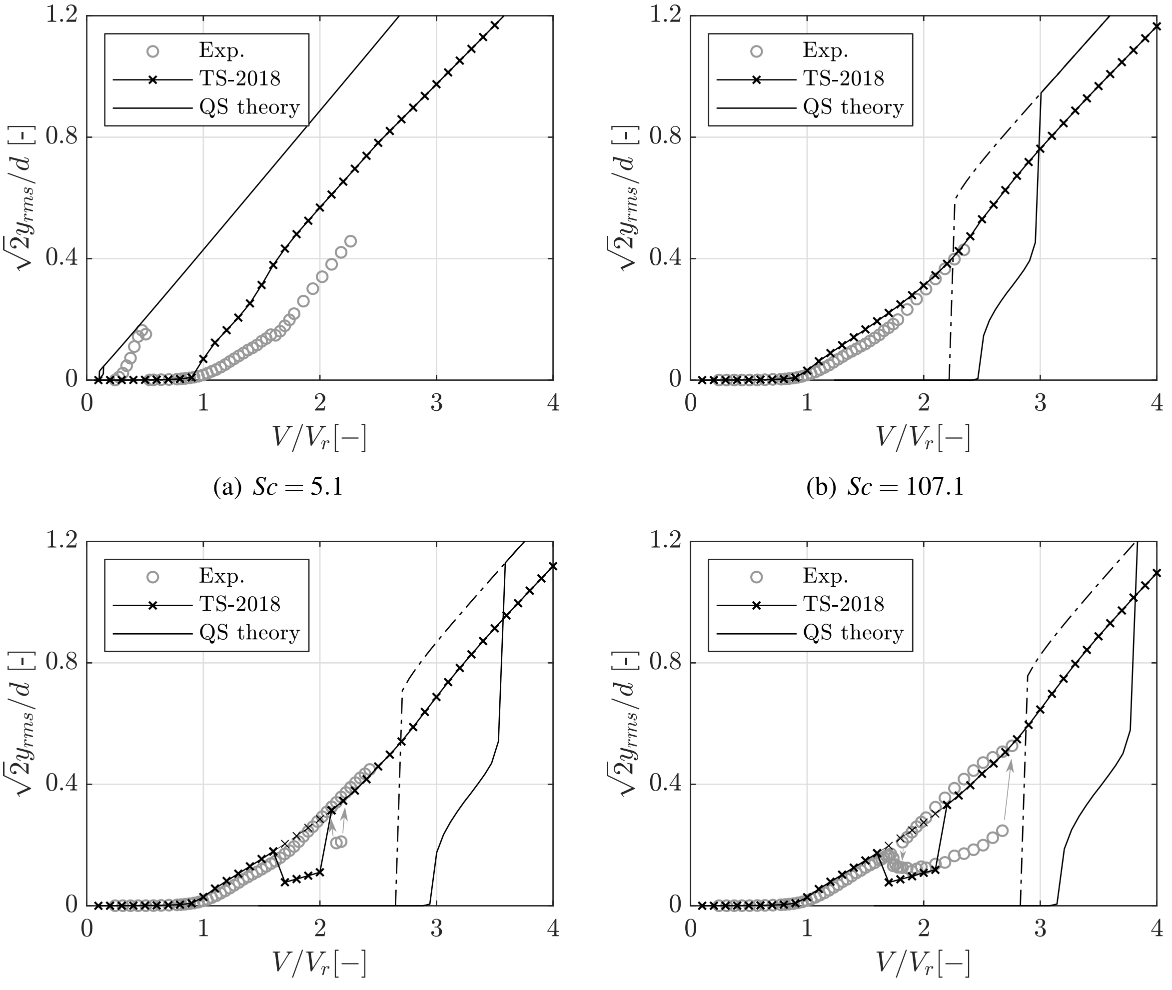

(a) $Sc = 5.1$

(b) $Sc = 107.1$

(c) $Sc = 127.9$

(d) $Sc = 136.6$

Fig. 5.4: Numerical solutions of the "TS-2018" wake oscillator model, in comparison with experimental results of the 2:1 rectangular cylinder. Heavy maker and solid line indicate solutions obtained with initial conditions $[Y, Y', \vartheta, \vartheta'] = [0.001, 0, 0, 0]$. Figure continued in next page.

the galloping onset wind speed. Interestingly, before the onset wind speed, a second amplitude branch is found, agreeing with the experimental ones. Finally, the mathematical model predict a large upper amplitude-branch behind the experimental VIV region, which is not observed in experiments.

Compared with the QS theory, the wake oscillator model clearly provide much better predictions. To be specific, several highlights should be pointed out for the wake oscillator model: a) the "Full-Interference" behavior is very well predicted, except the amplitude being overestimated to some acceptable extent for very low *Sc*; b) several important features of the "Partial-Interference" behavior have be captured, including the VIV peak amplitude, the co-existence of multiple amplitude branches just after the separation of VIV and galloping, as well as the increasing trend of the upper-amplitude branch; c) the classical VIV response in case of "Low-

Interference” is well captured for solutions attained from small initial conditions, as well as the being-advanced galloping onset than QS predictions; d) the solutions of wake oscillator model approach to the QS predictions at high reduced flow velocities, which is deemed reasonable.

Nevertheless, there are also some aspects needed to be further improved for predictions of wake oscillator model. A important one is the strong tendency to the high-amplitude branch for V properly higher than V_r. This tendency has led to some solutions which are not observed in the wind tunnel tests (e.g., $1.7 \leq V/V_r \leq 2.1$ for $Sc = 145.9$, $1.6 \leq V/V_r \leq 2.9$ for $Sc = 162.0$, and the two large amplitude branches after VIV regions for $Sc =$ 184.7-200.7). Moreover, for the last two cases ($Sc = 184.7$ and $Sc = 200.7$), amplitude lumps are observed at V slight higher than $3V_r$ (attained from large initial conditions). This is supposed to be a sub-harmonic exciting due to $n_{st}/3$. Finally, it is understandable that the mathematical model didn’t reflect the motion-induced-vortex exciting, which is experimentally observed at $V \approx 0.3V_r$ for $Sc = 5.1$ and induced by the ILEV mechanism.

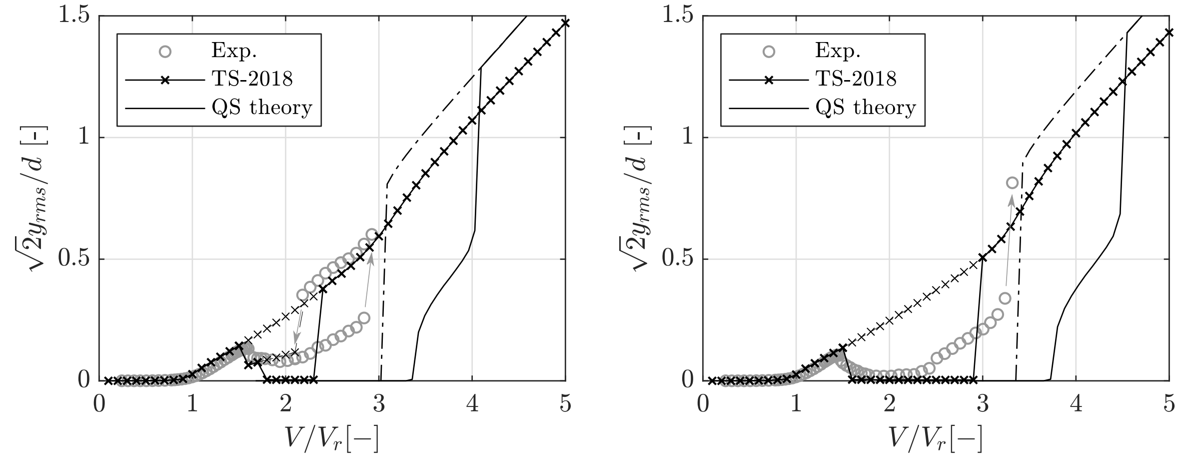

(e) $Sc = 145.9$ (f) $Sc = 162.0$

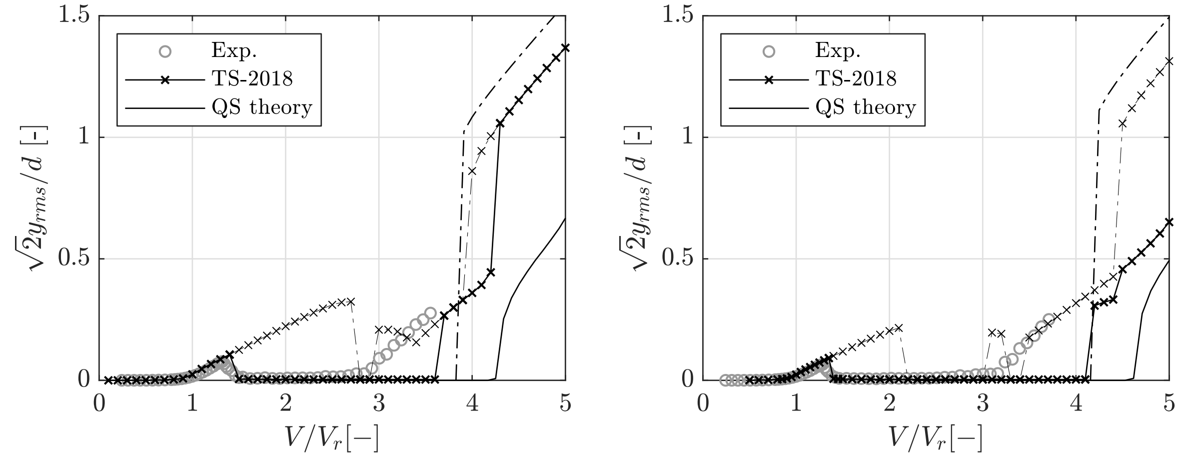

(g) $Sc = 184.8$ (h) $Sc = 200.7$

Fig. 5.4 (cont.)

5.1.2 The Bridge Deck at $\alpha_0 = 4°$

The “TS-2018” wake oscillator model was then applied to the bridge deck at its mean flow incidence of $\alpha_0 = 4°$, as schematized in Fig. 5.5. The pivot position O of the wake lamina was assumed at the centroid of the cross section.

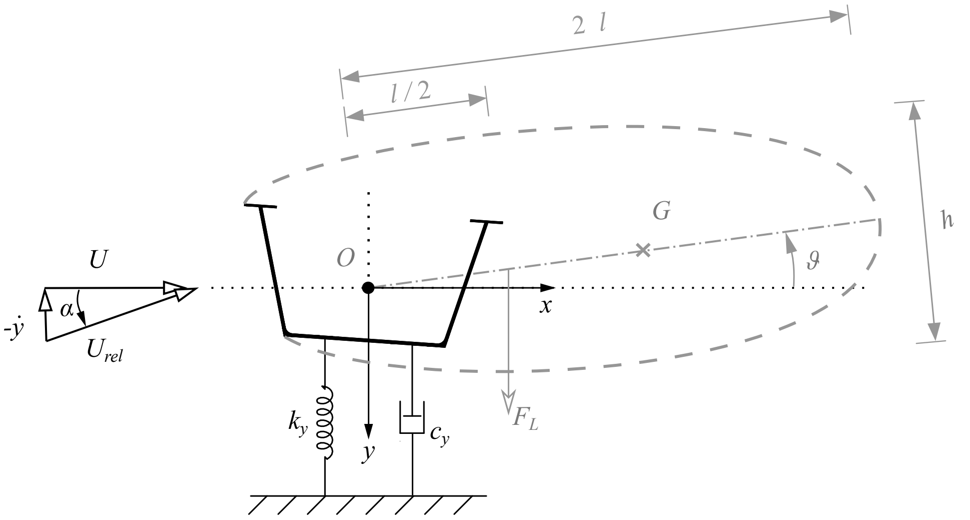

Fig. 5.5: Schematic of the “TS-2018” wake oscillator implemented for the bridge deck model at 4° mean flow incidence.

Parameter setting

The C^{QS}_{Fy} and C_{L0} coefficients approximated for the mathematical model are shown in Fig.5.6. For C^{QS}_{Fy}, a static shift has been performed (resetting $\alpha = 4°$ as the new null wind angle of attack

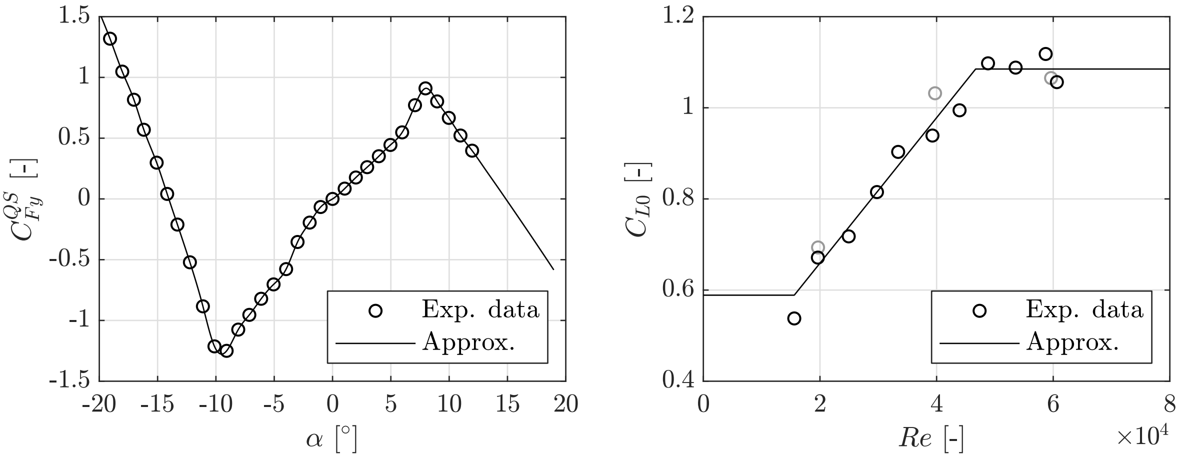

(a) (b)

Fig. 5.6: Approximating the static test results of the bridge deck model at $\alpha_0 = 4°$: (a) cubic spline interpolation and linear extrapolation of $C^{QS}_{Fy}(\alpha)$ data ($Re = 6 \cdot 10^4$, after static shift of the coefficient for $\alpha = 4°$); (b) piecewise-linear approximation of the $C_{L0}(Re)$ data (gray and black markers represent two sets of experimental data measured at different time periods).

for the C_D and C_L data, then applying Eq. 2.14 to obtain the C_{Fy}^{QS} curve, finally neglecting the part of C_{Fy}^{QS} inducing only static deformation). Moreover, the C_{Fy}^{QS} coefficient has been properly extrapolated (in a linear way) for $\alpha > 12°$. This is to ensure a stable numerical integration for large amplitude oscillations. The C_{L0} was also approximated as a piecewise-function of *Re*, in a same way as for the 2:1 rectangular cylinder. Compared with Fig. 4.12, it is easy to find that the problematic data points have been excluded. Finally, $St = 0.102$ was set.

Currently, there exists no reliable flow visualization for the estimation of the h^* parameter for this bridge deck. It is therefore decided to maintain the same value $h^* = 1.8$, as for the square cylinder (Tamura & Matsui 1979) and for the 3:2 rectangular cylinder (Mannini & al. 2018a). Thanks also to the sensitivity study of h^* in Mannini & al. (2018a), a rough estimation for this parameter is supposed to be acceptable for prediction purpose. Calibrating the key parameter f was then carried out, reporting $f = 15$ as the proper one as shown in Fig. 5.7.

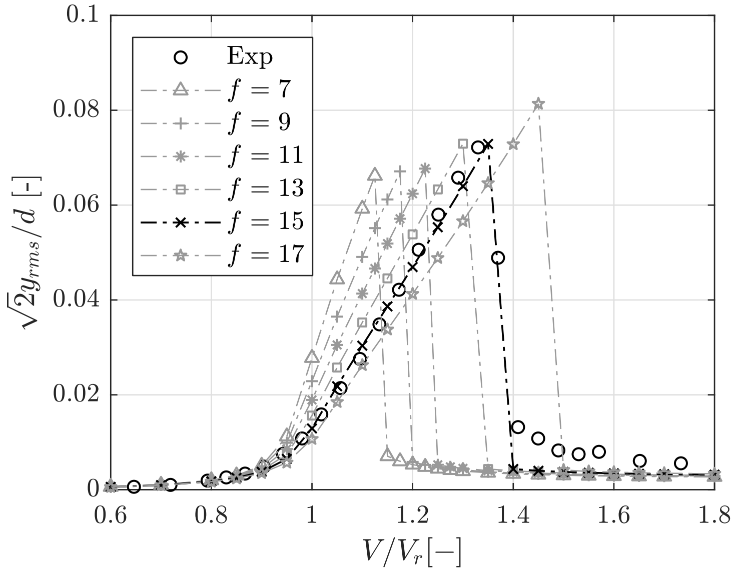

Fig. 5.7: Calibration of the f parameter with aeroelastic test results of $Sc = 115.8$, with $h^* = 1.8$ and initial condition $[Y, Y', \vartheta, \vartheta'] = [0.001, 0, 0, 0]$.

Numerical results

With $h^* = 1.8$ and $f = 15$ unvaried, the performance of the mathematical model is examined by comparison with experimental dynamic results (Fig. 5.8 and Fig. 5.9). For $Sc \leq 50.3$, both the mathematical model and experiments show "Full-Interference" behaviors. For $Sc = 69.6$, the mathematical model begins to predict a second branch of medium-amplitude, while this branch was not observed during the wind tunnel tests. Nevertheless, after a careful check of the time history records of manually releasing the wind tunnel model from rest, it is found at about $V = 2.13V_r$ the amplitude building-up process has shown a tendency to the medium-amplitude branch (additionally added in Fig. 5.8 (c)). It is therefore reasonable to conjecture that the medium-amplitude branch can be reached if a slightly higher *Sc* was considered in the

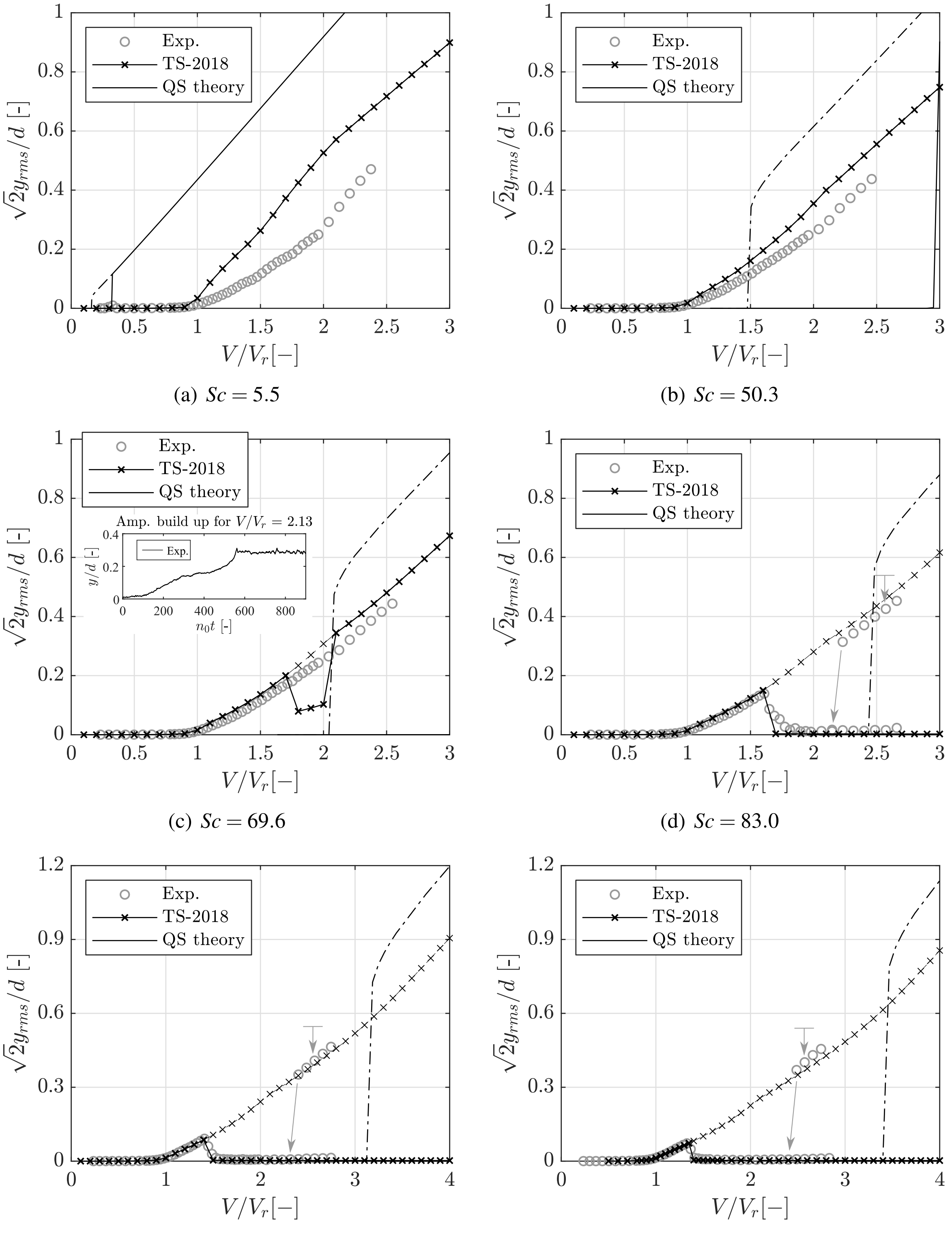

(a) $Sc = 5.5$

(b) $Sc = 50.3$

(c) $Sc = 69.6$

(d) $Sc = 83.0$

(e) $Sc = 106.4$

(f) $Sc = 115.8$

Fig. 5.8: Numerical solutions of the “TS-2018” wake oscillator model for the bridge deck at $\alpha_0 = 4°$, in comparison with the experimental results. Heavy maker and solid line indicate solutions obtained with initial conditions $[Y, Y', \vartheta, \vartheta'] = [0.001, 0, 0, 0]$.

experiments. For Sc = 83-115.8, the mathematical model very well predicted the VIV response when the solutions are attained from a small initial condition, including the VIV peak amplitude, lock-in velocity range and the amplitude-velocity curve. Moreover, the high-amplitude branches much after the VIV region (which were experimentally detected by releasing wind tunnel model from a high displaced position), are also captured by the mathematical model. Nevertheless, the tendency to the upper amplitude branch seems quite strong, leading to this branch extend down directly to the VIV lock-in region (similar to the conditions for the 2:1 rectangular cylinder).

In Fig. 5.9, additional results for $Sc = 83.0$ at higher V are given. There, both the QS theory and the wake-oscillator model predict a very large amplitude jump just at the galloping onset wind speed. Such a jump is very violent for the current experimental setup so that it was purposely avoided during experiments. Nevertheless, one can find the wake-oscillator has predicted a lower onset velocity than the QS theory. This lower onset velocity is deemed more reliable, considering that the better prediction capability of wake oscillator model has been confirmed for the 2:1 rectangular cylinder (Fig. 5.4) and the 3:2 rectangular cylinder (Mannini & al. 2018a).

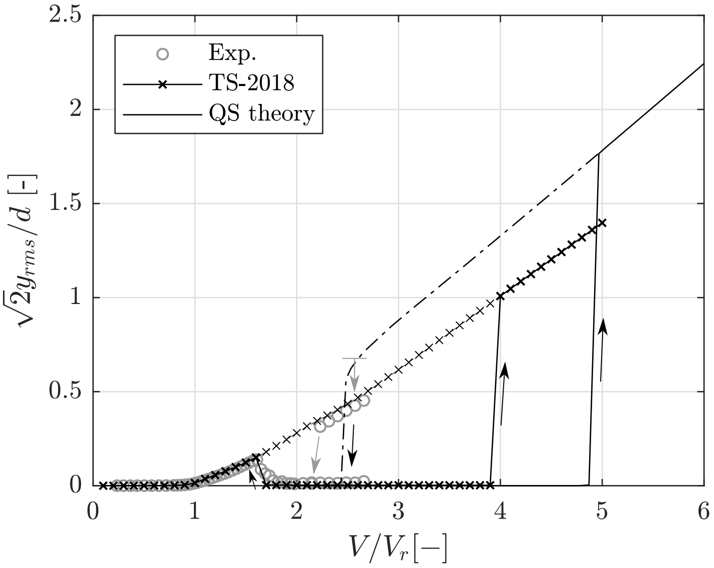

Fig. 5.9: Numerical solutions of the "TS-2018" wake oscillator model for the bridge deck at $\alpha_0 = 4°$. Extra results for $Sc = 83.0$ at larger V.

Finally, it is interesting to note, that form $Sc = 69.6$ to $Sc = 83.0$, the numerical solutions for the bridge deck did not show so many "Partial-Interference" behaviors as for the 2:1 rectangular cylinder. This is generally in line with the experimental results of the two wind tunnel models.

5.1.3 The Bridge Deck at $\alpha_0 = 0°$

Up to here, the wake oscillator model has exhibited quite satisfying capabilities in predicting the unsteady galloping behaviors due to inference with VIV, not only for the 2:1 rectangular cylinder which is well-known to undergo strong interference between galloping and VIV, but also for the bridge deck model whose geometry topology is rather complex. However, for the unsteady galloping not due to the interaction with VIV (namely the previously named *atypical unsteady galloping*), the wake oscillator model seems less applicable. Fig. 5.10 shows an attempt of applying the wake oscillator model to the bridge deck model at its $\alpha_0 = 0°$ (for parameter setting, see caption of Fig. 5.10). For a very low Scruton number ($Sc = 6.9$), the wake oscillator continues predicting a galloping onset at V_r, and varying the f value brings nearly no change to this threshold. In contrast, the galloping onset was experimentally observed at $V \approx 1.3V_r$. Remembering the observations for the square cylinder at $\alpha_0 = 9°$ (see Fig. 2.18 in Section 2.2.1), it may be questionable to set here the quasi-steady coefficient C_{Fy}^{QS} in the mathematical model, at least for $V_r < V < 1.3V_r$. A further discussion for this topic is presented in Section 5.5.2.

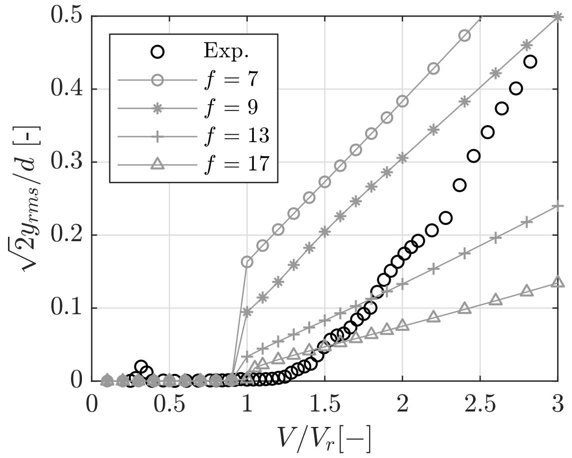

Fig. 5.10: Wake oscillator model results for the bridge deck at a mean flow incidence of 0°, considering a very low Scruton number $Sc = 6.9$. $C_{Fy}^{QS}(\alpha)$ at $Re = 6.0 \cdot 10^4$, constant $C_{L0} = 0.17$ of $Re = 2.0 \cdot 10^4$, $St = 0.109$ and $h^* = 1.8$ were set in the mathematical model.

5.2 Examination of the Physical Considerations in Wake Oscillator Model

From the above numerical results, the modified version of Tamura's wake oscillator (namely "TS-2018") clearly shows some satisfying capabilities in predicting the unsteady galloping due to interaction with VIV. Up to there, it may be reasonable to say that the "TS-2018" model serves as an effective analytical tool for practical use. In this Section, one of the so-called physical considerations in wake oscillator model, that St is determined by the near-wake geometry through a "local-effect" (Birkhoff's idea), will be examined with respect to sharp-edged bluff body such as rectangular cylinders. To be more comprehensive, it is deemed necessary to first introduce the basic knowledge about the physics of the near-wake behind bluff body.

5.2.1 Physics of the Fluid Wake behind Bluff Body

Unless very low Re, flow separation, vortex formation and shedding normally occur when flow passes bluff body. The disturbed flow field behind the obstacle is called wake. Typically, for bluff body of small side ratio, this wake is illustrated in Fig. 5.11. In particular, the region just behind the obstacle is called near-wake, where vortex grows to “maturity” and then shed (thus sometimes also called “vortex formation region” (Gerrard 1966) or “base region” (Lander & al. 2016; Lyn & al. 1995)). Here, the formation of vortex belongs to the Bénard-Kármán mechanism, due to the two-shear-layer instability in the wake (the existence of body is actually not necessary for the vortex formation, see, e.g., Pier & Huerre (2001) and Afanasyev & Korabel (2006)). According to Gerrard (1966), the streamwise length of this region is characterized by the formation length l_F, which can be experimentally quantified (elaborate later in details).

The wake in the more downstream region can be called far-wake, where the shed vortices are mature and distinct. This is where the famous vortex street can be observed. Typically, the vortices in the “street” are arranged in two rows, with opposite sign of vorticity. The spacing of these vortices can be characterized with streamwise distance l_V and across-flow distance h_V. In Fig. 5.11, the speed of vortex being transported downstream is also indicated, which is usually smaller than the free-stream velocity U. For viscous flow, the strength of vortices in the “street” will gradually decrease because of the viscosity dissipation, and finally vanish.

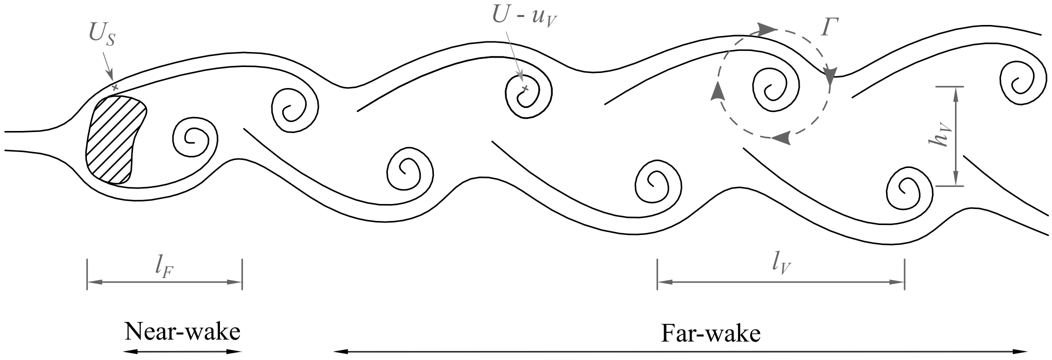

Fig. 5.11: schematic of the wake behind bluff body.

Classical explanation on vortex shedding frequency

Wake of bluff body is a complex phenomenon. “*Despite the fact that two-dimensional (2-D) and three-dimensional (3-D) vortical instabilities in wakes have been a subject of interest to engineers as well as to scientists for a great many years, an understanding of the flow behind a bluff body poses a great challenge*“ (Williamson 1996). “*The problem of bluff body flow remains almost entirely in the empirical, descriptive realm of knowledge*” (Roshko 1993). Particularly, for the periodicity of vortex formation and shedding, there exist various up-to-date explanations.

In the early but classical work of von Kármán (Von Kármán 1911, 1912), it was noticed that the transportation of vortices in the far-wake was governed by specific geometric arrangement. By assuming an ideal (non-viscous) flow and two arrays of concentrated vortex (point vortex) in equilibrium moving downstream with opposite sign of circulation Γ, von Kármán showed that the vortices have first-order instability, i.e., exponentially growing perturbations, except at one specific anti-symmetric configuration exhibiting neutral stability. This is the case for infinite vortex arrays with a spacing ratio of $l_V/h_V = 0.281$. The vortex shedding frequency can be determined through the stable geometric arrangement and the transportation velocity, namely $n_{st} = (U - u_V)/l_V$ provided another equation $\Gamma/(u_V l_V) = 2\sqrt{2}$ in von Kármán's theorem. Experimentally, somewhat larger values of l_V/h_V are found ($0.28 < l_V/h_V < 0.5$, summarized by Birkhoff (1953)), since h_V slightly increases downstream while l_V is trivially invariant. Although the original stability analysis of von Kármán spawned a great number of papers for the instability of the vortex arrays, it is unclear how to relate these studies to the vortex formation and shedding behind the bluff body. An attempt to build such a relation was made by Kronauer (1964): the vortex formation and shedding are mainly determined by the feedback of velocity fluctuations to the boundary layer separation point from the wake.

Some deeper descriptive understandings on the periodicity of vortex shedding comes from Gerrard (1966), who paid particular attentions to the near-wake just behind the bluff body: "*The growing of one vortex continues to be fed by circulation from the shear layer until the vortex becomes strong enough to draw the other shear layer across the wake. The approach of oppositely-signed vorticity in sufficient concentration cuts off further supply of circulation to the vortex, which then ceases to increase in strength. We may speak of the vortex as being shed from the body at this stage*". Clearly, based on above description, the "cutting-off" process plays the key role in the formation of discrete vortices, thus further determining the shedding frequency. Such an explanation is generally in line with the instantaneous-streamline patterns drawn by Perry & al. (1982) (based on flow visualization), as pointed out by Williamson (1996). Furthermore, Gerrard (1966) suggested two important characteristic lengths for the aforementioned mechanism. The first one is the previously mentioned vortex formation length l_F, whose decrease leads to the increase of the shedding frequency. This is explained as: the decrease of l_F will bring the two shear layers closer together so that their interaction is facilitated and the periodic time becomes shorter. The second characteristic length is called diffusion length l_D, which corresponds to the thickness of the shear layer when it reaches the region of strong interaction at the end of the formation region. When the shear layer is diffused (thicker), it will take a longer time for a sufficient concentration of vorticity to be carried across the wake and initiate shedding. Therefore, the increase of l_D tends to decrease the vortex shedding frequency.

More recently, although a conclusive explanation on the mechanism of vortex shedding is still not totally achieved, with the development of new experimental techniques and hence increased knowledge, following arguments seem robust: a) vortex shedding is a global instability in the sense that the whole wake is affected; b) the source of vortex shedding is the vorticity continuously produced by the shear layers; c) vortex shedding is the results of complex three-dimensional fluid-dynamics process (see the review paper by Williamson (1996)).

Other aspect

At this conjuncture, it is deemed necessary to supplement the knowledge about the relationship between the vorticity in the shear layer and the circulation carried by the downstream vortex. Roshko (1954b) showed that the rate of circulation (per unit time) produced by the vorticity of single-side shear layer can be calculated as $U_S^2/2$. Here, U_S is the flow velocity outside the shear layer close to the separation point, as illustrated in Fig. 5.11. Downstream in the far-wake, the rate at which circulation is carried by vortices is $n_{st}\Gamma$. Experimentally, Fage & Johansen (1928) showed that only a fraction ϵ of the vorticity in the shear layer is transferred to the downstream mature vortex. Therefore the relationship between upstream shear and downstream vortex can be built through the rate of circulation $n_{st}\Gamma = \epsilon U_S^2/2$. Fage & Johansen (1928) estimated the magnitude of ϵ is about 0.5, and more recent measurements showed this factor is usually lower than 0.5 (see Cantwell & Coles (1983) for a circular cylinder and Lyn & al. (1995) for a square cylinder). Apparently, a considerable portion of $U_S^2/2$ was "eaten" in the near-wake region, as explained by Lyn & al. (1995): "*the two separated shear layers with oppositely signed vorticity interact more directly and vigorously, resulting in substantial cancellation of vorticity*". In the far-wake, the circulation of single vortex also decreases during the transportation downstream but it is much slower.

5.2.2 Birkhoff's Explanation on Vortex Shedding Frequency (Linear Wake-oscillator)

Garrett Birkhoff provided a totally different perspective on the mechanism of near-wake oscillation behind bluff body. Early in the 1950s, he observed that "*behind the cylinder, the wake swings from side to side, somewhat like the tail of a swimming fish*" (Birkhoff 1953). He believed that the vortex shedding frequency is determined by the "local-effect" of near-wake, rather than the asymptotic downstream behavior (the aforementioned von Kármán's theorem).

Birkhoff considered the near-wake behind bluff body as a lamina, geometrically characterized by a length $2l$ up to its first bending and a width h for the dead-air region. The latter is actually a length scale relevant to the wake flow rather than the immersed bluff body, and, in Birkhoff's concept, the obstacle itself only served to anchor the forward end of the wake lamina. In the case of the circular cylinder, the anchor/pivot point was put about the centroid. The cross-force (restoring force) acting on the lamina was calculated by analogy to a thin airfoil of the same length $2l$ and displaced to the same angle of attack as the near-wake inclination ϑ. The theoretical lift coefficient $2\pi\vartheta$ was then obtained ("2π" is the theoretical slope of $C_L(\alpha)$ curve for thin airfoil, where C_L is the steady lift coefficient and α the wind angle of attack). Therefore, the magnitude of restoring force was calculated $F_L = \frac{1}{2}\rho U^2 \cdot 2l \cdot 2\pi\vartheta$, acting at one fourth of the chord of the lamina. On the other hand, the considered lamina has a mass ρh per unit length0. In the rotational degree of freedom about the pivot point, the torque due to the restoring force is $-\frac{1}{2}\rho U^2 \cdot 2l \cdot 2\pi\vartheta \cdot \frac{1}{2}l$ and the moment of inertia can be simplified as $\rho h2l \cdot l^2$ (the torque has an opposite sign to ϑ so that F_L is called restoring force). Further invoking Newton's second law, the equilibrium equation is obtained as $\rho h2l \cdot l^2 \cdot \ddot{\vartheta} = -\frac{1}{2}\rho U^2 \cdot 2l \cdot 2\pi\vartheta \cdot \frac{1}{2}l$, or

$$I_\vartheta \ddot{\vartheta} + k_\vartheta \vartheta = 0 \tag{5.3}$$

with $I_\vartheta = 2\rho hl^3$ and $k_\vartheta = \pi\rho U^2 l^2$. Solution of the equation gives an oscillation frequency for the near-wake lamina $n_{st} = U/\sqrt{8\pi hl}$, and the conventional Strouhal number is obtained as

$$St = 1/\sqrt{8\pi h^* l^*} \tag{5.4}$$

with $h^* = h/d$ and $l^* = l/d$. The presented deducing procedure is in line with Mannini & al. (2018a) and slightly different from Birkhoff (Birkhoff & Zarantonello 1957; Birkhoff 1953), but the final expression of St is the same. By putting $h = 1.33d$ and $2l = 1.5d$ (Birkhoff 1953) in Eq.5.4 (or, $h = 1.25d$ and $2l = 1.6d$ in Birkhoff & Zarantonello (1957)), Birkhoff finally obtained a Strouhal number $St \approx 0.2$ for the circular cylinder in the sub-critical region of Re. The geometric size, namely h and $2l$, was also deemed physically reasonable.

From Eq. 5.3, one can find the physical foundation behind Birkhoff's explanation is actually a mechanical oscillator. Although without damping item at this stage, it forms the basis for Tamura's further extension for a non-linear wake oscillator model (Tamura & Matsui 1979). Eq. 5.4 is called "local-effect" equation, where the geometrical parameters of the near-wake (l and h) are used to determine St. Its specific form can be found different due to modifications made for different purposes (Funakawa 1969; Tamura & Shimada 1987). Nevertheless, values of l, h and St should be realistic in fulfilling a "local-effect" equation, so that the considerations reflected by the "local-effect" equation can be called physically meaningful. Such physical consideration is obviously achieved for circular cylinders. However, for sharp-edged bodies (e.g., rectangular cylinder), base on the author's knowledge, a careful examination on this point is still in lack.

In following, attempts are first made to relate the two near-wake parameters to more specific length scales in the physical world of near-wake. This will facilitate the examination work for the 2:1 rectangular cylinder to be presented in next Section.

Near-wake length $2l$

Through a search in literature reports, two measurable length scales are supposed to be very relevant to the longitudinal dimension of the near-wake behind bluff bodies. The first one is called vortex closure length l_C (see, e.g., Norberg (1998) or Hu & al. (2006)), sometimes also known as recirculation length (e.g, Xu & al. (2011)). It characterizes the position, where the time-averaged flow velocity on the wake centerline transfers from negative to positive.

The second one is the aforementioned vortex formation length l_F. In particular, it is found this scale (l_F) matches very well with the "$2l$" conception in Birkhoff's idea, as shown by Fig. 5.12. The streamwise position of the first bending of the wake, according to Birkhoff's idea, is consistent with the explanation, that, at l_F, the growing vortex draws the irrotational free-stream across the wake centerline as shown by the arrows in Fig. 5.12 (a). Moreover, Bloor & Gerrard (1966) also concluded that the end of formation region is characterized by a strongest flow fluctuation on the wake centerline, as they described: "*the intensity of the fluctuations on the axis depends on the vortex strength, the position and the size of the vortex... all these factors contribute to the appearance of a maximum* (u'/U) *at the end of the formation region*". Here, u' is standard deviation of streamwise flow fluctuation. Based on that argument, l_F can be easily quantified by wake measurements with anemometer, e.g., the hot-wire probe, on the wake centerline. For the circular cylinder, $2l = 1.5d$ (or, $1.6d$) adopted by Birkhoff corresponds well to the measured l_F in Bloor & Gerrard (1966) at $Re \approx 2 \cdot 10^4$. In a later application of Birkhoff's idea, Funakawa (1969) modified the "local-effect" equation and took a near-wake length of $2.7d$ (from cylinder center to the downstream limit) based on his flow visualization at $Re = 1.4 \cdot 10^3$. This agrees also with the measured l_F in Bloor & Gerrard (1966) at the same Re (one may notice that the near-wake length gets increased at $Re = 1.4 \cdot 10^3$, which may be the reason for Funakawa (1969)'s modification of the "local-effect" equation). Recently, Lander

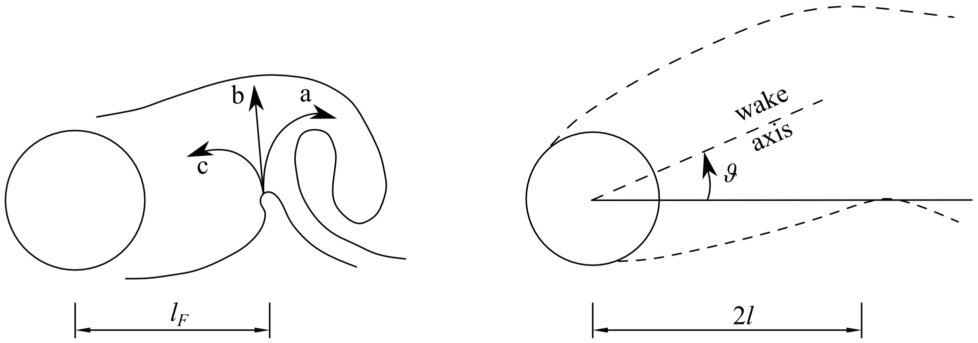

(a) (b)

Fig. 5.12: Resemblance of Gerrard's and Birkhoff's concepts for the near-wake length: (a) the vortex formation length l_F, reproduced from Gerrard (1966); (b) the near-wake length $2l$, up to the first bending of wake, reproduced from Birkhoff & Zarantonello (1957).

& al. (2016) used the long-duration time-resolved particle image velocimetry (PIV) technique to investigate the wake of a square cylinder at $Re = 5.0 \cdot 10^4$. Remarkable agreement has been found between the position of maximal v'/U and the downstream edge of formed vortex in the vorticity plot of near-wake (at a specific phase corresponding to the description of Gerrard (1966)). It is to note here, Lander & al. (2016) used v'/U rather than u'/U to identify l_F, being v' the standard deviation of across flow fluctuation.

For above reasons, the author of this thesis tends to believe, that a physically meaningful near-wake length for wake oscillator model is closely related to the vortex formation length l_F.

Near-wake width h

For the width of near-wake behind bluff body, there exist several length scales both given in a quantitatively definable manner. A well-known one is from Roshko (1954b)'s attempt for a universal Strouhal number, defined as $St^* = n_{st}h/U_S$. Here, the wake width h denotes the parallel distance between two idealized surface shear layers and is calculated by Roshko (1954a)'s hodograph theory. Another attempt for a universal Strouhal number was made by Bearman (1966), assuming the wake width as the distance between shear layers at the commencement of vortex formation and determined by Kronauer (1964)'s stability criterion. Clearly, these wake widths (either Roshko's or Bearman's) are determined through an analytical manner.

By measurements, Fage & Johansen (1928) defined the wake width as the maximum distance between the outer edges of shear layers in the near-wake region (see also the related comments in Roshko (1954b)). Here, the related shear layer is a time-averaged one, and its outer edge can be determined by analyzing the mean velocity distribution in the across-flow direction. For a circular cylinder, the measured wake width in this way is $1.45d$ at about $Re = 3.0 \cdot 10^4$ (Re roughly estimated by the author of this thesis). This width is larger than the one calculated according to Roshko's hodograph theory for a close Reynolds number (about $1.1d$ at $Re = 1.7 \cdot 10^4$, see Roshko (1954b) Table 1). Also for detecting the outer edges of shear layers, Mariotti & Buresti (2013) made the identification through the negative peaks of skewness of streamwise flow velocity fluctuation, measured from a set of monitoring points transversely arranged.

Simmons (1977) and Griffin (1981) made also attempts for a universal Strouhal number, determining the wake width through the method proposed by Calvert (1967). Here, the wake width is defined as the distance between the major peaks of transversely measured u', at a streamwise location where the static pressure reaches the minimum on the wake centerline. This position actually corresponds to the end of vortex formation region which is characterized by l_F, as pointed out by Simmons (1977) (see also Bloor & Gerrard (1966), in which different manners were outlined to find l_F). The wake width defined in this manner is facilitated for experimental measurements: for a given bluff body, the vortex formation length l_F can be first determined through $u'(x)$ on the wake centerline, then the wake width can be found by the peaks of $u'(y)$ measured at $x = l_F$ (here, x and y denote streamwise and across-flow directions). Moreover, Calvert (1967) noticed , that wake width determined in this way is closely equal to the width at which $U/U_0 = 0.6$ (here, U_0 is used to indicate the incoming flow speed and U is the mean flow velocity for a specific location). For a circular cylinder, Griffin (1981) reported that the wake width defined in this way is less dependent on Re for $500 < Re < 2 \cdot 10^5$, maintaining about $1.1d$. Based on several pieces of evidence, he further noticed that there exists a good agreement between the measured wake width with the predicted one by equation $h/d = -C_D/C_{pb}$, which is closely related to Roshko's hodograph theory (C_{pb} is the base pressure coefficient).

In addition, Williamson & Brown (1998) used an effective wake width for the universal Strouhal number. This wake width is defined as $d + 2\delta_s$, being δ_s the characteristic thickness of separated shear layer. They obtained a good collapse of the universal Strouhal number for the circular cylinder within $55 \leq Re \leq 1.4 \cdot 10^4$ by taking $\delta_s = \delta_{s,w}/2$, where $\delta_{s,w}$ is the shear layer vorticity thickness measured in the near-wake region ($1d$ downstream cylinder center).

From above literature reviews, it can be found that the definition of a near-wake width is frequently related to the efforts for a universal Strouhal number. On the other hand, it is interesting to note that the using of the "local-effect" to determine St (Birkhoff's idea) actually also reflects a universal Strouhal number. From Eq. 5.4, it can be easily written as

$$St^* = St\sqrt{h^*l^*} = 1/\sqrt{8\pi} \tag{5.5}$$

which means that multiplying St of a bluff body with its near-wake geometrical scale ($\sqrt{h^*l^*}$) will obtain $1/\sqrt{8\pi}$ as the result. Nevertheless, attempts are made now to relate the near-wake width in wake oscillator model to the more specific and quantifiable length scales.

For the circular cylinder, the wake width set in wake oscillator model was $h = 1.33d$ by Birkhoff (1953). Later, this value was varied to $h = 1.25d$ (Birkhoff & Zarantonello 1957). The same value was offered by Funakawa (1969) through flow visualization observation at $Re = 1.4 \cdot 10^3$, and was further used in Tamura & Matsui (1979). However, either $h = 1.33d$ or $h = 1.25d$ is larger than the measured ones collected by Griffin (1981) (about $1.1d$, by means of u'/U distribution at $x = l_F$), also representing the upper limit of Roshko (1954b)'s analytical results. In contrast, $h = 1.33d$ or $h = 1.25d$ is smaller than the measured value $1.45d$ by Fage & Johansen (1928), which was determined from the outer edges of shear layers. The used wake width $h = 1.25d$ (or $1.33d$) for the wake oscillator model, which is determined by "observing" the flow visualization, can be found between the two measured ones ($1.1d$ and $1.45d$).

For the square cylinder, the wake width for wake oscillator model was set $1.8d$ by Tamura & Shimada (1987) based on flow visualization reported in Mizota & Okajima (1981). On the other hand, by examining the u'/U distribution at l_F due to wake measurements reported in Lyn & al. (1995) and Lander & al. (2016), the distance between u'/U peaks is found just about $1d$ (estimated by the author of this thesis from the concerning graphics). Therefore, this measured wake width at l_F is much smaller than the $1.8d$ used by Tamura & Shimada (1987). Moreover, in Lander & al. (2016)'s measurements (Figure 15, to be more specific), one can also see a decrease of u'/U peaks' distance within the vortex formation region (from about $1.5d$ at $0.25d$ to the rear face of cylinder, to $1.0d$ at the end of vortex formation region).

From above analyses, for the near-wake width h of the wake oscillator model, it seems hard to relate it to a single length scale that can be quantified by wake measurements. However, it may be reasonable to conclude that the wake width used for the wake oscillator model should be between the one determined by peaks of u'/U distribution, and the other one corresponding to the outer edges of shear layers. This point will be further clarified later, combining with the wake measurements carried out for the 2:1 rectangular cylinder.

5.2.3 The 2:1 Rectangular Cylinder as an Examination Case

The 2:1 rectangular cylinder is used to examine one of the physical considerations in the wake oscillator model, namely the "local-effect" equation which relates St to the near-wake geometrical parameters h^* and l^*. The use of a rectangular cylinder, rather than the bridge deck model, is mainly due to its clean shape. Moreover, flow visualizations for this cylinder are available in literature reports so that comparison can be made. The wake measurements were carried out for the cylinder in the stationary state, with an incoming wind speed $U_0 \approx 9.8m/s$ (to make a difference, U_0 is especially used here). The measurements were performed with the Cobra Probe (see Section 3.2.3). Monitoring points in the wake region are outlined in Fig. 5.13, following three vertical reference lines L_{V1}, L_{V2} and L_{V3}, as well as the wake center line L_H.

Estimation of the vortex formation length l_F from wake measurements

To estimate l_F, instantaneous wind speeds need to be measured along the wake centerline (L_H). However, the used Cobra probe shows some limitations for this task, due to the inverse flow in the near-wake region. Fig. 5.14, through a time history record, shows these limitations. One can find that only the instantaneous streamwise velocity $\widetilde{U}$ of the positive sign was registered. The information about negative $\widetilde{U}$ is totally missing, replaced by unreal values close to null (for example, 99.558 s $< t <$99.572 s). The registration of lateral component $\widetilde{V}$ was also influenced: for the time segment where $\widetilde{U}$ is distorted, $\widetilde{V}$ is distorted at the same time. Fortunately, both the positive and negative values of the $\widetilde{V}$ signal were registered, although in an incomplete manner.

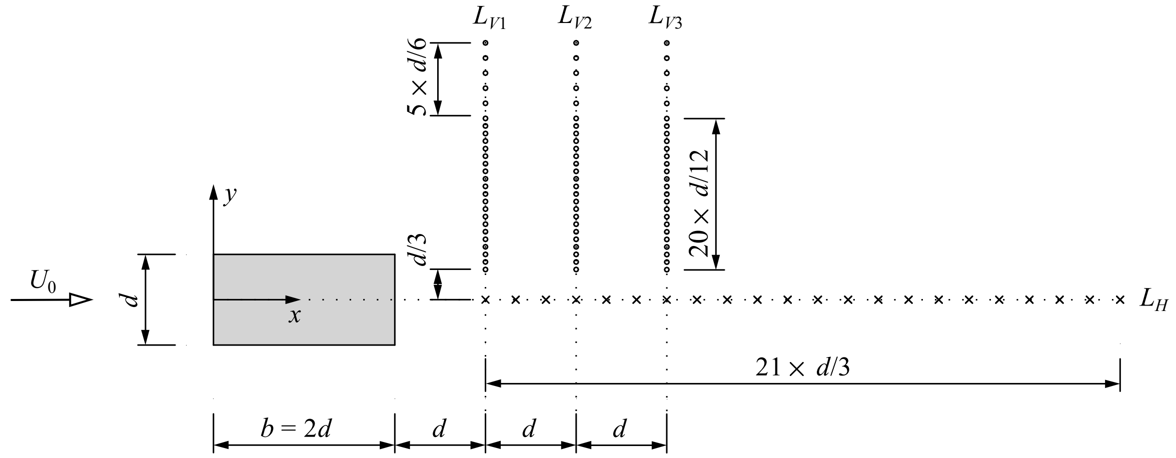

Fig. 5.13: Positions for flow velocity measurements in the wake of the 2:1 rectangular cylinder. L_{V1}, L_{V2}, L_{V3} and L_H represent reference lines for monitoring points (marked with ○ and ×).

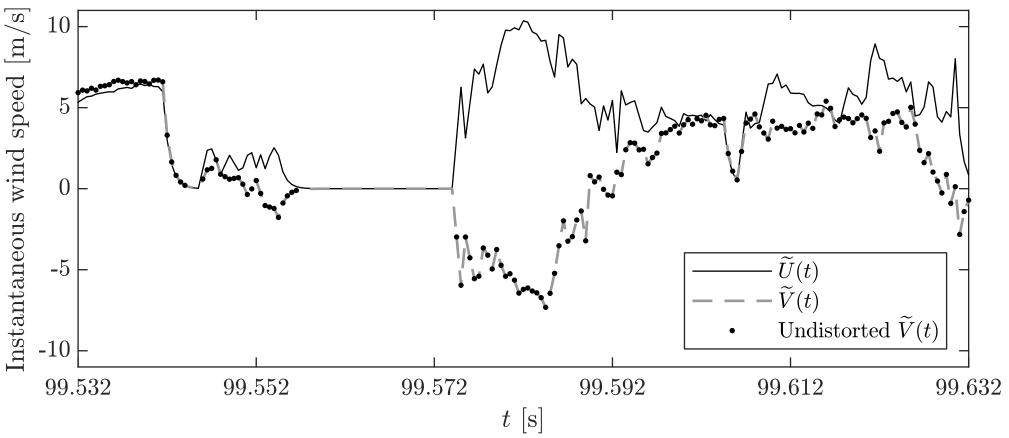

Fig. 5.14: Effect of inverse flow on the Cobra probe output for $\widetilde{U}(t)$ and $\widetilde{V}(t)$ (time history example of a monitoring point on reference line L_H, $x/d = 5$).

The lateral velocity component $\widetilde{V}$, rather than $\widetilde{U}$, is adopted for the estimation of l_F, following the same way in Lander & al. (2016). This is due to two considerations. Firstly, the registered $\widetilde{U}$ lost its negative counterpart due to instrument's limitation, so that it is unable to fulfill this task. Secondly, a careful analysis of Lyn & al. (1995)'s results for a square cylinder implies: a) the same values of l_F should be obtained, given that only the organized (or, coherent) part of $\widetilde{U}(t)$ or $\widetilde{V}(t)$ is adopted to estimate l_F; b) on the other hand, if the whole fluctuation part is considered, the result of l_F from the lateral velocity component will not change too much, but the one from the longitudinal component tends to vary. For b), it is explained that the coherent fluctuation part in $\widetilde{V}(t)$ is much stronger than its incoherent fluctuation (turbulence). It is also necessary to supplement that, a strict application of u'/U_0 for the l_F identification should only involve the organized fluctuation part as outlined in Bloor & Gerrard (1966).

Fig. 5.15 shows the distribution of std($\widetilde{V}$) along the wake centerline L_H. In calculating std($\widetilde{V}$), only the undistorted data points were used, as exemplified in Fig. 5.14. The ratio of $\widetilde{V}(t)$ data points being distorted to the total sampled population is also given in Fig. 5.15. In the same plot, the average of 10% largest peaks in time history of $\widetilde{V}(t)$ is also provided (defined with variable $\widetilde{V}_{10}$). To calculate this value, the $\widetilde{V}(t)$ data was first passed through a 10-order zero-phase Butterworth low-pass filter with cutoff frequency 50 Hz ($> 3n_{st} \approx 38.4$ Hz). The maximal peaks in the filtered signal were then identified, with a time interval not less than $0.8 \times 1/(n_{st})$ (for $x/d \geq 3.67$, Strouhal frequency n_{st} dominates the spectra of $\widetilde{V}(t)$). Subsequently, the 10% largest peaks were averaged to obtain $\widetilde{V}_{max10}$. Similarly, the minimum peaks were identified and the 10% lowest peaks were averaged to get $\widetilde{V}_{min10}$ (negative sign). Finally, $\widetilde{V}_{10} = (\widetilde{V}_{max10} - \widetilde{V}_{min10})/2$ is obtained. In Fig. 5.15, either std($\widetilde{V}$) or $\widetilde{V}_{10}$ is further normalized by U_0.

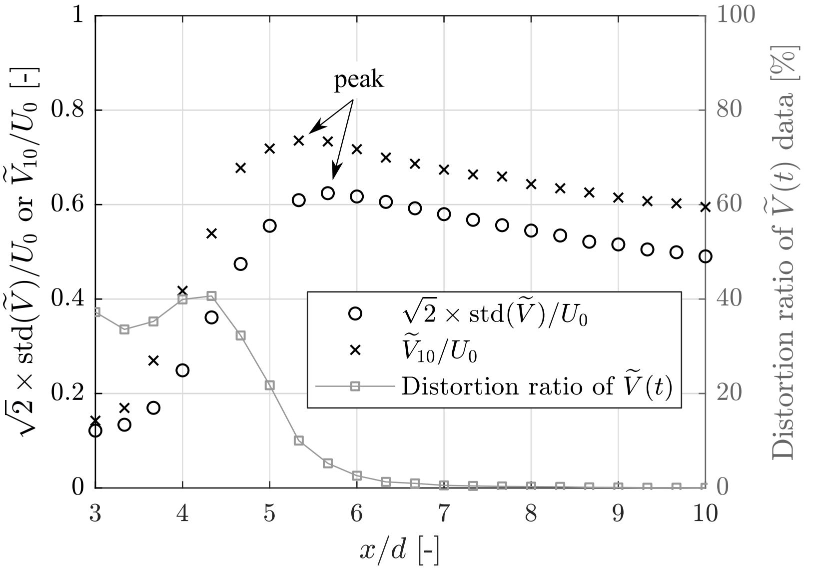

Fig. 5.15: Standard deviation of $\widetilde{V}(t)$ after removing the distorted data points, and 10% largest peaks in the filtered time histories of $\widetilde{V}(t)$. The ratio of problematic population to total sampled population is also indicated, being a rough criterion for distorted samplings $\widetilde{U}(t) < 0.1 m/s$.

The peak of std($\widetilde{V}$) appears at about $x/d = 5.67$. For $\widetilde{V}_{10}$, this is about $x/d = 5.33$, quite close to the former. In fact, the position of the $\widetilde{V}_{10}$ peak clearly represents, that, at this position, the instantaneous flow velocity in the lateral direction reaches its maximum for the whole wake centerline. Such a position agrees also with the characteristics at the end of vortex formation region: the vortex grows to its maximal strength and draws irrotational flow across the wake centerline (see also Fig. 5.12 (a)). Therefore, it is understandable that $\widetilde{V}_{10}$ is able to peak at a position quite close to the one of std($\widetilde{V}$). Moreover, the $\widetilde{V}_{10}$ value is supposed to be less influenced by the distorted data points, due to its particular calculation procedures (although not given here, the peak position of $\widetilde{V}_{10}$ of the un-filtered signal doesn't change). Upon these reasons, it is decided to take $l_F = 5.33d$ as the vortex formation length for the 2:1 rectangular cylinder (unlike the circular cylinder in Fig. 5.12 (a), l_F is defined here starting from the leading edge). By inspecting the flow visualizations in Mizota & Okajima (1981), a net vortex formation length about $l_{F,net} = 3d$ (from rear face of cylinder to the end of vortex formation region) is deemed reasonable for this cylinder. Finally, this $l_{F,net}$ is found much larger than the one for a square cylinder ($l_{F,net} = 1.21d$ or $l_{F,net} = 1.25d$, according to Lander & al. (2016) or Lyn & al. (1995), respectively).

Estimation of the near-wake width

Fig. 5.16 shows the statistical results of $\widetilde{U}(t)$ along the three vertical lines. For std($\widetilde{U}$), measurements along L_{V1}, L_{V2} and L_{V3} respectively report a peak at $y/d = 0.833$, $y/d = 0.75$ and $y/d = 0.583$. These lead to wake widths $h_{std,1} = 1.67d$, $h_{std,2} = 1.50d$ and $h_{std,3} = 1.17d$ for the three locations, defining wake width through peak distance of std$(\widetilde{U})/U_0$ (see Griffin (1981), but not limited at $x = l_F$). In line with Calvert (1967), it is found the y/d position, where std$(\widetilde{U})/U_0$

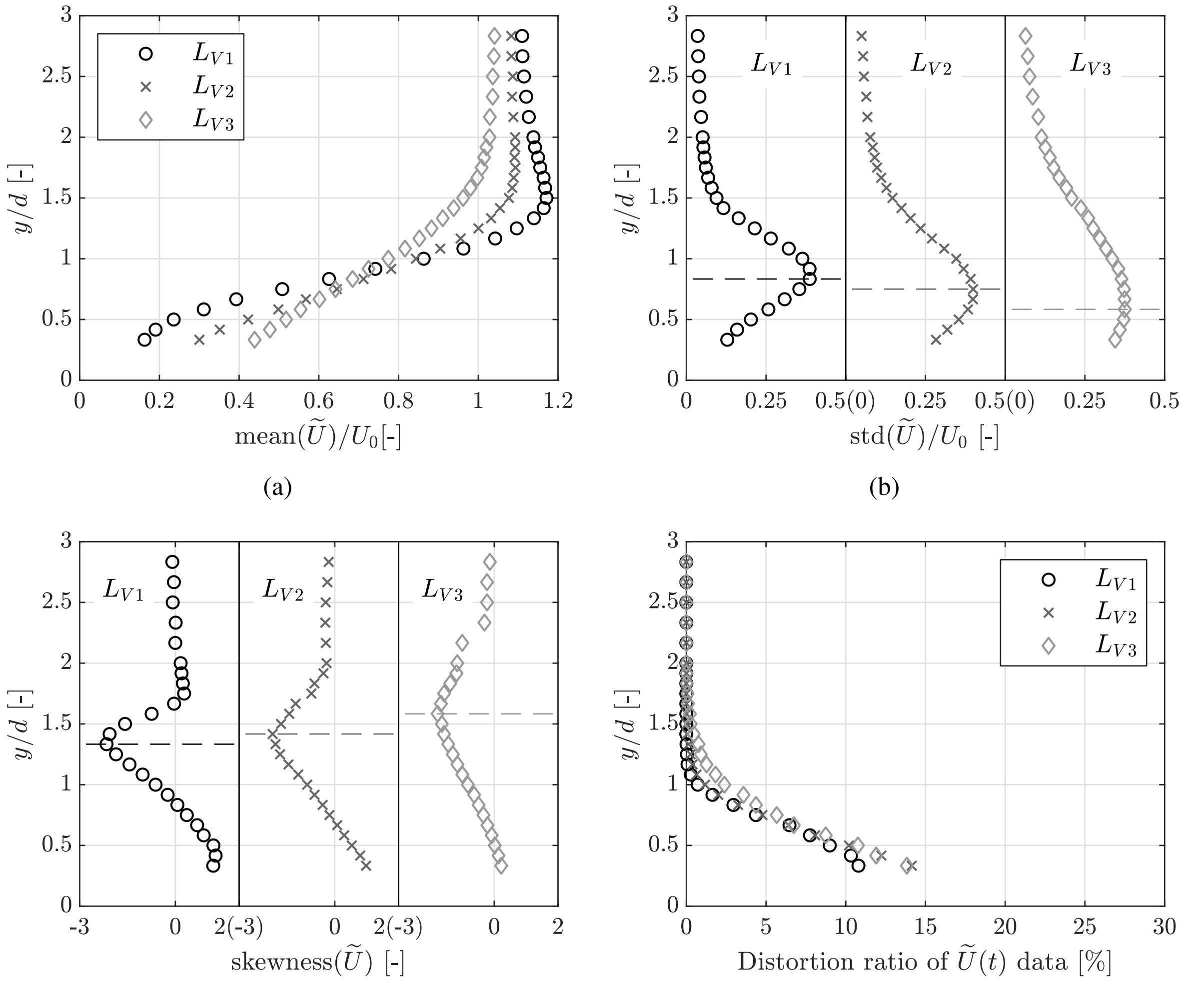

(a)

(b)

(c)

(d)

Fig. 5.16: Statistical results of $\widetilde{U}(t)$ measured at the reference lines L_{V1}, L_{V2} and L_{V3}: (a) time-averaged value; (b) standard deviation; (c) skewness; (d) distortion ratio of sampled $\widetilde{U}(t)$ population, being a rough criterion for distorted samplings $\widetilde{U}(t) < 0.1m/s$.

peaks, features a time-averaged flow velocity about $0.6U_0$ (either for L_{V1}, L_{V2} or L_{V3}). On the other hand, the time-averaged outer edges of shear layers are identified from the minus peaks of skewness of $\widetilde{U}(t)$ (Mariotti & Buresti 2013). When these minus peaks are used to define the wake width, they are $h_{sk,1} = 2.67d$, $h_{sk,2} = 2.83d$, and $h_{sk,3} = 3.17d$ for the three locations.

Still, neither h_{std} nor h_{sk} seems to agree with the one $h = 2.1d$, which is estimated from the flow visualizations of Mizota & Okajima (1981) and Shimada & Ishihara (2002). h_{std} is smaller than $2.1d$ and decreases with downstream location (similar to the square cylinder reported in Lander & al. (2016)), while h_{sk} is larger than $2.1d$ and increases with the downstream location. In contrast, if the averaged value $h_{avg} = (h_{std} + h_{sk})/2$ is considered (about $h_{avg} = 2.17d$ at the three reference lines), there is a good agreement with $h = 2.1d$. Therefore, it may be reasonable to consider h_{avg} as the measured wake width for wake oscillator model use. Finally, form Fig.5.16 (d), it is known that the used Cobra probe suffered also the inverse flow problem for $y/d < 1$. This is supposed to bring some influences, but in a limited way, to the appearing of $\mathrm{std}(\widetilde{U})/U_0$ peak on the y/d axis. The minus peaks of skewness of $\widetilde{U}(t)$ are not influenced.

Examining "TS-1987" and "TS-2018" wake oscillator models

Strouhal number St, non-dimensional near-wake width $h^* = h/d$ and length $l^* = l/d$ are constrained by the "local-effect" equations in wake oscillator models (Eq. 2.57 for "TS-1987" and Eq. 2.59 for "TS-2018"). If two of these parameters are known, the last one can be predicted by the "local-effect" equation. Supposing now h^* and St are the known ones, l^* is obtained

$$l^* = \frac{1}{4\pi h^* St^2} - b/d \qquad \text{for "TS-1987"} \qquad (5.6a)$$

$$l^* = \frac{1}{8\pi h^* St^2} \qquad \text{for "TS-2018"} \qquad (5.6b)$$

Further combined with the schematics shown in Fig. 2.19, a net near-wake length $l_{F,net}$, starting from the rear-face of body to the end of near-wake, can be defined as

$$l_{F,net}/d = 2l^* \qquad \text{for "TS-1987"} \qquad (5.7a)$$

$$l_{F,net}/d = 2l^* - 0.5b/d \qquad \text{for "TS-2018"} \qquad (5.7b)$$

Now, by putting in St and properly realistic h^* in to the "local-effect" equation, the predicted $l_{F,net}/d$ can be used to compare with the measured $l_{F,net}/d$. By doing so, it is able to know whether the concerned "local-effect" equation is physically meaningful or not.

Fig. 5.17 (a) shows the predicted $l_{F,net}$ for the 2:1 rectangular cylinder, by assigning $St = 0.079$, $h^* = 2.1$, and allowing at the same time a variation of h^* up to ± 30%. At $h^* = 2.1$, "TS-1987" predicts about $l_{F,net} = 8$, which is much larger than the measured one. "TS-2018" gives better results about $l_{F,net} = 5$ for $h^* = 2.1$, which is however still larger than the measured one.

Increasing h^* to about 2.7, predictions of both models tend to approach the measured one but still not reached. Since h^* also needs to hold its physical representation, it is less meaningful to further increase it. Nevertheless, if it also allows a variation up to ± 30% for the measured $l_{F,net}$, "TS-2018" is able to fulfill the so-called physical consideration for $h^* > 2.4$, while "TS-1987" seems still not reasonable. The similar condition is also encountered for the square cylinder, as shown in Fig. 5.17 (b). There, measured value of $St = 0.132$ and $l_{F,net} = 1.21d$ is according to Lander & al. (2016)'s experiments, while the basic value $h^* = 1.8$ is adopted due to Tamura & Shimada (1987).

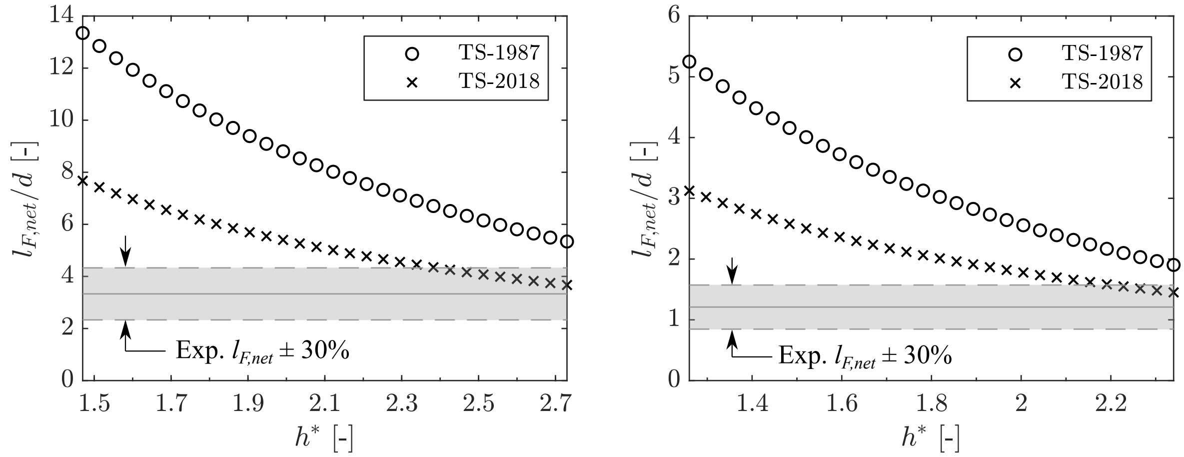

(a) 2 : 1 rectangular cylinder (b) Square cylinder

Fig. 5.17: Predicted and measured net near-wake length $l_{F,net}$. "∘" and "×" are the predicted ones (being h^* ± 30% varied), gray solid line is the measured one and the gray area denotes a ± 30% relaxation of it. (a) 2:1 rectangular cylinder: $h^* = 2.1$, $St = 0.079$, measured $l_{F,net}/d = 3.33$. (b) square cylinder: $h^* = 1.8$ reported by Tamura & Shimada (1987), $St = 0.132$ and $l_{F,net}/d = 1.21$ according to Lander & al. (2016).

In general, it is to conclude that, for the existing wake oscillator models, the physical consideration in the "local-effect" equations is less well respected on sharp-edge bodies such as square or 2:1 rectangular cylinder. The modified "TS-2018" form behaves better than the original one ("TS-1987") in this examination, but it still needs to be further improved in this regard.

5.3 Proposed Method for Estimating the f Parameter by Means of Wake Measurements

5.3.1 Rationale of the Method

In developing the non-linear wake oscillator, Tamura & Matsui (1979) assumed that the unsteady lift coefficient on the cylinder is proportional to the effective rotation angle of the near-wake lamina through a parameter f. That is $C_{L,un}(\tau) = f\left(\vartheta(\tau) - \frac{Y'(\tau)}{V}\right)$, as can be viewed in Eq. 2.55a (or Eq. 5.1a). For a stationary body and assuming the near-wake rotate to its maximum angle ϑ_0, there is $C_{L0} = f\vartheta_0$, being C_{L0} the amplitude of lift coefficient due to vortex shedding. It is easy to understand that the value of f can be directly calculated if ϑ_0 is known

$$f = \frac{C_{L0}}{\vartheta_0} \tag{5.8}$$

In Mannini & al. (2018a), it has been noticed that instantaneous flow visualization can be used to estimate this ϑ_0 value. However, the related equipment is not available in the current wind tunnel facility. Here, a new approach is conceived for a rough estimation of ϑ_0, adopting only simple anemometer instruments like Cobra or hot-wire probe.

The key of the proposed method is to detect the limit positions of the outer edge of shear layer during the near-wake vibration, based on the special velocity variation of monitoring points set close to these positions. Fig. 5.18 illustrates these limit positions, corresponding respectively to the maximal anti-clockwise and clockwise rotation of the near-wake during the steady vibration state. Assuming right now two monitoring points y_{U1} and y_{U2} in Fig. 5.18 (a), the difference of the measured flow velocity variations are supposed to be:

- compared with y_{U1}, the minimal instantaneous velocity at y_{U2} will show an apparent decrease. This is because the y_{U2} point is periodically enclosed into the upper shear layer (where the flow velocity varies intensively) during the near-wake rotation, while the y_{U1} point stays always outside the outer edge of shear layer.

On the other hand, for the assumed y_{L1} and y_{L2} points in Fig. 5.18 (b), the difference would be:

- compared with y_{L1}, the maximal instantaneous velocity at y_{L2} will show an apparent decrease. This is because the y_{L1} point is still able to stay periodically outside the outer edge of shear layer so that the maximal instantaneous velocity can be as high as the other monitoring points above it. However, this is not possible for the y_{L2} point, which stays always inside the outer edge of shear layer.

In practice, a set of monitoring points can be assigned laterally in the near-wake region. By analyzing the minimal and maximal instantaneous velocity distribution, the two limit positions of shear layer outer edge can be then roughly located. As also shown in Fig. 5.18, the thickness of shear layer actually increases with downstream position. This is supposed to influence the sharpness of the previously mentioned "apparent decrease" feature in the velocity distribution.

To relate the measured y_U and y_L to the ϑ_0 angle in a wake oscillator model, some features in wake oscillator model must be assumed for a physical near-wake. These include: a) the wake

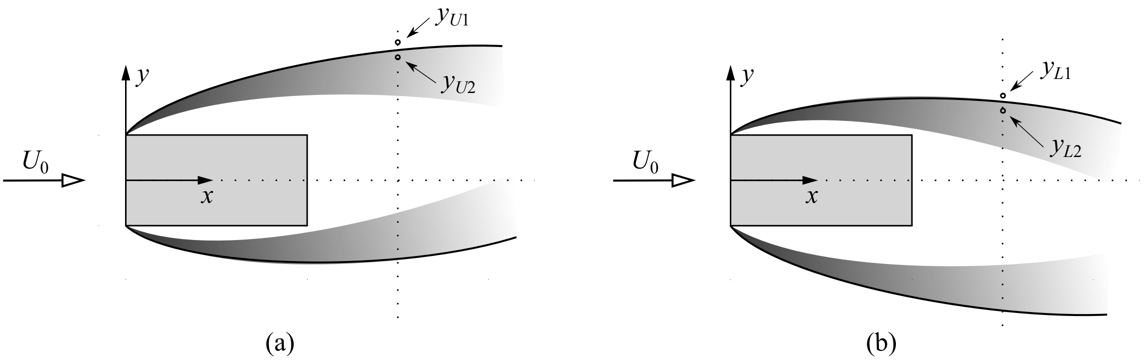

Fig. 5.18: Schematics of near-wake rotation at two limit states: (a) maximal anti-clockwise rotation; (b) maximal clockwise rotation. The black solid curve indicates the outer edge of shear layer, being the thickness of shear layer also illustrated by gray area. ∘ denotes monitoring point.

width at a specific downstream position does not change apparently during the near-wake vibration; b) the instantaneous near-wake centerline does not show apparent bending during the near-wake vibration. Thus, combined with the schematics of Fig. 5.19, the following relationships can be approximately built

$$y_U = x_1 \tan(\vartheta_0) + \frac{h'}{2} \cdot \frac{1}{\cos(\vartheta_0)} \tag{5.9a}$$

$$y_L = x_1 \tan(-\vartheta_0) + \frac{h'}{2} \cdot \frac{1}{\cos(-\vartheta_0)} \tag{5.9b}$$

Here, y_U and y_L are the two limit positions of shear layer outer edge (see Fig. 5.18), x_1 the distance between O and the vertical reference line where y_U and y_L is measured, $h'/2$ the distance of shear layer outer edge to the instantaneous near-wake centerline. Subtracting above two equations, ϑ_0 can be obtained as

$$\vartheta_0 = \arctan\left(\frac{y_U - y_L}{2x_1}\right) \tag{5.10a}$$

$$\text{or, } \vartheta_0 \approx \frac{y_U - y_L}{2x_1} \qquad \text{for small value of } \vartheta_0 \tag{5.10b}$$

After ϑ being determined, the value of f can be easily calculated from Eq.5.8, since C_{L0} can be measured from static tests.

5.3.2 The 2:1 Rectangular Cylinder as a Case study

The wake measurements for the 2:1 rectangular cylinder were used here to exhibit the above method (monitoring points see Fig. 5.13). As previously stated, the key step is to locate the y_U

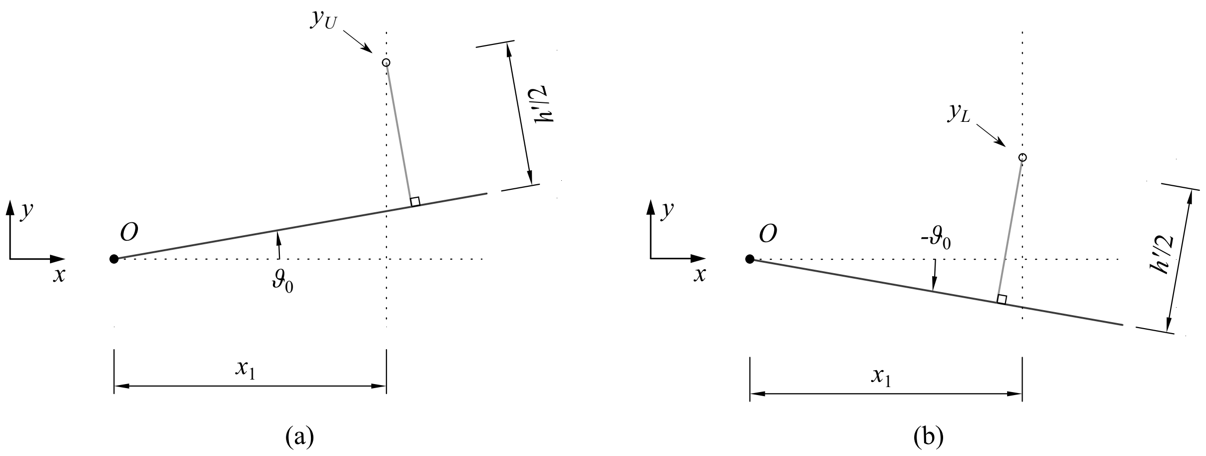

Fig. 5.19: Schematics for the relationship between ϑ_0 in wake oscillator model and the measured y_U and y_L positions. O is the pivot point of near-wake lamina, and the black solid line is the instantaneous near-wake centerline.

and y_L position, according to the characteristic "apparent decrease of maximal and minimal instantaneous flow velocities when an anemometer probe is transversely moved towards the wake centerline". To find these maximal and minimal instantaneous flow velocities, the $\widetilde{U}(t)$ data was first passed through a 10-order zero-phase Butterworth low-pass filter. The cutoff frequency is set at 50 Hz ($> 3n_{st} \approx 38.4$ Hz). Then the maximal and minimal peaks were then respectively identified, with a restriction on the minimum time interval $0.8/n_{st}$. These measures aim to utilize only the organized part of $\widetilde{U}(t)$, since the turbulent part of $\widetilde{U}(t)$ is able to influence the maximal or minimal value of a signal a lot. Finally, the averaged value of maximal (or minimal) peaks over the recording time length was used as representatives for the maximal (or minimal) instantaneous flow velocity, denoted by $\widetilde{U}_{max}$ (or $\widetilde{U}_{min}$).

The $\widetilde{U}_{max}$ and $\widetilde{U}_{min}$ distributions at the reference line L_{V1} are given in Fig. 5.20 (a). There, an apparent decrease of $\widetilde{U}_{min}$ can be found at about $y/d = 1.5$, while for $\widetilde{U}_{max}$ this occurs at about $y/d = 1.0$. In the same plot, the negative peak position of skewness of $\widetilde{U}(t)$ is also given, which is about $y/d = 1.33$. It is to remind that this peak position corresponds to the time-averaged position of shear layer outer edge, and one can find its value falls correctly into the range delimited by $y/d = 1.0$ and $y/d = 1.5$. At the reference line L_{V2}, the positions for a "apparent decrease" of $\widetilde{U}_{max}$ and $\widetilde{U}_{min}$ is difficult to locate. As previously mentioned, this is probably due to the increased shear layer thickness, leading to the flow velocity variation in the shear layer less intense.

The determination of ϑ_0 depends on the distance x_1 between the pivot point O and the reference line. This is influenced by the specific form of a wake oscillator model. Taking the reference line L_{V1}, the distance to O is $x_1 = 3d$ for "TS-1987" form and $x_1 = 2d$ for "TS-2018" form.

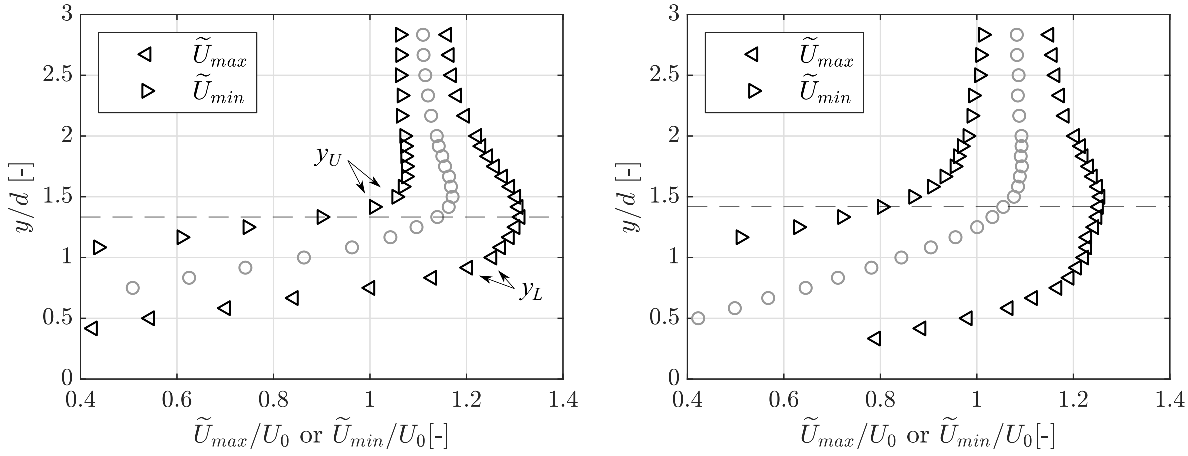

(a) Reference line L_{V1}

(b) Reference line L_{V2}

Fig. 5.20: Maximal and minimal instantaneous flow velocity ($\widetilde{U}_{max}$ and $\widetilde{U}_{min}$) at the reference lines L_{V1} and L_{V2}. Dashed line indicates the negative peak location of skewness of $\widetilde{U}(t)$ (see Fig. 5.16 (c)). The mean value of $\widetilde{U}(t)$ was also provided for reference (gray ○ marker).

Tab. 5.1 shows the estimated ϑ_0 adopting Eq. 5.10, and the further calculated f value adopting Eq. 5.8 (C_{L0} measured from the static tests). To be conservative, small ranges of y_U and y_L are used rather than specific values. For the "TS-2018" form, the estimated ϑ_0 is between 5.97° and 8.35°, leading to a f parameter about 7.0 to 9.8. On the other hand, due to the larger x_1, the estimated ϑ_0 is smaller for "TS-1987" from, thus resulting in a higher value of f.

Tab. 5.1: Estimated f value from the wake measurements for the 2:1 rectangular cylinder at the reference line L_{V1} (U_0 = 9.8 m/s)."O"is the pivot point of near-wake lamina. "S.P." and "C." respectively mean "Stagnation Point" and "Centroid".

Wake Oscillator model	O	y_U/d [-]	y_L/d [-]	x_1/d [-]	ϑ_0 [°]	C_{L0} [-]	f [-]
TS-1987	S.P.	1.417-1.5	0.917-1.0	3.0	3.98-5.57	1.02	10.50-14.68
TS-2018	C.			2.0	5.97-8.35		7.00-9.78

It is to note that, for the "TS-2018" form, the estimated f value is much lower than the one $f = 18$ identified according to Mannini & al. (2018a)'s method ("calibration with a set of aeroelastic tests of high Scruton number", see Fig. 5.3). However, Mizota & Okajima (1981)'s experimental results seems to support the estimated low value of f. There, one can estimate a ϑ_0 about 5.5° from the instantaneous streamline plots (Figure 16 in Mizota & Okajima (1981)). Combined with the reported $C_{L0} = 1.0$, a value of $f = 10.4$ is obtained. Moreover, Shimada & Ishihara (2002)'s CFD results seem also to imply a low value of f, where $\vartheta_0 \approx 3.0°$ at the moment of maximum lift can be estimated (Figure 7 of Shimada & Ishihara (2002)). With $C_{L0} \approx 0.62$ (Figure 6 (c) of Shimada & Ishihara (2002)), a value of $f = 11.8$ is finally obtained.

To summarize, for the 2:1 rectangular cylinder studied here, the proposed method provided a f value which is qualitatively comparable with the ones inferred from two sources of literature reports. Despite the fact that this value is quantitatively lower than the “calibrated” one, it qualitatively supports the using of a comparably high f value for this 2:1 rectangular cylinder, rather than somewhat $f \approx 1$ which is originally used for the circular cylinder. Moreover, in next section it will show that, if the form of wake oscillator model is further modified, the “calibration method” will result in a f closer to the measured one. Finally, it is to note that, from the Figure 14 and 16 in Mizota & Okajima (1981), one can observe a phase lag between the unsteady lift and the near-wake rotation. This issue will be particularly discussed in Section 5.5.1.

5.4 Further Modifications to the Wake Oscillator Model

5.4.1 Elaboration of the Modifications

Despite the good prediction capability of “TS-2018” in modeling the unsteady galloping due to the interaction with VIV (see Section 5.1), further modifications to the wake oscillator model are motivated by the analyses presented in Section 5.2 and 5.3. These modification are applicable for rectangular cylinders with small side-ratio or similar bluff bodies, for which the flow separation happens at the leading edges and no apparent flow reattachment occurs on the afterbody.

Fig. 5.21 shows the schematic for the further modified wake oscillator model. The concerned modifications include: a) the pivot point O is put back to the stagnation point as in “TS-1987”; b) the length scale $b+2l$ (starting from stagnation point to the end of near-wake) is used for calculating the restoring force F_L; c) the position of restoring force F_L being applied is $(b+2l)/4$ to the pivot point; d) only the net near-wake length, starting from the rear-face of body to the end of near-wake, is considered to calculate the inertia of moment of the wake lamina.

These adjustments are supposed to be supported by the following arguments:

a) Unlike circular cylinder, rectangular cylinders have flow separation at the leading edge. Therefore, rotation of near-wake about the stagnation point is supposed to be more reasonable than about the centroid. The operation of moving the pivot point from centroid to stagnation point was already made in the “TS-1987” form (Tamura & Shimada 1987), when Tamura’s wake-oscillator model (which was originally developed based on circular cylinder (Tamura & Matsui 1979)) was for the first time applied to a square cylinder.

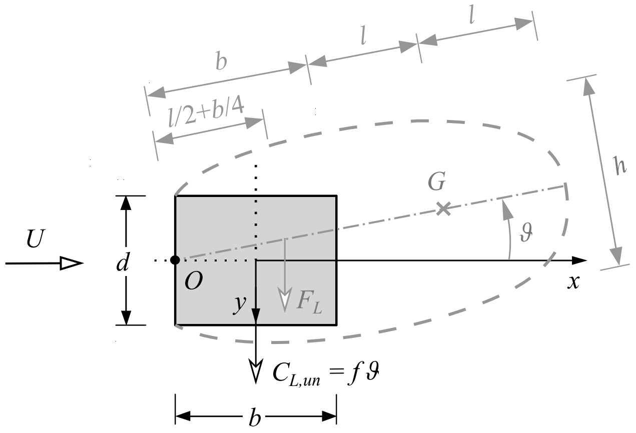

Fig. 5.21: Schematic of the further “Modified” wake oscillator model (on stationary body). See also Fig. 2.19, for comparison with “TS-1987” and “TS-2018” form.

b) Considering the flow field delimited by the shear layers up to the separation points is able to achieve a better analogy to a complete airfoil. Therefore, the portion “b” is included for the chord length, which is used to calculate the restoring force according to airfoil theory.

c) In airfoil theory, the lift acts at the one-fourth of chord to the leading edge.

d) Part of near-wake is occupied by the body itself, so that it is more reasonable to use the net near-wake length to calculate the inertia of moment.

Due to above adjustments, the restoring force for the near-wake lamina becomes $F_L = \frac{1}{2}\rho U^2 \cdot (2l+b)\cdot 2\pi\vartheta$ (the theoretical lift coefficient of a thin airfoil with displaced angle of attack ϑ is $2\pi\vartheta$), and its torque about O is $F_L \cdot \frac{1}{4}(2l+b) = -\frac{1}{2}\rho U^2(2l+b)2\pi\vartheta \cdot \frac{1}{4}(2l+b)$. On the other hand, the moment of inertia about O can be simplified as $2\rho hl\cdot(l+b)^2$. Now, invoking Newton’s second law for the rotation degree, there is $2\rho hl(l+b)^2 \cdot \ddot{\vartheta} = -\frac{1}{2}\rho U^2(2l+b)2\pi\vartheta \cdot \frac{1}{4}(2l+b)$. This equilibrium equation can be written in the same form of Eq. 5.3

$$I_\vartheta \ddot{\vartheta} + k_\vartheta \vartheta = 0$$

but with $I_\vartheta = 2\rho hl(l+b)^2$ and $k_\vartheta = \frac{1}{4}\pi\rho U^2(2l+b)^2$. The corresponding oscillation frequency for the near-wake lamina is given by

$$n_{st} = \frac{1}{2\pi}\sqrt{\frac{k_\vartheta}{I_\vartheta}} = U\sqrt{\frac{(2l+b)^2}{32\pi hl(l+b)^2}}$$

And the “local-effect” equation for Strouhal number becomes

$$St = \sqrt{\frac{(2l^* + b/d)^2}{32\pi h^* l^*(l^* + b/d)^2}} \tag{5.11}$$

The rest extension to a non-linear wake oscillator and the coupling to an oscillation body follows the same procedures in Tamura & Matsui (1979). The new expression of β is obtained as

$$\beta = \frac{2\sqrt{2}f(l^* + b/d)}{\pi^2(2l^* + b/d)^2} \tag{5.12}$$

The expression of λ, which is decided by the distance between O and G, holds the same as the "TS-1987" form (in Tamura & Shimada (1987), it is put $b/d = 1$ for the square cylinder)

$$\lambda = \frac{1}{l^* + b/d} \tag{5.13}$$

The two coupled equations, which govern the transverse motion of the cylinder and the near-wake rotation, maintain the same as Eq. 2.55. For convenience, they are re-written here

$$\begin{aligned} &Y'' + 2\zeta_0 Y' + Y = \frac{V^2}{m^*} f\left(\vartheta - \frac{Y'}{V}\right) + \frac{V^2}{m^*} C_{Fy}^{QS}(\frac{Y'}{V}) \\ &\vartheta'' - 2\beta\upsilon\left(1 - \frac{4f^2}{C_{L0}^2}\vartheta^2\right)\vartheta' + \upsilon^2\vartheta = \lambda Y'' + \upsilon^2\frac{Y'}{V} \end{aligned}$$

Above equations vary not among "TS-1987", "TS-2018" and the new "Modified" form. The differences of thees three forms are exhibited by the expressions of β and λ, as well as the "local-effect" equation $St(h^*, l^*)$. They are summarized in Tab. 5.2, including also notations about O, l_{FL}, l_I and $l_{FL,O}$ (see caption of Tab. 5.2). It is to remind that the definition of l is slightly different for "TS-2018" form (see Fig. 2.19 and Fig. 5.21).

Tab. 5.2: Comparison of different forms of wake oscillator models. Meanings of symbols: O, pivot position of near-wake lamina; l_{FL}, wake length scale used for calculating the restoring force F_L; $l_{FL,O}$, distance between the position F_L being applied and O; l_I, length of wake lamina used to calculate I_ϑ. $St(h^*, l^*)$ represents the "local-effect" equation, relating St to h^* and l^*. "S.P." and "C." represent respectively abbreviation of "Stagnation Point" and "Centroid".

	O	l_{FL}	$l_{FL,O}$	l_I	$St(h^*, l^*)$	β	λ
"TS-1987"	S. P.	$2l$	$l+b$	$2l$	$St^2 = \frac{1}{4\pi h^*(l^*+b/d)}$	$\frac{f}{2\sqrt{2}\pi^2 l^*}$	$\frac{1}{b/d+l^*}$
"TS-2018"	C.	$2l$	$\frac{l}{2}$	$2l$	$St^2 = \frac{1}{8\pi h^* l^*}$	$\frac{f}{\sqrt{2}\pi^2 l^*}$	$\frac{1}{l^*}$
Modified	S. P.	$2l+b$	$\frac{2l+b}{4}$	$2l$	$St^2 = \frac{(2l^*+b/d)^2}{32\pi h^* l^*(l^*+b/d)^2}$	$\frac{2\sqrt{2}f(l^*+b/d)}{\pi^2(2l^*+b/d)^2}$	$\frac{1}{b/d+l^*}$

5.4.2 Prediction Capability

The prediction capability of the new "Modified" form is examined by comparing with the wake oscillator model of "TS-2018" form, in case of the 2:1 rectangular cylinder. To achieve a fair comparison, all the parameter (C_{Fy}^{QS}, $C_{L0}(Re)$, $St = 0.079$ and $h^* = 2.1$) except f are maintained the same as the "TS-2018" form (see Section 5.1.1). The key parameter f is re-calibrated for the "Modified" form according to Mannini & al. (2018a)' method, resulting in $f = 16$.

Numerical integration was then carried out for test cases of varied Sc, showing a high agreement with the predictions of "TS-2018" form with $f = 18$. Fig. 5.22, for brevity and clarity reason, exemplifies only several test cases with numerical solutions attained from small initial conditions. Considerations for the selected test cases are: a) $Sc = 5.1$, the lowest Scruton number reached in experiments, which is the best choice to examine the *asynchronous quenching*

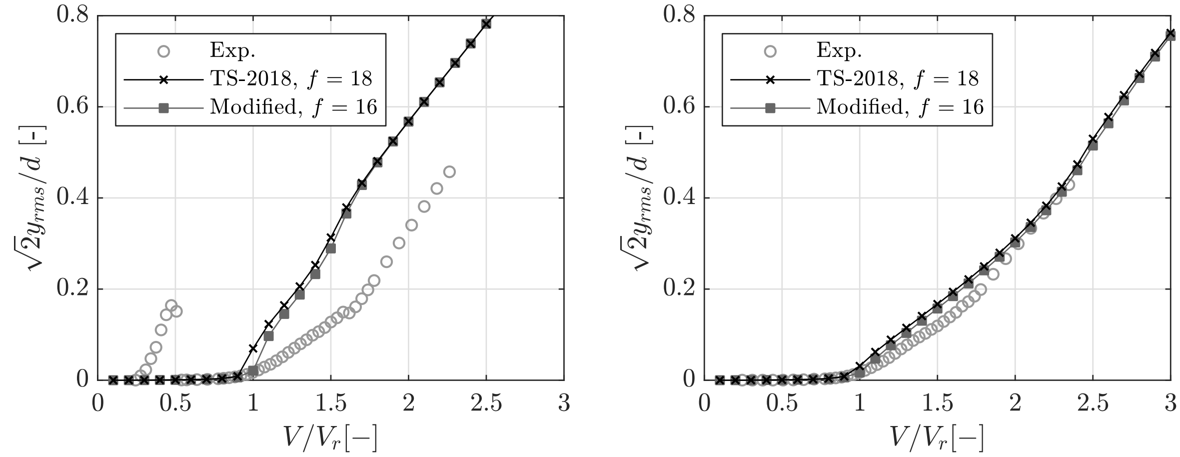

(a) $Sc = 5.1$ (b) $Sc = 107.1$

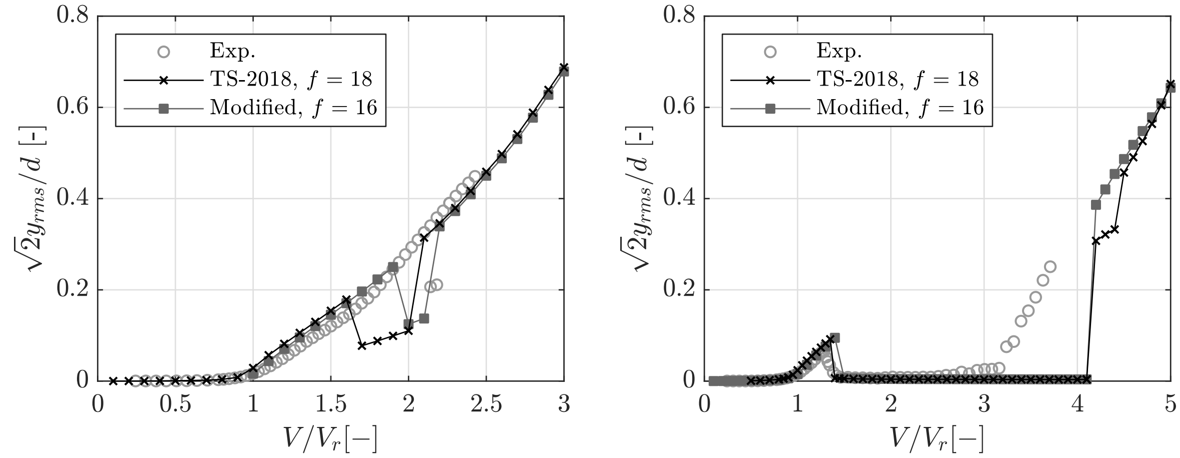

(c) $Sc = 127.9$ (d) $Sc = 200.7$

Fig. 5.22: Selected cases for comparing the prediction capability of the new "Modified" wake oscillator with "TS-2018" from. All numerical solutions are attained with small initial conditions.

effect of wake oscillator model (postponement of galloping onset until V_r); b) $Sc = 107.1$, a key Scruton number, up to which the "Full-Interference" is maintained; c) $Sc = 127.9$, a slightly higher Scruton number than the former, for which the "Partial-Interference" tends to occur; d) $Sc = 200.7$, the highest Scruton number reached in the wind tunnel tests. Clearly, the performance of the new "Modified" wake oscillator model is comparable as the "TS-2018" form. Interestingly, the "Modified" one with $f = 16$ actually gives nearly the same predictions as the "TS-2018" form with $f = 18$, except at several wind speeds where the amplitudes change intensely (e.g., Fig. 5.22 (c) around $V/V_r = 2$).

5.4.3 Physical Considerations for the Near-wake

From above numerical results, it is reasonable to conclude that the new "Modified" wake oscillator model maintains a comparable prediction capability as the "TS-2018" form, in dealing with the unsteady galloping interacted with VIV. In fact, the improvements achieved by the new "Modified" form are mainly about the physical considerations of the near-wake.

First of all, the value $f = 16$ obtained by Mannini & al. (2018a)'s "calibration" method can be found closer to the measured one f = 10.5-14.68 (see Tab. 5.1, with pivot point O at stagnation point). This improvement is mainly due to the movement of pivot point O from the centroid to the stagnation point. Nevertheless, one can find $f = 16$ is still higher than the measured one. A detailed discussion on the possibilities leading to this difference is presented in Section 5.5.1.

The second improvement is for the physical representation of the "local-effect" equation Eq. 5.11. Fig. 5.23 (a) shows the examination results for the 2:1 rectangular cylinder (as Fig. 5.17). For h^* close to 2.1, one can find the predicted net near-wake length $l_{F,net}$ by the Eq. 5.11 is closely around the measured one $l_{F,net} = 3.33d$. Very interesting is that, such an achievement is also reached for the square cylinder as shown by Fig. 5.23 (b). This improvement is quite apparent, in comparison with the predictions of "TS-1987" and "TS-2018" (see Fig. 5.17).

5.5 Discussion

5.5.1 On Identifying the f Parameter

In Section 5.3, it was found the parameter f identified through the maximal near-wake rotation tends to be lower than the one obtained according to the "calibration" method proposed by Mannini & al. (2018a), either for the "TS-2018" or the new "Modified" form wake oscillator model. The possible reasons contributed to this difference are discussed here.

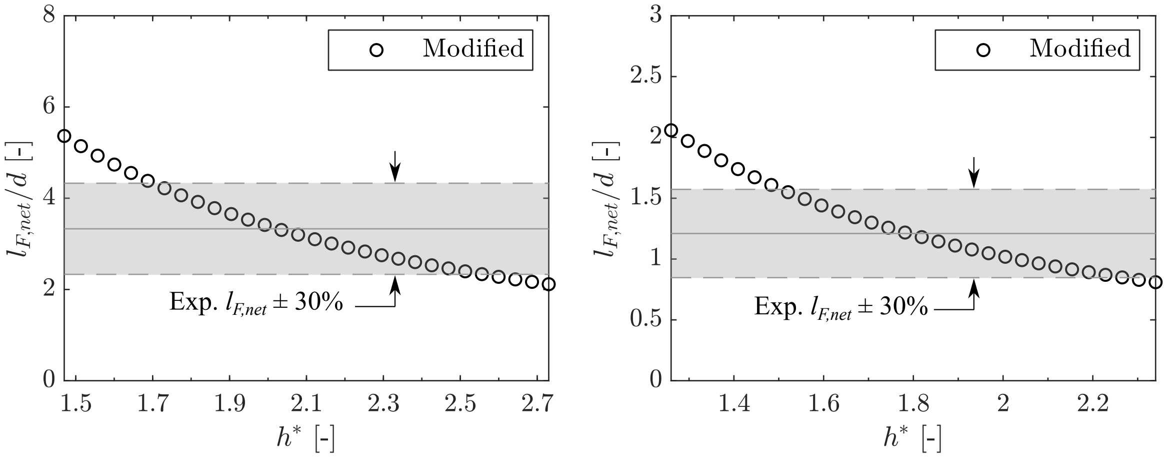

(a) 2:1 rectangular cylinder (b) square cylinder

Fig. 5.23: The calculated net near-wake length $l_{F,net}$ $(= l_l = 2l)$ through the "local-effect" equation of the "Modified" wake oscillator model, by setting the base value of h^* with ± 30% variation. Gray solid line denotes the measured $l_{F,net}$ and the gray dashed lines correspond to a ± 30% variation of it. (a) 2:1 rectangular cylinder: St = 0.079, measured $l_{F,net}/d = 3.33$, base value $h^* = 2.1$; (b) square cylinder: St = 0.132, measured $l_{F,net}/d = 1.21$, base value $h^* = 1.8$.

Phase lag between near-wake rotation and the resulting unsteady lift

As previously mentioned, in Figure 14 and 16 of Mizota & Okajima (1981), it is able to notice a phase lag between the unsteady lift and the near-wake rotation for the 2:1 rectangular cylinder. In contrast, in Tamura's non-linear wake oscillator model (Tamura & Matsui 1979), there is no consideration for this phase lag, due to the assumption that *"the unsteady lift coefficient is obtained in proportion to the angular displacement through the constant factor f"*, namely $C_{L,un}(t) = f \cdot \vartheta(t)$ for stationary cylinder.

To examine the effect of this possible phase lag, the equation can be varied as

$$C_{L,un}(t) = f \cdot \vartheta(t + t_{lag}) \tag{5.15}$$

for periodical motion of near-wake. The phase lag is included through the time lag t_{lag}, which depends on the oscillation frequency of the wake lamina n_{vs}. And it is easy to understand that the phase lag is $\varphi_{lag} = 2\pi n_{vs} t_{lag}$ for this situation. For oscillation cylinder with natural frequency n_0, the unsteady lift is determined by the effective near-wake rotation $\vartheta_{eff} = \vartheta - Y'/V$. Further invoking the non-dimensional time $\tau = 2\pi n_0 t$, the above equation can be written as

$$C_{L,un}(\tau) = f \cdot \vartheta_{eff}(\tau + \tau_{lag}) \tag{5.16}$$

Put this equation back to the two-coupled equations (Eq. 2.55) for tamura's nonlinear wake oscillator model, there are

$$Y'' + 2\zeta_0 Y' + Y = \frac{V^2}{m^*} f \vartheta_{eff}(\tau + \tau_{lag}) + \frac{V^2}{m^*} C_{Fy}^{QS}(\frac{Y'}{V}) \tag{5.17a}$$

$$\vartheta'' - 2\beta\upsilon\left(1 - \frac{4f^2}{C_{L0}^2}\vartheta^2\right)\vartheta' + \upsilon^2\vartheta = \lambda Y'' + \upsilon^2\frac{Y'}{V} \tag{5.17b}$$

The assignment of a specific phase lag into the mathematical model can be therefore performed by the reduced time lag $\tau_{lag} = n_0/n_{vs} \cdot \varphi_{lag}$, provided that n_{vs} is known in advance. Qualitatively speaking, n_{vs} could be either n_o or $n_{st} = USt/d$ for steady oscillation state, depending on whether the synchronization between cylinder and wake lamina occurs or not (n_o is the oscillation frequency of the cylinder). However, for transient behaviors, n_{vs} may transfer between n_{st} and n_o. Even more crucial is that, there is no clue indicating that the phase lag for a stationary body is maintained the same as an oscillation body. Perhaps, an equation must be established to describe how φ_{lag} involves with the oscillation state. Nevertheless, a sensitivity study of φ_{lag} aiming at particular oscillation state is still possible.

The 2:1 rectangular cylinder with $Sc = 107.1$ is considered for such a sensitivity study. The adopted wake oscillator model is the "TS-2018" from (same conclusions are expected for the new "Modified" form). The chosen reduced velocity range is from $V/V_r = 1.1$ to $V/V_r = 4.0$. From Fig. 5.4 (b), it is known for this particular situation the wake oscillator model exhibit "Full-Interference" behavior. It was also confirmed that the steady-state solutions of either Y or ϑ are characterized with a single frequency $n_o \approx n_0$ within $1.1 \leq V/V_r \leq 4.0$. For the sensitivity study in object, all the other parameters except φ_{lag} to be introduced, are maintained the same as in Section 5.1. In contrast, the initial condition is right now set with a large displacement ($[Y, Y', \vartheta, \vartheta'] = [tan(15°)V, 0, 0, 0]$) for each velocity point, so that the dominant frequency around n_0 is supposed to be maintained for the transient process at the beginning of numerical integration. The investigated phase lag φ_{lag} is within $-\pi/2$ to $\pi/2$ (too large magnitude of φ_{lag} seems unrealistic). The numerical integration was carried out with two rounds for each velocity points. The first round serves to find n_o by setting $\tau_{lag} = n_0/n_{vs} \cdot \varphi_{lag}$ with $n_{vs} = n_0$. In the second round, the more accurate n_o is set for n_{vs} and the integration is then repeated.

Fig. 5.24 shows the results of this sensitivity study. One can find that the introduced phase lag plays an important role in the amplitude solutions of wake oscillator model (a magnitude of φ_{lag} like $\pi/4$ can already bring apparent influence). In general, a positive φ_{lag} tends to increase the amplitude while a negative φ_{lag} works in the opposite way. The oscillation frequency is also influenced, but in a very limited extent. It is right now to remind that, in the "calibration" method for determining the f parameter, the alignment of amplitude slope of numerical solutions to experimental ones is the very important criterion. Because of this, one can expect a different value of f being calibrated, if a non-null phase lag was considered in the wake oscillator model. For the example of the studied 2:1 rectangular cylinder, if a negative φ_{lag} was set into the wake oscillator model, a lower value of f could be expected from the calibration process.

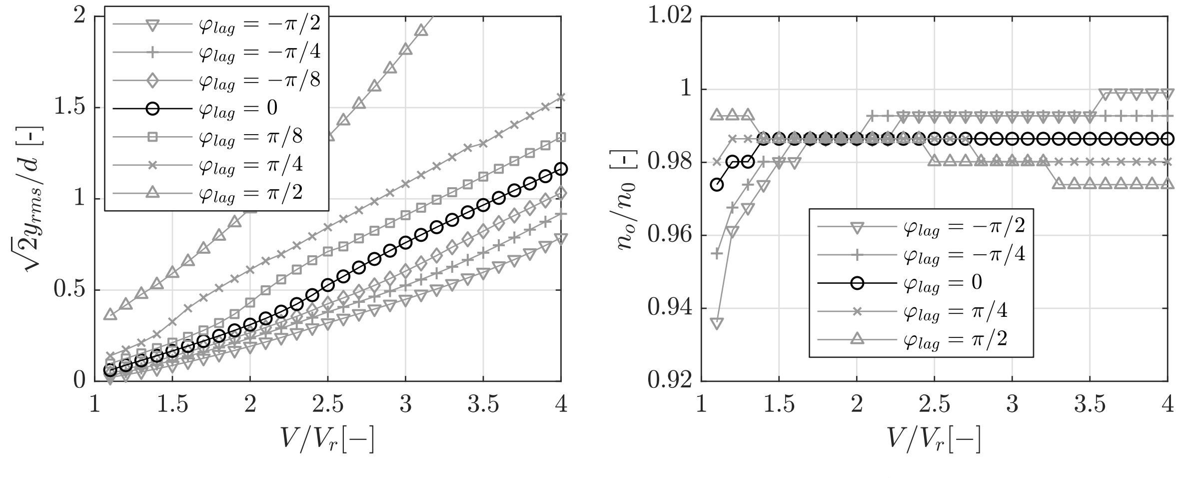

(a) (b)

Fig. 5.24: Effect of the introduced phase lag φ_{lag} on the numerical solutions of wake oscillator model: (a) amplitude; (b) oscillation frequency. “TS-2018” form wake oscillator model as an example, implemented for the 2:1 rectangular cylinder with $Sc = 107$.

However, as previously mentioned, the evolution of φ_{lag} with reduced flow velocity and oscillation amplitude may be very complicated. The sensitivity study carried out here only serves to reveal its important role and the potential influence on the “calibration” process of the f parameter. Fully integrating φ_{lag} in the wake oscillator model definitely needs further investigations.

Spanwise correlation of vortex shedding force

Another possible reason leading to a lower “measured” f value than the “calibrated” one could attribute to the spanwise correlation effect of vortex shedding force. In this thesis, the vortex shedding force coefficient $C_{L0} = \sqrt{2}C'_L$ is a result of force measurement on a prism body with aspect ratio $l_e/d = 21.7$. So, strictly speaking, C_{L0} represents for the whole prism body, rather than the strictly 2-dimensional one $c_{L0} = \sqrt{2}c'_L$, which has to be measured by pressure measurements. Here, C'_L and c'_L represent respectively the standard deviation of lift coefficient fluctuation due to vortex shedding for the whole prism body and for a unit length of the prism body. According to Holmes (2014), the following relationship holds between C'_L and c'_L

$$C'_L = c'_L \sqrt{\frac{\int_0^{l_e}\int_0^{l_e} \rho_r(|z_i - z_j|)\mathrm{d}z_i\mathrm{d}z_j}{l_e^2}} \tag{5.18}$$

in case of c'_L being constant along the spanwise coordinate z. $\rho_r(r)$ is the spanwise correlation function between the vortex shedding forces at two locations z_i and z_j of the prism body. For the full correlation case (an ideal situation), there is $\rho_r = 1$ constantly, so that the above equation becomes $C'_L = c'_L$. For partial correlation (which is the reality), $\rho_r(r)$ is normally a decaying function, gradually approaching to null with increased r ($\rho_r = 1$ for $r = 0$). Therefore, from Eq. 5.18, the measured C'_L is supposed to be lower than c'_L in reality, further leading to $C_{L0} < c_{L0}$.

In the determination of f through wake measurements (Section 5.3), the estimated ϑ_0 corresponds to, however, a real 2-dimensional condition. Therefore, c_{L0} should be used rather than C_{L0}, which leads to a lower f value for the same ϑ_0. Pressure measurements would be very interesting to obtain the c_{L0} coefficient, to examine this conjecture. In contrast, the f parameter, obtained through the "calibration" method, seems to be more representative for the whole prism body. In other words, the obtained f in this way may have included the spanwise correlation effect of vortex shedding.

Short summary

The above two analyses imply, that the "calibration" method for the f parameter probably encapsulates some unconsidered effects into this single parameter. For the purpose of a good prediction capability of the wake oscillator model, this is fine and even an advantage. From another point of view, these unconsidered effects, which may be also scientifically interesting and can be further explored for the wake oscillator model, are however hidden during this "calibration " process. Nevertheless, for the studied 2:1 rectangular cylinder, the measured f value provides at least a sound-solid basis for the calibrated high f value, rather than for a value like $f \approx 1$ which is originally for the circular cylinder (Tamura & Matsui 1979).

5.5.2 On Modeling the Atypical Unsteady Galloping

In Section 5.1.3, it showed that the wake oscillator model fails to capture the *atypical unsteady galloping* for the bridge deck model at $\alpha_0 = 0°$, even in a qualitative manner. The main reason for this failure is supposed to be the quasi-steady force coefficient C_{Fy}^{QS} set in the wake oscillator model. In fact, the use of quasi-steady theory at a low reduced wind speed should always be cautious (as mentioned by Gao & Zhu (2017)). But interesting is that, the wake-oscillator model does show some at least qualitative agreement with the experimental results for a few rectangular cylinders with the short side perpendicular to the flow (see Tamura & Shimada (1987) for the square cylinder, Mannini & al. (2018a) for the 3:2 rectangular cylinder, and the 2:1 rectangular cylinder presented in Section 5.1.1), also for the studied bridge deck model at $\alpha_0 = 4°$. The reasons behind that could be: i) for $V < V_r$, setting a proper value of f, the *asynchronous quenching* effect is able to suppress the self-excited motion (as discussed in Mannini & al. (2018a)), so that the inaccuracy of the quasi-steady force is irrelevant; ii) for $V > V_r$ but still low reduced wind speed, experimental results from forced-vibration tests show that the phase angle of the motion-induced aerodynamic lift changes its sign from negative to positive (thus suggesting a possible instability) at a reduced wind speed just slightly higher than V_r (Carassale & al. 2015; Ma & al. 2018; Washizu & al. 1978). This fact confirms the overall validity of the wake-oscillator model, also implying that the quasi-steady force set in the equations is qualitatively correct for this reduced wind speed range. However, attention must be paid to the phase angle evolution for the rectangular cylinders when a considerable large mean flow incidence is imposed. For example, Carassale & al. (2015) showed that the phase angle changes its sign from negative to positive at about $1.8V_r$ for the square cylinder with a mean flow incidence of 9°, being the concerned instability later confirmed by Dai (2019) (see Fig.2.18 for the reproduced results). In this case, the further use of a quasi-steady force in the wake-oscillator model for $V_r < V < 1.8V_r$ is very questionable. Despite the lack of experimental evidence, the unsteady galloping behavior observed for the bridge deck at 0° mean flow incidence is probably due to a phase angle evolution similar to that of the square cylinder at 9° mean flow incidence.

To model the *atypical unsteady galloping*, the C_{Fy}^{QS} item in the wake oscillator model needs to be replaced by more realistic unsteady motion-induced force coefficient (properly named it as C_{Fy}^{un}). As already mentioned in Section 2.2.3, a bold attempt to this direction has already been made by Luo & Bearman (1990) for the square cylinder (followed also by Liu & al. (2018)), adopting the thin-airfoil theory to modify the quasi-steady one. This is a a meaningful and inspirational attempt, but the direct application of thin-airfoil theory to sharp-edged bodies seems quite groundless. The author of this thesis believes that the proper expression of C_{Fy}^{un} would be the key to the modeling of the *atypical unsteady galloping* behavior. This should be further studied in the future.

5.6 Chapter Summary

In this chapter, mathematical modeling was carried out for the unsteady galloping behaviors observed in wind tunnel tests, combined with many explorations and discussions on the physical considerations in the used mathematical model.

Firstly, the modified form of Tamura's nonlinear wake oscillator model "TS-2018" (Mannini & al. 2018a) was implemented for the 2:1 rectangular cylinder and the bridge deck model. After setting the key parameter f according to the "calibration" method proposed in Mannini & al. (2018a), satisfying prediction capability was found for the typical unsteady galloping due to interference with VIV. However, for the peculiar unsteady galloping behavior observed at the null mean wind angle of attack of the bridge deck (named as *atypical unsteady galloping* in this thesis), the wake oscillator model shows considerable limitations.

Secondly, efforts were dedicated to examine the so-called physical considerations in the wake oscillator model. The basic knowledge concerning the physics of near-wake after bluff-body was first reviewed, highlighting the possibility to relate the parameters h^* and l^* in wake oscillator model to the physical vortex formation region after bluff body through comparably easy wake measurements. These measurements were then carried out for the 2:1 rectangular cylinder. The very important assumption in wake oscillator model, that the Strouhal number is determined by a "local-effect" via near-wake geometry (Birkhoff's idea, see Birkhoff (1953) and Birkhoff & Zarantonello (1957)), was then examined. The examination shows the "TS-2018" wake oscillator model exhibits a more physically meaningful "local-effect" equation than the original "TS-1987" form (Tamura & Shimada 1987). Nevertheless, there is still big space for a further improvement.

Thirdly, during the wake measurements, another approach to determine the key parameter f for the wake oscillator model was convinced. This idea is built upon the estimation of the maximum near-wake rotation angle ϑ_0 on a stationary body, through a set of monitoring points laterally arranged in the near-wake region. Then, the f value can be calculated according to its definition. The approach was applied to the 2:1 rectangular cylinder, with the identified f value well supported by flow visualizations reported in literature. However, for the "TS-2018" wake oscillator model, the identified f parameter was found lower than the "calibrated" one.

Fourthly, the wake oscillator model was further modified. The new "Modified" one is able to maintain a good prediction capability as the "TS-2018" form in dealing with the typical unsteady galloping interacted with VIV. The improvements in this "Modified" one are mainly on the physical considerations, being its "local-effect" equation more physically meaningful. The value of f determined by the two methods gets also closer for this "Modified" form.

Finally, discussions were made to several points on mathematically modeling the unsteady galloping with wake oscillator model.

6 Mathematically Modeling the Unsteady Galloping for Continuous Structural System

Continuous structural system refers here to the slender structure who has its main deformation continuously along one axis. They are represented by high-rise buildings, chimneys, towers, bridges, etc. Differing from prism body or wind tunnel sectional model, the interaction of flow with continuous structural system has more aspects needed to be considered, for example:

- the flexibility of structure along the axis;
- the variation of attacking wind condition along the axis, like mean wind speed profile;
- the change of aerodynamic properties along the axis, due to the cross section shape being varied or 3-dimensional flow condition (for example, the tip region of a cantilever).

The work in this chapter aims at applying the research results achieved on prism body to more realistic structural system. It will be mainly theoretical and numerical investigations, based on the classical beam theory and Tamura's wake oscillator model (whose performance has been confirmed in previous chapter). The concerned unsteady galloping problem is currently limited to the typical one, which arises due to the interaction with vortex induced vibration.

6.1 Extension of Wake Oscillator Model for Continuous System

6.1.1 Finite-element-method based Approach

Applying wake oscillator model to continuous system can already been found in some literature reports (e.g., Tamura & Amano (1983) and Violette & al. (2007)), but both for the VIV problem of structures with circular cross section. For example, in Tamura & Amano (1983), the near-wake rotation angle and the across-wind displacement of structure are rewritten as $\vartheta(t,z)$ and $y(t,z)$, which depend on the axis position z in the continuous system. By considering a single mode shape, the governing equations for $\vartheta(\tau,z)$ and $y(t,z)$ were finally expressed by one differential equation of order 4, with the mode shape and the mean wind profile collected in several constants. However, such a route was found technically hard to follow, if a non-circular cross section is in object. The main reason is, that the quasi-steady force coefficient C_{Fy}^{QS} for non-circular cross section is usually of higher orders of $\dot{y}/U$, rather than simply $C_D \cdot \dot{y}/U$ for the circular one. This leads the final differential equation much more complex, and prolix.

Therefore, it is decided in this thesis to realize the objective by coupling multiple discrete wake oscillators to the structural system which is described by finite element method. The implementation of this approach is outlined in detail as follows.

Coordinates and degrees of freedom

Fig 6.1 shows the schematic of the proposed approach. For galloping and VIV problems, the bending deformation of the beam in the across-wind direction, namely y, is relevant. Therefore, the plane beam element can be applied. Moreover, for most applications, considering only two degrees of freedom for each node, namely y and p shown in Fig. 6.1 (p is the rotation of node about x coordinate), is supposed to be enough for sufficiently high accuracy. When each node is implemented with wake oscillator, additional degree of freedom, namely the near-wake lamina rotation ϑ, has to be added for the dynamics of the whole system. Assuming the total number of nodes N, the degrees of freedom for the system without considering boundary conditions are:

- $y_1, y_2, y_3, ..., y_N$;
- $p_1, p_2, p_3, ..., p_N$;
- $\vartheta_1, \vartheta_2, \vartheta_3, ..., \vartheta_N$.

A total number of $3N$ degrees of freedom is therefore for the dynamics of the whole system.

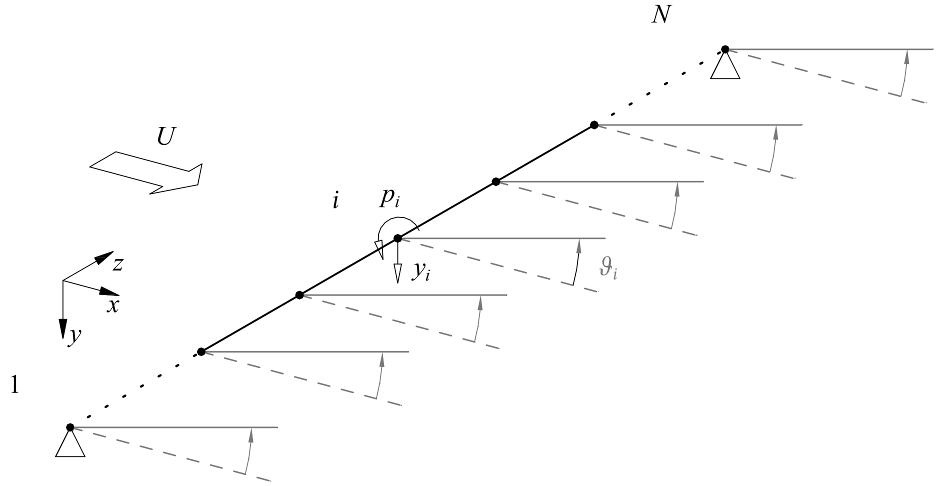

Fig. 6.1: Schematic of discrete wake oscillators coupled to a structural system described by finite element method.

Matrix form for structural dynamics

Based on finite element method, the dynamics of a structure can be described in matrix form

$$\boldsymbol{M_s}\ddot{\boldsymbol{\psi}}_{\boldsymbol{s}}+\boldsymbol{C_s}\dot{\boldsymbol{\psi}}_{\boldsymbol{s}}+\boldsymbol{K_s}\boldsymbol{\psi}_{\boldsymbol{s}}=\boldsymbol{q_s} \tag{6.1}$$

where $\boldsymbol{M_s}$, $\boldsymbol{C_s}$ and $\boldsymbol{K_s}$ represent respectively the global mass, damping and stiffness matrices, having a dimension of $(2N\times 2N)$ due to the ignorance of axis deformation

$$\boldsymbol{M_s}=\underset{(2N\times2N)}{\begin{bmatrix} m_{11} & m_{12} & m_{13} & \\ m_{21} & m_{22} & m_{23} & \\ m_{31} & m_{32} & m_{33} & \\ & & & \ddots \end{bmatrix}} \quad \boldsymbol{C_s}=\underset{(2N\times2N)}{\begin{bmatrix} c_{11} & c_{12} & c_{13} & \\ c_{21} & c_{22} & c_{23} & \\ c_{31} & c_{32} & c_{33} & \\ & & & \ddots \end{bmatrix}} \quad \boldsymbol{K_s}=\underset{(2N\times2N)}{\begin{bmatrix} k_{11} & k_{12} & k_{13} & \\ k_{21} & k_{22} & k_{23} & \\ k_{31} & k_{32} & k_{33} & \\ & & & \ddots \end{bmatrix}}$$

$\boldsymbol{\psi}_{\boldsymbol{s}}=[y_1,p_1,y_2,p_2,...,y_N,p_N]^\top$ is the displacement vector, with a dimension of $(2N\times 1)$. $\boldsymbol{q_s}$ is the force vector applying at nodes. Relating to the aerodynamic forces in wake oscillator model (Eq. 2.55 (a)), $\boldsymbol{q_s}$ can be written as

$$\boldsymbol{q_s}=\hat{\boldsymbol{A}}\boldsymbol{\vartheta}-\hat{\boldsymbol{B}}\boldsymbol{\psi}_{\boldsymbol{s}}+\boldsymbol{q}_{QS} \tag{6.2}$$

with

$$\hat{\boldsymbol{A}}=\underset{(2N\times N)}{\begin{bmatrix} \hat{a}_1 & 0 & & \\ 0 & 0 & & \\ & \hat{a}_2 & 0 & \\ & 0 & 0 & \\ & & \hat{a}_3 & \\ & & & \ddots \end{bmatrix}} \quad \hat{\boldsymbol{B}}=\underset{(2N\times2N)}{\begin{bmatrix} \hat{b}_1 & & & & & \\ & 0 & & & & \\ & & \hat{b}_2 & & & \\ & & & 0 & & \\ & & & & \hat{b}_3 & \\ & & & & & \ddots \end{bmatrix}} \quad \boldsymbol{q}_{QS}=\underset{(2N\times1)}{\begin{bmatrix} \hat{e}_1\cdot C^{QS}_{Fy,1}(\frac{\dot{y}_1}{U_1}) \\ 0 \\ \hat{e}_2\cdot C^{QS}_{Fy,2}(\frac{\dot{y}_2}{U_2}) \\ 0 \\ \hat{e}_3\cdot C^{QS}_{Fy,3}(\frac{\dot{y}_3}{U_3}) \\ \vdots \end{bmatrix}}$$

where $\hat{a}_i=\frac{1}{2}\rho U_i^2 d_i l_{s,i} f_i$, $\hat{b}_i=\frac{1}{2}\rho U_i d_i l_{s,i} f_i$ and $\hat{e}_i=\frac{1}{2}\rho U_i^2 d_i l_{s,i}$, being $l_{s,i}$ the spanwise reference length for aerodynamic force calculation for node i. The variables U, d, f and C^{QS}_{Fy} are also written with subscript "$_i$", to consider their possible dependence on the locations of nodes. Nevertheless, it is easy to understand that the complex "tip" effects at the free end of structure are not fully taken into account. Finally, with a dimension $(N\times 1)$, vector $\boldsymbol{\vartheta}=[\vartheta_1,\vartheta_2,\vartheta_3,...,\vartheta_N]^\top$ collects the degrees of freedom for wake oscillators.

Matrix form for wake oscillators

In lack of the correlation on stationary body, the degree of freedom for the wake oscillator at each node is independent from each other. However, it may be easy to understand that these wake oscillators will become not independent any more if the body is free to move. This is because the motion of each node is actually controlled by the modes of the structural system, and the implemented wake oscillators are excited externally by these "correlated" nodes. The normalized Eq. 2.55 (b) is first written back in physical time domain. At each node, there is

$$\ddot{\vartheta}_i - 2\beta_i \omega_{v,i} \dot{\vartheta}_i \left(1 - \frac{4f_i^2}{C_{L0,i}^2}\vartheta_i^2\right) + \omega_{v,i}^2 \vartheta_i = \lambda_i \frac{\ddot{y}_i}{d_i} + \omega_{v,i}^2 \frac{\dot{y}_i}{U_i} \tag{6.3}$$

where $\omega_{v,i}$ the circular vortex shedding frequency, defined by Strouhal law. The equations of all the implemented wake oscillators are collected together and written in matrix form

$$\bar{\boldsymbol{I}}\ddot{\boldsymbol{\vartheta}} - \bar{\boldsymbol{C}}\dot{\boldsymbol{\vartheta}} + \tilde{\boldsymbol{C}}(\dot{\boldsymbol{\vartheta}} \circ \boldsymbol{\vartheta} \circ \boldsymbol{\vartheta}) + \bar{\boldsymbol{K}}\boldsymbol{\vartheta} = \hat{\boldsymbol{G}}\ddot{\boldsymbol{\psi}}_{\boldsymbol{s}} + \hat{\boldsymbol{H}}\dot{\boldsymbol{\psi}}_{\boldsymbol{s}} \tag{6.4}$$

with

$$\bar{\boldsymbol{I}} = \underset{(N\times N)}{\begin{bmatrix} 1 & & & \\ & 1 & & \\ & & 1 & \\ & & & \ddots \end{bmatrix}} \quad \bar{\boldsymbol{C}} = \underset{(N\times N)}{\begin{bmatrix} \bar{c}_1 & & & \\ & \bar{c}_2 & & \\ & & \bar{c}_3 & \\ & & & \ddots \end{bmatrix}} \quad \tilde{\boldsymbol{C}} = \underset{(N\times N)}{\begin{bmatrix} \tilde{c}_1 & & & \\ & \tilde{c}_2 & & \\ & & \tilde{c}_3 & \\ & & & \ddots \end{bmatrix}}$$

$$\bar{\boldsymbol{K}} = \underset{(N\times N)}{\begin{bmatrix} \bar{k}_1 & & & \\ & \bar{k}_2 & & \\ & & \bar{k}_3 & \\ & & & \ddots \end{bmatrix}} \quad \hat{\boldsymbol{G}} = \underset{(N\times 2N)}{\begin{bmatrix} \hat{g}_1 & 0 & & & & \\ 0 & 0 & \hat{g}_2 & 0 & & \\ & & 0 & 0 & \hat{g}_3 & \\ & & & & & \ddots \end{bmatrix}} \quad \hat{\boldsymbol{H}} = \underset{(N\times 2N)}{\begin{bmatrix} \hat{h}_1 & 0 & & & & \\ 0 & 0 & \hat{h}_2 & 0 & & \\ & & 0 & 0 & \hat{h}_3 & \\ & & & & & \ddots \end{bmatrix}}$$

where $\bar{c}_i = 2\beta_i\omega_{v,i}$, $\tilde{c}_i = 2\beta_i\omega_{v,i}\frac{4f_i^2}{C_{L0,i}^2}$, $\bar{k}_i = \omega_{v,i}^2$, $\hat{g}_i = \frac{\lambda_i}{d_i}$, $\hat{h}_i = \frac{\omega_{v,i}^2}{U_i}$, and "$\circ$" denotes the Hadamard product between vectors.

Global matrix form

Eq. 6.1 and Eq.6.4 can be combined together to form a new equation

$$\boldsymbol{M_t}\ddot{\boldsymbol{\psi}}_{\boldsymbol{t}} + \boldsymbol{C1_t}\dot{\boldsymbol{\psi}}_{\boldsymbol{t}} + \boldsymbol{C3_t}(\dot{\boldsymbol{\psi}}_{\boldsymbol{t}} \circ \boldsymbol{\psi}_{\boldsymbol{t}} \circ \boldsymbol{\psi}_{\boldsymbol{t}}) + \boldsymbol{K_t}\boldsymbol{\psi}_{\boldsymbol{t}} = \boldsymbol{q_t} \tag{6.5}$$

where the new global matrices $\boldsymbol{M_t}$, $\boldsymbol{C1_t}$, $\boldsymbol{C3_t}$ and $\boldsymbol{K_t}$ all have a dimension of $(3N \times 3N)$, and are expressed as

$$\boldsymbol{M_t} = \underset{(3N\times 3N)}{\begin{bmatrix} \boldsymbol{M_s} & \boldsymbol{O} \\ -\hat{\boldsymbol{G}} & \bar{\boldsymbol{I}} \end{bmatrix}} \quad \boldsymbol{C1_t} = \underset{(3N\times 3N)}{\begin{bmatrix} \boldsymbol{C_s} + \hat{\boldsymbol{B}} & \boldsymbol{O} \\ -\hat{\boldsymbol{H}} & -\bar{\boldsymbol{C}} \end{bmatrix}} \quad \boldsymbol{C3_t} = \underset{(3N\times 3N)}{\begin{bmatrix} \boldsymbol{O} & \boldsymbol{O} \\ \boldsymbol{O} & \tilde{\boldsymbol{C}} \end{bmatrix}} \quad \boldsymbol{K_t} = \underset{(3N\times 3N)}{\begin{bmatrix} \boldsymbol{K_s} & -\hat{\boldsymbol{A}} \\ \boldsymbol{O} & \bar{\boldsymbol{K}} \end{bmatrix}}$$

Here, $\boldsymbol{O}$ is null matrix, with its dimension relied on its position in above matrices. Correspondingly, the new global vectors $\boldsymbol{\psi_t}$ and $\boldsymbol{q_t}$ are written

$$\boldsymbol{\psi_t} = \underset{(3N\times 1)}{\begin{bmatrix} \boldsymbol{\psi_s} \\ \boldsymbol{\vartheta} \end{bmatrix}} \quad \boldsymbol{q_t} = \underset{(3N\times 1)}{\begin{bmatrix} \boldsymbol{q_{QS}} \\ \boldsymbol{O} \end{bmatrix}}$$

Boundary conditions

The application of boundary conditions to Eq. 6.5 can be considered in two steps.

Firstly, for the displacement boundary conditions of the structural system, the reduction of concerned matrices ($\boldsymbol{M_s}$, $\boldsymbol{C_s}$, $\boldsymbol{K_s}$) and vector ($\boldsymbol{\psi_s}$) can be performed in the typical way of finite element method. Correspondingly, the related rows or columns in matrices ($\hat{\boldsymbol{G}}$, $\hat{\boldsymbol{B}}$, $\hat{\boldsymbol{H}}$, $\hat{\boldsymbol{A}}$) and vector ($\boldsymbol{q}_{QS}$) should be eliminated. If the eliminated degrees of freedom of the structure are coupled by wake oscillators, the matrices ($\bar{\boldsymbol{I}}$, $\bar{\boldsymbol{C}}$, $\tilde{\boldsymbol{C}}$, $\bar{\boldsymbol{K}}$) and vector $\boldsymbol{\vartheta}$ should be reduced accordingly. In this case, the matrices $\hat{\boldsymbol{G}}$, $\hat{\boldsymbol{H}}$ and $\hat{\boldsymbol{A}}$ need to be further reduced, and set the related element $\hat{b}_i$ in $\hat{\boldsymbol{B}}$ matrix as null. Finally, in some cases, additional lump mass or spring may be required for the structural system. This can be performed in the typical way of finite element method, bringing no changes to the matrices or vectors related to the wake oscillator part.

Secondly, in the situation where the implementation of wake oscillators is unnecessary at some nodes, the matrices $\bar{\boldsymbol{I}}$, $\bar{\boldsymbol{C}}$, $\tilde{\boldsymbol{C}}$, $\bar{\boldsymbol{K}}$ and vector $\boldsymbol{\vartheta}$ can be independently reduced. Corresponding reduction should be also made to the matrices $\hat{\boldsymbol{G}}$, $\hat{\boldsymbol{H}}$ and $\hat{\boldsymbol{A}}$, and setting the related element $\hat{b}_i$ in $\hat{\boldsymbol{B}}$ matrix as null. Attention should be paid to the $\boldsymbol{q}_t$ vector. If the quasi-steady contribution is ignored at the same time for these nodes, the $\hat{e}_i$ coefficient should be set as null. Otherwise, it should be maintained unchanged.

After applying the boundary conditions, Eq. 6.5 is convenient to be re-written with additional subscript "$_r$"

$$\boldsymbol{M}_{tr}\ddot{\boldsymbol{\psi}}_{tr} + \boldsymbol{C1}_{tr}\dot{\boldsymbol{\psi}}_{tr} + \boldsymbol{C3}_{tr}(\dot{\boldsymbol{\psi}}_{tr} \circ \boldsymbol{\psi}_{tr} \circ \boldsymbol{\psi}_{tr}) + \boldsymbol{K}_{tr}\boldsymbol{\psi}_{tr} = \boldsymbol{q}_{tr} \tag{6.6}$$

The total amount of degrees of freedom is now indicated with N_r, which is the summation of the amount of degrees of freedom for structural part N_{sr} and the one for wake oscillator part N_{wr}. Accordingly, the matrices and vectors in above equation become

$$\boldsymbol{M}_{tr} = \underset{(N_r \times N_r)}{\begin{bmatrix} \boldsymbol{M}_{sr} & \boldsymbol{O} \\ -\hat{\boldsymbol{G}}_{\boldsymbol{r}} & \bar{\boldsymbol{I}}_{\boldsymbol{r}} \end{bmatrix}} \quad \boldsymbol{C1}_{tr} = \underset{(N_r \times N_r)}{\begin{bmatrix} \boldsymbol{C}_{sr} + \hat{\boldsymbol{B}}_{\boldsymbol{r}} & \boldsymbol{O} \\ -\hat{\boldsymbol{H}}_{\boldsymbol{r}} & -\bar{\boldsymbol{C}}_{\boldsymbol{r}} \end{bmatrix}} \quad \boldsymbol{C3}_{tr} = \underset{(N_r \times N_r)}{\begin{bmatrix} \boldsymbol{O} & \boldsymbol{O} \\ \boldsymbol{O} & \tilde{\boldsymbol{C}}_{\boldsymbol{r}} \end{bmatrix}} \quad \boldsymbol{K}_{tr} = \underset{(N_r \times N_r)}{\begin{bmatrix} \boldsymbol{K}_{sr} & -\hat{\boldsymbol{A}}_{\boldsymbol{r}} \\ \boldsymbol{O} & \bar{\boldsymbol{K}}_{\boldsymbol{r}} \end{bmatrix}}$$

and

$$\boldsymbol{\psi}_{tr} = \underset{(N_r \times 1)}{\begin{bmatrix} \boldsymbol{\psi}_{sr} \\ \boldsymbol{\vartheta}_{\boldsymbol{r}} \end{bmatrix}} \quad \boldsymbol{q}_{tr} = \underset{(N_r \times 1)}{\begin{bmatrix} \boldsymbol{q}_{QSr} \\ \boldsymbol{O} \end{bmatrix}}$$

Here, the dimensions for the matrices and vectors are listed as below:

- $\boldsymbol{M}_{sr}$, $\hat{\boldsymbol{B}}_{\boldsymbol{r}}$, $\boldsymbol{K}_{sr}$, and $\boldsymbol{K}_{sr}$: $(N_{sr} \times N_{sr})$;
- $\bar{\boldsymbol{I}}_{\boldsymbol{r}}$, $\bar{\boldsymbol{C}}_{\boldsymbol{r}}$, $\tilde{\boldsymbol{C}}_{\boldsymbol{r}}$, and $\bar{\boldsymbol{K}}_{\boldsymbol{r}}$: $(N_{wr} \times N_{wr})$;
- $\hat{\boldsymbol{G}}_{\boldsymbol{r}}$ and $\hat{\boldsymbol{H}}_{\boldsymbol{r}}$: $(N_{wr} \times N_{sr})$;
- $\hat{\boldsymbol{A}}_{\boldsymbol{r}}$: $(N_{sr} \times N_{wr})$;
- $\boldsymbol{\psi}_{sr}$ and $\boldsymbol{q}_{QSr}$: $(N_{sr} \times 1)$
- $\boldsymbol{\vartheta}_{\boldsymbol{r}}$: $(N_{wr} \times 1)$.

Strategy for numerical integration

Eq. 6.6 is ready to be solved by means of numerical integration in time domain. However, for wind engineering, the lowest several modes of a structural system are more interested in, especially for the galloping problem. This is an advantage should be taken to accelerate the numerical integration in time domain. As an example, the lowest 6 modes of the structural system are considered. So the displacement vector of the structural system can be written as

$$\boldsymbol{\psi}_{sr} = \boldsymbol{\Phi}\boldsymbol{\xi} \tag{6.7}$$

where $\boldsymbol{\Phi}$ is the mode shape matrix, collecting the first 6 mode shape vectors

$$\boldsymbol{\Phi} = \underset{(N_{sr} \times 6)}{\begin{bmatrix} \boldsymbol{\phi_1} & \boldsymbol{\phi_2} & \boldsymbol{\phi_3} & \boldsymbol{\phi_4} & \boldsymbol{\phi_5} & \boldsymbol{\phi_6} \end{bmatrix}}$$

and $\boldsymbol{\xi} = [\xi_1, \xi_2, \xi_3, \xi_4, \xi_5, \xi_6]^\top$, of dimension (6×1), collects the generalized displacements in mode space. Utilizing Eq. 6.7, the $\boldsymbol{\psi}_{tr}$ vector in Eq. 6.6 can be written as

$$\boldsymbol{\psi}_{tr} = \boldsymbol{\Phi}_{\boldsymbol{e}} \boldsymbol{\psi}_{tn} \tag{6.8}$$

where

$$\boldsymbol{\Phi}_{\boldsymbol{e}} = \underset{(N_r \times (6+N_{wr}))}{\begin{bmatrix} \boldsymbol{\Phi} & \boldsymbol{O} \\ \boldsymbol{O} & \boldsymbol{I_a} \end{bmatrix}}$$

can be called the “expanded” mode shape matrix, with $\boldsymbol{I_a}$ the added unit matrix of dimension N_{wr}. And $\boldsymbol{\psi}_{tn}$ is the vector collecting $\boldsymbol{\xi}$ and $\boldsymbol{\vartheta_r}$

$$\boldsymbol{\psi}_{tn} = \underset{((6+N_{wr}) \times 1)}{\begin{bmatrix} \boldsymbol{\xi} \\ \boldsymbol{\vartheta_r} \end{bmatrix}}$$

Substituting Eq. 6.8 into Eq.6.6, and left-multiplying Eq. 6.6 with $\boldsymbol{\Phi}_{\boldsymbol{e}}^\top$, there is

$$\boldsymbol{M}_{tn} \ddot{\boldsymbol{\psi}}_{tn} + \boldsymbol{C1}_{tn} \dot{\boldsymbol{\psi}}_{tn} + \boldsymbol{C3}_{tn} (\dot{\boldsymbol{\psi}}_{tn} \circ \boldsymbol{\psi}_{tn} \circ \boldsymbol{\psi}_{tn}) + \boldsymbol{K}_{tn} \boldsymbol{\psi}_{tn} = \boldsymbol{q}_{tn} \tag{6.9}$$

with

$$\boldsymbol{M}_{tn} = \boldsymbol{\Phi}_{\boldsymbol{e}}^\top \boldsymbol{M}_{tr} \boldsymbol{\Phi}_{\boldsymbol{e}} = \underset{((6+N_{wr}) \times (6+N_{wr}))}{\begin{bmatrix} \boldsymbol{\Phi}^\top \boldsymbol{M}_{sr} \boldsymbol{\Phi} & \boldsymbol{O} \\ -\hat{\boldsymbol{G}}_{\boldsymbol{r}} \boldsymbol{\Phi} & \bar{\boldsymbol{I}}_{\boldsymbol{r}} \end{bmatrix}} \qquad \boldsymbol{C1}_{tn} = \boldsymbol{\Phi}_{\boldsymbol{e}}^\top \boldsymbol{C1}_{tr} \boldsymbol{\Phi}_{\boldsymbol{e}} = \underset{((6+N_{wr}) \times (6+N_{wr}))}{\begin{bmatrix} \boldsymbol{\Phi}^\top (\boldsymbol{C}_{sr} + \hat{\boldsymbol{B}}_{\boldsymbol{r}}) \boldsymbol{\Phi} & \boldsymbol{O} \\ -\hat{\boldsymbol{H}}_{\boldsymbol{r}} \boldsymbol{\Phi} & -\bar{\boldsymbol{C}}_{\boldsymbol{r}} \end{bmatrix}}$$

$$\boldsymbol{C3}_{tn} = \underset{((6+N_{wr}) \times (6+N_{wr}))}{\begin{bmatrix} \boldsymbol{O} & \boldsymbol{O} \\ \boldsymbol{O} & \tilde{\boldsymbol{C}}_{\boldsymbol{r}} \end{bmatrix}} \qquad \boldsymbol{K}_{tn} = \boldsymbol{\Phi}_{\boldsymbol{e}}^\top \boldsymbol{K}_{tr} \boldsymbol{\Phi}_{\boldsymbol{e}} = \underset{((6+N_{wr}) \times (6+N_{wr}))}{\begin{bmatrix} \boldsymbol{\Phi}^\top \boldsymbol{K}_{sr} \boldsymbol{\Phi} & -\boldsymbol{\Phi}^\top \hat{\boldsymbol{A}}_{\boldsymbol{r}} \\ \boldsymbol{O} & \bar{\boldsymbol{K}}_{\boldsymbol{r}} \end{bmatrix}}$$

and

$$\boldsymbol{q}_{tn} = \boldsymbol{\Phi}_{\boldsymbol{e}}^\top \boldsymbol{q}_{tr} = \underset{((6+N_{wr}) \times 1)}{\begin{bmatrix} \boldsymbol{\Phi}^\top \boldsymbol{q}_{QSr} \\ \boldsymbol{O} \end{bmatrix}}$$

Attention should be paid here to the derivation of expression for $\boldsymbol{C3}_{tn}$, it is a result of

$$\boldsymbol{\Phi}_{\boldsymbol{e}}^{\top}\boldsymbol{C3}_{tr}(\dot{\boldsymbol{\psi}}_{tr}\circ\boldsymbol{\psi}_{tr}\circ\boldsymbol{\psi}_{tr}) = \underset{((6+N_{wr})\times N_r)}{\begin{bmatrix}\boldsymbol{\Phi}^{\top} & \boldsymbol{O}\\ \boldsymbol{O} & \boldsymbol{I}_{\boldsymbol{a}}^{\top}\end{bmatrix}} \underset{(N_r\times N_r)}{\begin{bmatrix}\boldsymbol{O} & \boldsymbol{O}\\ \boldsymbol{O} & \tilde{\boldsymbol{C}}_{\boldsymbol{r}}\end{bmatrix}} \underset{(N_r\times 1)}{\begin{bmatrix}\dot{\boldsymbol{\psi}}_{sr}\circ\boldsymbol{\psi}_{sr}\circ\boldsymbol{\psi}_{sr}\\ \dot{\boldsymbol{\vartheta}}_{\boldsymbol{r}}\circ\boldsymbol{\vartheta}_{\boldsymbol{r}}\circ\boldsymbol{\vartheta}_{\boldsymbol{r}}\end{bmatrix}} = \underset{((6+N_{wr})\times 1)}{\begin{bmatrix}0\\ \tilde{\boldsymbol{C}}_{\boldsymbol{r}}(\dot{\boldsymbol{\vartheta}}_{\boldsymbol{r}}\circ\boldsymbol{\vartheta}_{\boldsymbol{r}}\circ\boldsymbol{\vartheta}_{\boldsymbol{r}})\end{bmatrix}}$$

$$= \underset{((6+N_{wr})\times(6+N_{wr}))}{\begin{bmatrix}\boldsymbol{O} & \boldsymbol{O}\\ \boldsymbol{O} & \tilde{\boldsymbol{C}}_{\boldsymbol{r}}\end{bmatrix}} \underset{((6+N_{wr})\times 1)}{\begin{bmatrix}\dot{\boldsymbol{\xi}}\circ\boldsymbol{\xi}\circ\boldsymbol{\xi}\\ \dot{\boldsymbol{\vartheta}}_{\boldsymbol{r}}\circ\boldsymbol{\vartheta}_{\boldsymbol{r}}\circ\boldsymbol{\vartheta}_{\boldsymbol{r}}\end{bmatrix}} = \boldsymbol{C3}_{tn}(\dot{\boldsymbol{\psi}}_{tn}\circ\boldsymbol{\psi}_{tn}\circ\boldsymbol{\psi}_{tn})$$

This can be seen as a “trick” to make the whole integration process of Eq. 6.9 clearer. Moreover, it is to note that, in the expression of $\boldsymbol{q}_{tn}$, there still exists $\boldsymbol{q}_{QSr}$, which needs the velocities of nodes $\dot{y}$ as input. This means additional calculation $\dot{\boldsymbol{\psi}}_{sr} = \boldsymbol{\Phi}\dot{\boldsymbol{\xi}}$ must be performed for every time step so that the quasi-steady transverse force can be obtained and then applied to nodes. This additional operation will lead to a loss of computational efficiency, but the numerical integration of Eq.6.9 is still much faster than directly integrating Eq.6.6.

Finally, the numerical integration in time domain was carried out with ODE45 solver of Matlab®. Related error tolerance was the same as in Chapter 5. Initial conditions were applied to the generalized displacements ξ and then distributed to each node according to mode shapes.

6.1.2 Validation of the Approach

Validation 1 - Comparison with single-wake-oscillator results of prism body

The proposed approach was first examined on the wind tunnel 2:1 rectangular cylinder, which features a mode shape $\phi_1(z) = 1$. By comparing with the numerical results presented in Section 5.1, the algorithm of the propose approach can be confirmed at the first stage.

The implementation of multiple wake oscillators on a spring-suspended wind tunnel model is illustrated in Fig. 6.2. The wind tunnel model is considered as a beam with 21 equally spaced nodes. Two springs with equal stiffness constants were applied at the node 1 and node 21, and the bending stiffness of the beam was assumed very high so that the motion of beam is nearly fully due to the deformation of springs. Other parameters, such as the effective oscillation mass and damping, were set the same as the wind tunnel model. A total number of 10 wake oscillators of the “TS-2018” form were coupled to every two nodes of the beam system. For this reason, the length of two elements, which relate directly to the node of a wake oscillator being coupled, was used as the reference length l_i for the aerodynamic force calculation. Other aerodynamic parameters (C_{Fy}^{QS}, St, $C_{L0}(Re)$, h^* and f) were maintained the same as that in Section 5.1. Only the fundamental mode of this beam system was taken into account. Nevertheless, attention must be paid to the numerically calculated mode shape, whose y component values are usually not exactly $\phi_1 = 1$. For the purpose of comparison with the single-wake-oscillator results, manually setting $\phi_1 = 1$ is therefore necessary. From Fig. 6.3, the perfect match of the two sets of results confirms the accuracy of the algorithm of the proposed approach.

Validation 2 - Comparison with Tamura & Amano (1983)'s results for VIV response

In Tamura & Amano (1983), the analytical solutions have been provided for the VIV response of three different continuous systems with circular cross section (see Fig. 6.4). Their results can been used for a comparison with the numerical results of the proposed approach. The second case, a simply supported beam under constant wind profile, is selected for this purpose (the third case is also suitable, but the structural properties along the Z axis must be carefully adjusted to perfectly match the normalized mode shape $Z^{1.8}$).

To apply the proposed approach, a 50 m long simple-supported beam was assumed, with a constant circular cross section of 1 m diameter and a mass ratio $m^* = m/(0.5\rho d^2) = 450$ (in Tamura & Amano (1983), the mass ratio is about 454-555). 10 wake oscillators were coupled to the structural system with equally longitudinal space. The wake oscillator model used herein is the one reported in Tamura & Amano (1983) ($C_{Fy}^{QS} = C_D \cdot \dot{y}/U$ for circular cross section). All the aerodynamic parameters will maintained the same as in Tamura & Amano (1983) (sub-critical Reynolds number range). Only the fundamental mode was considered, and properly large initial conditions were applied for a quick search of the maximal VIV amplitude response.

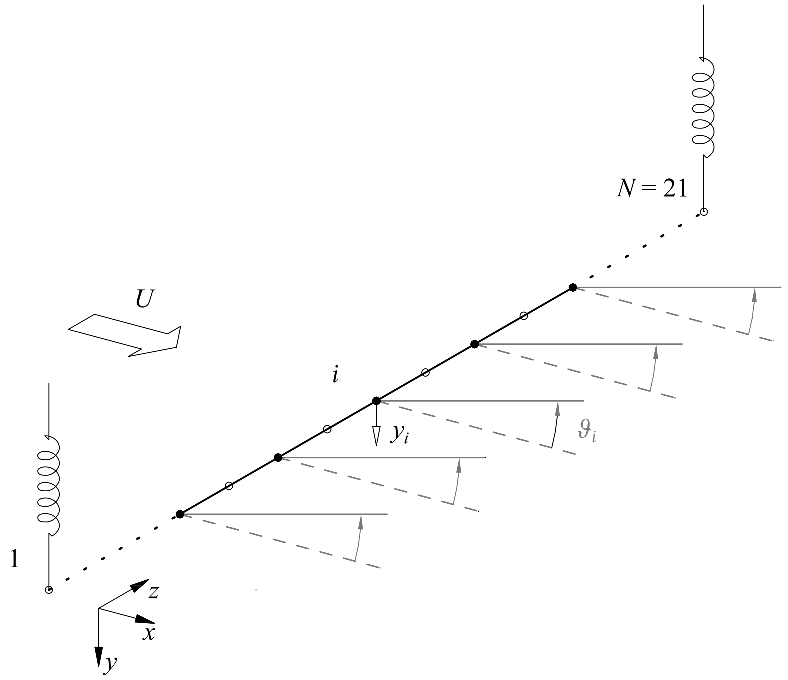

Fig. 6.2: Implementation of 10 wake oscillators to the 2:1 rectangular cylinder.

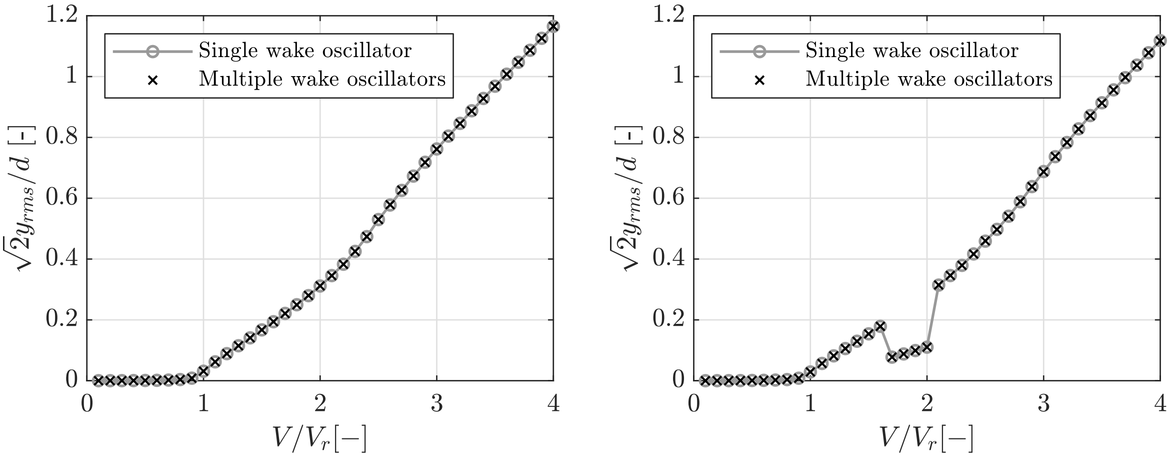

(a) $Sc = 107$ (b) $Sc = 128$

Fig. 6.3: Comparison of the numerical solutions of implementing single wake oscillator and multiple wake oscillators for the 2:1 rectangular cylinder (“TS-2018” form wake oscillator with small initial conditions).

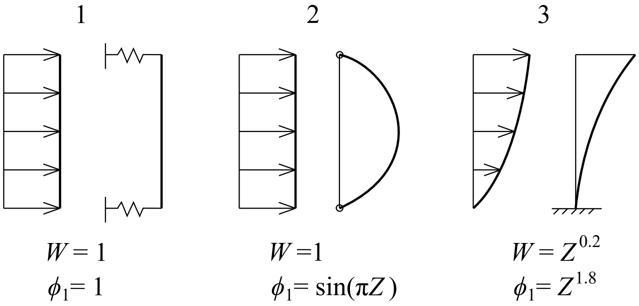

Fig. 6.4: Three normal mode shapes and flow velocity profiles considered in Tamura & Amano (1983). W represents the normalized wind profile, Z the normalized coordinate.

In Fig. 6.5, the numerical solutions of the propose approach are compared with Tamura & Amano (1983)’s analytical approximations, with respect to the VIV peak amplitude. A good agreement can be found. Nevertheless, the presented ones are found slightly lower than the analytical ones. This is probably due to some overestimation in the analytical approximations. Because, in Tamura & Amano (1983), numerical integration of the aforementioned differential equation of order 4 was carried out for the cantilever case in trans-critical Reynolds number range, and the slight overestimation of the analytical ones can be also found.

Finally, a quick test for the convergence of numerical results were carried out with a Scruton number $Sc = 2\pi m^* \zeta_1 = 3.21$, coupling respectively 5, 10 or 20 wake oscillators to the continuous system with equal space. Results show the peak VIV amplitudes at mid-span, respectively, $0.256d$, $0.259d$ and $0.259d$. This suggests the consideration of 10 wake oscillators for the single span is proper.

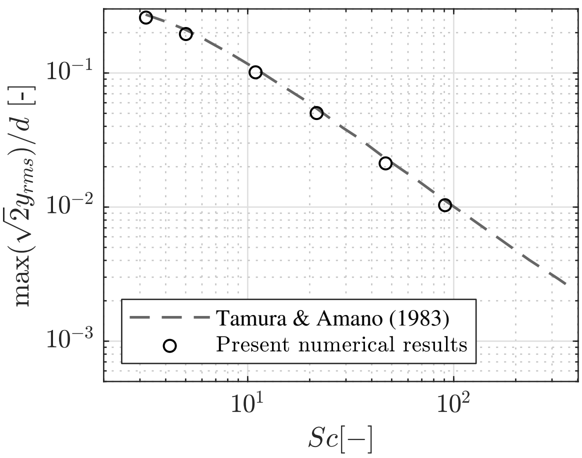

Fig. 6.5: Comparison of the numerical results of the proposed approach with Tamura & Amano (1983)' analytical approximation, with respect to the VIV peak amplitude of a simply supported beam of circular cross section understand constant wind profile.

6.2 Bridge Launching in Critical Phase as a Case Study

6.2.1 Engineering Background

The Aftetal Bridge (Germany) during its critical launching phase, early mentioned in Section 1.2, is employed here as a case study. It is a 7-span continuous beam bridge, with a span arrangement of 94 m + 5 × 119.5 m + 94 m. The critical launching phase considered here corresponds to the moment shown in Fig. 1.2, before the launched girder reaching the fourth pier from right side. In this case, the length of the cantilever reaches its maximum 119.5 m (and 68.8 m above the ground). For investigating the unsteady galloping issue, the bridge deck with open cross section is considered rather than the one treated by aerodynamic optimization (see Fig. 1.3). During the launching of Aftetal Bridge, a 30 long lattice launching nose was utilized. Here, as a case study, the situation without launching nose will be also studied.

6.2.2 Implementation of the Proposed Approach

The superstructure of Aftetal Bridge during the critical launching is first described by finite element method, as shown in Fig. 6.6. It includes 92 elements and 93 nodes. The open cross section has a height of 5 m, and the mass per unite length is about 7.7 ton/m. The second moment of area of this cross section is set to about $I_{xx} = 4.89$ m^4 , and the Young's modulus $E = 210 \cdot 10^9$ N/m^2 and the Poisson's ratio 0.3 are considered for the material properties. At this stage, the 30 m long lattice launching nose was assumed with a square cross section of 5 m height. The launching nose was simply treated as beam elements, having the same bending stiffness as the main girder but weighing 3.0 ton/m. The structural damping matrix was obtained by assuming the classical Rayleigh damping, setting the 1st and 2nd modes with the same damping ratios. In this case study, varied damping ratio, starting with ζ_0 = 0.17%, was investigated.

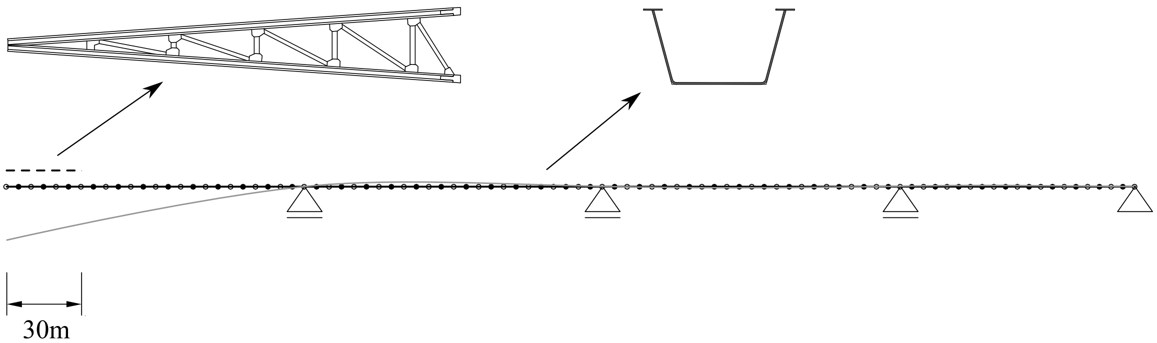

Fig. 6.6: Description of the superstructure of Aftetal Bridge with finite element method, being the nodes indicated by the small dots on the beam. Additionally, the first bending mode shape of the superstructure is indicated by the gray line, indicated meanwhile the cross section of the beam.

The total number of implemented wake oscillators, dependent on with or without launching nose, is 43 or 46. For the latter, the first 30 m long cantilever features also the open cross section, three more wake oscillators are therefore considered. The aerodynamic properties of the open cross section is assumed as same as the experimentally tested one in this thesis, and the mean flow incidence is set at 4° so that the parameters for the "TS-2018" wake oscillator model are maintained the same as in Section 5.1.2. In case of existence of launching nose, the contribution of drag and lift to flow-structure interaction is also considered in a quasi-steady way, although no wake oscillator is implemented here. The drag and lift force coefficients measured from the launching nose model (see Section 3.1 for the wind tunnel model, Section 3.2.1 for the test setups, and Section 3.3.4 for the flow condition) is provided in Fig. 6.7, and defined as:

$$C_D = \frac{D}{0.5\rho U^2 d_{ref} l_{ref}} \qquad C_L = \frac{L}{0.5\rho U^2 d_{ref} l_{ref}} \tag{6.10}$$

where D and L represent mean drag and lift of steady measurements of 60 s, under an incoming wind speed $U = 10.36$ m/s. d_{ref} = 0.06 m and l_{ref} = 0.36 m were used to calculate C_D and C_L, thus these two coefficients stand for the overall-averaged values for the launching nose. Since the mean wind incidence $\alpha_0 = 4°$ is considered, the C_D and C_L needs to be also shifted by resetting $\alpha = 4°$ as the new null wind angle of attack, then calculate the C_{Fy}^{QS} coefficient and neglect at the same time the part of C_{Fy}^{QS} inducing only static deformation. Finally, it is to mention that a correction of the friction force induced on the end-plate has not been considered for the presented results in Fig. 6.7. Although this friction force may lead to the reported C_D overestimated to some extent ($\approx$ 13%, estimated based on a friction coefficient reported in Schlichting & Gersten (2016)), it is more important to maintain a 2-dimensional flow condition at the root of the launching nose model (especially for the modified launching nose models to be presented in Section 6.3).

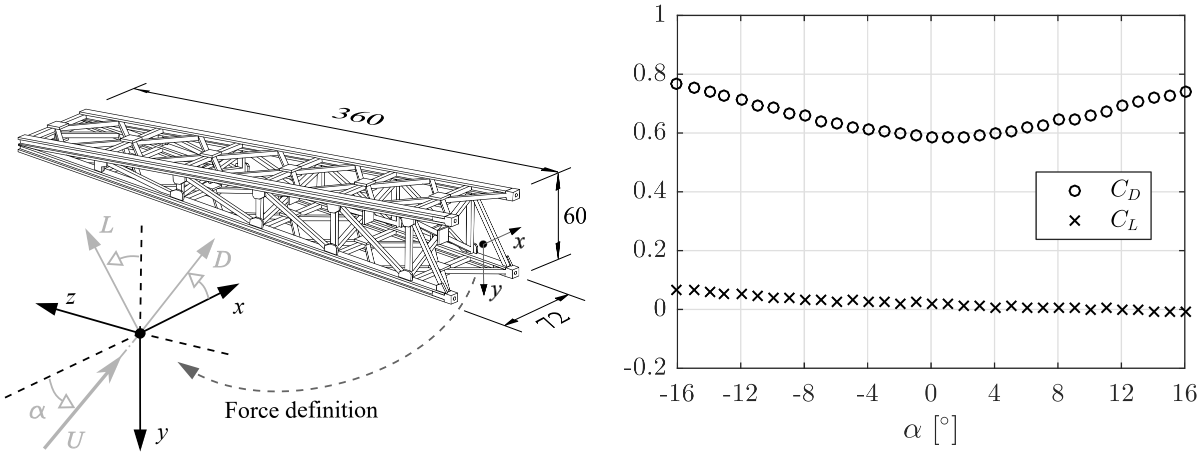

(a)

(b)

Fig. 6.7: Drag and lift coefficient measured for the lattice launching nose.

The calculated first bending frequency reports 0.387 Hz in presence of launching nose, and 0.305 Hz without launching nose (the first mode shape is depicted in Fig. 6.6). Combined $St = 0.102$ for the open cross section at its 4° mean flow incidence, the critical wind speed for VIV can be estimated 19.0 m/s and 14.9 m/s, respectively. The second bending frequency of the structural system is rather high (more than 3.9 times the first one), either with or without launching nose. It is therefore decided to take only the first mode into account.

6.2.3 Pre-discussion

Prior to the numerical integration, some first-discussions are deemed necessary.

The incoming wind

According to the location of the Aftetal Bridge (Bad Wünnenberg, Germany), Euro-code 1 (EN 1991-1-4 2010), combined with the national appendix for Germany (DIN EN 1991-1-4/NA 2010), specifies a 50-year design wind speed 22.5 m/s (the German wind zone “WZ1”). The terrain analysis in Niemann & Hölscher (2013) has shown a low vegetation area for the valley below Aftetal Bridge (the German terrain category “GK II”, featuring a roughness length 0.05 m and an exponent 0.16 for power-law wind profile). The vertical wind profile is therefore

$$U(y) = 22.5\left(\frac{y}{10}\right)^{0.16} \tag{6.11}$$

For the considered case study, the design wind speed at the altitude of the cantilever is U = 30.6 m/s (by putting $y = 66.8$ into above equation). The previously estimated critical wind speed for VIV (19.0 m/s or 14.9 m/s) is clearly within this design wind speed limit. The realistic wind condition for the bridge site could be more complicated, especially considering that the valley may bring acceleration effect for the incoming wind. In lack of full-scale measurements or wind tunnel tests, the highest wind speed for the numerical calculation was considered up to at least 3 times the critical wind speed for VIV. Moreover, to stand on the safe side, a constant wind profile was assumed along the bridge. Finally, turbulence in incoming wind was ignored.

Differences of m^* and C_{L0} between wind tunnel tests and full-scale

The open cross section used in this case study is 5 m high and weighs 7.7 ton/m, resulting in a mass ratio $m^* \approx 500$ as the full-scale condition. However, for the wind tunnel model, this value is about $m^* \approx 1300$. This difference is to be discussed, although for wind engineering the combined mass-damping parameter is usually known more dominant. Moreover, the Reynolds number for full-scale (in an order of 10^6) is also quite different from the wind tunnel tests (in an order of 10^4). According to trend outlined in Fig. 5.6 (b), the used value of C_{L0} will be constant at about 1.085 for the full scale, but it is varied with Re for wind tunnel model.

Prior to the computation for the continuous structural system, the effects of these differences were first examined on wind tunnel sectional model implemented with single wake oscillator, by means of manually adjusting the value of m^* and C_{L0}. It is to note that, when the mass ratio is decreased to $m^* \approx 500$, the damping of the system was increased to keep a same Scruton number for comparison purpose. Moreover, the spring stiffness was also adjusted so that the natural frequency will not be changed. As shown by Fig. 6.8, three different Scruton numbers were selected to investigate these effects, with the gray "○" markers correspond to the original wind tunnel test condition. The C_{L0} coefficient was first set to 1.085, which is the value will be used for full scale. This operation leads to slightly higher amplitude response for $V/V_r < 2$, but one can find that the amplitude-velocity curve is not essentially changed. Subsequently, the mass ratio is decreased to about 500, reaching a close condition as the full-scale (both for m^* and C_{L0}). For most reduced velocities, as long as the same Scruton number being maintained, the amplitude response is nearly the same as the high mass ratio case. However, in Fig. 6.8 (b) around $V/V_r = 1.9$, the medium amplitude branch become invisible any more when the solutions are attained with small initial conditions. Moreover, in Fig. 6.8 (c) the critical wind speed for galloping onset is also slightly advanced. Nevertheless, considering that the oscillation state at these specific velocities may be of high sensitivity to parameter change, the difference due to a mass ratio variation is understandable.

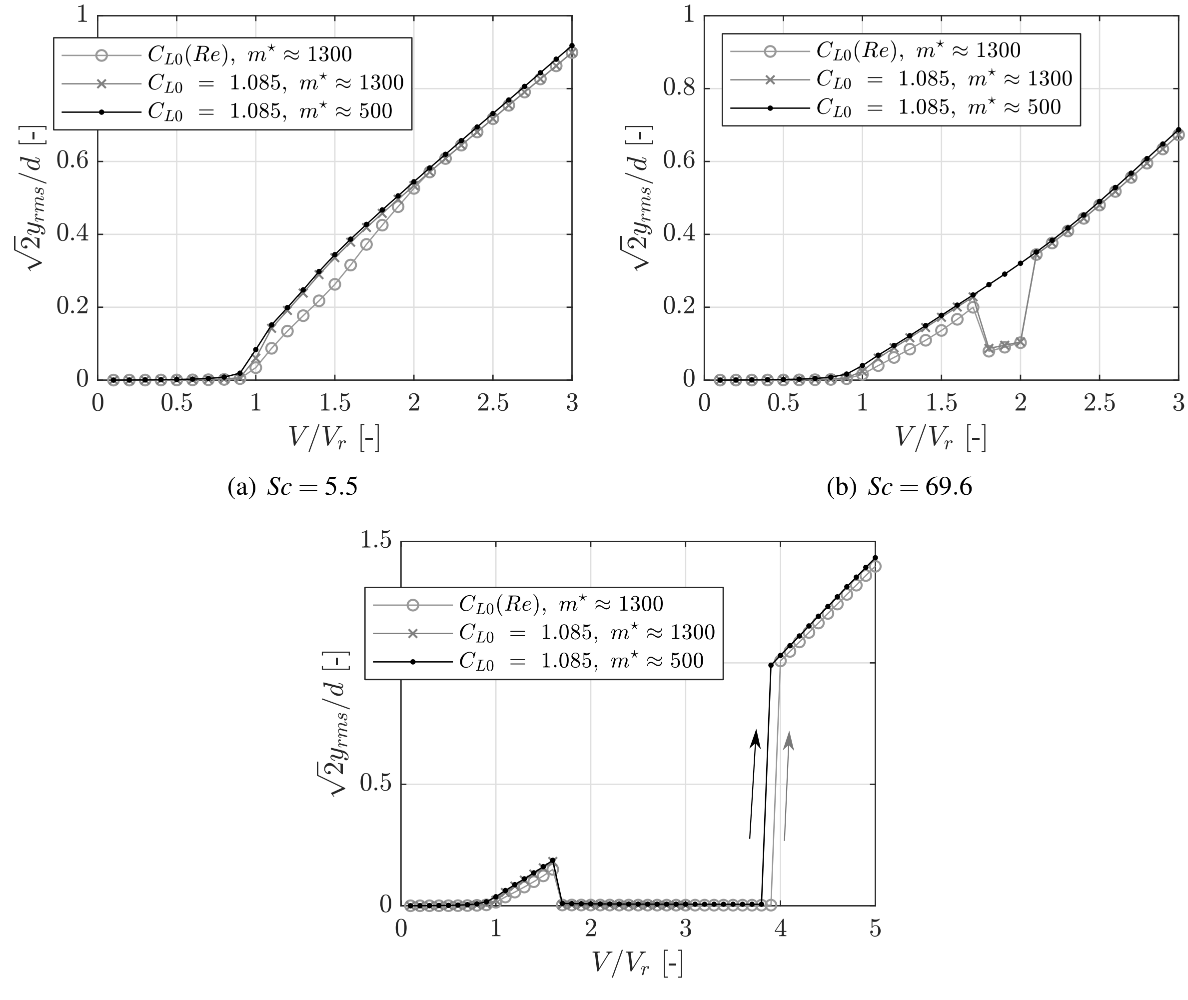

(a) $Sc = 5.5$

(b) $Sc = 69.6$

(c) $Sc = 83$

Fig. 6.8: Numerical solutions of “TS-2018” wake oscillator model, with manually changed m^* and C_{L0} for the wind tunnel bridge deck model. Solutions attained with small initial conditions.

6.2.4 Numerical Results

The numerical results for the case study are presented in following four parts.

Effect of the mode shape

First of all, the effect of the flexibility of the continuous system is studied. For a fair comparison with the numerical results of wind tunnel sectional model, no launching nose is considered in the continuous system. Moreover, $m^* \approx 500$ and $C_{L0} = 1.085$ are manually set for the wind sectional model. By doing so, the only difference between the sectional wind tunnel and the continuous system is the mode shape. Fig. 6.9 presents the comparison, with respect to the amplitude response at the tip of the cantilever. In views of the comparison, one can find that the mode shape of the continuous system mainly exhibits an amplification effect for the responses of a sectional model, being the shape of amplitude-response curve not essentially changed.

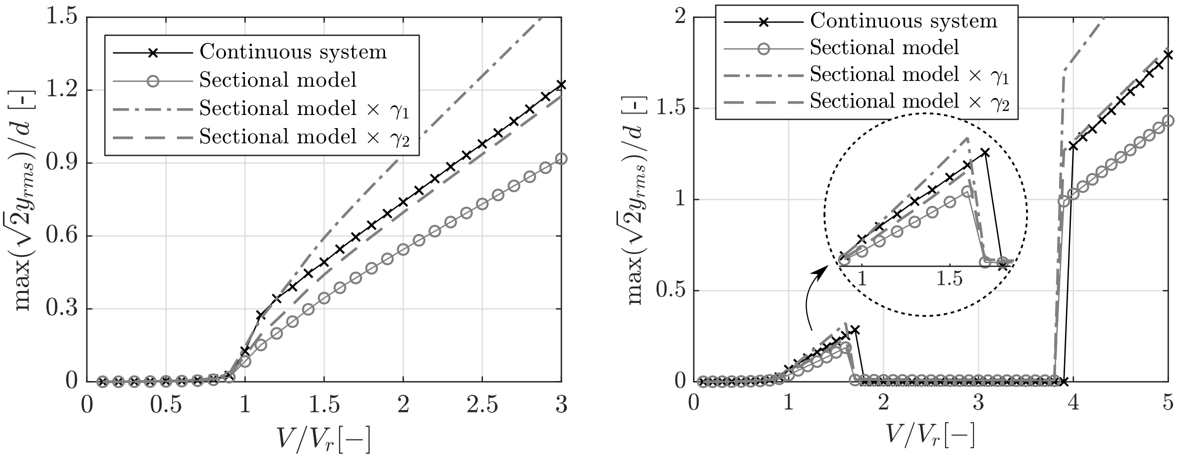

(a) $Sc = 5.5$ (b) $Sc = 83.0$

Fig. 6.9: Comparison of the numerical solutions between wind tunnel sectional model and the studied continuous structural system. No launching nose is considered for the structural system, and $m^* \approx 500$ and $C_{L0} = 1.085$ are set for the wind tunnel sectional model. Mode shape factor $\gamma_1 = 1.72$ and $\gamma_2 = 1.28$.

Attempts of converting the results on wind tunnel sectional model to the continuous system are also made, through the mode shape factor in classical VIV theories. The expression of a mode shape factor is, however, dependent on the VIV models. For the simple harmonic VIV model, it can be written as (see, e.g., Irwin (1998), Macdonald & al. (2002), Marra & al. (2017))

$$\gamma_1 = \frac{\int_{l'} |\phi(z)| \mathrm{d}z}{\int_{l'} \phi^2(z) \mathrm{d}z} \tag{6.12}$$

for the fully correlated VIV cases. Here, l' denotes the length of structure applied with vortex shedding force. For the studied case of its first mode shape (Fig. 6.6), $\gamma_1 = 1.72$ is obtained by taking the whole length of the structural system as l'. On the other hand, for Scanlan's non-linear VIV model, the mode shape factor is written (Ehsan & Scanlan 1990; Scanlan 1981)

$$\gamma_2 = \sqrt{\frac{\int_{l'} \phi^2(z) \mathrm{d}z}{\int_{l'} \phi^4(z) \mathrm{d}z}} \tag{6.13}$$

also for fully correlated VIV cases. In this case, the mode shape factor reports $\gamma_1 = 1.28$.

The results of multiplying the responses of wind tunnel model with γ_1 and γ_2 are also given in Fig. 6.9. Interestingly, for a wide range of V except very close to V_r, the results multiplied with γ_2 show a good agreement with the numerical ones directly calculated for the flexible structural system. A straightforward explanation for this good agreement is still in lack, although it is noticed that the Van der Pol oscillator is also used in Scanlan's non-linear VIV model. On the other hand, for V quite close to V_r, the multiplication with γ_1 results in better agreement.

Finally, it should be mentioned that, in the non-linear quasi-steady galloping theory, the shape of the amplitude-velocity curve of a continuous system will depend on the specific mode shape function (see, e.g., Novak (1969)). Because of this, it is theoretically unable to use a single mode shape factor to convert the post-galloping response of a prism body to a continuous system.

synchronicity of the discrete wake oscillators

In the coupling of wake oscillators to the nodes of structural system, no correlation has been assumed between the discrete wake oscillators. If the structural system is totally stationary, this means two nearby wake oscillators will vibrate independently, depending only on their respective initial conditions. This is apparently in conflict with the many physical observations, for example, the correlation function of vortex shedding force on stationary prism body (see Fig. 2.7). However, it is very interesting that, the implemented discrete wake oscillators become correlated when the structural system is free to move. Fig. 6.10 shows the $\vartheta(t)$ time histories of selected wake oscillators at different positions of the structural system. The oscillation state of the structural system corresponds to the VIV peak amplitude show in Fig. 6.9 (b).

For the two wake oscillators located at the tip of the cantilever (Fig. 6.10 (b)), one can find their $\vartheta(t)$ records are quite synchronous, oscillating at the same frequency n_0 with nearly no phase angle difference. A lower amplitude for $\vartheta_{45}(t)$ is probably the only visible difference in Fig.6.10 (b). With a large distance to the position of $\vartheta_{46}(t)$, the time-history of $\vartheta_{40}(t)$ exhibits a clear phase angle difference as well as a lower oscillation amplitude. However, $\vartheta_{40}(t)$ still features an oscillation frequency n_0 as can be learned from Fig. 6.10 (c). For the next wake oscillator (Fig. 6.10 (c)), the time records of $\vartheta_{39}(t)$ begin to show a high frequency component. This high frequency component becomes the dominant one for $\vartheta_{35}(t)$, whose location is nearly at the root of cantilever. This high frequency is actually the Strouhal frequency $n_{st} = 1.7n_0$. From above analysis, it is easy to understand that the wake oscillators, numbered from 46 to 40, are in a full synchronization with the structural oscillation. They also correlate to each other through a phase angle shift. On the other hand, the wake oscillators numbered from 39 to 35 seem to oscillate differently from former ones, due to the emergence (or dominance) of n_{st} in $\vartheta(t)$.

In another attempt, small initial conditions, in a manner of random vector, are given to $\boldsymbol{\vartheta}$ (rather than ξ_1). The final oscillation state are the same as that shown in Fig. 6.10, although much longer time was needed to achieve the steady oscillation state.

For $Sc = 5.5$ at $V/V_r = 1.7$ (structural response see Fig. 6.9 (a)), the $\vartheta(t)$ time histories are also examined. It is found the wake oscillators in full-synchronization state expand to $\vartheta_{38}(t)$, as indicated in Fig. 6.11. Since the oscillation amplitude of the structural system in this case is larger than the case of $Sc = 83.0$, it seems reasonable to conclude that the larger structural oscillation has promoted more wake oscillators on the cantilever entering into the synchronization state.

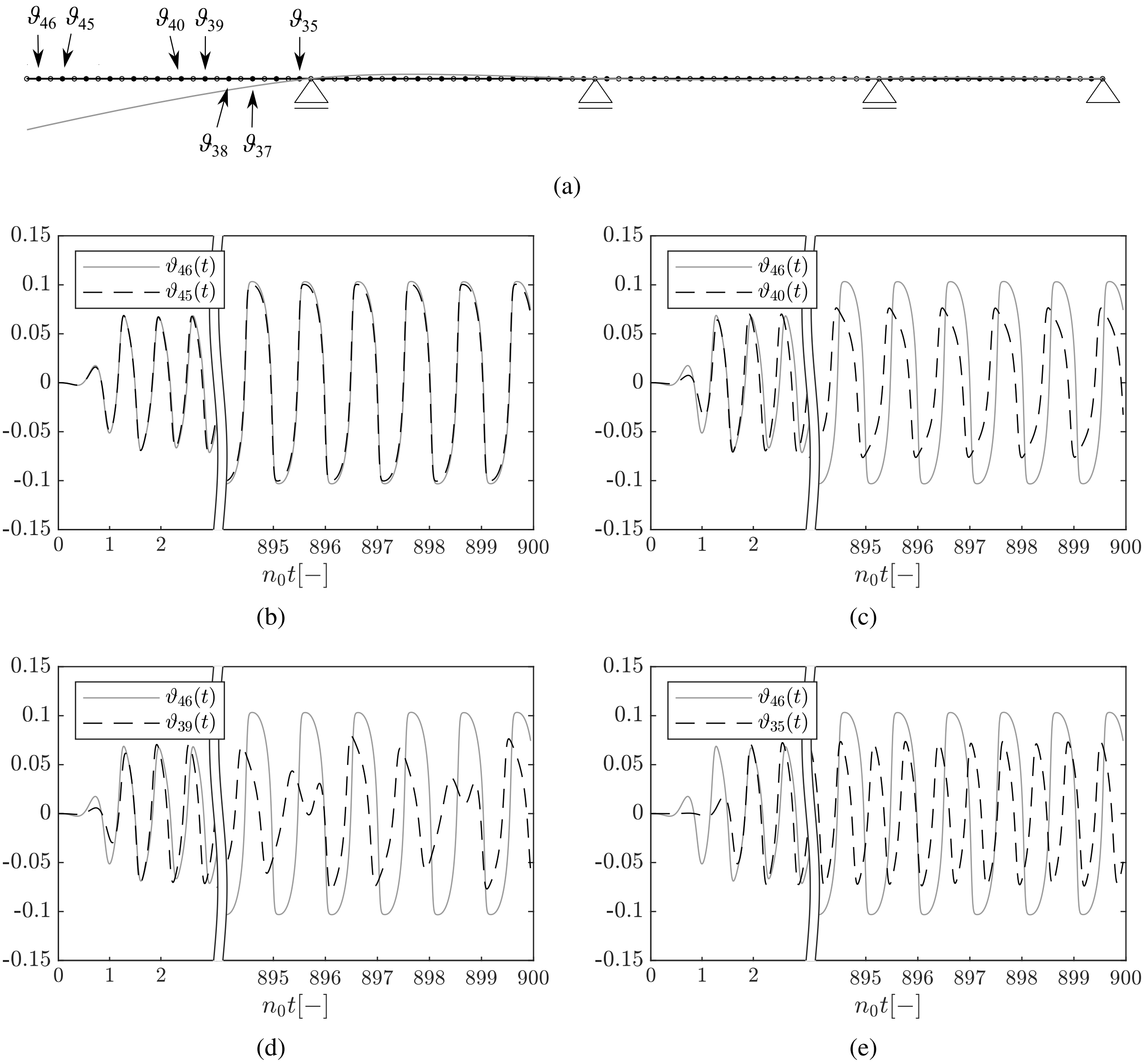

Fig. 6.10: Time history records of wake oscillators at various positions of the structural system: (a) positions of the implemented wake oscillators, (b)-(e) time history solutions of ϑ_i with $Sc = 83.0$ at $V/V_r = 1.7$ (corresponding to the VIV peak shown in Fig. 6.9 (b)).

Contribution of the launching nose

For bridge construction with incremental launching method, the use of a light-weight launching nose will not only increase the first bending frequency for the critical launching phase, but may also help to stabilize the possible wind induced vibration. Fig. 6.12 shows the effect of launching nose, considered a very low damping ratio for the first mode. With or without consideration of the launching nose, the wake oscillator model predicted a galloping onset both at V_r. However, from the quasi-steady solutions, one can find the galloping onset has been postponed a lot for the case with launching nose. This is a result of the drag force of the launching nose played a stabilizing effect for the whole structural system. Although the drag coefficient of a lattice

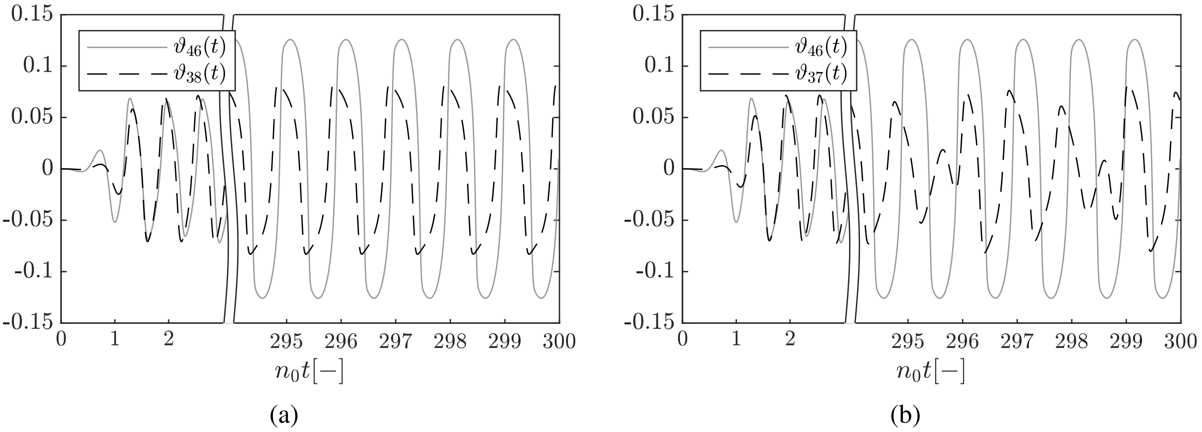

(a) (b)

Fig. 6.11: Time history solutions of ϑ_i with $Sc = 5.5$ at $V/V_r = 1.7$. See also Fig. 6.10 (a) for the locations of the implemented wake oscillators, and Fig. 6.10 (a) for the structural amplitude response.

structure is low, the special location of the launching nose has made this stabilizing effect quite pronounced. The concerned mechanism can be better understood by following equation

$$\int_{l'} m(z)\phi^2(z)\mathrm{d}z \cdot \left[\ddot{\xi}(t) + 2\zeta_0\omega_0\dot{\xi}(t) + \omega_0^2\xi(t)\right] = \frac{1}{2}\rho U^2 d \left[\int_{l'} A_1(z)\phi^2(z)\mathrm{d}z\right] \frac{\dot{\xi}(t)}{U} \quad (6.14)$$

which is the dynamic equation for a structural system about its equilibrium position (fundamental mode). It is derived from equilibrium equation unit length of the beam system

$$m(z)\left[\ddot{y}(z,t) + 2\zeta_0\omega_0\dot{y}(z,t) + \omega_0^2 y(z,t)\right] = \frac{1}{2}\rho U^2 d A_1(z)\frac{\dot{y}(z,t)}{U} \quad (6.15)$$

by expressing $y(z,t) = \phi(z)\xi(t)$, multiplying both sides with $\phi(z)$ and then integrating over the whole length of structural system l'. Here, the linear part of quasi-steady aerodynamic force is considered, i.e., $C_{Fy}^{QS}(\dot{y}/U) = A_1(\dot{y}/U)$. For the lattice launching nose, there is $A_1 \approx -C_D$. From Eq.6.14, one can find the coefficient $A_1(z)$ actually works with $\phi^2(z)$ to determine the stability of a structural system. And, at the location of launching nose, the value of $\phi(z)$ is quite large.

The stabilizing effect of the launching nose becomes also apparent in the solutions of wake oscillator model, when the damping of the system is further increased, as shown in Fig. 6.13. At a damping ratio of 1.17% (logarithmic damping δ_0 = 0.074), the response with launching nose turns into a VIV response rather than a galloping starting at V_r. However, such a behavior is still not reached for the one without launching nose, up to a damping ratio of 1.54% (logarithmic damping δ_0 = 0.097). Moreover, it is to mention that the structural system with launching nose features a lower equivalent mass ratio m_{equ} than the one without launching nose, because the launching nose has been assumed 50% lighter than the main girder per unit length. Therefore, for the same damping level, the Scruton number calculated with m_{equ} is actually lower for the structural system with launching nose.

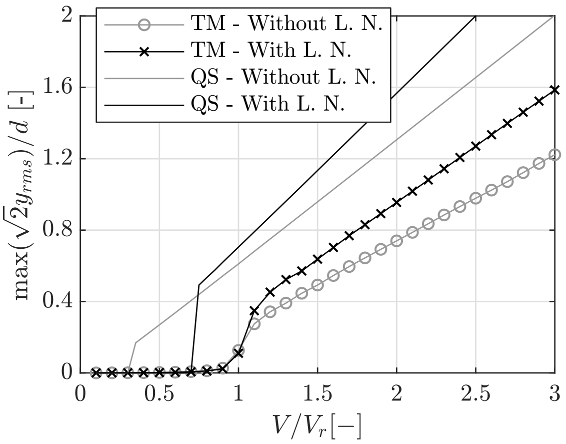

Fig. 6.12: Effect of the launching nose for a very low damping ratio of 0.17% (logarithmic damping δ_0 = 0.011). Solutions are obtained with small initial conditions. "TS" denotes "TS-2018" wake oscillator model, "QS" nonlinear quasi-steady galloping model, and "L. N." the abbreviation of "Launching Nose".

Dominance of the cantilever

It is to note that the implementation of many wake oscillators on the structural system has brought a quite high computational cost. On the other hand, for a structural system shown in Fig. 6.6, the main contribution to the dynamic response of the system may just come from the cantilever part. Therefore, it is decided to check whether precise enough results can be obtained when only the cantilever is implemented with wake oscillators. Specifically, the 34 wake oscillators implemented on the other spans were all removed, as well as the quasi-steady aerodynamic force contribution. By doing so, there are only 9 wake oscillators remained on the cantilever, and the quasi-steady aerodynamic force for the launching nose is still maintained.

The computational speed was found about 3 times faster than the case with wake oscillators implemented on the full structure, and the resultant amplitude was found slightly lower but still acceptable as shown in Fig. 6.14. This is somewhat understandable, due to the high dominance of the cantilever portion in the mode shape (see Fig. 6.6). The numerical investigations carried out here seems also to support the idea, that for the critical bridge laughing phase the consideration of the single cantilever, rather than the whole bridge, might be sufficient for wind tunnel aeroelastic tests. Nevertheless, if a higher accuracy is wanted, including at the same time the adjacent span will be sufficiently enough (as indicated also in Fig. 6.14).

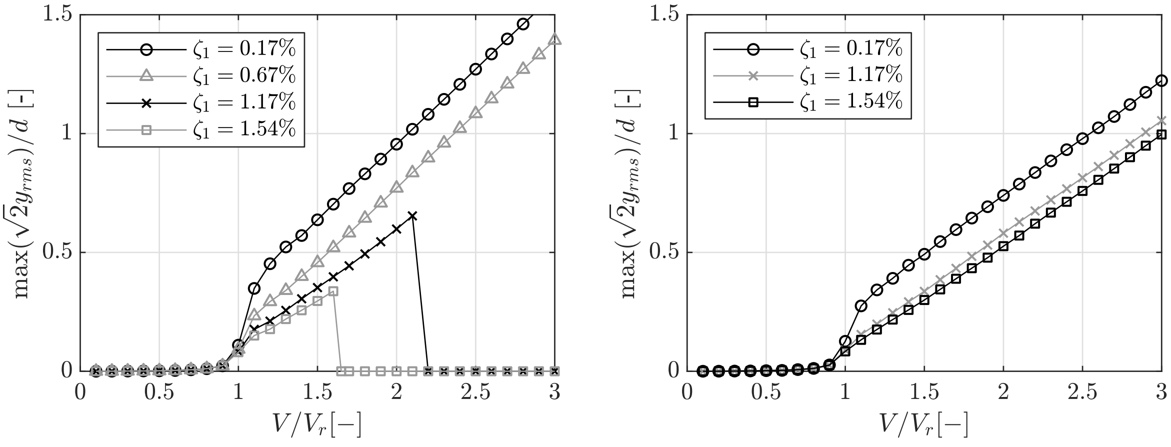

(a) With Launching nose (b) Without Launching nose

Fig. 6.13: Wake oscillator model solutions for the structural system with and without launching nose, at different damping levels. Solutions attained from small initial condition.

6.3 Aerodynamic Optimization for the Launching Nose

From the case study, it is learned that the aerodynamic properties of the launching nose is able to play an important role for the aeroelastic behaviors of the whole structural system. From another perspective, this also implies a potential way to suppress the galloping issue during bridge launching phase, in an efficient and economic manner. That is a particular optimization for the aerodynamics of the launching nose, to make it generate more stabilizing force (positive aerodynamic damping). This implication has promoted the author of this thesis to make some preliminary optimizations for the used launching nose model, as shown in Fig. 6.15 (a) and (b). Here, the concerned preliminary optimization was simply performed by closing the top side (“Optim. 1”), or both top and bottom side (“Optim. 2”), of the lattice launching nose with wood plate. Measuring also at $U \approx 10.36$ m/s, the steady C_D and C_L coefficients for the optimized launching noses are provided in Fig. 6.15, including also those of the original lattice launching nose for a comparison.

Once the aerodynamic optimization is applied, either for “Optim. 1” or “Optim. 2”, one can find the lift emerges and varies intensively with α. In particular, “Optim. 2” clearly features a quite good $C_L - \alpha$ curve, which presents always positive slope in the investigated flow incidences. Based on the measured C_D and C_L, the galloping factor A_1, according to Den Hartog criterion, can be calculated for the launching noses and presented in Tab. 6.1 for two mean wind angles of attack. Further assuming A_1 of the launching noses constant along its axis, an equivalent A_1 factor can be derived form Eq.6.14 to indicate the stability of the structural system

$$m_{equ} \cdot \left[\ddot{\xi}(t) + 2\zeta_0\omega_0\dot{\xi}(t) + \omega_0^2\xi(t)\right] = \frac{1}{2}\rho U^2 d \cdot A_{1,equ} \cdot \frac{\dot{\xi}(t)}{U} \tag{6.16}$$

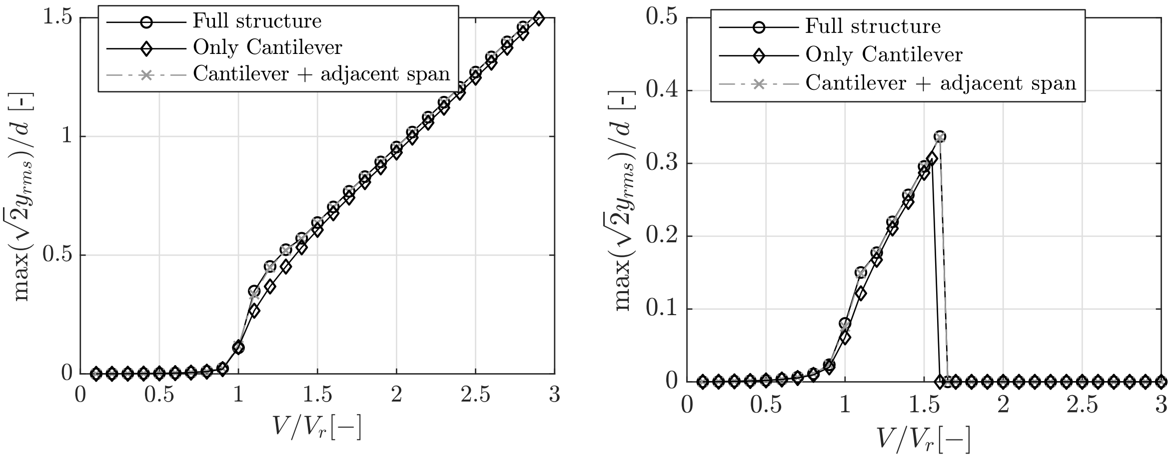

(a) $\zeta_0 = 0.17\%$ (b) $\zeta_0 = 1.54\%$

Fig. 6.14: Comparison of the numerical results, between wake oscillators implemented on the full structure and on only the cantilever part.

in a quasi-steady galloping manner. Here, m_{equ} is the equivalent mass

$$m_{equ} = \frac{\int_{l'} m(z)\phi^2(z)\mathrm{d}z}{\int_{l'} \phi^2(z)\mathrm{d}z} \tag{6.17}$$

and $A_{1,equ}$ is the equivalent A_1 factor

$$A_{1,equ} = \frac{\int_{l'} A_1(z)\phi^2(z)\mathrm{d}z}{\int_{l'} \phi^2(z)\mathrm{d}z} \tag{6.18}$$

Tab. 6.1: A_1 factor evaluated for the three configurations of launching nose, at two mean wind angles of attack. Range of wind incidence for evaluating A_1: $\alpha_0 - 1^\circ \leq \alpha \leq \alpha_0 + 1^\circ$.

	Original	Optim. 1	Optim. 2
$\alpha_0 = 0^\circ$	-0.46	-5.19	-6.75
$\alpha_0 = 4^\circ$	-0.52	0.68	-2.41

Now, it is supposed the “Optim. 2” launching nose being used for the case study. With $A_1 = 4.17$ for the bridge deck at $\alpha_0 = 4^\circ$, $A_1 = -2.41$ for the “Optim. 2” launching nose, and the mode shape of the structural system (see Fig. 6.6), it is able to obtain $A_{1,equ} = 0.035$. Such a low value suggests the galloping instability problem of the system is almost eliminated. Furthermore, if we assume that the optimization of launching nose is specially made for $\alpha_0 = 4^\circ$ of the bridge deck, then the galloping factor $A_1 = -6.75$ of “Optim. 2” at $\alpha_0 = 0^\circ$ might be simply taken as an more efficient optimization. In this situation, the calculated equivalent galloping factor reports $A_{1,equ} = -2.70$. Fig. 6.16 provided wake oscillator model solutions for these two cases, for a very low damping (see also caption of Fig. 6.16). Clearly, no galloping was predicted at V_r with

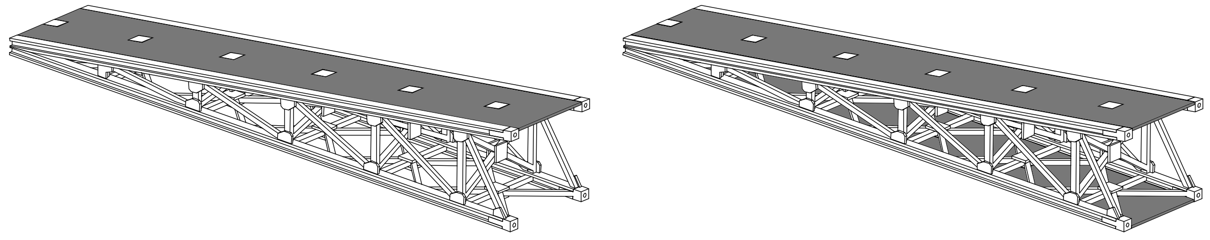

(a) Optim. 1 (b) Optim. 2

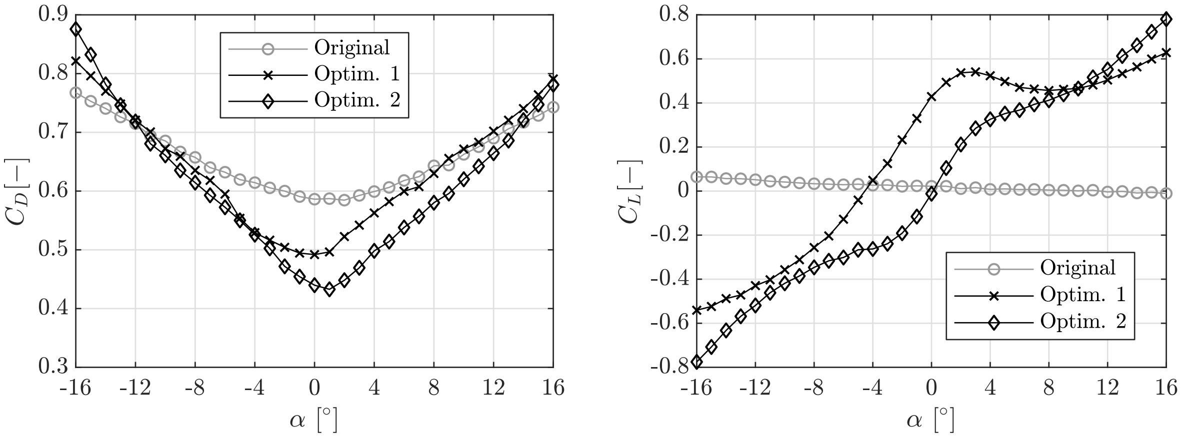

(c) Drag coefficient (d) Lift coefficient

Fig. 6.15: (a) and (b), two optimizations for the launching nose; (c) and (d), the drag and lift coefficients measured by wind tunnel static tests.

the optimized launching nose, although the “Optim. 2a” has reported quite large VIV responses due to the fact that $A_{1,equ} = 0.035$ is close to null in this case. In contrast, for “Optim.2b” with $A_{1,equ} = -2.70$ the VIV response is also significantly reduced.

Finally, it is needed to point out that the above analyzes are based on considering the aerodynamic forces of an oscillation launching nose in a quasi-steady manner. This is fine for the original lattice launching nose, since its dominant aerodynamic force (drag) is unlikely to change too much during the oscillation. For the two modified launching noses, featuring large-size impermeable plates, the aeroelastic forces might differ quantitatively from the quasi-steady estimation. Because of this, aeroelastic tests on the optimized launching nose would be necessary, to understand how much aerodynamic stabilizing force can be really introduced. Moreover, the aerodynamic coefficients (like C_D, C_L) may vary along the launching nose axis, especially for the studied tapered one. This effect should be also further taken into account in the future study.

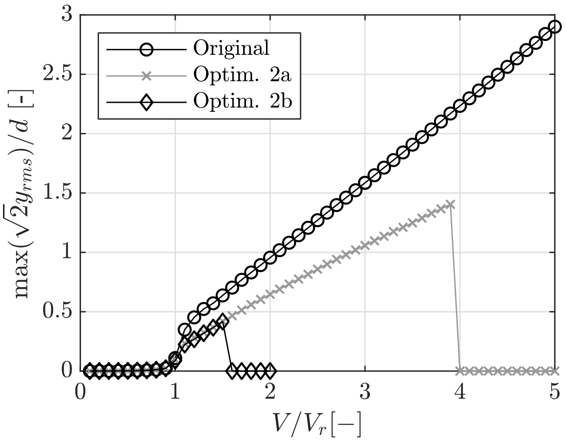

Fig. 6.16: Wake oscillator model solutions with the “Optim. 2” launching nose, for $\zeta_0 = 0.17\%$. “Optim. 2a” denotes the wind attacking the launching nose at $\alpha_0 = 4°$, while “Optim. 2b” at $\alpha_0 = 0°$ (say, the launching nose is orientated $-4°$ relative to the bridge deck).

6.4 Chapter Summary

Based on finite element method, the approach of extending Tamura’s wake-oscillator model to the continuous structural system has been presented. Multiple wake oscillators are coupled to nodes of the structural system to consider the flow-structure interaction. Compared with a similar approach proposed by Tamura & Amano (1983), which is for the VIV problem of continuous system with circular cross section, the presented approach is more suitable for non-circular cross sections in dealing with the unsteady galloping problem (also VIV). This approach enables a higher flexibility for practical use, since the variation of either structural or aerodynamic parameters along the axis can be easily considered. Moreover, this approach can consider multiple modes participation and has the potential of being further extended to take into account the structural non-linearity as well as the incident turbulence.

After validating the algorithm, the critical launching phase of a steel-concrete composite bridge was considered as a case study. There, the mode shape effect and the synchronicity of the coupled multiple wake oscillators were presented and discussed. Practically maybe very meaningful, the used lattice launching nose was found able to mitigate the unsteady galloping of the structural system in an efficient way, thus implying a economic way to suppress the galloping problem by optimizing the aerodynamic shape of the launching nose. Inspired by this, some preliminary optimizations have been made to the used tapered lattice launching nose. The static test results and the associated wake oscillator model predictions confirmed the previous implication at the first stage. Finally, aeroelastic tests on, e.g., a pivoted cantilever model are needed, not only to confirm the prediction capability of the proposed approach, but also to examine the real performance of the optimized launching nose.

7 Conclusions

The studies presented in this thesis are originally motivated by the incremental launching of steel-concrete composite bridges. After a statistical survey on the bridge deck geometry and Scruton number distribution for this particular situation, the potential threat of unsteady galloping to these bridges was revealed. Wind tunnel tests, mathematical modelings and attempts of suppressing the unsteady galloping were then carried out, aiming at a better understanding of the phenomenon itself, on the scientific side, and how to predict and suppress it on the engineering side. These works composed the main content of this thesis.

7.1 Summary and Main Contributions

The main original contributions and findings in this thesis are summarized as follows.

Experimental data set Extensive wind tunnel tests have been carried out based on three sectional wind tunnel models and a lattice launching nose model. Especially, the bridge deck model with an open cross section, which is typical during the construction phase of steel-concrete composite bridges but less well studied, was paid particular attentions. Static tests on this bridge deck model first revealed a negative slope of C_L within the flow incidence $-5°$ to $12°$, indicating the possibility of across-wind galloping instability. Aeroelastic tests confirmed this instability and also highlighted the sensitivity of unsteady galloping behaviors to the mean flow incidence angle α_0. For the bridge deck model at $\alpha_0 = 2°$ and especially $\alpha_0 = 4°$, the typical unsteady galloping due to an interaction with VIV was observed, being its threshold at the reduced Kármán-vortex resonance wind speed V_r. However, for $\alpha_0 = -2°$ and $\alpha_0 = 0°$, the unsteady galloping arose in manner more difficult to understand, being the onset velocity clearly higher than V_r even for a very low Scruton number (this behavior was named *atypical unsteady galloping* in this thesis). Although it may be not a direct evidence, it was found the strength of vortex shedding force coefficient C_{L0} is quite different between the typical unsteady galloping and the atypical one, being the latter characterized with a much weaker C_{L0}. Such a connection was also noticed for the 2:1 rectangular cylinder and the trapezoidal cylinder. Nevertheless, if the typical unsteady galloping occurred, a quite high Scruton number was found to be needed to decouple the interaction with VIV. For the studied bridge deck at $\alpha_0 = 4°$, the galloping onset was fixed at V_r for Scruton number up to at least 70. This value is much larger than the typical one, $Sc =$ 15-25, for this kind of bridges in launching phase. With respect to the typical unsteady galloping behaviors, the bridge deck model also showed some differences from the other two cylinder models, such as the “Partial-Interference” behavior outlined by Mannini & al. (2016b) being not observed. In small-scale turbulent flow ($L_u/d \approx 0.5$, I_u = 9.2%-14.9%), the bridge deck model also showed a strong tendency to galloping instability. Differing from that in smooth flow, the typical unsteady galloping due to interaction with VIV was not observed anymore. Instead, for very low Sc, the galloping arose clearly behind V_r, in a similar manner as the *atypical unsteady galloping* observed in smooth flow.

Mathematical modeling on prism body The nonlinear wake oscillator model of Tamura’s form was considered for the mathematical modeling of the unsteady galloping due to interference with VIV. To be more specific, the actually used wake oscillator model is a slightly modified one by Mannini & al. (2018a) (named “TS-2018” in this thesis), adopting also their method for identifying the key parameter f (by means of calibrating with a set of aeroelastic test results of high Scruton number in the VIV region). Maintaining the identified f parameter unvaried in the mathematical model, numerical predictions were compared with the aeroelastic test results in a wide range of Scruton number. Satisfying agreements were obtained not only for the 2:1 rectangular cylinder, but also for the bridge deck model at $\alpha_0 = 4°$. In particular, the typical unsteady galloping behavior, that lower than a certain value of Sc the galloping onset is fixed at V_r, is perfectly captured by the wake oscillator model. It is also worth noting here that this is probably the first time to apply the wake oscillator model to a generic bridge deck model of complex geometry. Moreover, additional efforts have been contributed to examine the so-called physical considerations in the wake oscillator model, based on the 2:1 rectangular cylinder due to its clean shape. This part of work has promoted further modifications for the wake oscillator model. This further “Modified” one maintains a comparable prediction capability as the “TS-2018” form, but its wake geometric parameters agree better with the physical near-wake of sharp-edged bluff body. Such a better agreement was achieved not only for the 2:1 rectangular cylinder studied in this thesis, but also for the square cylinder reported by other researchers (e.g., Lander & al. (2016)). Finally, efforts were also made to estimate the key parameter f for wake oscillator model by means of direct wake flow measurements. The estimated f value qualitatively supports the use of a high value of f for the sharp-edge bluff bodies, rather than a low value like $f = 1.16$ which is originally derived for circular cylinder. However, a quantitative agreement is not achieved with the f value due to the calibration method proposed by Mannini & al. (2018a). A discussion on this point is particularly presented.

Predictions for the continuous system A approach of extending the wake oscillator model for continuous structural system is proposed. In this approach, multiple wake oscillators were coupled to the nodes of the structural system, which is described by finite element method.

This approach can be seen as an improved one of the approach proposed by Tamura & Amano (1983), particularly suitable for unsteady galloping problem. It is of high flexibility to consider the variation of either structural or aerodynamic parameters along the axis of a continuous system, and has the potentiality to be further extended for considerations of the structural nonlinearity as well as the turbulence in incoming flow. A case study, which corresponds to the structural system of a steel-concrete composite bridge during its critical launching phase, was presented for the proposed approach. The mode shape effect of the flexible structural system and the synchronicity of the coupled multiple wake oscillators were presented and discussed. Moreover, through this case study, the role of the aerodynamics of the launching nose was highlighted, revealing at the same time a potentially efficient way to mitigate the unsteady galloping by means of aerodynamic optimization for the launching nose. Wind tunnel static tests on a tapered lattice launching nose and its optimized configurations, associated with the wake oscillator model predictions, together confirmed this potentiality at the preliminary stage.

Unsatisfying results There are also some unsatisfying results or weaknesses in this thesis, and should be pointed out:

- For some Scruton numbers in certain reduced wind speed ranges, the numerical solutions of the wake oscillator model presented a high amplitude oscillation branch, which is, however, not observed on in the wind tunnel aeroelastic tests.
- For the *atypical unsteady galloping* arising at $\alpha_0 = 0^\circ$ of the bridge deck model, the mathematical modeling with wake oscillator model was unsuccessful.
- For flow velocity measurements in the near-wake of bluff body, the used anemometer (Cobra probe) is unable to deal with the inverse flow. Due to this reason, some reported data points are affected. Fortunately, several key features are supposed to be not influenced or in a very limited manner.
- In the wind tunnel tests, the generated turbulent flow features a rather small integral length compared to full-scale engineering practices. Attentions should be paid to this difference, when the reported experimental data in this thesis is used for full-scale purposes.

7.2 Outlooks and Future Works

Either due to a time limitation or laboratory restrictions, there are some works not complemented or some ideas not put in practice in this thesis. They are considered as future works:

- As previously mentioned, the experimentally generated turbulent flow in this thesis has a relatively small length scale. A very recent publication (Mannini & al. 2018b) indicated, however, that the turbulence integral length may also play an important role for the galloping instability. Due to this reason, further investigations in large-scale turbulent flow would be very meaningful. However, the generation of large scale turbulence, maintaining at the same time a high turbulence intensity, is usually difficult in wind tunnel, considering that the geometrical scaling ratio of a bridge deck cannot be very small so that details can be well-reproduced. Alternatively, the computational fluid dynamic (CFD) technique maybe a good choice for this purpose, considering the rapid increase of computation capability in these years.

- The wind tunnel tests on a cantilever model should be considered as a future work, for following three reasons: a) the galloping problem of steel-concrete composite bridges during launching phase can be studied in a way more close to the full-scale conditions; b) aeroelastic results from the cantilever model can be used to examine the prediction capability of the wake oscillator model for continuous structural system; c) the idea of suppressing unsteady galloping through aerodynamic optimizations for the launching nose can be better confirmed.

- The unsteadiness in flow-structure interaction has been a research topic for many decades, and it is supposed to be also interesting in the future. With respect to the studied unsteady galloping problem, the nature of the unsteadiness of motion-induced aerodynamic force is still not fully understood. The failure in mathematically modeling the *atypical unsteady galloping* clearly implies the insufficiency of putting the quasi-steady force item in the controlling equations of wake oscillator model (Eq. 2.55). To attain the mathematical modeling of the *atypical unsteady galloping*, an essential modification to the quasi-steady force item may be needed.

- Finally, for the studied bridge deck with open cross section, the across-wind galloping instability was found as the dominant issue probably due to its comparably small side-ratio ($b/d = 2.0$). For open cross section with larger side-ratio, the instability in torsional degree of freedom may arise and suppose to be also interesting.

Appendix

A.1 Analytical Approach to the Nonlinear Across-wind Galloping with Quasi Steady Theory

Here, based on the classical quasi-steady theory, the analytical approach to the nonlinear behaviors of across-wind galloping is supplemented. As an example, the square cylinder is taken as an object for this analysis. First of all, the static-test measured C_{Fy} coefficient is plotted as a function of $\tan(\alpha)$, as shown in Fig. A.1. Then, polynomials are used to approximate the experimental data. Due to the symmetrical geometry of the square cross section, odd polynomials up to 7^{th} order are enough to provide a good approximation (Parkinson & Smith 1964). Therefore, the C_{Fy} coefficient can be written as

$$C_{Fy} = A_1[\tan(\alpha)] + A_3[\tan(\alpha)]^3 + A_5[\tan(\alpha)]^5 + A_7[\tan(\alpha)]^7 \tag{A.1}$$

where A_i is the coefficient for the $[\tan(\alpha)]^i$ item.

Considering now for an osculation body, due to $\tan(\alpha) = \dot{y}/U$, Eq. A.1 can be written as

$$C_{Fy} = A_1\left(\frac{\dot{y}}{U}\right) + A_3\left(\frac{\dot{y}}{U}\right)^3 + A_5\left(\frac{\dot{y}}{U}\right)^5 + A_7\left(\frac{\dot{y}}{U}\right)^7 \tag{A.2}$$

Substituting Eq.A.2 in the governing equation of motion (Eq. 2.16), there is

$$m\ddot{y} + c_y\dot{y} + k_y y = \frac{1}{2}\rho d U^2 \left[A_1\left(\frac{\dot{y}}{U}\right) + A_3\left(\frac{\dot{y}}{U}\right)^3 + A_5\left(\frac{\dot{y}}{U}\right)^5 + A_7\left(\frac{\dot{y}}{U}\right)^7\right] \tag{A.3}$$

For convenience, the above equation can be further written in non-dimensional form, by defining $Y = y/d$ as the non-dimensional displacement, $V = U/(\omega_0 d)$ as the reduced velocity and $m^* = m/(0.5\rho d^2)$ as the mass ratio. Moreover, non-dimensional time $\tau = \omega_0 t$ is used and $(\,)'$ denotes the differentiate with respect to τ. The above equation becomes

$$Y'' + 2\zeta_0 Y' + Y = \frac{V^2}{m^*}\left[A_1\left(\frac{Y'}{V}\right) + A_3\left(\frac{Y'}{V}\right)^3 + A_5\left(\frac{Y'}{V}\right)^5 + A_7\left(\frac{Y'}{V}\right)^7\right] \tag{A.4}$$

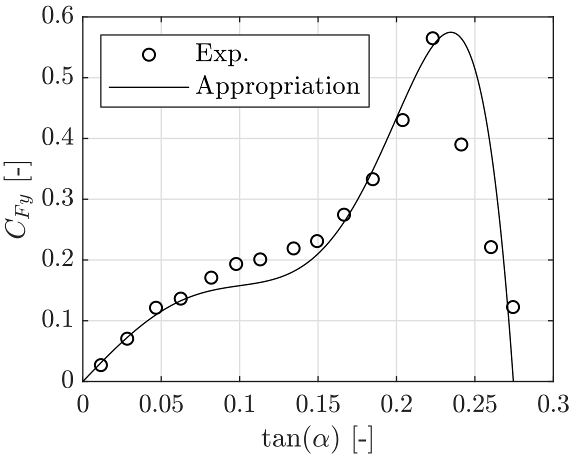

Fig. A.1: Transverse coefficient C_{Fy} *vs.* tan(α) for a square cross section. Experimental data, as well as the coefficients for the 7-order odd polynomials approximation ($A_1 = 2.69$, $A_3 = -168$, $A_5 = 6270$, $A_7 = -59900$), are taken from Parkinson & Smith (1964).

To analytically solve the above equation, the routine reported in Parkinson & Smith (1964) and Parkinson (1989) is followed, which is based on the first approximation method of Krylov and Bogoliubov (Minorsky 1962). Above equation can be further re-written in the form

$$\begin{aligned} Y'' + Y &= \frac{A_1}{m^*}\left[\left(V - \frac{2\zeta_0 m^*}{A_1}\right)Y' + \left(\frac{A_3}{A_1 V}\right)Y'^3 + \left(\frac{A_5}{A_1 V^3}\right)Y'^5 + \left(\frac{A_7}{A_1 V^5}\right)Y'^7\right] \\ &= \tilde{\mu} f(Y'),\ \tilde{\mu} = \frac{A_1}{m^*} \ll 1 \text{ for air flow.} \end{aligned} \tag{A.5}$$

Eq. A.5 has the form of weakly nonlinear autonomous differential equation. For $\tilde{\mu} = 0$, the solution is the familiar sinusoidal form

$$Y = \bar{Y}\cos(\tau + \phi), \quad Y' = -\bar{Y}\sin(\tau + \phi) \tag{A.6}$$

where $\bar{Y}$ is constant. For $\tilde{\mu} \neq 0$ but small, the method of Krylov and Bogoliubov allows the assumption of a solution consisting of a series in powers of $\tilde{\mu}$:

$$Y = \bar{Y}\cos(\tau + \phi) + \tilde{\mu} Y_1(\bar{Y}, \phi, \tau) + \tilde{\mu}^2 Y_2(\bar{Y}, \phi, \tau) + ... \tag{A.7}$$

where $\bar{Y}$ and ϕ are now the slowly varying functions of τ. In most applications, the first approximation (the first item at the right-side of Eq. A.7) is enough to given an accurate estimate of the oscillation phenomenon. Moreover, in this first approximation, Parkinson & Smith (1964) have shown that the phase angle ϕ is constant over a complete period, and it is convenient to set it as zero. Therefore, for the first approximation, it is able to write

$$Y = \bar{Y}\cos(\tau), \quad Y' = -\bar{Y}\sin(\tau) \tag{A.8}$$

with $\bar{Y}$ still as a function of τ. Multiplying both side with Y', Eq. A.5 can be re-written as

$$Y''Y' + Y'Y = \frac{1}{2}\frac{\mathrm{d}(Y'^2 + Y^2)}{\mathrm{d}\tau} = \tilde{\mu} f(Y') \cdot Y' \tag{A.9}$$

Further substituting Eq. A.8, the above equation becomes

$$\frac{1}{2}\frac{\mathrm{d}\bar{Y}^2}{\mathrm{d}\tau} = -\tilde{\mu} f(-\bar{Y}\sin(\tau)) \cdot \bar{Y}\sin(\tau) \tag{A.10}$$

It can be found from Eq.A.10 that the amplitude variation with τ is also small because of $\tilde{\mu}$, so that the change of $\bar{Y}$ is negligible over one oscillation cycle. Therefore, it will be satisfactory to replace the right side of Eq.A.10 by its average over one cycle, namely

$$\frac{\mathrm{d}\bar{Y}^2}{\mathrm{d}\tau} = -\frac{\tilde{\mu}}{\pi}\int_0^{2\pi} f(-\bar{Y}\sin(\nu)) \cdot \bar{Y}\sin(\nu)\mathrm{d}\nu \tag{A.11}$$

Substituting in the expression of "$f()$", the integration of the right-side of Eq.A.11 yields

$$\frac{\mathrm{d}\bar{Y}^2}{\mathrm{d}\tau} = \frac{A_1}{m^*}\left[\left(V - \frac{2\zeta_0 m^*}{A_1}\right)\bar{Y}^2 + \frac{3}{4}\left(\frac{A_3}{A_1 V}\right)\bar{Y}^4 + \frac{5}{8}\left(\frac{A_5}{A_1 V^3}\right)\bar{Y}^6 + \frac{35}{64}\left(\frac{A_7}{A_1 V^5}\right)\bar{Y}^8\right] \tag{A.12}$$

Eq.A.12 can be written in brief form

$$\frac{\mathrm{d}R}{\mathrm{d}\tau} = F(R) = a_1 R + a_3 R^2 + a_5 R^3 + a_7 R^4 \tag{A.13}$$

where $R = \bar{Y}^2$, and a_1, a_3, a_5 and a_7 are the coefficients dependent only on the parameters of a given system. Clearly, in a differential form, Eq. A.13 describes how the amplitude of the system evolves with the reduced time τ. For steady-state oscillation, there is the condition $\mathrm{d}R/\mathrm{d}\tau = 0$ (oscillation amplitude does not change anymore with τ), so that the steady-state amplitudes include $R = 0$, and the real positive roots given by the cubic equation

$$a_1 + a_3 R + a_5 R^2 + a_7 R^3 = 0 \tag{A.14}$$

In particular, $R = 0$, the initial position of the equilibrium, represents a singular point at the origin called a focus. The other positive roots R_i of Eq. A.14, if exists, define the trajectories in the phase plane $(Y, \dot{Y})$ called limited cycles (concentric circles of radius $\bar{Y}_{s_i} = \sqrt{R_i}$). For the stability of the limit cycle or the focus, it is determined by the differential of $F(R)$ with respect to R about the root R_i

$$\left.\frac{\mathrm{d}F(R)}{\mathrm{d}R}\right|_{R_i} = a_1 + 2a_3 R_i + 3a_5 R_i^2 + 4a_7 R_i^3 \tag{A.15}$$

There are three possibilities:

- $\left.\frac{\mathrm{d}F(R)}{\mathrm{d}R}\right|_{R_i} < 0$, stable.

  Since $F(R_i) = 0$ and the slope around R_i is negative, in the close region $(R_i - \delta R,\, R_i + \delta R)$, there are $F(R_i - \delta R) > 0$ and $F(R_i + \delta R) < 0$. Remembering $F(R) = \mathrm{d}R/\mathrm{d}\tau$, $F(R_i - \delta R) > 0$ means that the amplitude of the oscillator will increase if the amplitude is displaced from R_i to a slightly lower one $R_i - \delta R$. On the other hand, if the amplitude of the oscillator is displaced from R_i to a slightly larger one $R_i + \delta R$, the amplitude will decrease in the following time because of $F(R_i + \delta R) < 0$. These imply that the considered limit cycle oscillation is resistant to small perturbation.

- $\left.\frac{\mathrm{d}F(R)}{\mathrm{d}R}\right|_{R_i} > 0$, unstable.

  This case is in contrast to the last one. Since the slope of $F(R)$ about R_i is positive, in the close region $(R_i - \delta R,\, R_i + \delta R)$, there are $F(R_i - \delta R) < 0$ and $F(R_i + \delta R) > 0$. The amplitude of the oscillator will decrease when the amplitude is displaced from R_i to $R_i - \delta R$, while it will increase if the amplitude is displaced from R_i to $R_i + \delta R$. In other words, any small perturbations will make the oscillation leave its original limit cycle.

- $\left.\frac{\mathrm{d}F(R)}{\mathrm{d}R}\right|_{R_i} = 0$, partial unstable.

  For this case, the slope of $F(R)$ around R_i must have different signs for the close regions $(R_i - \delta R,\, R_i)$ and $(R_i,\, R_i + \delta R)$. Therefore, for the perturbation in one close region the oscillation is able to return back to its original limit cycle, but unable for the other close region.

Here, it is convenient to combine the square cylinder (Parkinson & Smith 1964) for further analysis. For the given mechanical properties, the solutions of steady-state amplitude $\bar{Y}_s$ at various reduced velocity V are plotted in Fig. A.2. Roots of $F(R) = 0$ (Eq.A.13) and the limit cycles in phase plane are reported in Fig. A.3 for different situations. They are separately discussed as follows.

- $V < V_0$ (Fig. A.3 (a)). Here $V_0 = V_g = 2\zeta_0 m^*/A_1$ is critical wind speed for galloping in reduced form. Solution of $F(R) = 0$ reports only one non-negative real root that is at $R = 0$, namely the focus. This solution is stable as indicated by the arrow in phase plane (clearly, $a_1 < 0$).

- $V_0 < V < V_1$ (Fig. A.3 (b)). Solution of $F(R) = 0$ reports a real positive root R_1, and the solution at $R = 0$ becomes unstable. Small perturbation applied to the focus or the limit cycle will finally return to the only limit cycle featuring a radius of $\bar{Y}_{s1}$.

- $V = V_1$ (Fig. A.3 (c)). Solution of $F(R) = 0$ reports two real positive root R_1 and R_2. In particular, R_2 is also a local maximum, reflected by $F(R)$-curve's slope changing its sign. Its corresponding limit cycle oscillation is partial unstable (with radius $\bar{Y}_{s2}$). For perturbation from the higher amplitude side the oscillation is able to return back to the original limit cycle, while perturbation from the lower amplitude side will make oscillation leave the original limit cycle and finally go to the $\bar{Y}_{s1}$ one. This partial unstable solution corresponds to the point 5 in Fig. A.2.

- $V_1 < V < V_2$ (Fig. A.3 (d)). Solution of $F(R) = 0$ reports three real positive roots R_1, R_2 and R_3. In particular, the limit cycle corresponding to R_2 is unstable, any small perturbation will make the oscillation leaves its original limit cycle, dropping to the stable one with lower amplitude or jumping to the stable one with higher amplitude.

- $V = V_2$ (Fig. A.3 (e)). Solution of $F(R) = 0$ reports two real positive roots R_1 and R_2. In particular, R_1 is right now a local minimum. The inability of its corresponding limit cycle is in contrast to the $V = V_1$ case, namely the higher amplitude side is unstable while the lower amplitude side is stable. This partial unstable solution corresponds to the point 2 in Fig. A.2.

- $V > V_2$ (Fig. A.3 (f)). Solution of $F(R) = 0$ reports only one real positive roots R_1, which corresponds to a stable limit cycle.

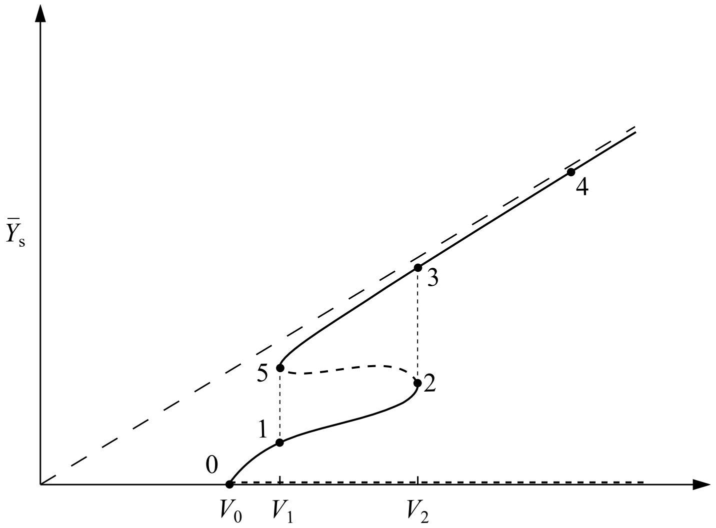

Fig. A.2: $\bar{Y}_s$ - V curve for a square cylinder according to the nonlinear quasi-steady galloping theory, reproduced from Parkinson & Smith (1964). Short dash line represents unstable solutions, while long dash line corresponds to the asymptotic line for high reduced wind speed solutions.

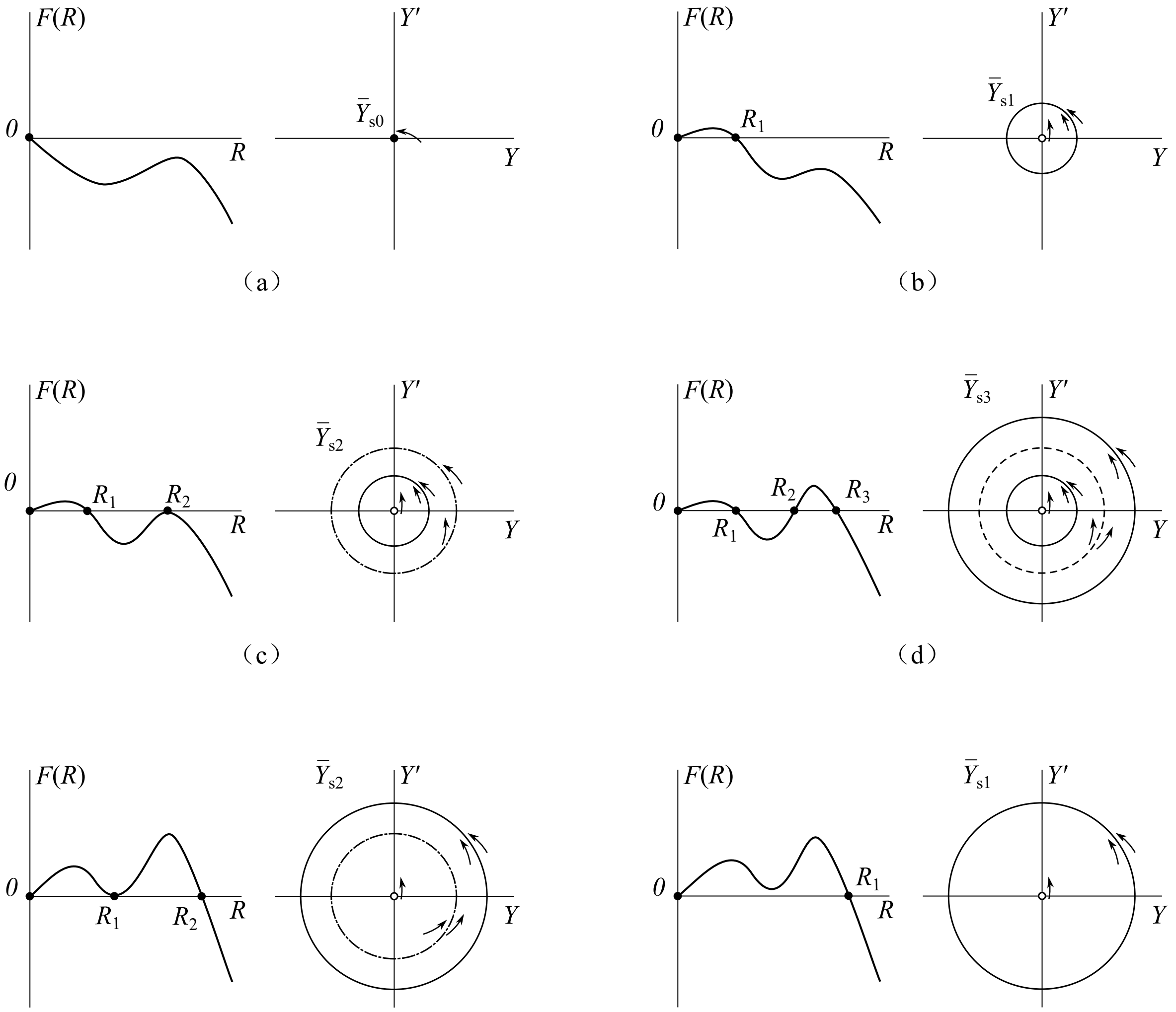

(a) (b)

(c) (d)

(e) (f)

Fig. A.3: Roots of $F(R) = 0$ and limit cycles in phase plane. The arrow indicates the amplitude development after a small perturbation to the limit cycle or the focus.

It can be also observed in Fig. A.2, the oscillation amplitude will follow the trajectory “0-1-2-3-4” for continuously increased V, while another trajectory “4-3-5-1-0” will be followed for continuously decreased V. A hysteresis loop therefore exists in the amplitude-velocity curve. Moreover, there are two another important characteristics for the amplitude-velocity curve of galloping.

Firstly, if the left side of Eq. A.12 is set null, then further divided by $A_1 V \bar{Y}_s^2 / m^*$, there is

$$0 = \left(1 - \frac{2\zeta_0 m^*}{A_1 V}\right) + \left(\frac{3A_3}{4A_1}\right)\left(\frac{\bar{Y}_s}{V}\right)^2 + \left(\frac{5A_5}{8A_1}\right)\left(\frac{\bar{Y}_s}{V}\right)^4 + \left(\frac{35A_7}{64A_1}\right)\left(\frac{\bar{Y}_s}{V}\right)^6 \tag{A.16}$$

Assuming $V \to \infty$, the $\frac{2\zeta_0 m^*}{A_1 V}$ item will vanish in Eq. A.16. In this case, solution of Eq. A.16 is dependent only on parameter A_i and V. Further defining $\bar{r} = \frac{\bar{Y}_s}{V}$, Eq. A.16 becomes

$$0 = 1 + \left(\frac{3A_3}{4A_1}\right)\bar{r}^2 + \left(\frac{5A_5}{8A_1}\right)\bar{r}^4 + \left(\frac{35A_7}{64A_1}\right)\bar{r}^6 \quad \text{with, } V \to \infty \tag{A.17}$$

Clearly, the root of Eq.A.17, if a positive real value exists, is a constant. This means, for $V \to \infty$, the $\bar{Y}_s$ -V curve becomes asymptotic to a line through the origin of slope $\bar{r}$.

Secondly, if the left side of Eq. A.12 is also set to null, but then divided by V_0^3 ($V_0 = 2\zeta_0 m^*/A_1$), there is

$$0 = \left(\frac{V}{V_0} - 1\right)\left(\frac{\bar{Y}_s}{V_0}\right)^2 + \left(\frac{3A_3}{4A_1(\frac{V}{V_0})}\right)\left(\frac{\bar{Y}_s}{V_0}\right)^4 + \left(\frac{5A_5}{8A_1(\frac{V}{V_0})^3}\right)\left(\frac{\bar{Y}_s}{V_0}\right)^6 + \left(\frac{35A_7}{64A_1(\frac{V}{V_0})^5}\right)\left(\frac{\bar{Y}_s}{V_0}\right)^8 \tag{A.18}$$

The solution $\bar{Y}_s/V_0$ can be right now found dependent only on V/V_0, rather than m^* or ζ_0. This means $\bar{Y}_s/V_0$ - V/V_0 curve is universal and results of different m^* and ζ_0 will collapse on this curve.

Finally, although not shown here for brevity, Parkinson's nonlinear quasi-steady galloping theory has been quantitatively confirmed by the experimental results of a square cylinder at high reduced flow velocities, not only for the amplitude predictions but also for the hysteresis phenomenon as well as the asymptotic behavior. Moreover, the above analytical approach, which is based on polynomials approximating the experimental data, provides comprehensive understandings for the nature of the galloping phenomenon. For more complicated $C_{Fy}(\alpha)$ curve, higher order of polynomials can be introduced to enhance the approximation of experimental data (like in Novak (1972) and Andrianne & Dimitriadis (2014)). To solve the equation of motion described by Eq. 2.16, there exist also many other methods as introduced by Vio & al. (2007). In particular, direct numerical integration is nowadays a powerful tool, which also allows more complicated curved fitting to fully use the experimental data.

A.2 Additional Results of Incoming Flow Measurements

A.2.1 Smooth Flow

Mean flow velocity and turbulence intensity at each monitoring point are presented in Fig. A.4, for five selected rotation speeds of the wind tunnel turbine.

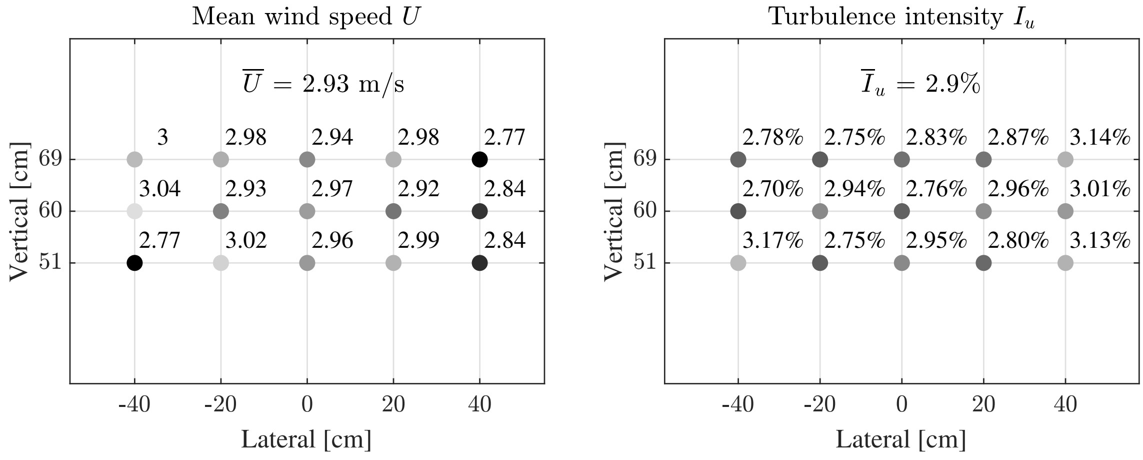

(a) Rotation speed of wind tunnel turbine = 178 rpm

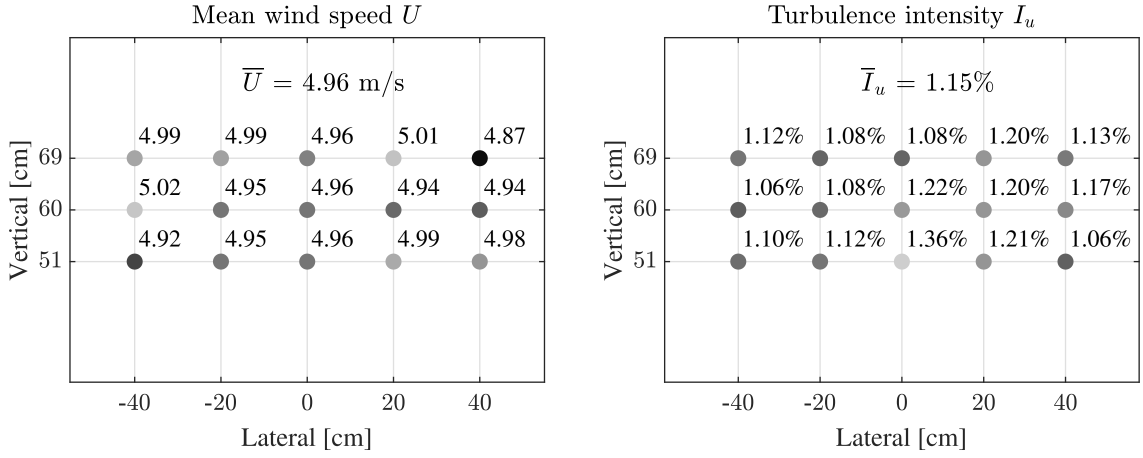

(b) Rotation speed of wind tunnel turbine = 280 rpm

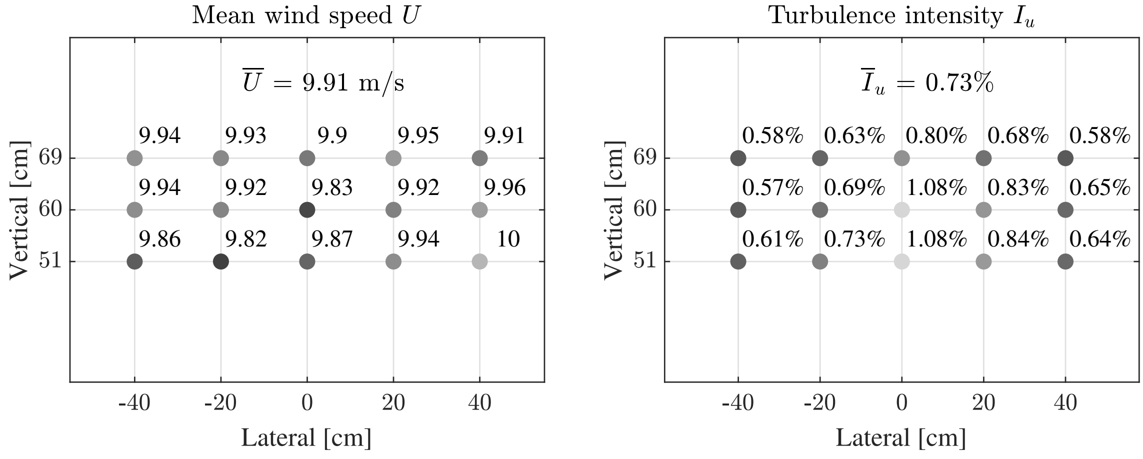

(c) Rotation speed of wind tunnel turbine = 498 rpm

Fig. A.4: Distribution of the mean wind speed U (left) and turbulence intensity I_u (right) among the monitoring points, with variation of the rotation speed of wind tunnel turbine. Figure continued in next page.

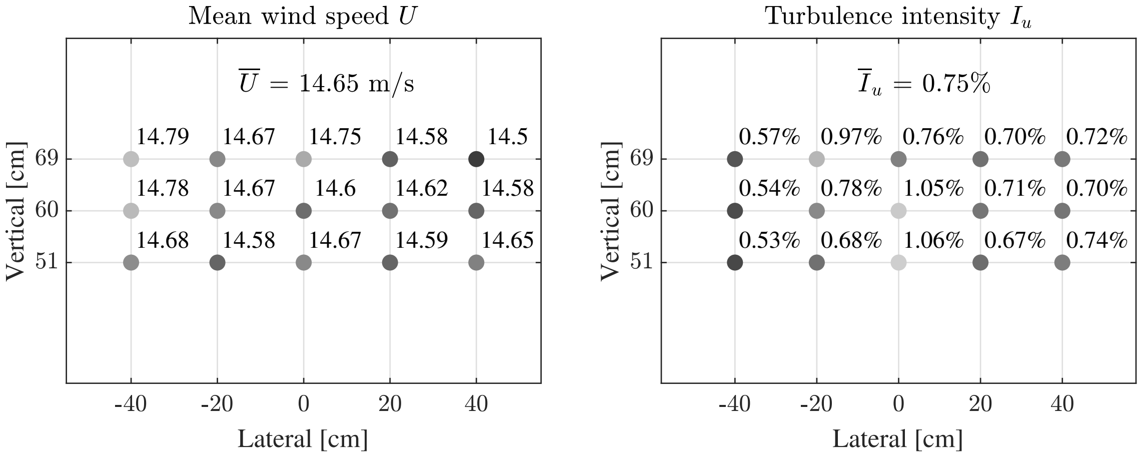

(d) Rotation speed of wind tunnel turbine = 704 rpm

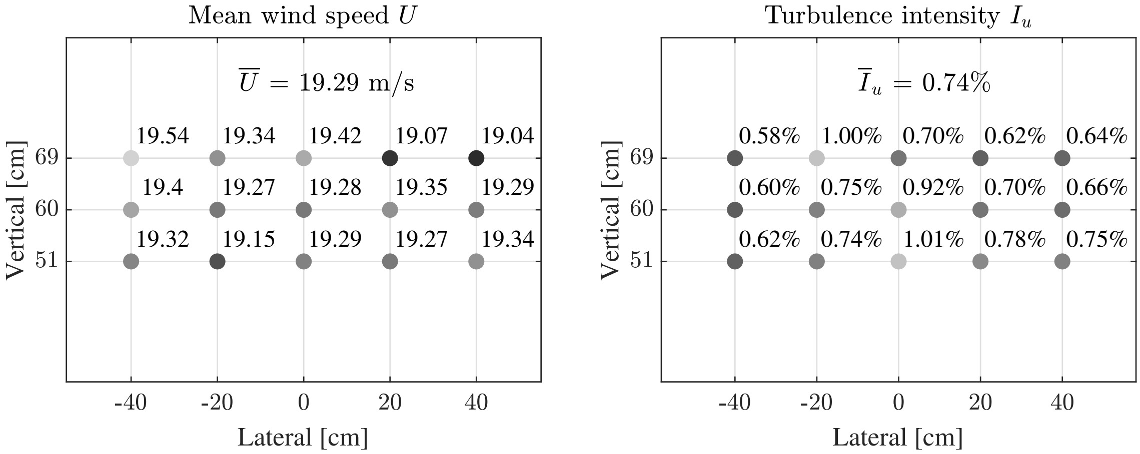

(e) Rotation speed of wind tunnel turbine = 912 rpm

Fig. A.4 (cont.)

A.2.2 Turbulent Flow

Distribution of mean flow velocity, turbulence intensity and turbulence integral length among the monitoring points are presented in Fig. A.5- Fig. A.7, for three turbulence gird configurations at a mean wind speed about 10 m/s.

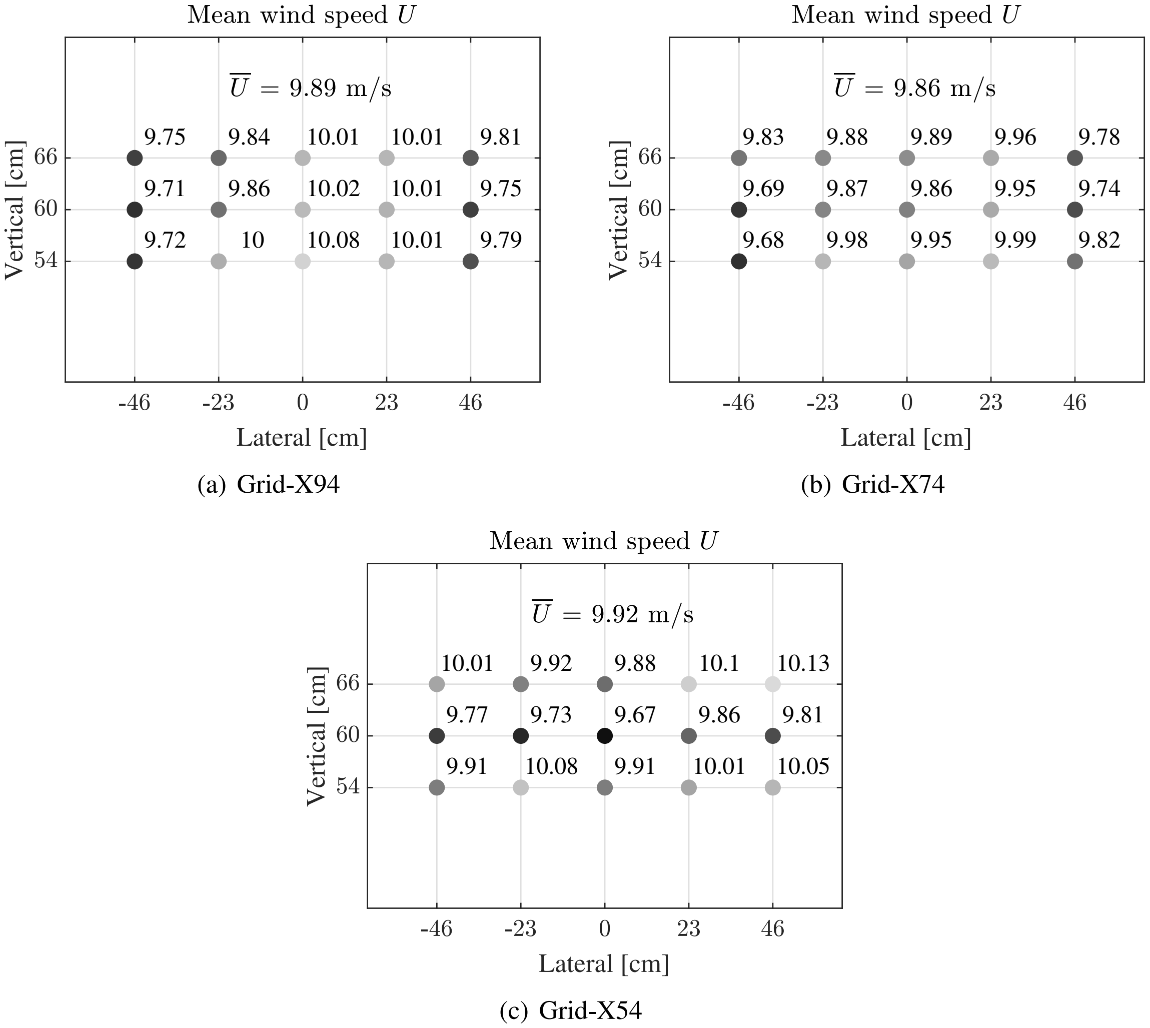

(a) Grid-X94

(b) Grid-X74

(c) Grid-X54

Fig. A.5: Distribution of the mean wind speed U among the monitoring points, for three turbulence grid configurations (example of rotation speed of wind tunnel turbine at 600 rpm)

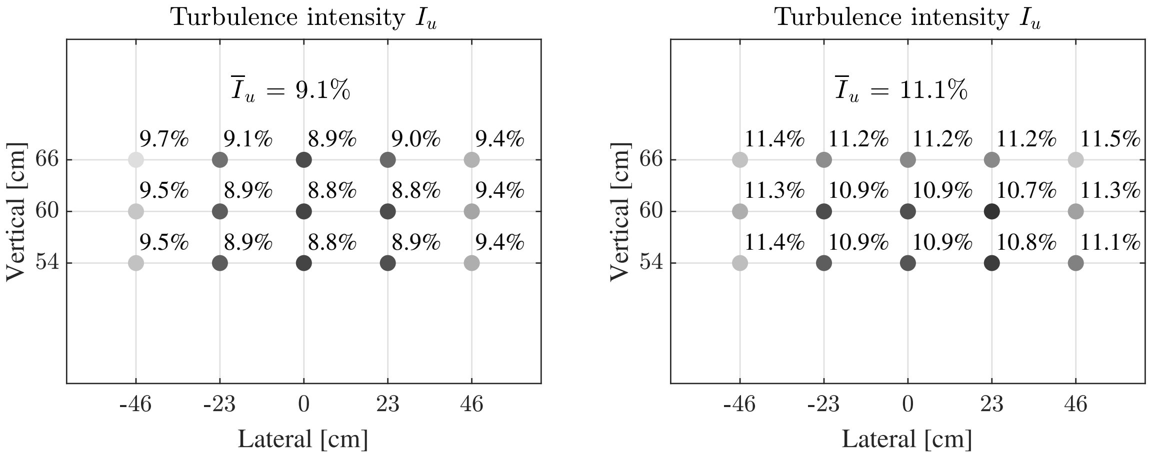

(a) Grid-X94 (b) Grid-X74

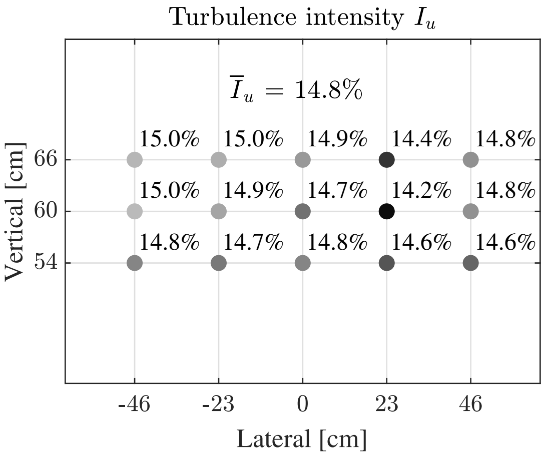

(c) Grid-X54

Fig. A.6: Distribution of the turbulence intensity I_u among the monitoring points, for three turbulence grid configurations (example of rotation speed of wind tunnel turbine at 600 rpm)

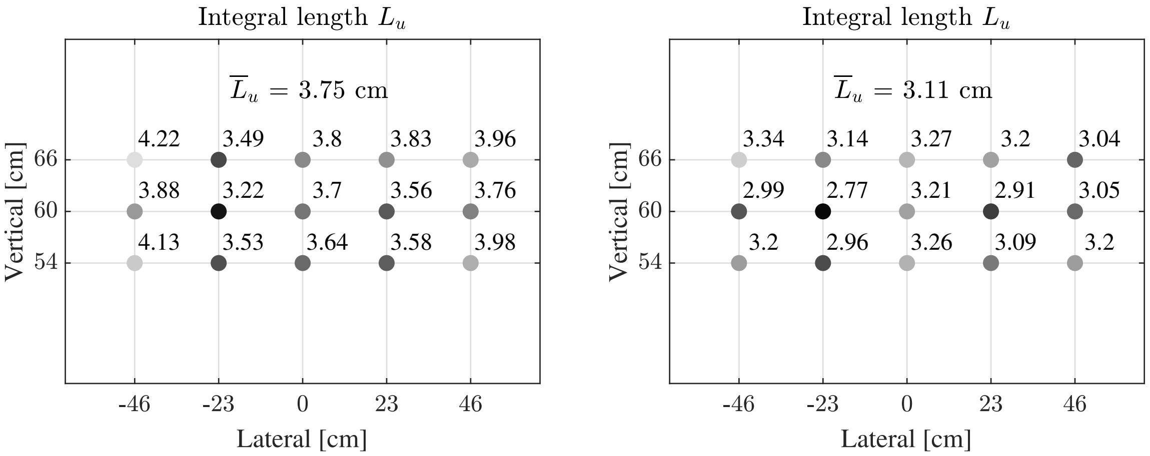

(a) Grid-X94 (b) Grid-X74

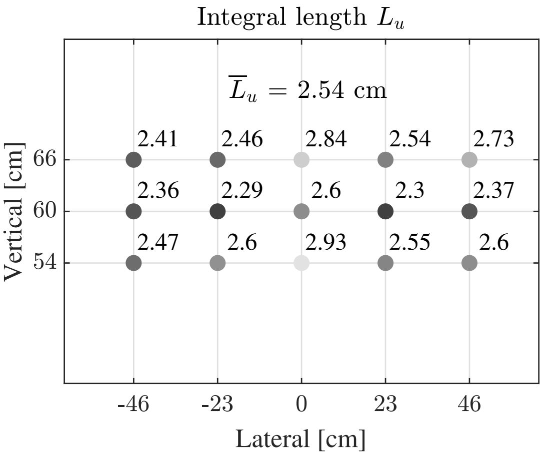

(c) Grid-X54

Fig. A.7: Distribution of the turbulence integral L_u among the monitoring points, for three turbulence grid configurations (example of rotation speed of wind tunnel turbine at 600 rpm)

A.3 Extra Results for the Trapezoidal Cylinder

A.3.1 Effects of Scruton Number on the Aeroelastic Response

Tab. A.1 lists the aeroelastic test cases for the trapezoidal cylinder, for the investigations of the effect of Scruton number.

Tab. A.1: Characteristics of aeroelastic test cases for the trapezoidal cylinder at $\alpha_0 = 0°$ and $\alpha_0 = 3°$, with various Sc.

α_0 [deg]	Static results		Aeroelastic test cases								
	St [-]	A_1 [-]	Config.	M_e [kg]	n_0 [-]	ρ [-]	ζ_0 [%]	Sc [-]	V_r [-]	V_g [-]	V_g/V_r [-]
0	0.091	1.50	#T0-0	3.88	9.27	1.15	0.076	6.8	1.75	1.44	0.83
			#T0-1			1.16	0.161	14.6		3.10	1.78
			#T0-2			1.17	0.256	23.0		4.88	2.80
			#T0-3			1.16	0.428	38.7		8.23	4.72
			#T0-4			1.16	0.572	51.9		11.0	6.32
			#T0-5			1.14	0.727	67.0		14.2	8.16
			#T0-6	3.97	9.17	1.18	0.972	88.5	1.75	18.8	10.8
			#T0-7			1.19	1.096	98.7		21.0	12.0
			#T0-8			1.19	1.322	119.2		25.3	14.5
3	0.089	5.96	#T3-0	3.88	9.27	1.17	0.070	6.3	1.78	0.33	0.19
			#T3-1			1.16	0.152	13.7		0.73	0.41
			#T3-2			1.18	0.262	23.4		1.25	0.70
			#T3-3			1.17	0.425	38.2		2.04	1.14
			#T3-4			1.18	0.578	51.6		2.76	1.55
			#T3-5			1.17	0.748	67.3		3.60	2.02
			#T3-6			1.16	0.937	85.0		4.54	2.55
			#T3-7	3.97	9.17	1.20	1.198	107.3	1.78	5.73	3.22
			#T3-8	8.07	6.43	1.20	0.610	110.8	1.78	5.92	3.32
			#T3-9			1.19	0.756	138.4		7.39	4.15
			#T3-10			1.22	0.875	156.4		8.36	4.69

Aeroelastic results are first presented for the $\alpha_0 = 3°$ mean flow incidence (Fig. A.8 to Fig. A.10), where a stronger interaction of VIV and galloping occurs. The dynamic responses under various Sc are qualitatively the same as the 2:1 rectangular cylinder at $\alpha_0 = 0°$. Nevertheless, there are some quantitative differences: a) the "Full-Interference" behavior is maintained up to $Sc = 67.3$ ($V_g/V_r = 2.02$), while this is $Sc = 107.1$ ($V_g/V_r = 2.49$) for the rectangular cylinder; b) the "Partial-Interference" is maintained up to $Sc = 110.8$ ($V_g/V_r = 3.32$), while this is $Sc =$

145.9 ($V_g/V_r = 3.40$) for the rectangular cylinder; c) for $Sc = 156.4$ ($V_g/V_r = 4.69$), the actual galloping occurs at about $0.8V_g$ (see Fig. A.10), while this is at about $0.7V_g$ for the rectangular cylinder which features a even higher Scruton number $Sc = 200.7$ ($V_g/V_r = 4.67$). From the point of view of Scruton number, the interaction effect between galloping and VIV is weaker for the trapezoidal cylinder. However, if the V_g/V_r ratio is taken as indicator, the interaction effect for the two cylinders seems close to each other.

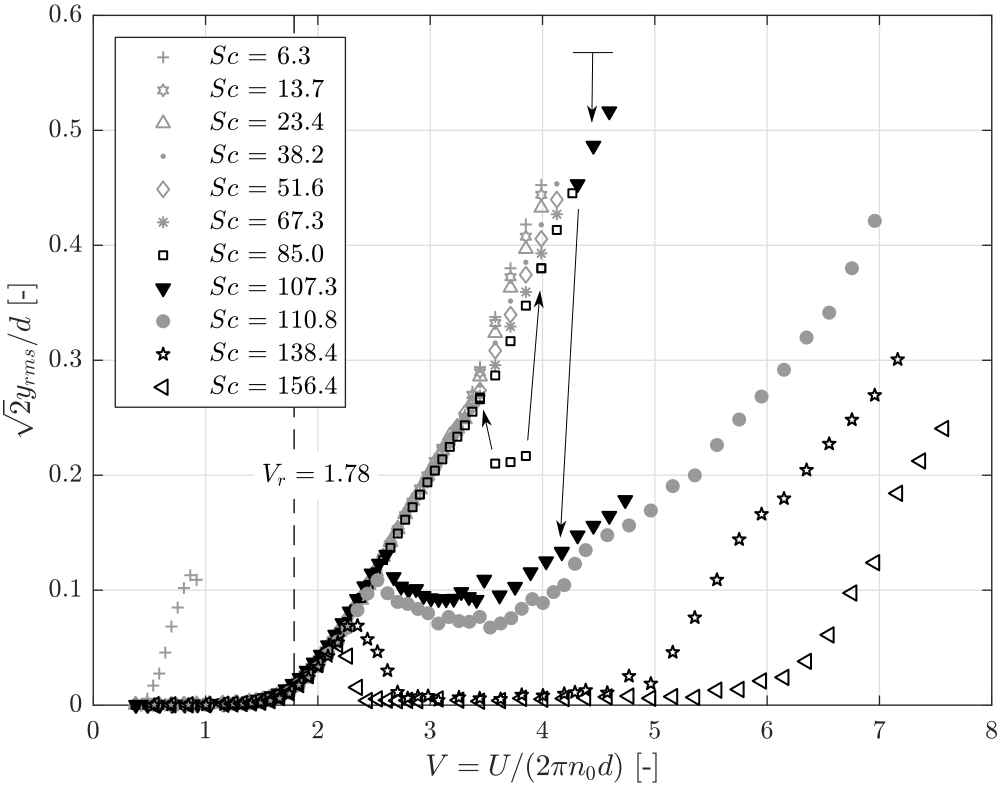

Fig. A.8: Effect of Scruton number on the across-wind response of the trapezoidal cylinder at $\alpha_0 = 3°$.

Besides, some other points should be mentioned. In Fig. A.9 (a), one can find that the unaffected amplitude of Sc variation is maintained up to about $\sqrt{2}y_{rms}/d = 0.26$, corresponding to a velocity range $1 < V/V_r < 1.9$, which is slightly wider than the 2:1 rectangular cylinder. Also, clear and regular amplitude modulation phenomenon was observed for this velocity range. In Fig. A.9 (c), for the test case of $Sc = 107.3$, the upper amplitude branch was obtained by releasing the wind tunnel model from a higher displaced position as indicated by the arrow. The possible spontaneous jump was purposely not reached due to a safety consideration (since the wind speed in the wind tunnel is already quite high). Nevertheless, the test case of $Sc = 110.8$, which was carried out with added mass to decrease n_0 (so that a higher reduced velocity is easier to reach), shows that the possible jump has not occurred up to $V = 7$.

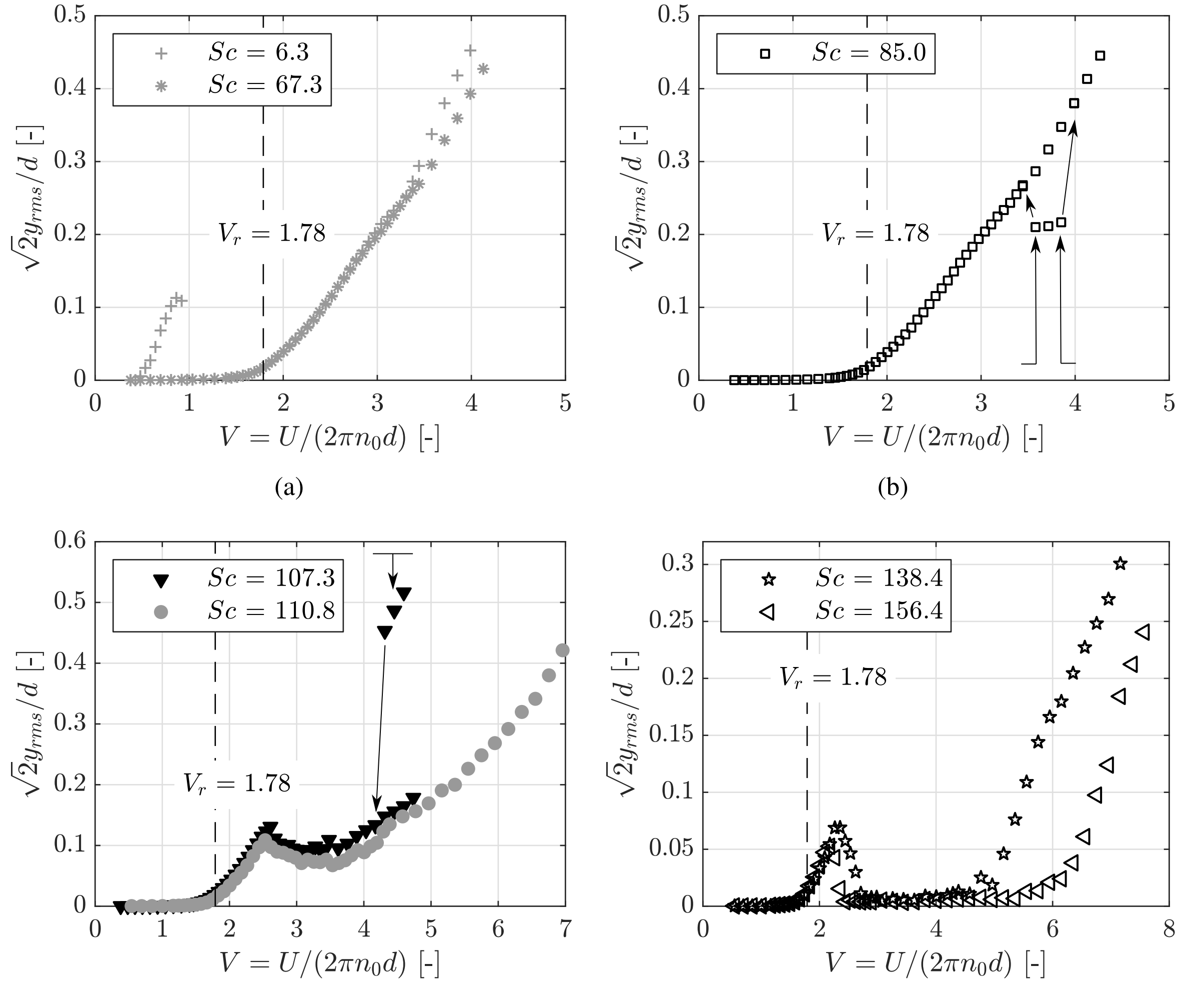

(a)

(b)

(c)

(d)

Fig. A.9: Same results as in Fig. A.8 but with divided plots for better view.

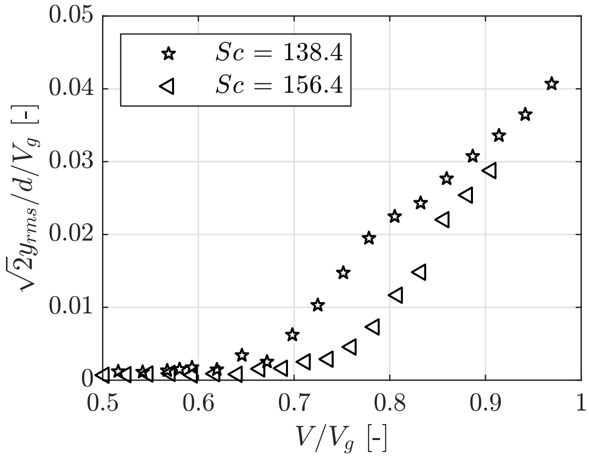

Fig. A.10: Last two test cases (#T3-9 and #T3-10) of the trapezoidal cylinder in universal plot ($\alpha_0 = 3°$).

Effects of varying Scruton number for the trapezoidal cylinder at its null mean wind angle of attack are shown in Fig. A.11 and Fig. A.12. From the static results, this angle of attack features a C_{L0} about 25% lower than that at the 3° wind angle of attack (see Fig. 4.8 (b) for $Re = 2.0 \cdot 10^4$). Moreover, the galloping factor is considerably lower ($A_1 = 1.50$ compared to $A_1 = 5.96$, see Tab. A.1), combined also with a worse linearization of the lift coefficient around this wind angle of attack (see Fig. 4.7 (b)).

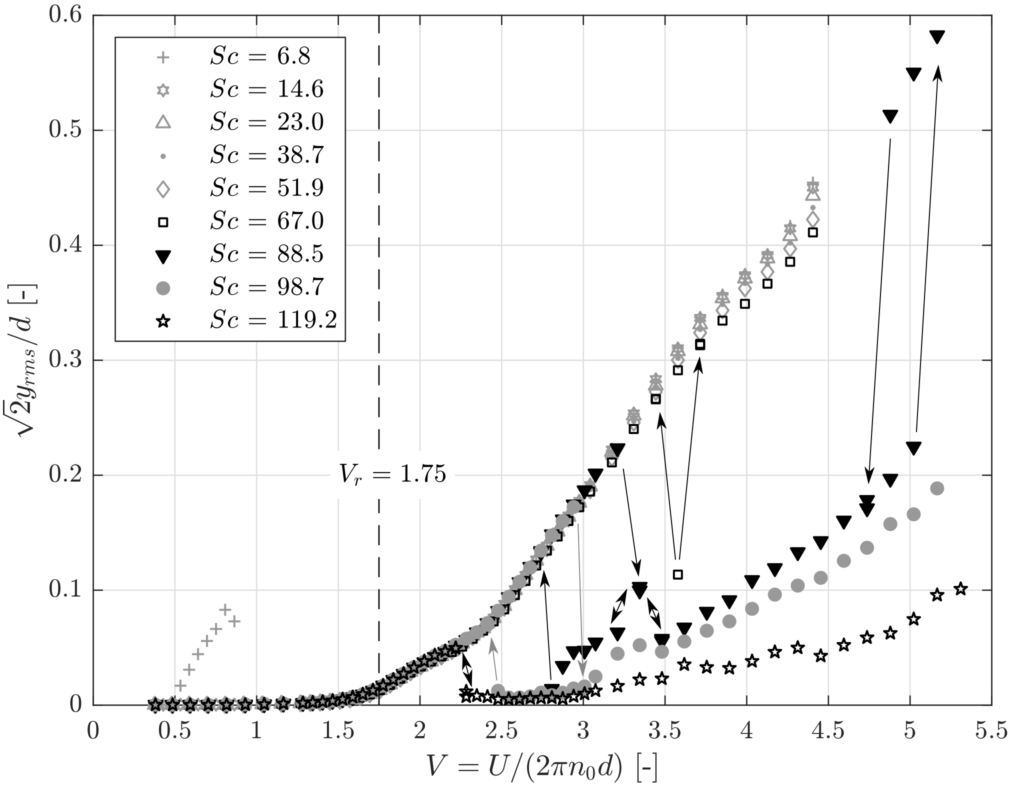

Fig. A.11: Effect of Scruton number on the across-wind response of the trapezoidal cylinder at $\alpha_0 = 0°$.

Nevertheless, from the dynamic test results at $\alpha_0 = 0°$, the "Full-Interference" behavior is still able to be maintained for Scruton number up to $Sc = 51.9$, corresponding to $V_g/V_r = 6.32$. Moreover, from Fig.A.12 (a), one can notice an increase of the amplitude slope occurring at about $V = 2.5$. Qualitatively speaking, from the point of view of quasi-steady theory, this may be attributed to the steeper C_L slope for larger apparent wind angle of attack during the oscillation (so that more negative aerodynamic damping can be introduced in). For $Sc = 88.5$, the oscillation exhibits a sort of "Partial-Interference" behavior. While an anti-clockwise hysteresis loop is observed in the high reduced velocity range, a clock-wise hysteresis loop in the VIV region is also observed. This clock-wise hysteresis loop is maintained further for $Sc = 98.7$ but disappears for $Sc = 119.2$. Despite that the amplitude slope is considerably small, galloping oscillation is already initiated at about $V = 3$ for $Sc = 119.2$. For this case, the quasi-steady prediction of galloping onset is $V_g = 14.5V_r$, which is far away from the actual observation.

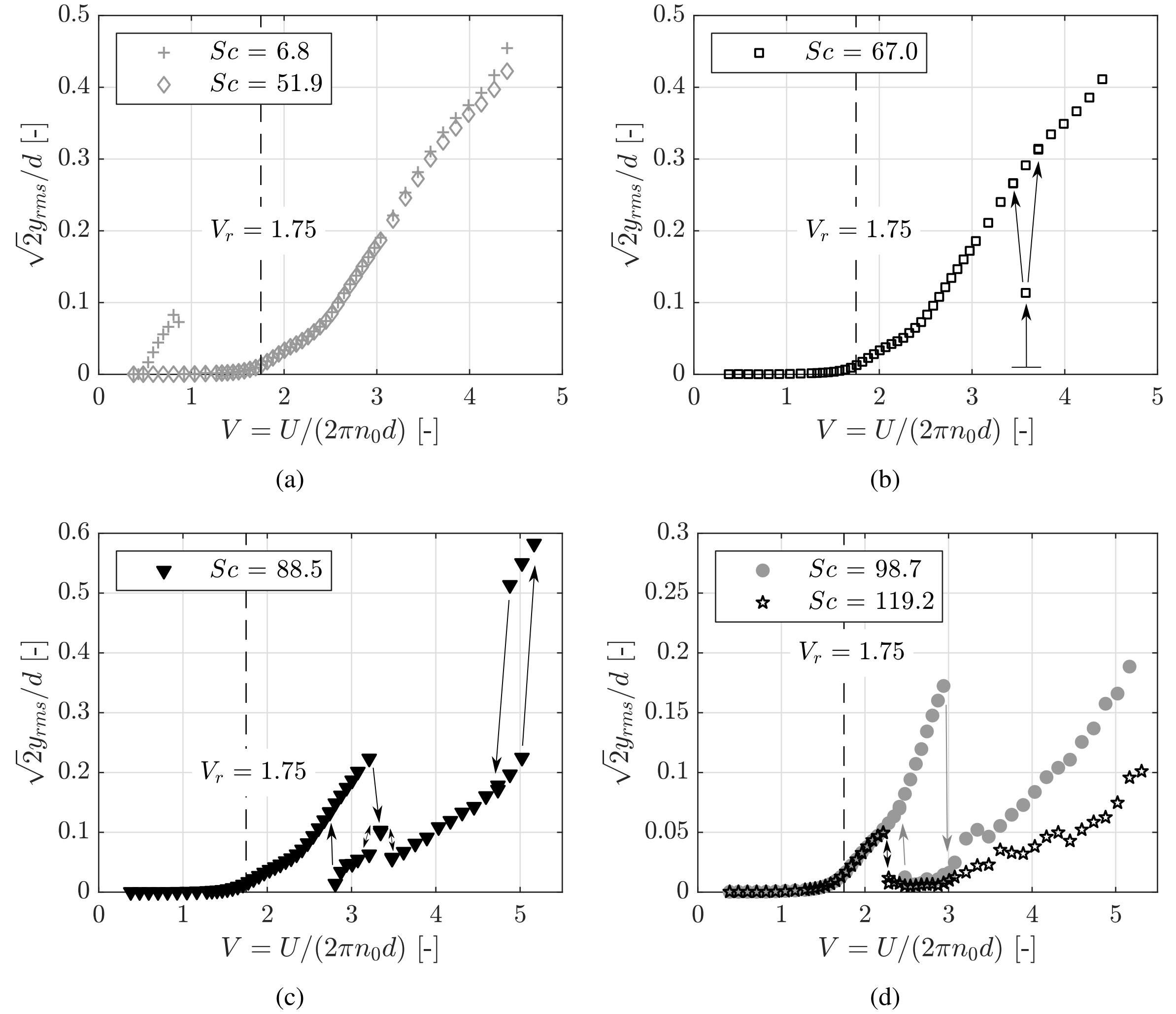

(a) (b)

(c) (d)

Fig. A.12: Same results as in Fig. A.11 but with divided plots for better view.

Clearly, the interaction of VIV and galloping occurred for this mean flow incidence. However, the use of V_g/V_r ratio as an indicator, to judge the interaction behavior or to judge when the quasi-steady should work, seems rather meaningless here. Due to the low value of A_1, the V_g/V_r ratio can easily go beyond 10, but the actual galloping may just occur at a much lower reduced velocity (for the example of $Sc = 119.2$, galloping occurs at $V = 1.7V_r$, while the ratio of V_g/V_r is already 14.5).

References

Abdel-Rohman 2001

ABDEL-ROHMAN, Mohamed: Effect of unsteady wind flow on galloping of tall prismatic structures. In: *Nonlinear Dynamics* 26 (2001), Nr. 3, pp. 233–254

Afanasyev & Korabel 2006

AFANASYEV, YD ; KORABEL, VN: Wakes and vortex streets generated by translating force and force doublet: laboratory experiments. In: *Journal of Fluid Mechanics* 553 (2006), pp. 119

Aldasoro 2014

ALDASORO, Hodei A.: *On Gust Buffeting Design of Slender Chimneys-Building Interference and Fatigue*. Shaker, 2014

Andrianne 2012

ANDRIANNE, Thomas: *Experimental and numerical investigations of the aeroelastic stability of bluff structures*, PhD Thesis, University of Liège, Diss., 2012

Andrianne & Dimitriadis 2014

ANDRIANNE, Thomas ; DIMITRIADIS, Grigorios: Empirical modelling of the bifurcation behaviour of a bridge deck undergoing across-wind galloping. In: *Journal of Wind Engineering and Industrial Aerodynamics* 135 (2014), pp. 129–135

Anistoroaiei & al. 2013

ANISTOROAIEI, Christian ; HEYMEL, Ulrich ; JUNG, Rolf ; SAGNER, Michael E.: Bridge across the Lochkov Valley, Prague Ring Road–a strutted frame construction of a special kind. In: *Steel Construction* 6 (2013), Nr. 2, pp. 163–170

Bearman 1966

BEARMAN, PW: On vortex street wakes / NATIONAL PHYSICAL LAB TEDDINGTON (UNITED KINGDOM) AERODYNAMICS DIV. 1966. – Technical report

Bearman & al. 1987

BEARMAN, PW ; GARTSHORE, IS ; MAULL, DJ ; PARKINSON, GV: Experiments on flow-induced vibration of a square-section cylinder. In: *Journal of Fluids and Structures* 1 (1987), Nr. 1, pp. 19–34

Bearman & Luo 1988

BEARMAN, PW ; LUO, SC: Investigation of the aerodynamic instability of a square-section cylinder by forced oscillation. In: *Journal of Fluids and Structures* 2 (1988), Nr. 2, pp. 161–176

Bearman & Morel 1983

BEARMAN, PW ; MOREL, T: Effect of free stream turbulence on the flow around bluff bodies. In: *Progress in aerospace sciences* 20 (1983), Nr. 2-3, pp. 97–123

Bearman & Obasaju 1982

BEARMAN, PW ; OBASAJU, ED: An experimental study of pressure fluctuations on fixed and oscillating square-section cylinders. In: *Journal of Fluid Mechanics* 119 (1982), pp. 297–321

Berthellemy 2001

BERTHELLEMY, J: Composite construction—Innovative solutions for road bridges. In: *Proc., 3rd Int. Meeting on Composite Bridges, Luleå Univ. of Technology, Luleå, Sweden*, 2001

Billah & Scanlan 1991

BILLAH, K Y. ; SCANLAN, Robert H.: Resonance, Tacoma Narrows bridge failure, and undergraduate physics textbooks. In: *American Journal of Physics* 59 (1991), Nr. 2, pp. 118–124

Binder & al. 2005

BINDER, Bernd ; THAUERN, Bernd ; PFEIFFER, Michael: Die Haseltalbrücke bei Suhl–Ausführungsplanung, Fertigung und Montage. In: *Stahlbau* 74 (2005), Nr. 12, pp. 883–890

Birkhoff & Zarantonello 1957

BIRKHOFF, G ; ZARANTONELLO, E.H.: Jets, wakes and cavities. In: *F.N. Frenkiel (Ed.), Applied Mathematics and Mechanics*, Academic Press Inc., New York, US, 1957

Birkhoff 1953

BIRKHOFF, Garrett: Formation of vortex streets. In: *Journal of Applied Physics* 24 (1953), Nr. 1, pp. 98–103

Bisplinghoff & al. 1996

BISPLINGHOFF, RL ; ASHLEY, H ; HALFMAN, RL: *Aeroelasticity*. 1996

Blevins 1977

BLEVINS, Robert D.: Flow-induced vibration / Van Nostrand Reinhold. 1977. – Technical report

Blevins 1990

BLEVINS, Robert D.: Flow-induced vibration / Van Nostrand Reinhold. 1990. – Technical report

Bloor & Gerrard 1966

BLOOR, M S. ; GERRARD, JH: Measurements on turbulent vortices in a cylinder wake. In: *Proceedings of the Royal Society of London. Series A. Mathematical and Physical Sciences* 294 (1966), Nr. 1438, pp. 319–342

Bokaian & Geoola 1983

BOKAIAN, AR ; GEOOLA, F: ON THE CROSS FLOW RESPONSE OF CYLINDRICAL STRUCTURES. In: *Proceedings of the Institution of Civil Engineers* 75 (1983), Nr. 3, pp. 397–418

Bouclin 1979

BOUCLIN, Denis N.: *Hydroelastic oscillations of square cylinders*. 1979

Brooks 1960

BROOKS, Peter Noel H.: *Experimental investigation of the aeroelastic instability of bluff two-dimensional cylinders*. 1960

Bruno & Khris 2003

BRUNO, Luca ; KHRIS, S: The validity of 2D numerical simulations of vortical structures around a bridge deck. In: *Mathematical and computer modelling* 37 (2003), Nr. 7-8, pp. 795–828

Calvert 1967

CALVERT, JR: Experiments on the low-speed flow past cones. In: *Journal of Fluid Mechanics* 27 (1967), Nr. 2, pp. 273–289

Cammelli & al. 2017

CAMMELLI, Stefano ; BAGNARA, Anna ; NAVARRO, Jessica G.: VIV-galloping interaction of the deck of a footbridge with solid parapets. In: *Procedia engineering* 199 (2017), pp. 1290–1295

Cantwell & Coles 1983

CANTWELL, Brian ; COLES, Donald: An experimental study of entrainment and transport in the turbulent near wake of a circular cylinder. In: *Journal of fluid mechanics* 136 (1983), pp. 321–374

Cao 2015

CAO, Shuyang: Towards better understanding of bridge aerodynamics - turbulence effects. In: *Proceedings of the 14th International Conference on Wind Engineering, Porto Alegre, Brazil*, 2015, pp. 21–26

Carassale & al. 2015

CARASSALE, Luigi ; FREDA, Andrea ; BANFI, Lorenzo: Motion-excited forces acting on a square prism: a qualitative analysis. In: *14th International Conference on Wind Engineering (ICWE 14)*, 2015, pp. 12–26

Cattafesta III & al. 2008

CATTAFESTA III, Louis N. ; SONG, Qi ; WILLIAMS, David R. ; ROWLEY, Clarence W. ; ALVI, Farrukh S.: Active control of flow-induced cavity oscillations. In: *Progress in Aerospace Sciences* 44 (2008), Nr. 7-8, pp. 479–502

Chen & al. 2020

CHEN, Cong ; MANNINI, Claudio ; BARTOLI, Gianni ; THIELE, Klaus: Experimental study and mathematical modeling on the unsteady galloping of a bridge deck with open cross section. In: *Journal of Wind Engineering and Industrial Aerodynamics* 203 (2020), pp. 104170

Cheng & al. 2002

CHENG, C-M ; LU, P-C ; TSAI, M-S: Acrosswind aerodynamic damping of isolated square-shaped buildings. In: *Journal of Wind Engineering and Industrial Aerodynamics* 90 (2002), Nr. 12-15, pp. 1743–1756

Clobes 2008

CLOBES, Mathias: *Identifikation und Simulation instationärer übertragung der Windturbulenz im Zeitbereich.* Shaker, 2008

Corless & Parkinson 1988

CORLESS, Robert M. ; PARKINSON, GV: A model of the combined effects of vortex-induced oscillation and galloping. In: *Journal of Fluids and Structures* 2 (1988), Nr. 3, pp. 203–220

Costa & Borri 2006

COSTA, Carlotta ; BORRI, Claudio: Application of indicial functions in bridge deck aeroelasticity. In: *Journal of Wind Engineering and Industrial Aerodynamics* 94 (2006), Nr. 11, pp. 859–881

Dai 2019

DAI, Bingyu: *Experimental Investigation on the Aeroelastic Galloping Instability of a Square Cylinder.* 2019

Dauner & al. 2000

DAUNER, H-G ; DECORGES, Guy ; STUCKI, Dieter: Web buckling strength for the launching of a box girder with a 130 m main span (Stegbeulen beim Einschub eines Kastenträgers über eine Spannweite von 130 m). In: *Stahlbau* 69 (2000), Nr. 10, pp. 775–780

Davenport 1961

DAVENPORT, Alan G.: The spectrum of horizontal gustiness near the ground in high winds. In: *Quarterly Journal of the Royal Meteorological Society* 87 (1961), Nr. 372, pp. 194–211

Davison 1930

DAVISON, AE: Dancing conductors. In: *Transactions of the American Institute of Electrical Engineers* 49 (1930), Nr. 4, pp. 1444–1449

Den Hartog 1932

DEN HARTOG, JP: Transmission line vibration due to sleet. In: *Transactions of the American Institute of Electrical Engineers* 51 (1932), Nr. 4, pp. 1074–1076

Deniz & Staubli 1997

DENIZ, S ; STAUBLI, Th: Oscillating rectangular and octagonal profiles: interaction of leading-and trailing-edge vortex formation. In: *Journal of Fluids and Structures* 11 (1997), Nr. 1, pp. 3–31

DIN EN 1991-1-4/NA 2010

DIN EN 1991-1-4/NA: *Nationaler Anhang – Einwirkungen auf Tragwerken - Teil 1-4: Allgemeine Einwirkungen-Windlasten.* Berlin : Beuth Verlag GmbH, 2010

Ehsan & Scanlan 1990

EHSAN, Fazl ; SCANLAN, Robert H.: Vortex-induced vibrations of flexible bridges. In: *Journal of Engineering Mechanics* 116 (1990), Nr. 6, pp. 1392–1411

EN 1991-1-4 2010

EN 1991-1-4: Eurocode 1. Actions on structures—Part 1-4: General actions—Wind actions. (2010)

Fage & Johansen 1928

FAGE, Arthur ; JOHANSEN, FC: XLII. The structure of vortex sheets. In: *The London, Edinburgh, and Dublin Philosophical Magazine and Journal of Science* 5 (1928), Nr. 28, pp. 417–441

Feng 1968

FENG, CC: *The measurement of vortex induced effects in flow past stationary and oscillating circular and d-section cylinders*, University of British Columbia, Diss., 1968

Funakawa 1969

FUNAKAWA, Masaya: The vibration of a cylinder caused by wake force in a flow. In: *Bulletin of JSME* 12 (1969), Nr. 53, pp. 1003–1010

Fung 1955

FUNG, Yuan-cheng: *An introduction to the theory of aeroelasticity*. Wiley, 1955

Fung 1993

FUNG, Yuan C.: *An introduction to the theory of aeroelasticity*. Dover Publications, Inc., New York, 1993

Gao & Zhu 2016

GAO, G ; ZHU, L: Measurement and verification of unsteady galloping force on a rectangular 2: 1 cylinder. In: *Journal of Wind Engineering and Industrial Aerodynamics* 157 (2016), pp. 76–94

Gao & Zhu 2017

GAO, Guang-zhong ; ZHU, Le-dong: Nonlinear mathematical model of unsteady galloping force on a rectangular 2: 1 cylinder. In: *Journal of Fluids and Structures* 70 (2017), pp. 47–71

Gao & al. 2020

GAO, Guangzhong ; ZHU, Ledong ; LI, Jiawu ; HAN, Wanshui: Modelling nonlinear aerodynamic damping during transverse aerodynamic instabilities for slender rectangular prisms with typical side ratios. In: *Journal of Wind Engineering and Industrial Aerodynamics* 197 (2020), pp. 104064

Gartshore 1973

GARTSHORE, Ian S.: *The Effects of Free Stream Turbulance on the Drag of Rectangular Two-dimentional Prism*. University of Western Ontario, Faculty of Engineering Science, Boundary . . . , 1973

Ge & al. 2002

GE, YJ ; LIN, ZX ; CAO, FC ; PANG, JB ; XIANG, HF: Investigation and prevention of deck galloping oscillation with computational and experimental techniques. In: *Journal of Wind Engineering and Industrial Aerodynamics* 90 (2002), Nr. 12-15, pp. 2087–2098

Gerrard 1966

GERRARD, JH: The mechanics of the formation region of vortices behind bluff bodies. In: *Journal of fluid mechanics* 25 (1966), Nr. 2, pp. 401–413

Griffin 1981

GRIFFIN, OM: Universal Similarity in the wakes of Stationary and Vibrating Bluff Structures. In: *Trans. ASME, J. Fluids Eng.* 103 (1981), pp. 52

Gu & Quan 2004

GU, Ming ; QUAN, Yong: Across-wind loads of typical tall buildings. In: *Journal of Wind Engineering and Industrial Aerodynamics* 92 (2004), Nr. 13, pp. 1147–1165

Gu & al. 2000

GU, Ming ; ZHANG, Ruoxue ; XIANG, Haifan: Identification of flutter derivatives of bridge decks. In: *Journal of Wind Engineering and Industrial Aerodynamics* 84 (2000), Nr. 2, pp. 151–162

Hansen 2013

HANSEN, SO: Wind loading design codes. In: *Proceedings*, 2013

Hanswille 2014

HANSWILLE, Gerhard: Anwendung der Teile 2 der Eurocodes 3 und 4 für Stahl-und Verbundbrücken: Erste Erfahrungen und europäische Überlegungen zur Weiterentwicklung der Regelwerke. In: *Stahlbau* 83 (2014), Nr. 4, pp. 217–226

Hartlen & Currie 1970

HARTLEN, Ronald T. ; CURRIE, Iain G.: Lift-oscillator model of vortex-induced vibration. In: *Journal of the Engineering Mechanics Division* 96 (1970), Nr. 5, pp. 577–591

Hémon & Santi 2002

HÉMON, P ; SANTI, F: On the aeroelastic behaviour of rectangular cylinders in cross-flow. In: *Journal of Fluids and Structures* 16 (2002), Nr. 7, pp. 855–889

Hirai & al. 1993

HIRAI, S ; HONDA, A ; KATO, H ; YOSHIDA, O ; OKAUCHI, I: Aerodynamic stability of trans-tokyo bay bridge. In: *Journal of Wind Engineering and Industrial Aerodynamics* 49 (1993), Nr. 1-3, pp. 487–496

Hoebbel & al. 2018

HOEBBEL, Thomas ; THIELE, Klaus ; CLOBES, Mathias: Wind turbulence parameters from three dimensional full-scale measurements at 344 m high guyed mast site Gartow 2. In: *Journal of Wind Engineering and Industrial Aerodynamics* 172 (2018), pp. 341–350

Holmes 2014

HOLMES, John D.: *Wind loading of structures (third version).* CRC press, 2014

Hu & al. 2015

HU, Gang ; TSE, Kam-Tim ; KWOK, Kenny C.: Galloping of forward and backward inclined slender square cylinders. In: *Journal of Wind Engineering and Industrial Aerodynamics* 142 (2015), pp. 232–245

Hu & al. 2006

HU, JC ; ZHOU, Y ; DALTON, C: Effects of the corner radius on the near wake of a square prism. In: *Experiments in Fluids* 40 (2006), Nr. 1, pp. 106

Irwin 1998

IRWIN, PA: The role of wind tunnel modeling in the prediction of wind effects on bridges. In: *Bridge aerodynamics* (1998)

Itoh & Tamura 2002

ITOH, Y ; TAMURA, T: The role of separated shear layers in unstable oscillations of a rectangular cylinder around a resonant velocity. In: *Journal of Wind Engineering and Industrial Aerodynamics* 90 (2002), Nr. 4-5, pp. 377–394

Jones 1945

JONES, W P.: Aerodynamic forces on wings in non-uniform motion. In: *ARC Technical Report, R. & M. No. 2117* (1945)

Kareem & al. 1996

KAREEM, A ; GURLEY, K & al.: Damping in structures: its evaluation and treatment of uncertainty. In: *Journal of wind engineering and industrial aerodynamics* 59 (1996), Nr. 2, pp. 131–157

Khalak & Williamson 1997

KHALAK, A ; WILLIAMSON, CHK: Fluid forces and dynamics of a hydroelastic structure with very low mass and damping. In: *Journal of Fluids and Structures* 11 (1997), Nr. 8, pp. 973–982

Kobayashi & al. 1990

KOBAYASHI, H ; KAWATANI, M ; NAKADE, O: Vortex-induced oscillation of two dimensional rectangular cylinders in large scale turbulence. In: *Journal of Wind Engineering and Industrial Aerodynamics* 33 (1990), Nr. 1-2, pp. 101–106

Kronauer 1964

KRONAUER, RE: Predicting eddy frequency in separated wakes. In: *IUTAM symposium on concentrated vortex motions in fluids*, 1964

Kuhlmann & al. 2008

KUHLMANN, C ; BRAUN, B ; FELDMANN, M ; NAUMES, J ; MARTIN, PO ; GALÉA, Y ; JOHANSSON, B ; COLLIN, P ; ERIKSEN, J ; DEGÉE, H ; HAUSOUL, N ; CHICA, J ; RAOUL, J ; DAVAINE, L ; PETEL, A: COMBRI-Handbuch Brücken - Teil II: Stand der Technik und Entwurf von Stahl- und Verbundbrücken. 2008 (Mitteilung Nr. 2008-66X, RFCS- Projekt RFS2-CT-2007-00031). – Technical report

Lander & al. 2016

LANDER, DC ; LETCHFORD, CW ; AMITAY, M ; KOPP, GA: Influence of the bluff body shear layers on the wake of a square prism in a turbulent flow. In: *Physical Review Fluids* 1 (2016), Nr. 4, pp. 044406

Laneville & al. 1977

LANEVILLE, A ; GARTSHORE, IS ; PARKINSON, GV: An explanation of some effects of turbulence on bluff bodies. In: *Proceedings of the 4th International Conference on Wind Effects on Buildings and Structures, Heathrow, UK, Sep. 8–12, 1975.*, 1977, pp. 333–341

Laneville & Parkinson 1971

LANEVILLE, A ; PARKINSON, GV: Effects of turbulence on galloping of bluff cylinders. In: *Proceedings of the 3rd Int. Conf. on Wind Effects on Buildings and Structures*, 1971, pp. 787–797

Laneville 1973

LANEVILLE, André: *Effects of turbulence on wind induced vibrations of bluff cylinders*, University of British Columbia, Diss., 1973

Larsen 2000

LARSEN, Allan: Aerodynamics of the Tacoma Narrows Bridge-60 years later. In: *Structural Engineering International* 10 (2000), Nr. 4, pp. 243–248

Lindner 1992

LINDNER, H: Simulation of the turbulence influence on galloping vibrations. In: *Journal of Wind Engineering and Industrial Aerodynamics* 43 (1992), Nr. 1-3, pp. 2023–2034

Liu & al. 2018

LIU, YZ ; MA, CM ; LI, QS ; YAN, BW ; LIAO, HL: A new modeling approach for transversely oscillating square-section cylinders. In: *Journal of Fluids and Structures* 81 (2018), pp. 492–513

Luo & Bearman 1990

LUO, SC ; BEARMAN, PW: Predictions of fluctuating lift on a transversely oscillating square-section cylinder. In: *Journal of fluids and structures* 4 (1990), Nr. 2, pp. 219–228

Luo & al. 2003

LUO, SC ; CHEW, YT ; NG, YT: Hysteresis phenomenon in the galloping oscillation of a square cylinder. In: *Journal of Fluids and Structures* 18 (2003), Nr. 1, pp. 103–118

Luo & al. 1994

LUO, SC ; YAZDANI, Md G. ; CHEW, YT ; LEE, TS: Effects of incidence and afterbody shape on flow past bluff cylinders. In: *Journal of wind engineering and industrial aerodynamics* 53 (1994), Nr. 3, pp. 375–399

Luo 1985

LUO, Siao C.: *A forced oscillation study of the aerodynamic instability of a square section cylinder*, Imperial College London, Diss., 1985

Luongo & Zulli 2011

LUONGO, Angelo ; ZULLI, Daniele: Parametric, external and self-excitation of a tower under turbulent wind flow. In: *Journal of Sound and Vibration* 330 (2011), Nr. 13, pp. 3057–3069

Lyn & al. 1995

LYN, Dennis A. ; EINAV, S ; RODI, W ; PARK, J-H: A laser-Doppler velocimetry study of ensemble-averaged characteristics of the turbulent near wake of a square cylinder. In: *Journal of Fluid Mechanics* 304 (1995), pp. 285–319

Ma & al. 2018

MA, CM ; LIU, YZ ; LI, QS ; LIAO, HL: Prediction and explanation of the aeroelastic behavior of a square-section cylinder via forced vibration. In: *Journal of Wind Engineering and Industrial Aerodynamics* 176 (2018), pp. 78–86

Macdonald & al. 2002

MACDONALD, John H. ; IRWIN, Peter A. ; FLETCHER, Malcolm S.: Vortex-induced vibrations of the Second Severn Crossing cable-stayed bridge—full-scale and wind tunnel measurements. In: *Proceedings of the Institution of Civil Engineers-Structures and Buildings* 152 (2002), Nr. 2, pp. 123–134

Mannini & al. 2014

MANNINI, C ; MARRA, AM ; BARTOLI, G: VIV–galloping instability of rectangular cylinders: Review and new experiments. In: *Journal of wind engineering and industrial aerodynamics* 132 (2014), pp. 109–124

Mannini 2006

MANNINI, Claudio: *Flutter Vulnerability Assessment of Flexible Bridges*, University of Florence, Diss., 2006

Mannini 2015

MANNINI, Claudio: Applicability of URANS and DES simulations of flow past rectangular cylinders and bridge sections. In: *Computation* 3 (2015), Nr. 3, pp. 479–508

Mannini 2020

MANNINI, Claudio: Incorporation of turbulence in a nonlinear wake-oscillator model for the prediction of unsteady galloping response. In: *Journal of Wind Engineering and Industrial Aerodynamics* 200 (2020), pp. 104141

Mannini & al. 2016a

MANNINI, Claudio ; BELLOLI, Marco ; MARRA, Antonino M. ; BAYATI, Ilmas ; GIAPPINO, Stefano ; ROBUSTELLI, Fabio ; BARTOLI, Gianni: Aeroelastic stability of two long-span arch structures: A collaborative experience in two wind tunnel facilities. In: *Engineering Structures* 119 (2016), pp. 252–263

Mannini & al. 2015a

MANNINI, Claudio ; MARRA, Antonino M. ; MASSAI, Tommaso ; BARTOLI, Gianni: VIV-galloping instability of a rectangular cylinder in turbulent flow. In: *Proceedings of the 14th International Conference on Wind Engineering*, 2015

Mannini & al. 2016b

MANNINI, Claudio ; MARRA, Antonino M. ; MASSAI, Tommaso ; BARTOLI, Gianni: Interference of vortex-induced vibration and transverse galloping for a rectangular cylinder. In: *Journal of Fluids and Structures* 66 (2016), pp. 403–423

Mannini & al. 2017

MANNINI, Claudio ; MARRA, Antonino M. ; PIGOLOTTI, Luca ; BARTOLI, Gianni: The effects of free-stream turbulence and angle of attack on the aerodynamics of a cylinder with rectangular 5: 1 cross section. In: *Journal of Wind Engineering and Industrial Aerodynamics* 161 (2017), pp. 42–58

Mannini & al. 2015b

MANNINI, Claudio ; MASSAI, Tommaso ; MARRA, Antonino M. ; BARTOLI, Gianni: Modelling the interaction of VIV and galloping for rectangular cylinders. In: *red* 3 (2015), Nr. 3, pp. 1

Mannini & al. 2018a

MANNINI, Claudio ; MASSAI, Tommaso ; MARRA, Antonino M.: Modeling the interference of vortex-induced vibration and galloping for a slender rectangular prism. In: *Journal of Sound and Vibration* 419 (2018), pp. 493–509

Mannini & al. 2018b

MANNINI, Claudio ; MASSAI, Tommaso ; MARRA, Antonino M.: Unsteady galloping of a rectangular cylinder in turbulent flow. In: *Journal of Wind Engineering and Industrial Aerodynamics* 173 (2018), pp. 210–226

Mansperger & al. 2017

MANSPERGER, Tobias ; JUNG, Rolf ; KÖBERLIN, Thomas ; HERTLE, Robert: Planung und Prüfung der Talbrücke. In: *Stahlbau* 86 (2017), Nr. 2, pp. 139–147

Mariotti & Buresti 2013

MARIOTTI, Alessandro ; BURESTI, Guido: Experimental investigation on the influence of boundary layer thickness on the base pressure and near-wake flow features of an axisymmetric blunt-based body. In: *Experiments in fluids* 54 (2013), Nr. 11, pp. 1612

Marra & al. 2011

MARRA, Antonino M. ; MANNINI, Claudio ; BARTOLI, Gianni: Van der Pol-type equation for modeling vortex-induced oscillations of bridge decks. In: *Journal of Wind Engineering and Industrial Aerodynamics* 99 (2011), Nr. 6-7, pp. 776–785

Marra 2011

MARRA, Antonino M.: *Risk assessment of bridge decks prone to vortex induced vibrations*, University of Florence, Diss., 2011

Marra & al. 2015

MARRA, Antonino M. ; MANNINI, Claudio ; BARTOLI, Gianni: Measurements and improved model of vortex-induced vibration for an elongated rectangular cylinder. In: *Journal of Wind Engineering and Industrial Aerodynamics* 147 (2015), pp. 358–367

Marra & al. 2017

MARRA, Antonino M. ; MANNINI, Claudio ; BARTOLI, Gianni: Wind tunnel modeling for the vortex-induced vibrations of a yawed bridge tower. In: *Journal of Bridge Engineering* 22 (2017), Nr. 5, pp. 04017006

Matsuda & al. 2013

MATSUDA, Kazutoshi ; KATO, Kusuo ; HISADOMI, Keigo ; HARADA, Kentaro: Low speed instability of two-dimensional rectangular prisms. In: *Pressure Vessels and Piping Conference* Bd. 55683 American Society of Mechanical Engineers, 2013, pp. V004T04A037

Matsumoto & al. 1996

MATSUMOTO, M ; KOBAYASHI, Y ; SHIRATO, H: The influence of aerodynamic derivatives on flutter. In: *Journal of Wind Engineering and Industrial Aerodynamics* 60 (1996), pp. 227–239

Matsumoto & al. 1993

MATSUMOTO, M ; SHIRAISHI, N ; SHIRATO, H ; STOYANOFF, S ; YAGI, T: Mechanism of, and turbulence effect on vortex-induced oscillations for bridge box girders. In: *Journal of Wind Engineering and Industrial Aerodynamics* 49 (1993), Nr. 1-3, pp. 467–476

Matsumoto 1996

MATSUMOTO, Masaru: Aerodynamic damping of prisms. In: *Journal of Wind Engineering and Industrial Aerodynamics* 59 (1996), Nr. 2-3, pp. 159–175

Matsumoto & al. 1997

MATSUMOTO, Masaru ; DAITO, Yoshiyuki ; YOSHIZUMI, Fumitaka ; ICHIKAWA, Yasuo ; YABUTANI, Tadahiro: Torsional flutter of bluff bodies. In: *Journal of Wind Engineering and Industrial Aerodynamics* 69 (1997), pp. 871–882

Mills & al. 2002

MILLS, Richard ; SHERIDAN, John ; HOURIGAN, Kerry: Response of base suction and vortex shedding from rectangular prisms to transverse forcing. In: *Journal of Fluid Mechanics* 461 (2002), pp. 25

Minorsky 1962

MINORSKY, Nicholas: Nonlinear oscillations. (1962)

Miyata & al. 1983

MIYATA, T ; MIYAZAKI, M ; YAMADA, H: Pressure distribution measurements for wind induced vibrations of box girder bridges. In: *Proceedings*, 1983, pp. 223–234

Mizota & Okajima 1981

MIZOTA, Taketo ; OKAJIMA, Atsushi: Experimental studies of unsteady flows around rectangular prisms. In: *Proceedings of the Japan Society of Civil Engineers* Bd. 1981 Japan Society of Civil Engineers, 1981, pp. 49–57

Nakaguchi 1968

NAKAGUCHI, Hiroshi: An experimental study on aerodynamic drag of rectangular cylinders. In: *J. JSASS* 16 (1968), pp. 1–5

Nakamura & Hirata 1991

NAKAMURA, Y ; HIRATA, K: Pressure fluctuations on oscillating rectangular cylinders with the long side normal to the flow. In: *Journal of fluids and structures* 5 (1991), Nr. 2, pp. 165–183

Nakamura & Matsukawa 1987

NAKAMURA, Yasuharu ; MATSUKAWA, Tohru: Vortex excitation of rectangular cylinders with a long side normal to the flow. In: *Journal of fluid mechanics* 180 (1987), pp. 171–191

Nakamura & Mizota 1975

NAKAMURA, Yasuharu ; MIZOTA, Taketo: Unsteady lifts and wakes of oscillating rectangular prisms. In: *Journal of the Engineering Mechanics Division* 101 (1975), Nr. 6, pp. 855–871

Nakamura & Nakashima 1986

NAKAMURA, Yasuharu ; NAKASHIMA, Masamichi: Vortex excitation of prisms with elongated rectangular, H and [vdash] cross-sections. In: *Journal of Fluid Mechanics* 163 (1986), pp. 149–169

Nakamura & Ohya 1984

NAKAMURA, Yasuharu ; OHYA, Yuji: The effects of turbulence on the mean flow past two-dimensional rectangular cylinders. In: *Journal of Fluid Mechanics* 149 (1984), pp. 255–273

Nakamura & Ozono 1987

NAKAMURA, Yasuharu ; OZONO, Shigehira: The effects of turbulence on a separated and reattaching flow. In: *Journal of Fluid Mechanics* 178 (1987), pp. 477–490

Naudascher & Rockwell 1994

NAUDASCHER, E ; ROCKWELL, D: Flow Induced Vibrations – An Engineering Guide. In: *AA Balkema, Rotterdam, Holland* (1994)

Naudascher & Wang 1993

NAUDASCHER, E ; WANG, Yinhi: Flow-induced vibrations of prismatic bodies and grids of prisms. In: *Journal of Fluids and Structures* 7 (1993), Nr. 4, pp. 341–373

Naudascher & Rockwell 2012

NAUDASCHER, Eduard ; ROCKWELL, Donald: *Flow-induced vibrations: an engineering guide*. Courier Corporation, 2012

Navarro & al. 2000

NAVARRO, Miguel G. ; LEBET, Jean-Paul ; BEYLOUNÜ, Roland: Launching of the Vaux Viaduct. In: *Structural engineering international* 10 (2000), Nr. 1, pp. 16–18

Nguyen & al. 2018

NGUYEN, Dinh T. ; HARGREAVES, David M. ; OWEN, John S.: Vortex-induced vibration of a 5: 1 rectangular cylinder: a comparison of wind tunnel sectional model tests and computational simulations. In: *Journal of Wind Engineering and Industrial Aerodynamics* 175 (2018), pp. 1–16

Niemann & Hölscher 2012

NIEMANN, H.J. ; HÖLSCHER, N.: BAB A46 Neubau der Talbrücke Nuttlar – Aerodynamische Untersuchungen zum Überbau in Kritischen Montagezuständen – Windlastangaben und Analyse der Aerodynamischen Stabilität / Ingenieurgesellschaft Niemann & Partner GbR, Bochum. 2012. – Technical report

Niemann & Hölscher 2013

NIEMANN, H.J. ; HÖLSCHER, N.: Neubau B480, OU Bad Wünnenberg – Entwurfsplanung Aftetalbrücke – Windtechnologisches Gutachten / Ingenieurgesellschaft Niemann & Partner GbR, Bochum. 2013. – Technical report

Norberg 1998

NORBERG, C: LDV-measurements in the near wake of a circular cylinder. In: *ASME Paper No. FEDSM98-521* (1998)

Novak & Tanaka 1972

NOVAK, M ; TANAKA, H: Pressure correlations on vertical cylinder. In: *Proc. 4th International Conference on Wind Effects on Structures*, 1972, pp. 227–232

Novak & Tanaka 1977

NOVAK, M ; TANAKA, H: PRESSURE CORRELATIONS ON A VIBRATING CYLINDER. In: *IN: Proc. Fourth International Conference on Wind Effects on Buildings and Structures,Cambridge, U.K.,1975*, 1977, pp. 227–232

Novak 1969

NOVAK, Milos: Aeroelastic galloping of prismatic bodies. In: *Journal of the Engineering Mechanics Division* 95 (1969), Nr. 1, pp. 115–142

Novak 1971

NOVAK, Milos: Galloping and vortex induced oscillations of structures. In: *Proceedings of the third interrational conference on Wind effect on building and structures*, 1971

Novak 1972

NOVAK, Milos: Galloping oscillations of prismatic structures. In: *Journal of Engineering Mechanics* (1972)

Novak & Davenport 1970

NOVAK, Milos ; DAVENPORT, Alan G.: Aeroelastic instability of prisms in turbulent flow. In: *Journal of the Engineering Mechanics Division* 96 (1970), Nr. 1, pp. 17–39

Novak & Tanaka 1974

NOVAK, Milos ; TANAKA, Hiroshi: Effect of turbulence on galloping instability. In: *Journal of the engineering mechanics division* 100 (1974), Nr. 1, pp. 27–47

Obasaju 1979

OBASAJU, E.D.: On the effects of end plates on the mean forces on square sectioned cylinders. In: *Journal of Wind Engineering and Industrial Aerodynamics* 5 (1979), Nr. 1-2, pp. 179–186

Okajima & al. 1985

OKAJIMA, A ; MIZOTA, T ; TANIDA, Y: Observation of flow around rectangular cylinders. In: *flvi* (1985), pp. 381–386

Païdoussis & al. 2010

PAÏDOUSSIS, Michael P. ; PRICE, Stuart J. ; DE LANGRE, Emmanuel: *Fluid-structure interactions: cross-flow-induced instabilities*. Cambridge University Press, 2010

Parkinson 1989

PARKINSON, Geoffrey: Phenomena and modelling of flow-induced vibrations of bluff bodies. In: *Progress in Aerospace Sciences* 26 (1989), Nr. 2, pp. 169–224

Parkinson 1965

PARKINSON, G.V.: Aeroelastic galloping in one degree of freedom. In: *wind Effects on Buildings and Structures: Proceedings of the Conference held at the National Physical Laboratory, Teddington, UK, June 26–28, 1963*, HMSO, 1965, pp. 581–609

Parkinson 1971

PARKINSON, GV: Wind-induced instability of structures. In: *Philosophical Transactions of the Royal Society of London. Series A, Mathematical and Physical Sciences* 269 (1971), Nr. 1199, pp. 395–413

Parkinson & Brooks 1961

PARKINSON, GV ; BROOKS, NPH: On the Aeroelastic Instability of Bluff Cylinders. In: *Journal of Applied Mechanics* 28 (1961), pp. 252

Parkinson & Smith 1964

PARKINSON, GV ; SMITH, JD: The square prism as an aeroelastic non-linear oscillator.

In: *The Quarterly Journal of Mechanics and Applied Mathematics* 17 (1964), Nr. 2, pp. 225–239

Parkinson & Sullivan 1979

PARKINSON, GV ; SULLIVAN, PP: Galloping response of towers. In: *Journal of Wind Engineering and Industrial Aerodynamics* 4 (1979), Nr. 3-4, pp. 253–260

Perry & al. 1982

PERRY, AE ; CHONG, MS ; LIM, TT: The vortex-shedding process behind two-dimensional bluff bodies. In: *Journal of Fluid Mechanics* 116 (1982), pp. 77–90

Pier & Huerre 2001

PIER, Benoît ; HUERRE, Patrick: Nonlinear self-sustained structures and fronts in spatially developing wake flows. (2001)

Pigolotti 2017

PIGOLOTTI, Luca: *On the flutter response of two-degree-of-freedom flat plates for energy harvesting applications*, Diss., 2017

Podolny & Muller 1994

PODOLNY, Walter ; MULLER, Jean M.: *Construction and design of prestressed concrete segmental bridges*. John Wiley and Sons, 1994

Pons 2014

PONS, Jonas: *Entwicklung und auslegung eines wirbelstromdämpfersystems zur schwingungsdämfung von windkanalmodellen*. 2014

Roach 1987

ROACH, PE: The generation of nearly isotropic turbulence by means of grids. In: *International Journal of Heat and Fluid Flow* 8 (1987), Nr. 2, pp. 82–92

Rockwell & Naudascher 1978

ROCKWELL, D ; NAUDASCHER, Et: Self-sustaining oscillations of flow past cavities. (1978)

Roshko 1954a

ROSHKO, Anatol: A new hodograph for free-streamline theory. (1954)

Roshko 1954b

ROSHKO, Anatol: On the drag and shedding frequency of two-dimensional bluff bodies. (1954)

Roshko 1993

ROSHKO, Andrey: Perspectives on bluff body aerodynamics. In: *Journal of Wind Engineering and Industrial Aerodynamics* 49 (1993), Nr. 1-3, pp. 79–100

Ruscheweyh 1994

RUSCHEWEYH, H: Vortex excited vibrations. In: *Wind-excited vibrations of structures*. Springer, 1994, pp. 51–84

Ruscheweyh & al. 1996

RUSCHEWEYH, Hans ; HORTMANNS, Michael ; SCHNAKENBERG, Claudia: Vortex-excited vibrations and galloping of slender elements. In: *Journal of wind engineering and industrial aerodynamics* 65 (1996), Nr. 1-3, pp. 347–352

Salenko & al. 2017

SALENKO, S.D. ; OBUKHOVSKIY, A.D. ; GOSTEEV, Y.A.: Aerodynamic studies of the beam bridge. In: *Proceedings of the XXV Conference on High-Energy Processes in Condensed Matter, June 5-9, Novosibirsk, Russia*, 2017

Santosham 1966

SANTOSHAM, Thomas V.: *Force measurements on bluff cylinders and aeroelastic galloping of a rectangular cylinder*. 1966

Scanlan 1981

SCANLAN, RH: On the state-of-the-art methods for calculation of flutter, vortex-induced and buffeting response of bridge structures. In: *FHWA Report* (1981), pp. FHWA–RD

Scanlan & al. 1974

SCANLAN, Robert H. ; BÉLIVEAU, Jean-Guy ; BUDLONG, Kathleen S.: Indicial Aerodynamic Functions for Bridge Decks. In: *Journal of the Engineering Mechanics Division* 100 (1974), Nr. 4, pp. 657–672

Scanlan & Tomko 1971

SCANLAN, Robert H. ; TOMKO, John J.: Airfoil and Bridge Deck Flutter Derivatives. In: *Journal of the Engineering Mechanics Division* 97 (1971), Nr. 6, pp. 1717–1737

Schewe 2013

SCHEWE, Günter: Reynolds-number-effects in flow around a rectangular cylinder with aspect ratio 1: 5. In: *Journal of Fluids and Structures* 39 (2013), pp. 15–26

Schlichting & Gersten 2016

SCHLICHTING, Hermann ; GERSTEN, Klaus: *Boundary-layer theory*. Springer, 2016

Scruton 1960

SCRUTON, C: *The Use of Wind Tunnels in Industrial Aerodynamic Research.* Advisory Group for Aeronautical Research and Development, 1960 (AGARD report)

Shimada & Ishihara 2002

SHIMADA, Kenji ; ISHIHARA, Takeshi: Application of a modified k–ε model to the prediction of aerodynamic characteristics of rectangular cross-section cylinders. In: *Journal of fluids and structures* 16 (2002), Nr. 4, pp. 465–485

Shimada & Ishihara 2012

SHIMADA, Kenji ; ISHIHARA, Takeshi: Predictability of unsteady two-dimensional k- ε model on the aerodynamic instabilities of some rectangular prisms. In: *Journal of Fluids and Structures* 28 (2012), pp. 20–39

Shiraishi & Matsumoto 1983

SHIRAISHI, Naruhito ; MATSUMOTO, Masaru: On classification of vortex-induced oscillation and its application for bridge structures. In: *Journal of Wind Engineering and Industrial Aerodynamics* 14 (1983), Nr. 1-3, pp. 419–430

Siedziako 2017

SIEDZIAKO, Bartosz: *Modelling of the self-excited forces for bridge decks subjected to random motions: an experimental study*, Diss., 2017

Simiu & Scanlan 1996

SIMIU, Emil ; SCANLAN, Robert H.: Wind effects on structures: fundamentals and applications to design. (1996)

Simmons 1977

SIMMONS, JEL: Similarities between two-dimensional and axisymmetric vortex wakes. In: *The Aeronautical Quarterly* 28 (1977), Nr. 1, pp. 15–20

Skop & Griffin 1973

SKOP, RA ; GRIFFIN, OM: A model for the vortex-excited resonant response of bluff cylinders. In: *Journal of Sound and Vibration* 27 (1973), Nr. 2, pp. 225–233

Slater 1969

SLATER, Jonathan E.: *Aeroelastic instability of a structural angle section*, University of British Columbia, Diss., 1969

Smith 1962

SMITH, John D.: *An experimental study of the aeroelastic instability of rectangular cylinders*, University of British Columbia, Diss., 1962

Stokes & Welsh 1986

STOKES, AN ; WELSH, MC: Flow-resonant sound interaction in a duct containing a plate, II: Square leading edge. In: *Journal of Sound and Vibration* 104 (1986), Nr. 1, pp. 55–73

Strecha 2014

STRECHA, Johannes: *Flow induced vibrations of a U-shaped belt*, Diss., 2014

Strouhal 1878

STROUHAL, V: Über eine besondere Art der Tonerregung. In: *Annalen der Physik und Chemie* (1878), pp. 216–251

Sullivan 1977

SULLIVAN, Peter P.: *Aeroelastic galloping of tall structures in simulated winds*, University of British Columbia, Diss., 1977

Takeuchi & Matsumoto 1992

TAKEUCHI, Takafumi ; MATSUMOTO, Masaru: Aerodynamic response characteristics of rectangular cylinders in tandem arrangement. In: *Journal of Wind Engineering and Industrial Aerodynamics* 41 (1992), Nr. 1-3, pp. 565–575

Tamura & Amano 1983

TAMURA, Y ; AMANO, A: Mathematical model for vortex-induced oscillations of continuous systems with circular cross section. In: *Journal of Wind Engineering and Industrial Aerodynamics* 14 (1983), Nr. 1-3, pp. 431–442

Tamura & Matsui 1979

TAMURA, Y ; MATSUI, G: Wake-oscillatormodel of vortex-induced oscillation of circular cylinder. In: *Proceedings of the 5th International Conference on Wind Engineering, Jul. 8-14, 1979, Forth Collins, US*, 1979, pp. 1085–1094

Tamura & Shimada 1987

TAMURA, Y ; SHIMADA, K: A mathematical model for the transverse oscillations of square cylinders. In: *Proc. of International Conference on Flow Induced Vibrations, May 12-14, 1987, Bowness-Windermere, UK*, Springer-Verlag, 1987, pp. 267–276

Theodorsen 1934

THEODORSEN, Theodore: General theory of aerodynamic instability and the mechanism of flutter. In: *NACA, Technical Report* (1934), Nr. 496, pp. 413–433

Vickery 1966

VICKERY, BJ: Fluctuating lift and drag on a long cylinder of square cross-section in a smooth and in a turbulent stream. In: *Journal of Fluid Mechanics* 25 (1966), Nr. 3, pp. 481–494

Vio & al. 2007
VIO, Gareth A. ; DIMITRIADIS, Grigorios ; COOPER, Jonathan E.: Bifurcation analysis and limit cycle oscillation amplitude prediction methods applied to the aeroelastic galloping problem. In: *Journal of Fluids and Structures* 23 (2007), Nr. 7, pp. 983–1011

Violette & al. 2007
VIOLETTE, R ; DE LANGRE, Emmanuel ; SZYDLOWSKI, J: Computation of vortex-induced vibrations of long structures using a wake oscillator model: comparison with DNS and experiments. In: *Computers & structures* 85 (2007), Nr. 11-14, pp. 1134–1141

Von Kármán 1911
VON KÁRMÁN, Th: Über den Mechanismus des Widerstandes, den ein bewegter Körper in einer Flüssigkeit erfährt. In: *Nachrichten von der Gesellschaft der Wissenschaften Göttingen, Mathematisch-Physikalische Klasse* (1911), pp. 509–517

Von Kármán 1912
VON KÁRMÁN, Th: Über den Mechanismus des Widerstandes, den ein bewegter Körper in einer Flüssigkeit erfährt. In: *Nachrichten von der Gesellschaft der Wissenschaften Göttingen, Mathematisch-Physikalische Klasse* (1912), pp. 547–556

Von Kármán 1948
VON KÁRMÁN, Theodore: Progress in the statistical theory of turbulence. In: *Proceedings of the National Academy of Sciences of the United States of America* 34 (1948), Nr. 11, pp. 530

Wagner 1925
WAGNER, Herbert: Über die Entstehung des dynamischen Auftriebes von Tragflügeln. In: *ZAMM-Journal of Applied Mathematics and Mechanics/Zeitschrift für Angewandte Mathematik und Mechanik* 5 (1925), Nr. 1, pp. 17–35

Wagner 2013
WAGNER, Peter: Entwicklungspotenzial im Straßenbrückenbau durch den Einsatz von hybriden Tragstrukturen–Teil 1: Balkenbrücken. In: *Stahlbau* 82 (2013), Nr. 10, pp. 726–741

Wang & al. 2015
WANG, JF ; LIN, JP ; XU, RQ: Incremental launching construction control of long multi-span composite bridges. In: *Journal of Bridge Engineering* 20 (2015), Nr. 11, pp. 04015006

Washizu & al. 1978

WASHIZU, K ; OHYA, A ; OTSUKI, Y ; FUJII, K: Aeroelastic instability of rectangular cylinders in a heaving mode. In: *Journal of Sound and Vibration* 59 (1978), Nr. 2, pp. 195–210

Wawzonek 1979

WAWZONEK, Mitchell A.: *Aeroelastic behavior of square section prisms in uniform flow*, University of British Columbia, Diss., 1979

Wilkinson 1981

WILKINSON, RH: Part II: Spanwise correlation and loading. In: *The Aeronautical Quarterly* 32 (1981), Nr. 2, pp. 111–125

Williamson 1996

WILLIAMSON, Charles H.: Vortex dynamics in the cylinder wake. In: *Annual review of fluid mechanics* 28 (1996), Nr. 1, pp. 477–539

Williamson & Roshko 1988

WILLIAMSON, Charles H. ; ROSHKO, Anatol: Vortex formation in the wake of an oscillating cylinder. In: *Journal of fluids and structures* 2 (1988), Nr. 4, pp. 355–381

Williamson & Brown 1998

WILLIAMSON, CHK ; BROWN, GL: A series in $1/\sqrt{Re}$ to represent the Strouhal–Reynolds number relationship of the cylinder wake. In: *Journal of Fluids and Structures* 12 (1998), Nr. 8, pp. 1073–1085

Williamson & Govardhan 2004

WILLIAMSON, CHK ; GOVARDHAN, R: Vortex-induced vibrations. In: *Annu. Rev. Fluid Mech.* 36 (2004), pp. 413–455

Wyatt & Scruton 1981

WYATT, TA ; SCRUTON, C: 1 A brief survey of the aerodynamic stability problem of bridges. In: *Bridge Aerodynamics*. Thomas Telford Publishing, 1981, pp. 21–31

Xu & al. 2011

XU, Fu Y. ; YING, Xu Y. ; ZHANG, Zhe: Prediction of unsteady flow around a square cylinder using RANS. In: *Applied Mechanics and Materials* Bd. 52 Trans Tech Publ, 2011, pp. 1165–1170

Yamada & Miyata 1984

YAMADA, Hitoshi ; MIYATA, Toshio: Evaluation of galloping of 1: 2 rectangular cylinder by its unsteady pressure characteristics. In: *Doboku Gakkai Ronbunshu* 1984 (1984), Nr. 344, pp. 235–241

Yu & Kareem 1998

YU, Dahai ; KAREEM, Ahsan: Parametric study of flow around rectangular prisms using LES. In: *Journal of Wind Engineering and Industrial Aerodynamics* 77 (1998), pp. 653–662